Passive Multichannel Analysis of Surface Waves (MASW) study over salt dissolution voids

Dissertation submitted to

Department Angewandte Geowissenschaften und Geophysik

Lehrstuhl für Angewandte Geophysik

Montanuniversität Leoben, Austria

March, 2015

Birgit Leitner

I declare in lieu of oath, that I wrote this thesis and performed the associated research myself, using only the literature cited in this volume.

BIRGIT LEITNER

Acknowledgement

Ich möchte mich in erster Linie beim Universitäts- Zentrum für Angewandte Geowissenschaften (UZAG) für die Möglichkeit der Durchführung dieser Arbeit bedanken.

Ein besonderes Dank gilt dem Kansas Geological Survey, insbesondere Dr. Rick Miller, für Unterstützung in fachlicher, organisatorischer und menschlicher Hinsicht, Dr. Julian Ivanov und der gesamten "Seismic Crew".

Mein Dank geht auch an das gesamte Angewandte Geophysikalische Department der Montanuniversität Leoben für menschliche, fachliche und organisatorische Unterstützung, insbesondere Prof. Dr. Karl Millahn und Christiane Pretzenbacher.

Besonders danken möchte ich Ronald und meiner Familie für ständige Motivation, Geduld und alles andere was nicht gesagt werden kann und muss.

Als die Zeit erschaffen wurde, wurde genug davon gemacht! (nach einem irischen Sprichwort)

TABLE OF CONTENTS

Abstract

The passive Multichannel Analysis of Surface Waves (MASW) provides information about the shear wave velocity structure of the subsurface by using background noise (traffic, wind, etc.) as seismic source. Especially sensible areas profit from the fact that no additional vibrations have to be performed. Furthermore, the sources used in passive MASW provide signals with lower frequencies, which enable higher investigation depths. For these characteristics the passive MASW method is mainly applied in this study.

A former salt dissolution-mining field in Hutchinson, Kansas (USA) is the testing area used in this study. In succession of excessive mining, voids formed in the subsurface and in some cases, as a consequence of migrating processes, sink holes. As the former mining field borders directly on the city and is intersected by a busy railroad line, some of the former production wells have been chosen, to investigate existing voids underneath and classify their risk of collapse, by determining the shear wave velocity and indirectly, the stress/strain conditions over the voids.

The study exposes on the one hand developments of the passive MASW method and on the other hand the study reveals the condition of different migrating voids and their surroundings, with the help of the new developments in the method.

The real datasets of Hutchinson were processed with the aid of the program SurfSeis® and further software developed as part of this study. To obtain an optimal result in resolution, depth of investigation and in the amount of depth profiles, a 2D receiver array is necessary. With the 2D spread it is possible to locate the direction of the recorded energy. From the overall array several sub-arrays were selected. The sub-arrays have receivers within a narrow rectangle that is orientated towards the maximum incoming energy. The signals of each rectangle are stacked over narrow limits around the azimuth of maximum incoming energy.

The trains as passive sources produced signals with frequencies down to 3.5Hz and due to the developments of the passive MASW method the signals could be resolved and investigation depths up to 70m were achieved (active MASW limit in the Hutchinsons area approx. 20m). An obvious difference in the shear wave velocities and subsequently in the stress field were determined, between areas with voids underneath and analogy terrains with no voids underneath. Also evidences for an existence of galleries between voids could be detected. A differentiation for a relative risk of collapse between the investigated locations was possible.

Zusammenfassung

Die passive Multichannel Analysis of Surface Waves (MASW) liefert, mit Hintergrundlärm als seismische Quelle (Verkehr, Wind,...), Informationen über Scherwellen-Geschwindigkeitsabfolgen im Untergrund. Besonders sensible Areale profitieren von der Tatsache dass keine zusätzlichen Vibrationen auf den Untergrund ausgelöst werden müssen. Zudem liefern, die in der passiven MASW verwendeten Quellen, niedrigere Frequenzen, die eine größere Erkundungstiefe zulassen. Diese Charakteristika sind der Hauptgrund für die Anwendung der passiven MASW in dieser Studie

Testareal für die vorliegende Arbeit war ein ehemaliges Feld für Salzgewinnung, in Hutchinson, Kansas, (USA). Wegen exzessiver Salzgewinnung in der Vergangenheit, haben sich um mehrere Förderbohrungen Hohlräume gebildet und in einigen Fällen als Folge von Migrations-Prozessen Erdfall/Einsturzschlünde aufgetan. Da das ehemalige Salzgewinnungsfeld direkt an der Stadtgrenze liegt und von einer viel befahrenen Eisenbahnlinie durchquert wird, wurden einige der ehemaligen Förderbohrungen ausgewählt, um mit Hilfe der Schwellen-Geschwindigkeiten und indirekt dem Spannungsfeld, existierende Hohlräume zu untersuchen und ihr Einsturzpotential zu klassifizieren.

Die Studie zeigt einerseits die Entwicklungen der passiven MASW Methode und andererseits, mit Hilfe der weiterentwickelten Methode, die Zustände verschiedener Hohlräume und deren Umgebung.

Die Echt-Datensätze von Hutchinson wurden mit Hilfe des Programms SurfSeis® und zusätzlich während dieser Arbeit entwickelten Programmteilen bearbeitet. Um optimale Ergebnisse in Auflösung, Erkundungstiefe und der Anzahl von Tiefenprofilen zu erhalten, ist eine 2D Geophon-Anordnung notwendig. Mit der 2D Anordnung ist es möglich die Richtung der aufgenommenen Energie zu lokalisieren. Von der gesamten Geophon-Auslage werden kleinere Geophongruppen ausgewählt. Die Geophone liegen dabei innerhalb eines schmalen Rechtecks, wobei die Längsachse einer Verlängerung der Richtung der maximal einkommenden Energie entspricht. Die Signale jeder Geophon-Untergruppe werden über schmale Limits um die Richtung der maximalen Energie gestapelt.

Durch die Verwendung von Zügen als seismische Quelle können Frequenzen bis zu 3,5 Hz erreicht werden und auf Grund der Entwicklungen in der passiven MASW Methode konnten diese Signale aufgelöst und Erkundungstiefen bis zu 70m erreicht werden. (aktiv MASW Limit im Hutchinson Areal bis 20m). Auf Grund der Unterschiede in den ermittelten Scherwellen Geschwindigkeiten war es möglich zwischen Gebieten mit unterlagernden Hohlräumen und unbeeinflussten Analogie –Gebieten zu schließen. Ebenso konnten Anzeichen auf vorhandene Tunnels zwischen den Hohlräumen erkannt werden. Durch einen Vergleich der umliegenden Geschwindigkeitsfelder war es mögliche das relative Potential für die Gefahr eines Einsturzes zwischen den untersuchten Arealen zu ermitteln.

1 Introduction

Seismic surface waves generated by earthquakes have been used for a long time for investigations of the Earth's crust and upper mantle. These methods have been adapted to shallow investigations using controlled sources and small arrays of receivers.

The Multichannel Analysis of Surface Waves (MASW) provides information about the shear wave velocity structure of the subsurface and is, depending on the used source, divided into active (controlled, in locality and time; use of sledgehammer, weight drops, explosives, etc.) and passive (background noise, traffic, wind, etc.) MASW. Passive MASW provides signals with lower frequencies that enable higher investigation depths. For these characteristics the passive MASW method is mainly applied in this study.

Several authors already experimented with the application of passively originated surface waves (e.g. Aki, 1957, Asten, 1978, Louie, 2001, Okada, 2003, Suzuki & Hayashi, 2003, Yoon & Rix, 2004, Park et al., 2004, Park et al, 2005, Park, 2008, Park & Miller, 2008). The passive MASW method has been formed out of the Microtremor Survey Method developed in Japan more than 50 years ago and has been divided in the later years into 2D passive remote MASW and 1D passive roadside MASW.

The extremely high number of geophones (up to 360 receivers) used for this study and the ideal test area which provides known underground voids and uninfluenced analogy areas, should make it possible, to test the passive MASW applicability, to find constrains and to achieve further improvements of the method.

The testing area it's a former salt dissolution-mining field, in Hutchinson Kansas. Because of excessive mining, voids have been formed and in some cases as a consequence sink holes.

For this study some of the former production wells have been chosen, to investigate existing voids underneath and classify their risk of collapse, by using the passive MASW method and determining the shear wave velocity and indirectly, the stress/strain conditions over the voids.

The present study was undertaken with three specific goals:

1. Investigations on the passive MASW process on various real datasets, with a moving train as source and a large number of receivers.

2. Applicability test: detection of s-wave-velocity differences, of the passive MASW method (in combination with active MASW) over relatively deep existing salt dissolution voids (60 m and deeper).

3. If applicable, to reveal the relative risk of collapse for certain voids and the detection of eventually existing galleries with optimally tuned receiver configurations; to give advices if there is a need for filling up the voids and, if possible, to give recommendations for a priority list for the filling process.

The Investigation on the passive MASW method is discussed in chapter *6.Advances in the Passive MASW method.* Applicability of the method, the results from the different sites and the evaluation of the risk of collapse are handled in chapter *7.Results and interpretation of the investigated areas.*

2 Surface waves

Any disturbance of an elastic solid generates waves. There are body waves (compressional and shear waves) as well as surface waves. The latter are the one discussed in this paper. Surface waves are, as the name already implies, bond to and traveling along the earths free surface. Two different types are generally distinguished: Love and Rayleigh waves (**Figure 2.1**).

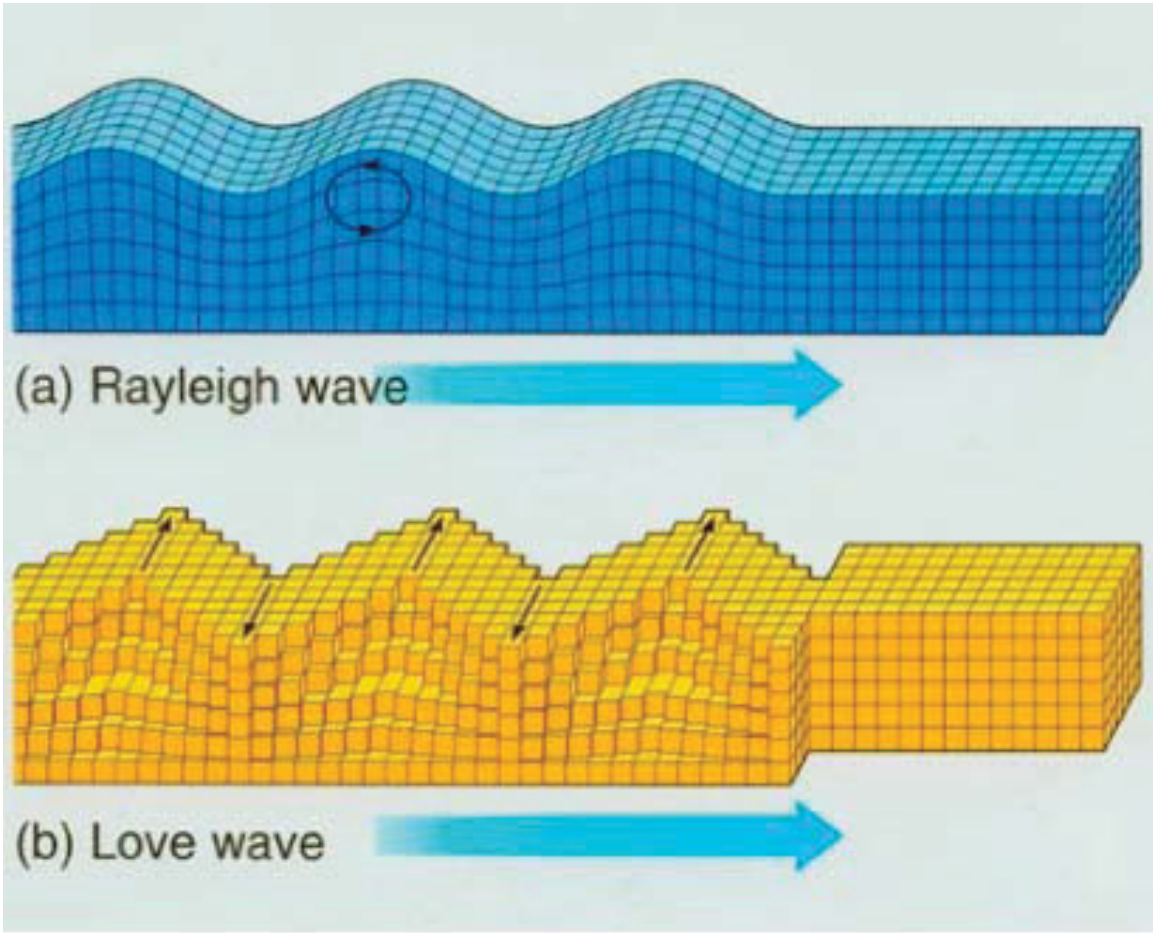

Figure 2.1 *a) Rayleigh waves have a particle displacement, which lies parallel to the direction of the propagation and normal to the Earth's surface; b) Love waves have a particle displacement, which is normal to the propagation direction and parallel to the Earth's free surface (after Brown & Musset, 1981).*

2.1 Rayleigh wave

Rayleigh waves develop from the interference of compressional or longitudinal waves (P waves) and transversal or shear waves (S waves). S waves are generally split into a vertically (SV) and horizontally polarized (SH) wave. SH waves are complex to generate. SV waves comprise motion in vertical direction and can develop easily. In more detail, when an incident P wave interacts with a free surface as illustrated in Figure 2.2a, as result reflected P waves and reflected SV waves are produced. In Figure 2.2b is shown the contrary situation, when the SV wave is the incident wave and reflected P and SV waves are produced.

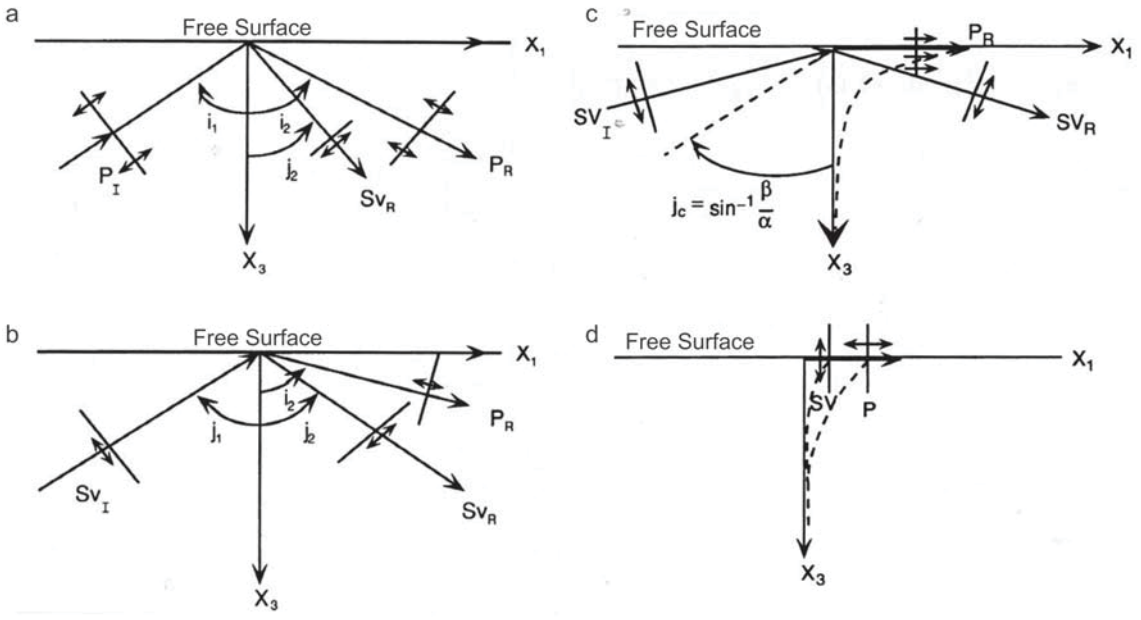

Figure 2.2 *a) Interactions of an incident P wave with a free surface. b) Interactions of an incident SV wave with a free surface. c) SV wave with a postcritical incident angle on a free surface results in a evanescent P wave and a reflected, phase shifted SV wave. d) The interference of evanescent P and SV waves, that propagate along the free surface, results in the Rayleigh wave. (From Lay & Wallace, 1995)*

If an incident SV wave interacts with the free surface at a critical angle j_c (=j_1 in Figure 2.2b) the reflected P wave travels along the free surface (Figure 2.2c). In Eq. 2.1 i_2 has 90° when j_1 becomes critical. If j_1 becomes post critical the P wave is captured along the free surface.

$$p = \frac{\sin(j_1)}{\beta} = \frac{\sin(i_2)}{\alpha}$$
$$\alpha > \beta$$
$$j_c = \sin^{-1}\left(\frac{\beta}{\alpha}\right)$$
$$i_2 = 90° \qquad (2.1)$$

The captured P wave is called evanescent wave, because the amplitude is decaying exponentially with depth. The evanescent P wave motion transmits no energy back into the underground. Because of the traction free behavior of the free surface, an evanescent P wave cannot travel alone on the free boundary. For a horizontally trapped SV wave the same rules are effective. Lord Rayleigh ((former) Strutt, 1887) found that the surface boundary conditions are fulfilled, if evanescent P waves and evanescent SV wave are traveling simultaneously along the free surface (Figure 2.2d). Thereby it is necessary that the propagation velocity (c) of the resulting wave is lower than the shear wave velocity β of the medium (c<β<α = P wave velocity). Otherwise the SV energy is reflected from the boundary and the situation is again as illustrated in Figure 2.2c. The interference of the coupled P and SV wave is called Rayleigh wave.

The Rayleigh wave spreads cylindrical and the amplitude decays as $1/\sqrt{r}$ with distance r from a source. The vertical particle motion exceeds the horizontal one by 1.5 and is hence elliptical. On the surface the particle displacements is retrograde, which means contrary to the propagation direction. The wavelength (λ) of a Rayleigh wave is defined as the horizontal length between two soil particles, which have the identical horizontal and vertical displacement (Figure 2.3).

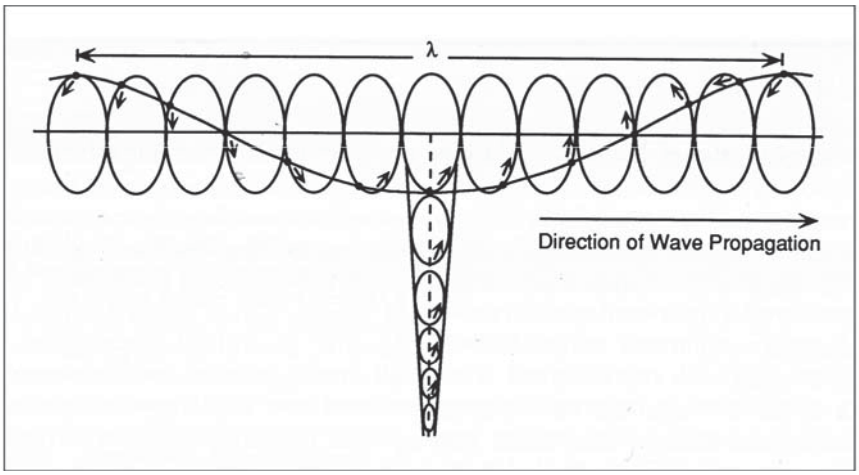

Figure 2.3 *Particle motion of a Rayleigh wave and fast decay of amplitude with depth (from Lay & Wallace, 1995).*

At a depth of about λ/5 (=h in Figure 2.4) the horizontal displacement is zero (Lay and Wallace, 1995). Below the depth were there is no horizontal particle motion, the elliptical motion changes the sense of rotation hence the Rayleigh wave is traveling with a prograde particle sense. At a depth of λ/2 the horizontal motion has again increased to 10% of the surface motion, and the vertical motion reaches 30% of the vertical motion on the free surface.

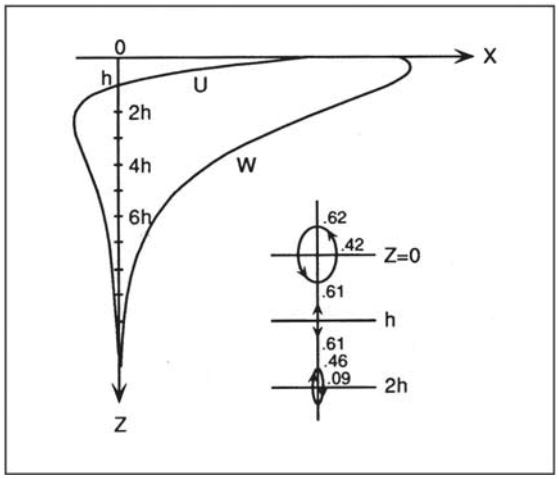

Figure 2.4 *Horizontal (U) and vertical (W) displacements of particles in a homogenous half space. Above depth h (=λ/5) the particle motion is retrograde, below prograde. (From Lay & Wallace, 1995)*

Rayleigh waves propagate in a homogeneous halfspace non dispersive; in the real layered earth model they show dispersion. Figure 2.5 shows seismic record of a geophone registering vertical movement. After the arrival of the P waves (P, pP, PP, pPP) and the S wave (sS) the Rayleigh wave is recorded (LR). The Rayleigh wave signal lasts in the record of Figure 2.5 for 10 min. The high amplitude signal shows perfectly the effect of the dispersion: Signal with longer wavelength arrive first, signal with shorter wavelength arrive later.

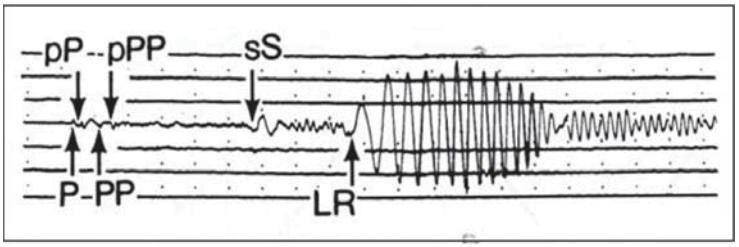

Figure 2.5 *A vertical component geophone has registered body wave arrivals (P, pP, PP, pPP, sS) and a dispered Rayleigh wave (LR). (From Lay & Wallace, 1995)*

2.2 Love wave

SH- waves trapped in a near surface layer were first detected by A. E. H. Love in 1911, and were therefore named Love waves. For the explanations below, a model is used, where one layer (shear wave velocity β_1) is placed above a half space (shear wave velocity β_2).

SH- waves are always totally reflected by the free surface. To trap SH waves they have to be reflected from a layer boundary back to the surface (Figure 2.6). If the velocity of the upper layer is larger than the one of the half space, automatically the angle of the transmitted wave (j_T) is smaller than the angle of the incident wave (j_I), ($\beta_1 > \beta_2, j_T < j_I$). Hence, transmitted energy will always depart from the boundary and travel into the half space.

For the situation, where a low velocity layer is located above a high velocity half space, the angle of transmitted wave is larger than the one of incident wave ($\beta_1 < \beta_2, j_T > j_I = j_R$). In this case the transmitted wave is refracted closer towards the low velocity layer, but is still leaking energy away into the half space. In the situation where we have a low velocity layer over a half space, there must exist a critical incident angle ($j_I = j_C$), where the resulting Transition wave angle (j_T) becomes 90°, and the wave is hence behaving as a head wave. In case of a post critical incident angle ($j_I > j_C$), the SH wave is reflected totally between free surface and layer boundary which implies the SH wave is trapped in the near surface layer.

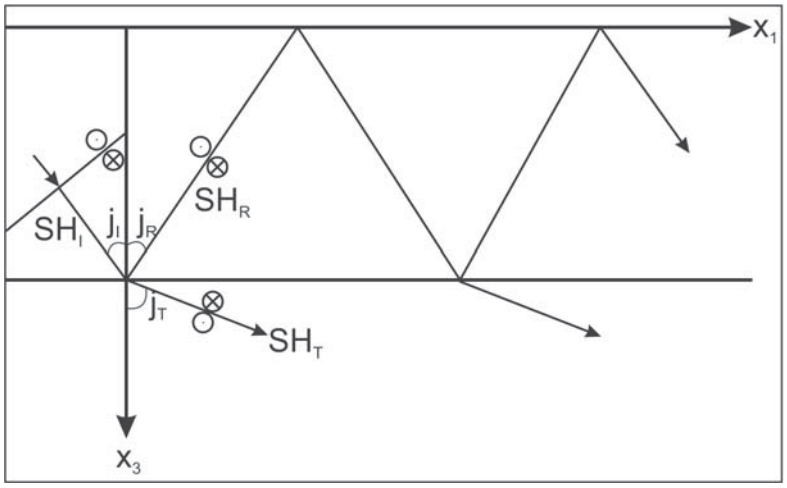

Figure 2.6 *Geometry of a repeatedly reflected SH wave. (After Lay & Wallace, 1995)*

The MASW method used for this study is based on Rayleigh waves. When in the following chapters the term “surface waves” is used, it implies exclusively the Rayleigh waves, unless explicitly mentioned.

2.3 Dispersion

For an accurate explanation of the dispersion, the term “velocity” has to be refined into phase velocity and group velocity. The phase velocity is the velocity of a signal that travels with one certain frequency. If a ground is stimulated with a seismic source, waves covering a range of frequencies are generated. Waves with different frequencies interfere with each other, constructively or destructively and determine the ground motion. If two or more different harmonic waves interfere constructively, the envelope of the cyclic interference pattern travels with a certain group velocity. In Figure 2.7 the green curves show waves of a certain frequency (f) that travel with a certain phase velocity (C_f). The result of the interference is shown by the blue curve in the bottom of Figure 2.7. The red dotted line is the envelope of the interference pattern. The envelope of the multi frequency signal moves with a certain group velocity.

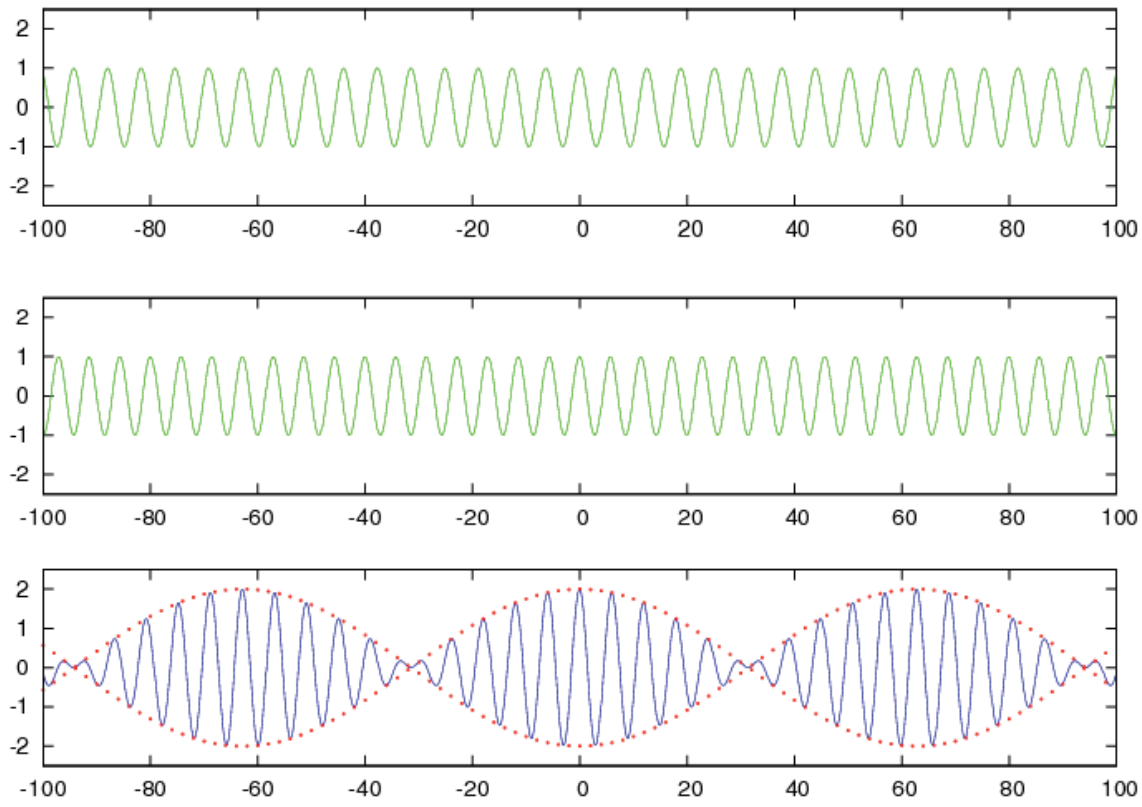

Figure 2.7 *The green waves differ in frequency and phase from each other and travel each with a certain phase velocity. The blue curve in the bottom is the interference pattern of the two upper green curves. The red dotted envelope travels with the group velocity. (From Subirana et al., 2011)*

The earth is composed of a variety of layers, with different properties, which is essential for the development of the dispersion of Rayleigh waves.

Directly at the moment of triggering a source, the surface wave can be considered as an undispersed pulse. Signals with larger wavelength (λ) reach deeper into the earth because of the elliptical propagation of the Rayleigh wave, and are therefore affected by the properties (thickness of layer, density, P- and S wave velocity etc.) of deeper layers (Figure 2.8). As the density normally increases with depth and with it also the velocity of a layer, larger waves travel with faster phase velocity (C_f).

$$\lambda = C_f / f \qquad (2.2)$$

If a Rayleigh wave is propagating along the surface, away from the source, the initial energy is splitting up and the wave train gets more extended with increasing distance to the source (Figure 2.5).

Note: Dispersion is the ability of a wavetrain to split up into waves with different travel velocities. In case of the Rayleigh wave the elliptical movement determines for each frequency the achievable depth zone and with the velocity properties of each distinctive wave.

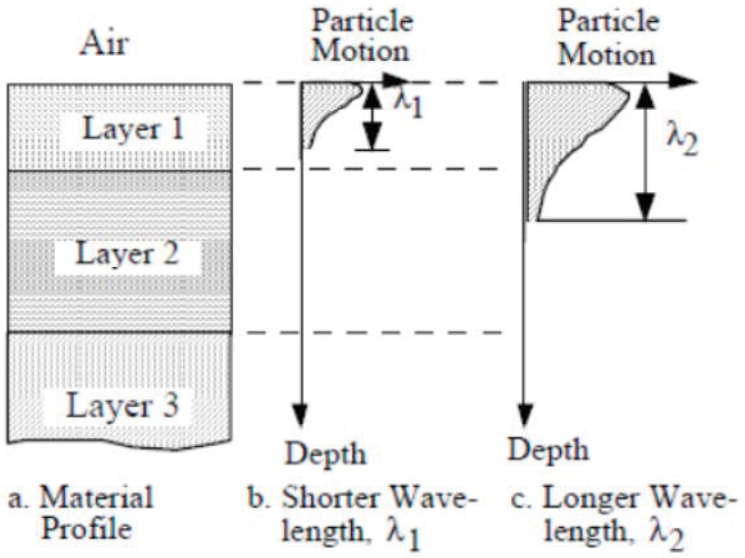

Figure 2.8 *Particle motions of surface waves with different wave length (from Rix and Stokoe, 1989).*

Splitted Rayleigh waves can have for one specific frequency, a variety of phase velocities and inversely. The lowest velocity of a given frequency belongs to the fundamental mode; the next higher velocity is associated with the second mode and so on. Figure 2.9 shows a one-dimensional example illustrating these modes of propagation. A string is fixed at two end

points. The fundamental mode (n=0) has no nodes, there are no places where the motion is zero The strings that have one or more nodes (n>0) belong to a higher mode function.

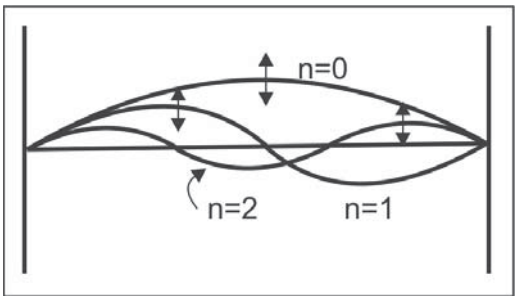

Figure 2.9 *Three strings with fixed endpoints show the first three modes that are allowed by the given boundary conditions. (From Lay & Wallace, 1995)*

3 Surface Wave Analysis

3.1 History of Surface Wave methods

The aim of surface wave investigation in the past was studying the layered earth model to extract information mainly about shear wave velocity (Vs), compressional wave velocity (Vp) and the thickness of the earth layers (h) (Ewing et al, 1957; Dorman et al, 1960; Dorman and Ewing, 1962; Bullen, 1963; Knopoff 1972; Kovach 1978; Keilis-Borok et al., 1989; Mokhart et al., 1988; Al-Eqabi and Herrmann, 1993; Herrmann and Al-Eqabi, 1991).

Engineering applications to investigate dynamic soil properties start in the 1950's (Van der Pol, 1951; Jones, 1955) and so the first surface wave method was evolved: the Steady-State Vibration technique. For this method a constant (steady-state) sinusoidal signal (mono-frequency) is induced into the soil; it follows a constant vertical sinusoidal displacement of particles in the surrounding subsurface. Two vertical sensitive receivers are positioned, and repositioned until the two recorded signals are both in-phase (Figure 3.1). After one in-phase point is found, the farther distant receiver from the source is repositioned to find the next in-phase position.

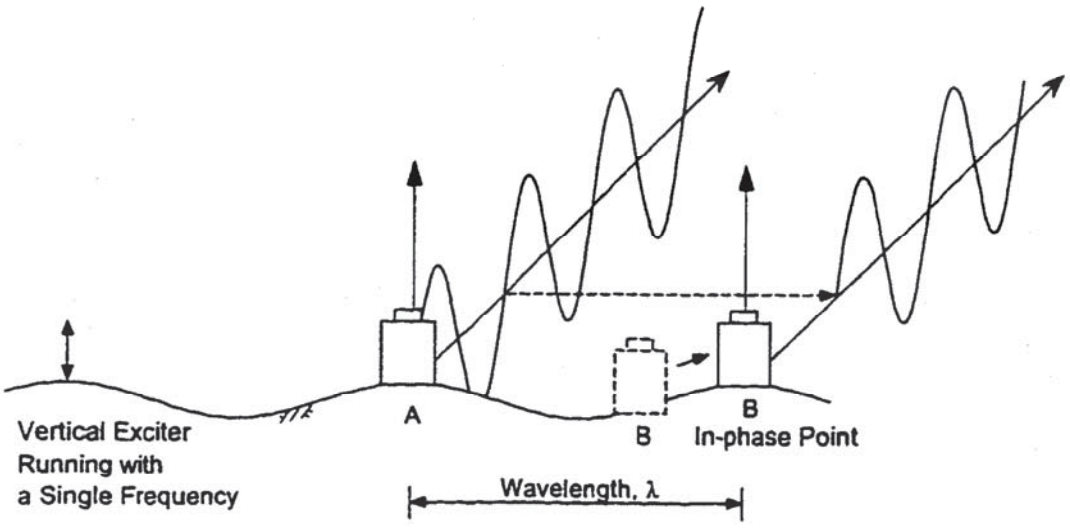

Figure 3.1 *Principles of Steady- State Vibration Measurements (From Joh, 1996)*

The procedure is repeated several times and with several frequencies. Figure 3.2 shows the curves, which have been created out of a set of measurements. The horizontal axis of the diagram represents the distance between two receivers. When the receivers are in-phase, the distance is a multiple of the wavelength of the emitted wave. The wavelength can be taken easily out of the diagram. The frequency is assumed identical to the initial signal, which has

been induced into the ground. The phase velocity is calculated with the simple relation between phase velocity (c_f), frequency (f) and wavelength (λ), shown in Eq 3.1.

$$c_f = f * \lambda \qquad (3.1)$$

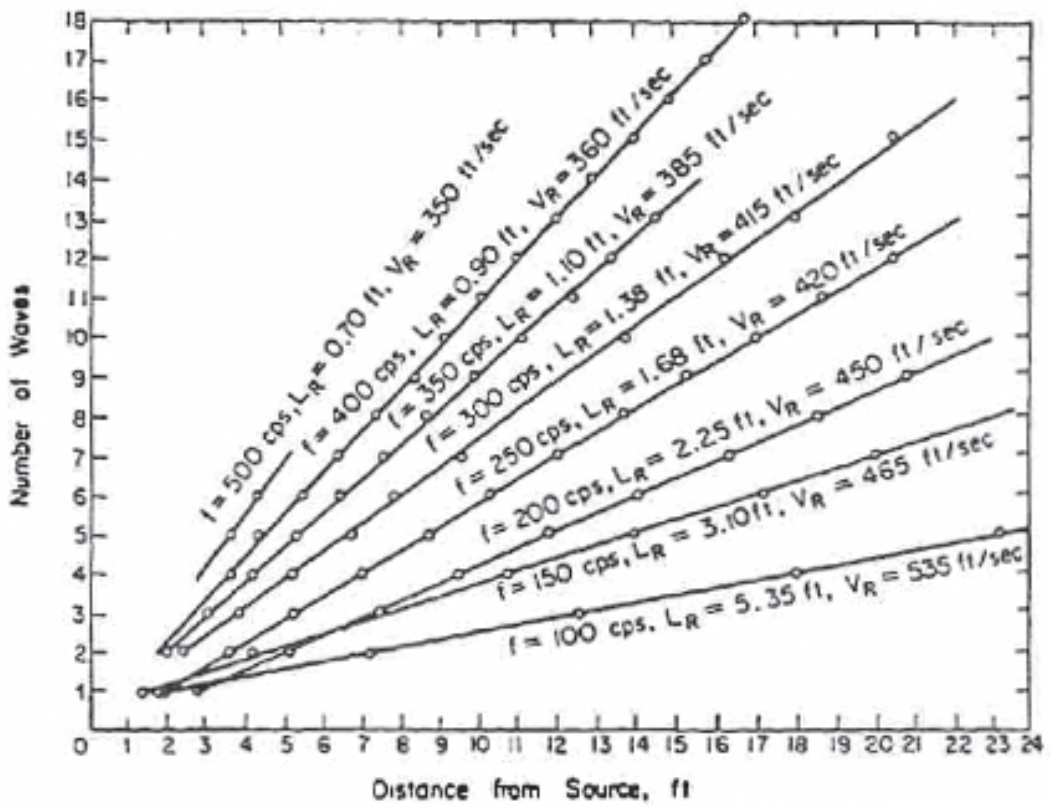

Figure 3.2 *Collected results out of a steady state measurement (From Richards, 1970)*

With the results it was possible to establish a dispersion curve. The dominant velocity for a investigation depth of λ/2 has been assumed as the velocity of the Rayleigh wave with wavelength λ. The phase velocities have been inverted with an empirically relation shown in Eq. 3.2 into shear wave velocities (Vs).

$$Vs \approx 1.1 * c_f \qquad (3.2)$$

The Steady-State Vibration method is a very time consuming technique, based on simplified models of earth and Rayleigh wave propagation.

The Steady-State Vibration technology has been further developed with the upgrading of processing equipment into the now known Spectral Analysis of Surface Waves (SASW). Nazarian and Stokoe (1984) used an active source (impulsive or harmonic) and recorded the Rayleigh wave field with two receivers varying several times the receiver spacing. With the digital signal analyzer in the 1980's it became possible to solve frequency-domain calculations immediately. It made the acquisition of data and the quality check easier. The generation of multi frequency signals allowed analyzing the surface waves with Fast Fourier Transformation (FFT). The separation of the multi frequency signal via FFT improved the method in comparison to the former Steady-State Vibration method considerably.

The next section discusses more in detail the Multichannel Analysis of Surface Waves (MASW) and with it also the basics for data acquisition, dispersion curve analysis, and inversion, which are partly also effective for the former methods.

3.2 Multichannel Analysis of Surface Waves (MASW)

The MASW method tries to reduce time and effort in the field during data acquisition and also to reduce processing time, using a multichannel system. Depending on the used source type, active source (hammer, weight drop, accelerated weight drop, explosives) or passive source (traffic, wind and other background noise), the method is divided into passive and active MASW. The main processing steps are similar for both methods. As the position of passive sources is unclear the passive MASW method needs some additional processing steps, which will be explained and investigated later in more detail.

The MASW procedure is separated in three main steps: Data Acquisition, Dispersion Curve Analysis and Inversion.

3.2.1 Data Acquisition

The MASW acquisition process in general and the geophone array configuration in particular are very similar to the methods used in standard reflection seismics. Figure 3.3 shows the concepts for data acquisition: A multichannel seismograph is connected with a set of receivers. The number of receivers depends on the properties of the subsurface, the depth of investigation and the desired resolution.

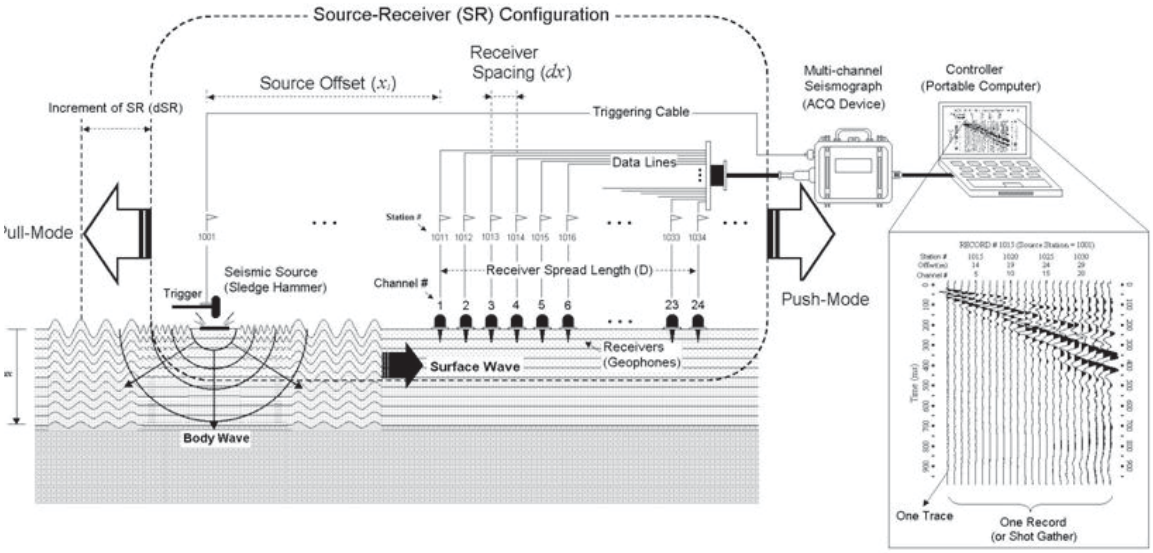

Figure 3.3 *Schematic Illustration of the Field surveying method for active MASW (from www.masw.com)*

A relatively complicated passive MASW array is demonstrated in Figure 3.4. For complex arrays it is necessary to design the geometry of the geophones and the seismograph positions in advance. A scheme (Figure 3.4c) that shows position and connection of geophones, seismographs and cables avoids errors on the field and confusion afterwards in the office.

To record Rayleigh waves, vertical low frequency receivers must be used. The data collected for this work are recorded with 4.5 Hz geophones. As the ratio of amplitudes between signals of different frequencies has no influence on the results, also lower frequencies, as the guaranteed 4.5Hz, can be recorded, analyzed and interpreted. Even if spike-coupled geophones are unmatched in their sensitivity, landstreamer deliver still adequate results and are therefore often used in engineering applications.

To trigger the recording of a shot gather the seismograph is also connected over a trigger cable with the source. There are different methods for triggering. If the source is a sledgehammer a contact trigger can be attached on a metal plate. When sledgehammer and plate are in contact, the circuit is closed and the system starts to record. Another method to trigger recording, works over a vibration trigger. This trigger can be attached with a tape one the handle of the sledgehammer, by hitting the plate the system starts to record.

There are various types of sources. For the active method a simple sledgehammer can be used. The generated frequencies are generally inversely proportional to the power, which is used to produce the signal. To excite low frequencies, which imply a higher depth of investigation, a weight drop, or better an accelerated weight drop (Figure 3.5) is recommended. For Passive

Remote MASW and Passive Roadside MASW (e.g. Park et al., 2007) ambient noise (trains, traffic noise...) is used as source. Passive sources in general are characterized by low frequency signals and may provide greater depths of investigation than active sources.

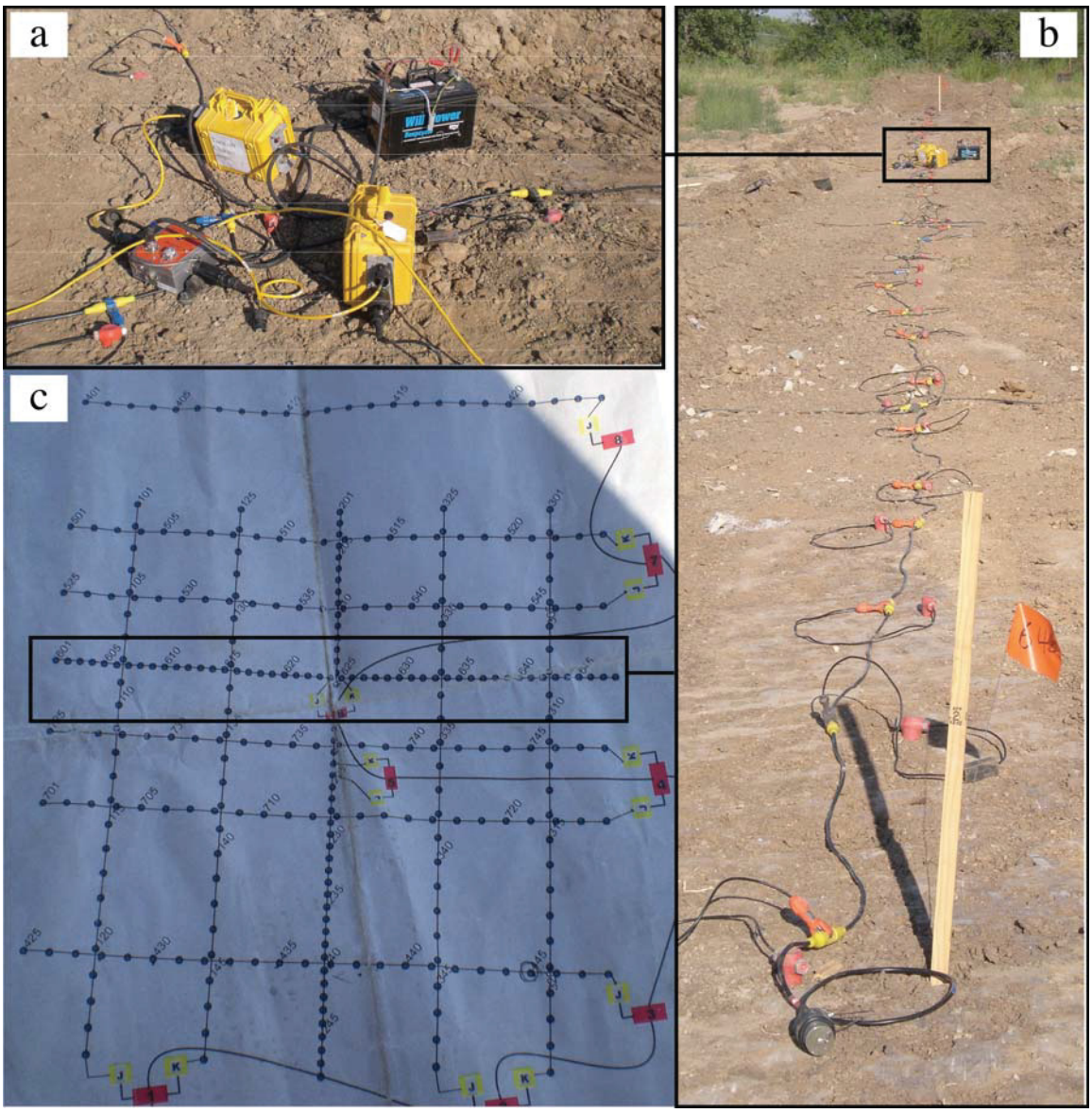

Figure 3.4 *a) 24-channel seismograph powered over a car battery and attached to the geophone cables. b) Line of 24 4.5Hz spike geophones. c) To avoid confusion in the field, complicated receiver arrays (for passive MASW) have to be planned in advance.*

Figure 3.5 *Accelerated weight drop on a tool cat, designed by the Geophysical Department of the Kansas Geological survey.*

The investigation depth Z_{max} corresponds roughly to one half of the longest wavelength recorded (Eq. 3.3, Rix and Leipski, 1991). The length *D* of the receiver spread determines the longest wavelength (at the lowest frequency) that may be recorded ($D \approx \lambda_{max}$). Selection of receiver spread and source are therefore key points in the planning of the data acquisition.

$$Z_{max} = \frac{C_{f\,min}}{2 f_{min}} = 0.5 * \lambda_{max} \qquad (3.3)$$

Z_{max} ... maximum investigation depth

C_{fmin} ... phase velocity of the wave with the lowest frequency

f_{min} ... lowest frequency produced

λ_{max} ... maximum wave length

The smallest recordable wavelength depends on the receiver spacing (dx). The receiver spacing defines hence the shallowest resolvable depth of investigation (Z_{min}).

$$Z_{min} = k * dx \quad (0.3 \leq k \leq 1) \qquad (3.4)$$

Z_{min} ... shallowest resolvable depth

dx ... receiver spacing

k ... empirical factor depending on soil composition

Topographic changes should be less than about 10% of the receiver spread otherwise surface wave generation is not continuous. A continuous change in topography over several receiver spreads causes no difficulties for surface wave generation. Figure 3.6 shows simple sketches providing guidelines for a reasonable approach for data acquisition on field with various topographies.

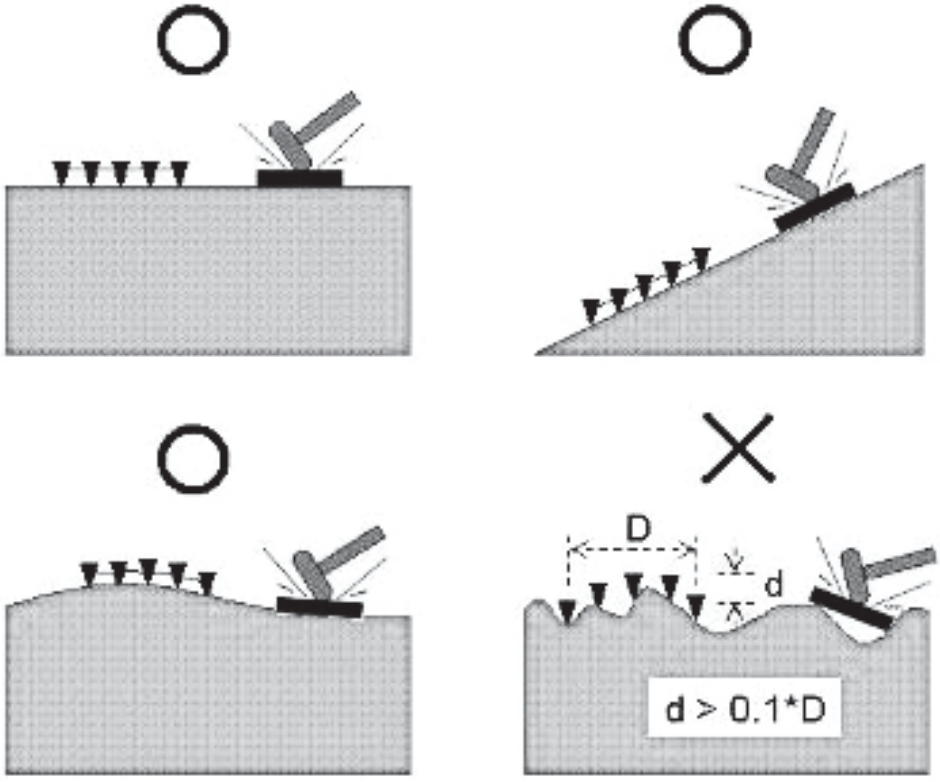

Figure 3.6 *Different terrain conditions, marked as convenient (O) and inconvenient (X) for MASW (after www.masw.com).*

Furthermore, the so called near field effect has to be considered. This effect plays a role when the source receiver offset is too short. As indicated in chapter 2, Rayleigh waves develop as interference pattern between P and SV waves, and they need a certain propagation distance (x_1) from the source to fully evolve (Richart et al., 1970). All calculations for surface waves are based on models with Rayleigh waves traveling as plane waves. According to Stokoe et al. (1994) the near source receiver offset (x_1) has to be half the longest wavelength (λ_{max}) to work exclusively with plane waves, which is equal with the maximum depth of investigation (Eq. 3.5).

$$x_1 \geq Z_{max} \qquad (3.5)$$

In addition to the near field effect, there is a far field effect to be considered, which is determined by the distance between source and furthest receiver. High frequency signals are attenuated more strongly than low frequency signals when traveling from the source through the receivers. If the receiver spread is too large, the high frequency surface wave signals are contaminated with body wave signals. This phenomenon can be seen for example in a decrease of the ground roll slope in the further traces, which appears as an increased apparent phase velocity.

For active MASW the typical receiver layout is a line with parameters (e.g. receiver spacing, source receiver offset, ...) calculated with the equations discussed above. For passive MASW a 2D receiver layout is necessary, to calculate the location or more exactly the direction of the origin of noise. Typical receiver layouts that have been used are circular or cross arrays (Park et al., 2005). The optimal receiver layout for passive MASW will be discussed in the following chapters in more detail.

As length of recording time, one second is usually chosen, with a sampling rate of 1 ms. A sampling rate of 1 ms allows to analyze frequencies up to 500 Hz, which corresponds to the Nyquist frequency. The Nyquist frequency is consistent with half of the sampling rate. In general, one recommends to analyze frequencies up to 50 or 60% Nyquist. Appropriate bandwidth limitations in acquisition or adjustments of sampling rate are part of correct survey planning.

As for active MASW suitable frequencies usually range between 5 and 70 Hz, a 1ms sampling rate is sufficient. The recording time of 1 second is in most cases ideal, because it avoids ambient noise from additional listening time. If extremely low velocities (<100m/s) occur, a longer recording time is advisable. In case of the passive MASW, longer recording times (e.g >20s) are beneficial so that the records can be split afterwards, according to sequences with most input. The sampling rate in the case of passive MASW can be reduced to 2ms, because the attention is focused on the lower, deeper reaching frequencies.

If the seismograph is normally also used for reflection seismic, it has to be taken into account that there is no low cut analog filter active.

3.2.3 Dispersion curve Analysis

The result of the data acquisition is a multichannel record, containing all the different wave types with variable arrival times at the geophones. Figure 3.7 shows a typical raw multichannel record, without any filter correction. More than 60% of the signals recorded in this multichannel record represent surface waves; the remaining part belongs to the body waves.

To create dispersion curves the data can be transformed from the time (t) - offset (x) domain into either a frequency (f) - wave number (k) domain or into a frequency (f) - phase velocity (C) domain. Several methods can be used for the transformation, for example for the f-k domain, the traditional f-k method can be used, or for the f-C domain, the Pi-Omega transformation (McMechan and Yedlin, 1981) and the Phase-Shift method (Park et al., 1998) can be applied. The SurfSeis© program used in this work is based on the Phase-Shift method and should therefore be explained below after Park et al. (1998).

A record R(x,t) with N channels is transformed with the Fast Fourier Transformation (FFT) into single frequency components $R_i(w)$ (i=1, 2, ..., N). The angular frequency (w) is calculated as $2\pi f$, *f representing frequency*. $R_i(w)$ can be expressed as a multiplication of a Phase term, $P_i(w)$, and an Amplitude term, $A_i(w)$. $P_i(w)$ is determined by the Phase velocity(c) for each frequency:

$$P_i(w) = e^{-j\Phi_i(w)} \qquad (3.6)$$

where

$$\Phi_i(w) = \frac{wx_i}{c} = \frac{w\{x_1 + (i-1)dx\}}{c} \qquad (3.7)$$

x_i... source receiver offset (i= channel number)

dx... receiver spacing

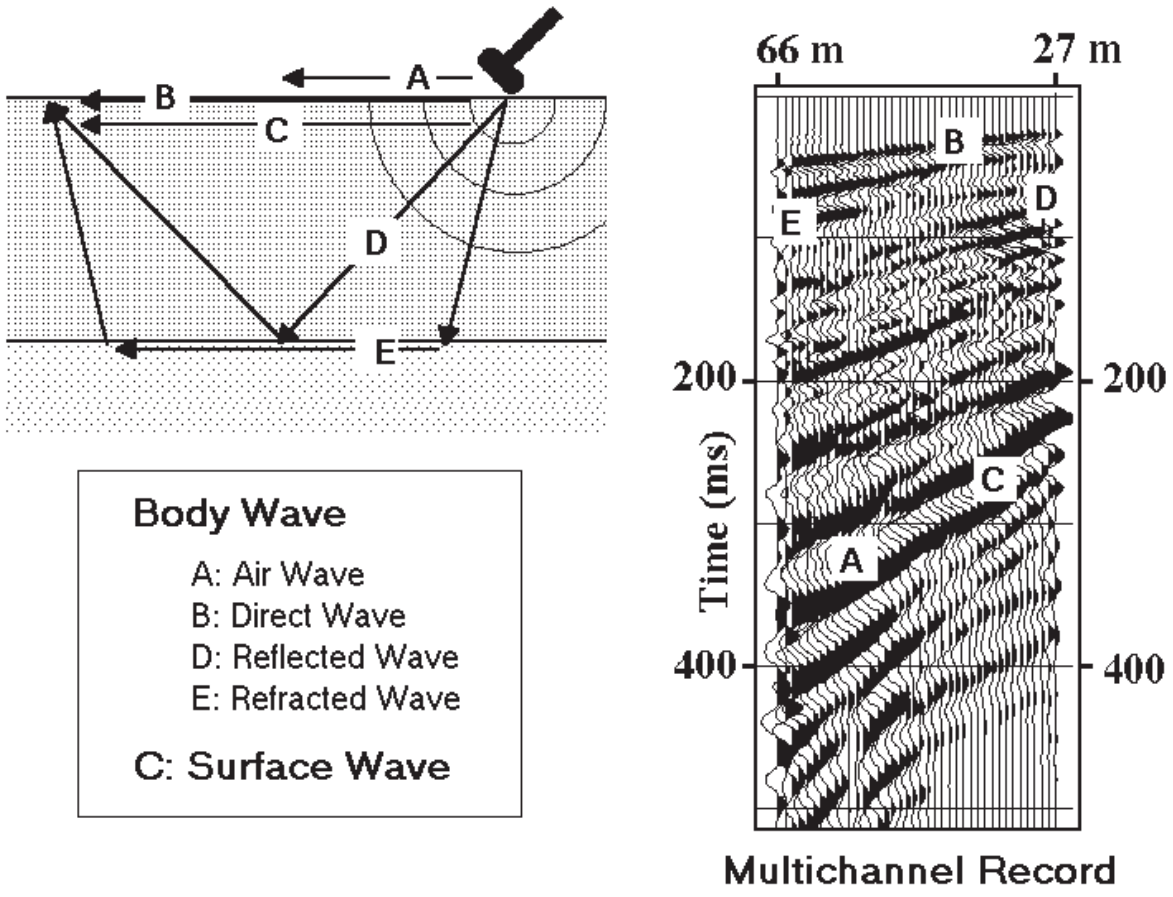

Figure 3.7 *Mutichannel record with different wave types(Park et al., 2001).*

The next processing step is an amplitude normalization for $R_i(w)$, to avoid unequal weighting caused by the offset dependent effect of attenuation and spherical divergence. As the amplitude information is not related to the phase velocity component, the normalization can be executed without loss of information needed for surface wave analysis.

$$R_{i,norm}(w) = \frac{R_i(w)}{|R_i(w)|} = P_i(w) \qquad (3.8)$$

Figure 3.8a illustrates a multichannel array in the time domain. The array has been transformed via FFT, in a Record with only 20 Hz signals. The uniform amplitudes demonstrate that the record is already amplitude normalized. As next step the amplitudes are summed up along a slope of a certain phase velocity. It shall be understood as an offset and phase velocity depended time shift of each trace and further a summation off all traces over the offset range (delay and

sum). The summation can be executed in the frequency domain:

$$A(c_T) = e^{-j\delta_{1,T}} R_{1,norm}(w) + e^{-j\delta_{2,T}} R_{2,norm}(w) + \ldots + e^{-j\delta_{N,T}} R_{N,norm}(w) \qquad (3.9)$$

where

$$\delta_{i,T} = w[\frac{\{x_1 + (i-1)dx\}}{c_T}] \qquad (3.10)$$

c_T... *testing phase velocity*

$A(c_T)$ is a complex number. The absolute value ($|A(c_T)|$) corresponds to the summed amplitude in the time domain.

In practice the array is scanned for a range of phase velocities, e.g. from 1m/s to 1000m/s, with a scanning increment of e.g. 10m/s. If the signals of the traces show along a slope of a certain velocity, C_{20Hz} (in Figure 3.8, 140 m/s), the same phases, the amplitude will reach a value A_{max}. If the phase velocity varies from C_{20Hz} the amplitude will be smaller than A_{max}.

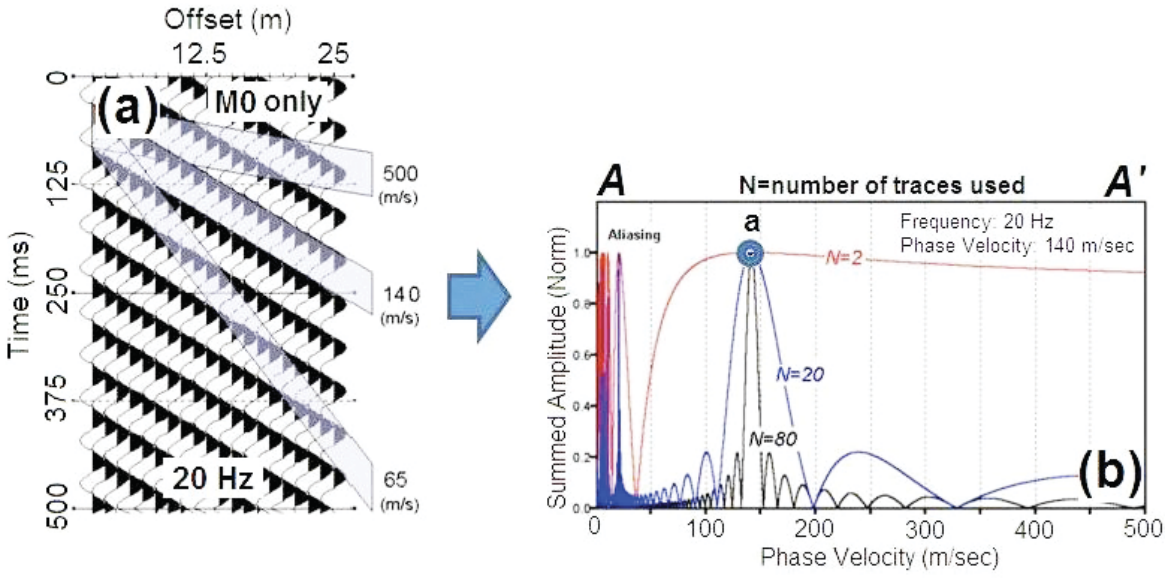

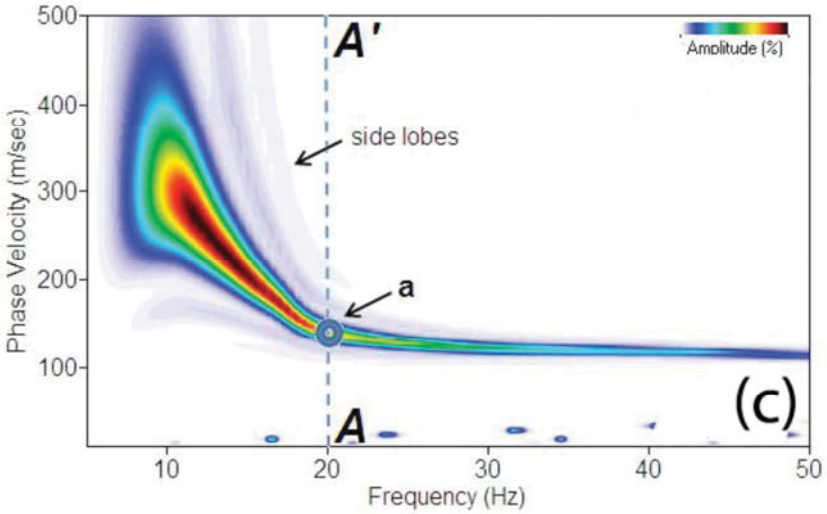

Figure 3.8 *a) A multichannel record for a frequency of 20Hz, amplitude normalized, with a phase velocity of 140 m/s. b) Summed amplitudes for phase velocities slopes between 0 and 500 m/s and variable a amount of traces. c) Frequency Phase velocity diagram showing a dispersion curve. (From Park et al 1998)*

The phase velocity versus amplitude diagram (Figure 3.8b) illustrates the behavior for the record in Figure 3.8a. Accuracy and resolution of the result increase with the number of available channels or traces.

If the record contains several modes, the amplitude phase velocity diagram Figure 3.8b will indicate more than one peak for one certain frequency.

Once a record is analyzed following this procedure for all the frequencies of interest, the amplitude distribution can be shown in a frequency phase velocity diagram, the energy pattern will appear as a dispersion curve (Figure 3.8c).

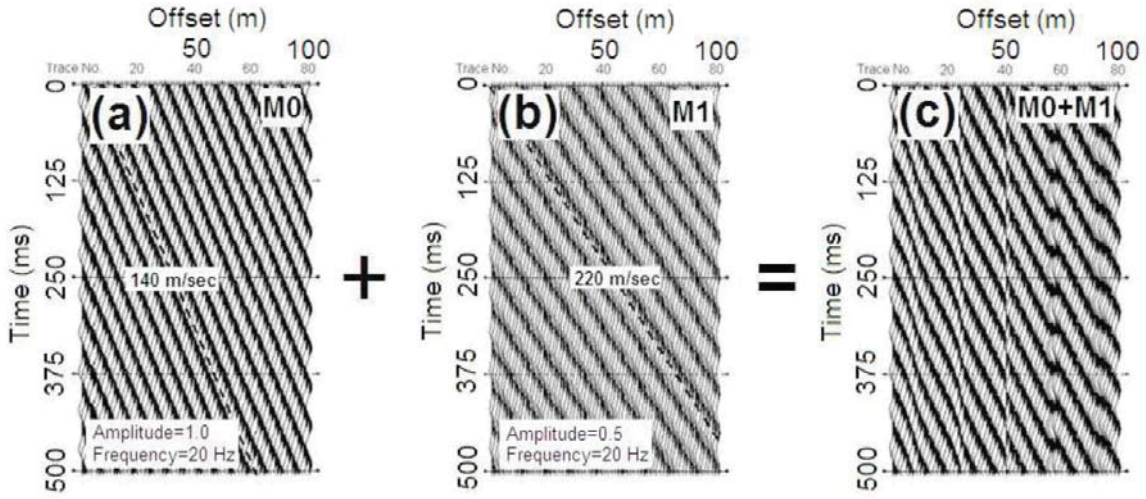

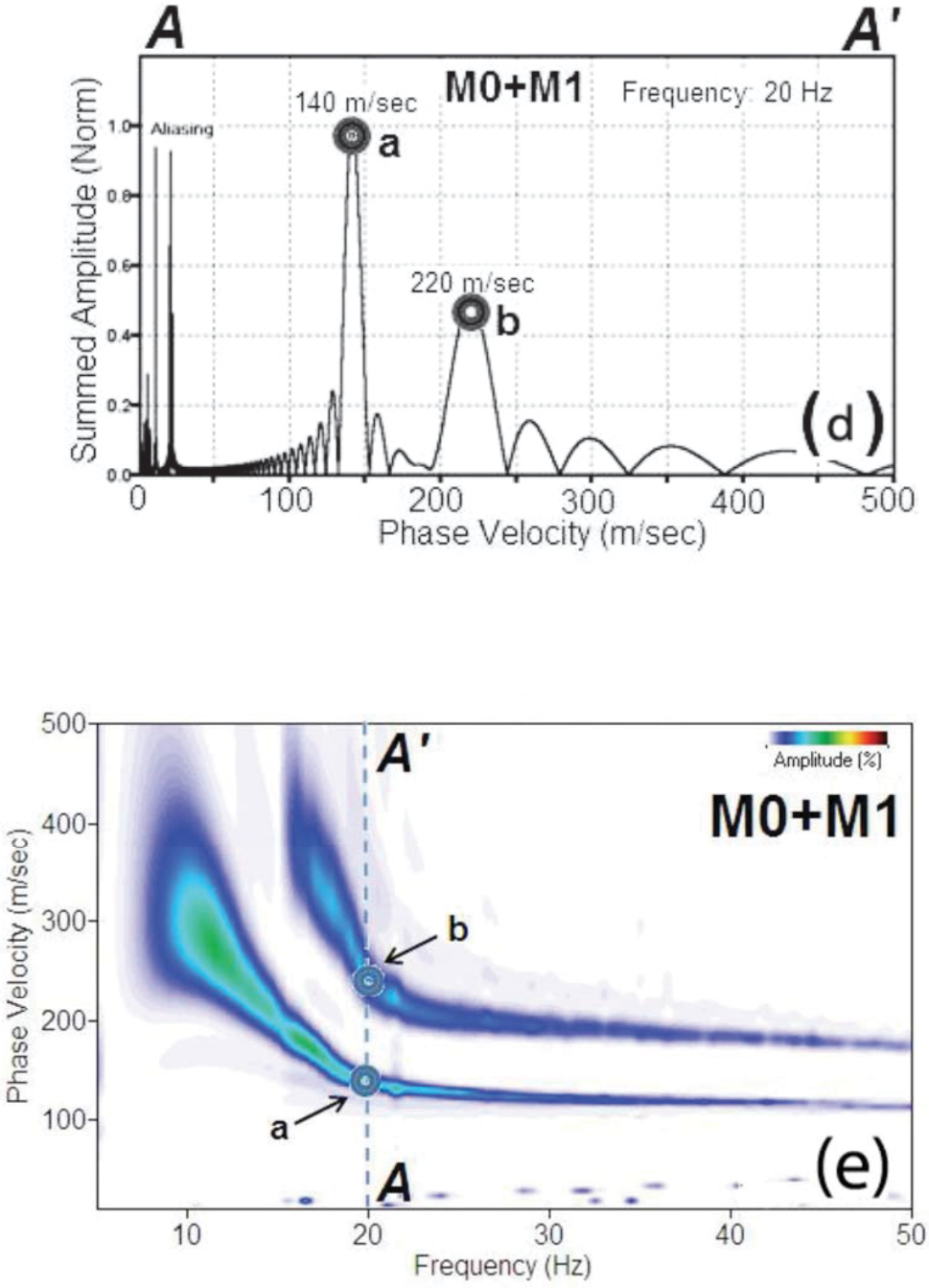

Figure 3.9 *a) A multichannel record for a frequency of 20Hz, amplitude normalized, with a phase velocity of 140 m/s. b) A multichannel record for a frequency of 20Hz, amplitude normalized, with a phase velocity of 220 m/s.), c) superposition of a) and b). d) Summed amplitudes for phase velocities slopes between 0 and 500 m/s, e) Phase velocity, frequency and energy diagram showing dispersion curves of fundamental mode and a higher mode. (From Park et al., 1998)*

If during recording of seismic data more than one mode of the surface waves has been produced or the amplitudes of the body waves are large enough, more than one mode can be present at one frequency. Figure 3.9a and b illustrate different phase velocities for a frequency of 20 Hz. The superposition of both records is shown in Figure 3.9c. If this record undergoes a full phase velocity scan, the amplitude phase velocity diagram (Figure 3.9d) will show a summation of two individual curves, and two peaks at different velocities. The peaks of higher modes can be found at higher velocities and are normally weaker in their amplitude than the fundamental mode. Whether the additional phase velocity is generated from a higher mode surface wave or a body wave can be seen, when all frequencies have been scanned.

Higher mode signals show in the summation of the energies in a 3D diagram with the parameters, phase velocity, frequency and amplitude a second dispersion curve that is consistent of energy concentrations at higher phase velocities for each frequency than the fundamental mode.

Because the source position in the Passive MASW method is, in general, unknown, the dispersion curve analysis of Passive MASW needs an azimuth as additional scanning parameter. More detail is discussed in later chapters.

3.2.4 Inversion

After accurate picking of a dispersion curve, the subsequent step is the search of an appropriate earth model that fits the data. The step, to find a cause (earth model), which has led to the result, is called inversion.

There are several possible types of surface wave input data (e.g. raw data, dispersion curves) that can be used for inversion to estimate the original earth model. The typical procedure used for the MASW method, is to invert the dispersion curves. Thereby a dispersion curve is compared with a various set of calculated (forward modeling) dispersion curves. By adjusting the calculated dispersion curve to the measured curve the calculated earth parameter should approach the original one (Figure 3.10).

The calculation of the theoretical dispersion curves follows the processing scheme developed by Schwab and Knopoff (1972).

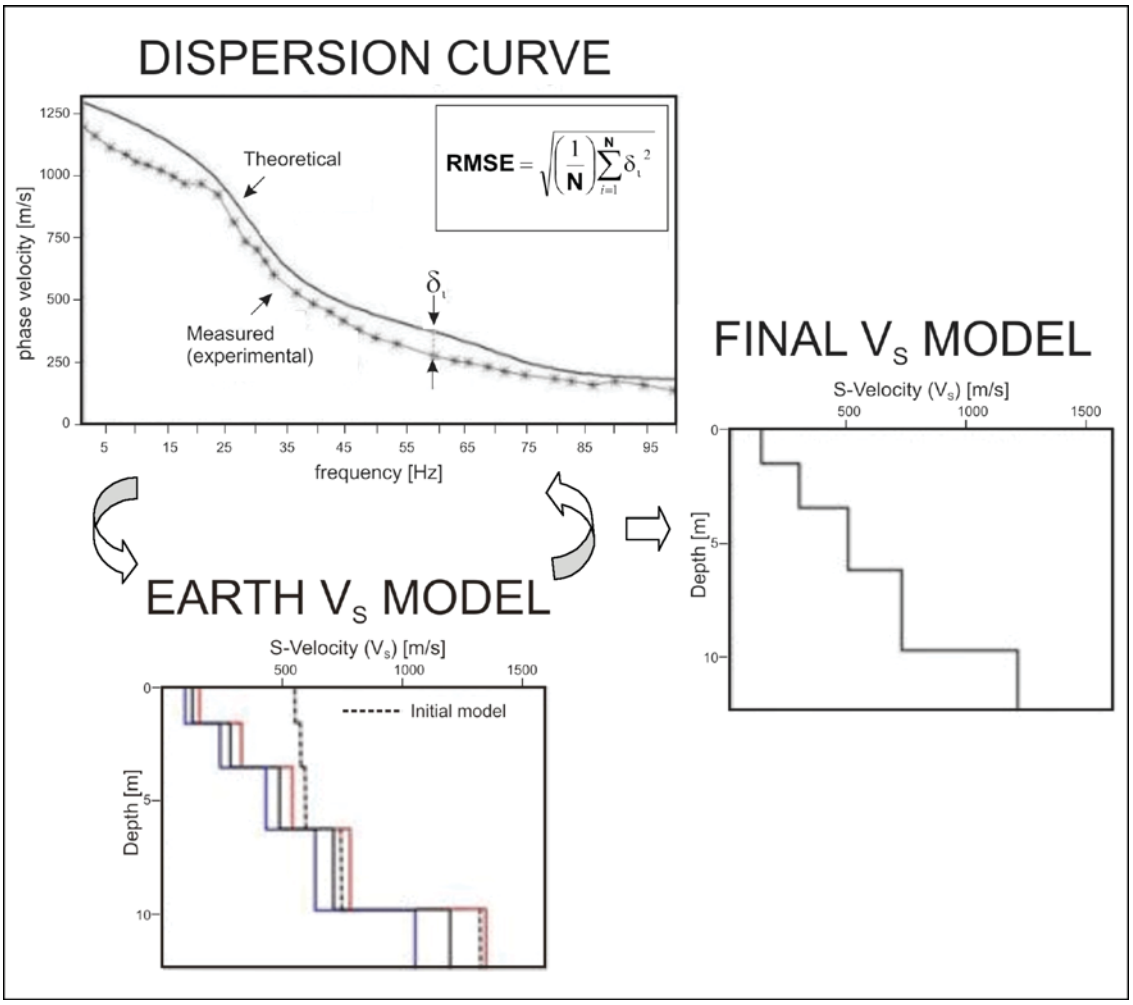

Figure 3.10 *Up: Approximation of the of theoretical dispersion curves to the measured one, quality factor for this method is the root mean square error. Bottom: Shear wave velocity Earth models for the theoretical dispersion curves. Right: Final model after approximation technique is completed. (After www.masw.com)*

The method is based on the fact that every layered earth model (defined by the earth elastic parameter) has a specific dispersion curve or in a more precise definition, the dispersion curve is depending mainly of the Vs structure of the earth. Rayleigh wave phase velocity extracted from the dispersion curve analysis is a function of S-wave velocity, Vs, P-wave velocity, Vp, density, ρ, and thickness of each layer, h. To visualize the sensitivity of each parameter Xia et al. (1999) for example, compared model data by changing each parameter at a time by 25%. Figure 3.11 summarizes their results. An increase of Vp changes the dispersion curve of the original model in average less than 3%. A change in density causes an average deviation of less than 10%. When increasing the layer thickness by 25%, the phase velocities change by an average of 16%. When increasing the Vs by 25% the phase velocities deviate from the original ones by an average of 39%. The results of this sensitivity analysis show that Vs affects the phase velocity

most, which means vice versa that the Rayleigh phase velocity for each frequency or the dispersion curve respectively is characteristic for the Vs structure of an earth model.

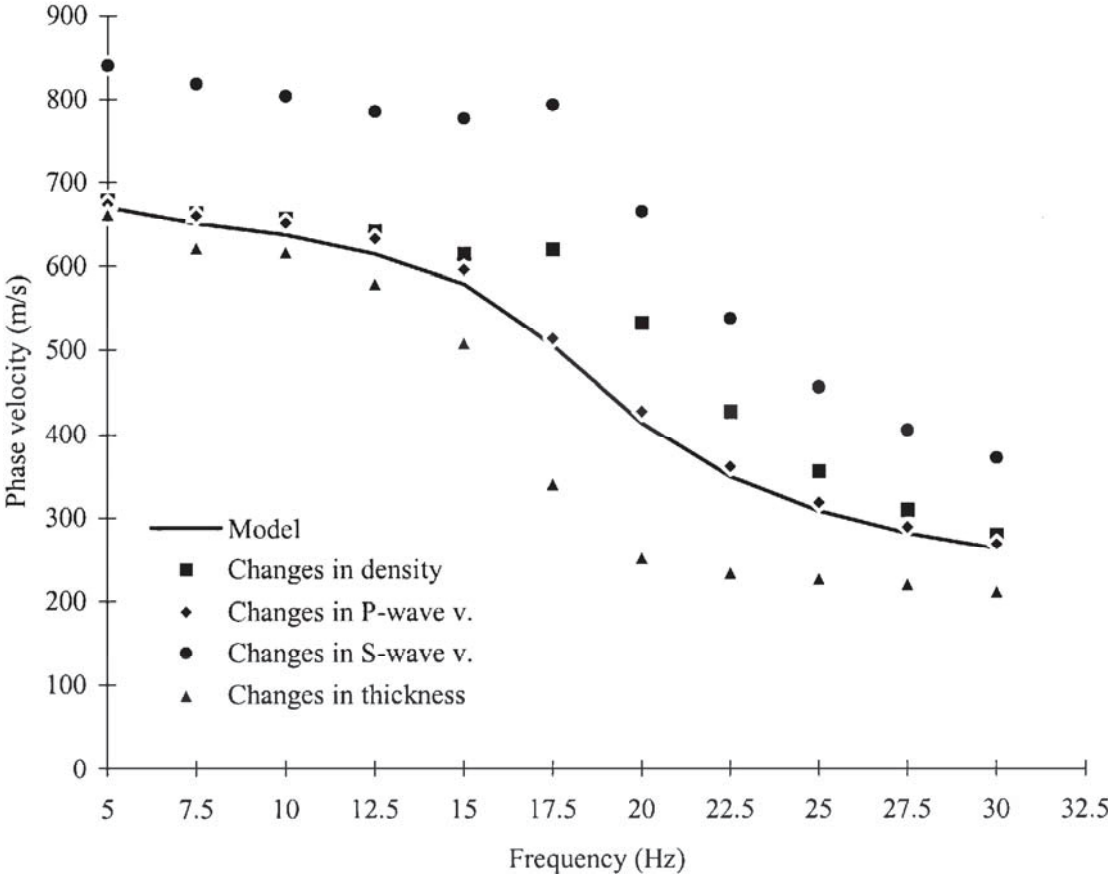

Figure 3.11 *Effects on a model dispersion curve (continuous line) by changing each time one earths parameter by 25% of the original values. The filled circles stand for a 25% increase of shear wave velocity and show the largest deviation from the model data. (From Xia et al., 1999)*

After comparing Shear wave velocities from several direct borehole measurements with results of the MASW method, Xia et. al (2002) found out that the deviation between borehole results and inverted MASW results lies below 15%.

3.2.5 Application of the method

The importance of the MASW method lies in the easy, inexpensive and fast acquisition and interpretation technique and overall in the recuperation of the shear wave velocity of the subsurface in a noninvasive way.

The following formulas show the dependency of the shear wave velocity on the stress and strain conditions of investigated structures:

$$V_s = \sqrt{\frac{\mu}{\rho}} \tag{3.11}$$

$$\mu = \frac{\sigma}{\gamma} = \frac{\left(\frac{\Delta F}{A}\right)}{\left(\frac{\Delta L}{L}\right)} \tag{3.12}$$

$$E = \frac{\left(\frac{\Delta F}{A}\right)}{\left(\frac{\Delta L}{L}\right)} = 2\mu(1+\nu) = \rho V_s^2 \frac{3\left(\frac{V_p}{V_s}\right)^2 - 4}{\left(\frac{V_p}{V_s}\right)^2 - 1} \tag{3.13}$$

$$\nu = \frac{\left(\frac{\Delta W}{W}\right)}{\left(\frac{\Delta L}{L}\right)} \ldots \approx 0 \; to \; 1/2 \tag{3.14}$$

$$\frac{V_p}{V_s} = \frac{1}{\sqrt{\frac{0.5-\nu}{1-\nu}}} \ldots \approx 1.4 \; to \; 1.7 \tag{3.15}$$

$\mu \ldots Shear\ Modulus$
$\rho \ldots Density$
$\sigma \ldots Stress$
$\gamma \ldots Strain$
$E \ldots Young's\ Modulus$
$\nu \ldots Poisson's\ Ratio$

(*After Sheriff* (2002) & *Suto* (2007))

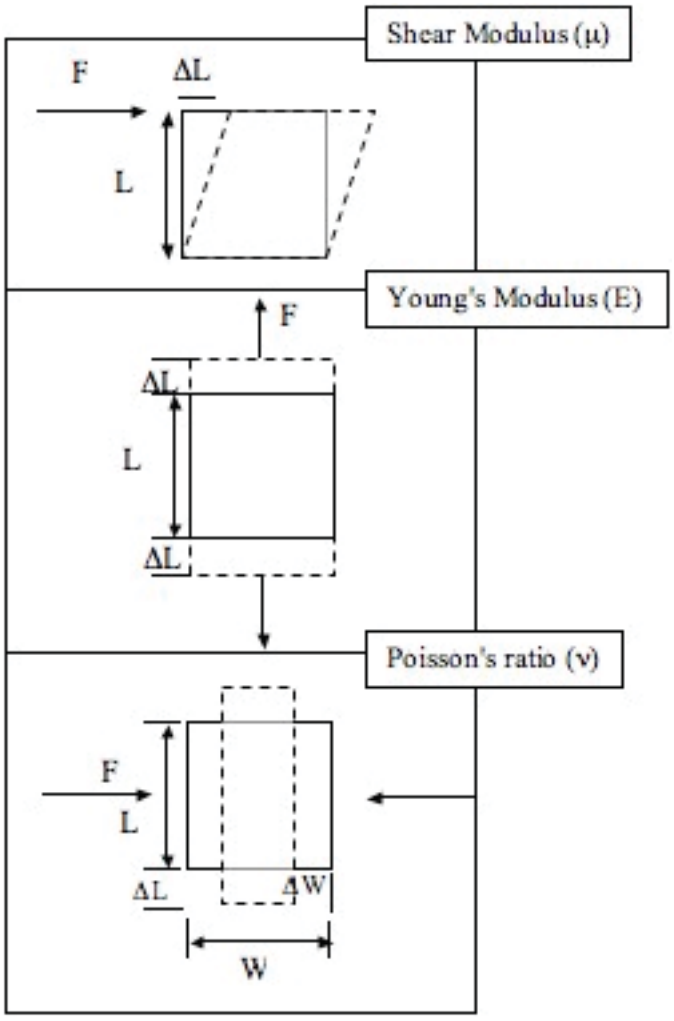

Figure 3.12: Explaining pictures for Equations 3.11 to 3.15.

Equation 3.11 indicates that the shear wave velocity is mainly depending on the shear modulus, considering negligible small differences in density (assuming a constant underground composition). That again implies that considering Eq. 3.12 that the shear wave velocity is defined by the stress and strain conditions of the underground. This dependency can also be obtained by considering the perpendicular particle motion to the Shear wave propagation direction and the nonexistence of shear waves in fluids because of the lack of shear resistance. The Young's Modulus (E) strong dependency on Shear wave velocity is recognizable from the Equations 3.13, 3.14 and 3.15.

Khaksar et. al (1999) showed beside others (e.g. Eberhart-Phillips et al. (1989), Freund (1992), Jones (1995)) in laboratory test of reservoir sandstones that an increased confining stress results in a (non linear) increase of P and S- wave velocities.

The application of the MASW method in this dissertation is to recognize dissolution voids with

high roof tensions that have a potential to collapse. Therefore with the inverted shear velocities a typical stress and strain pattern around potentially collapsing voids should be found.

The stress field studies around underground cavities are well developed for mining and tunneling purposes (examples below from www.rockscience.com). Figure 3.13 shows the principal in situ stress directions, which are effective in the underground: vertical in situ stress σ_V and the two horizontal in situ stresses σ_{H1} and σ_{H2}. If a cavity is now added to the system, in the example of Figure 3.13 a horizontal tunnel, additional stress is induced to the particles adjacent to the tunnel. The maximal induced principal stress is nominated as σ_1 and the minimal induced principal stress as σ_3.

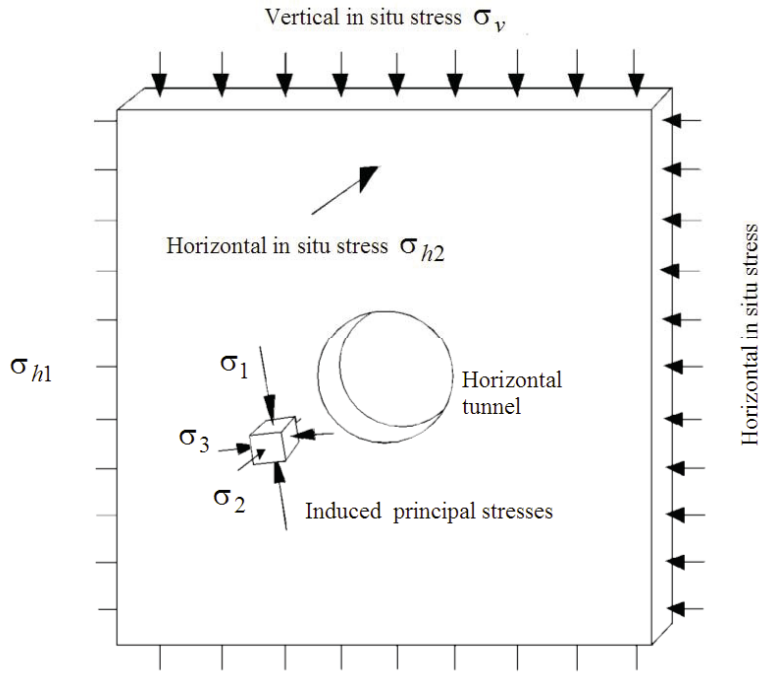

Figure 3.13 *Interaction of in situ stresses and induced stresses on a particle in the adjacency of a tunnel. (www.rocscience.com/education/hoeks_corner)*

The induced stresses are perpendicular to each other but can stand in a certain angle to the in-situ stresses. In Figure 3.14 the horizontal in-situ stress correspond to three times the vertical in situ stress. The longer lines equates to the maximal principal stress, the shorter to the smallest principal stress. The orientation and the length of the lines is the result of the summation of all the effective stresses that affect the rock surrounding the tunnel.

Figure 3.14 shows a circular tunnel and its surrounding stress field. The diagram indicates the

maximal (σ_1) and the minimal (σ_3) principal stresses divided by the in situ stress of the surrounding rocks. It can be seen that the increased stress variations are concentrated around the tunnel, whereas in a distance of about three times the radius of the cavity the stress level is again approximately at the level of the in-situ stress.

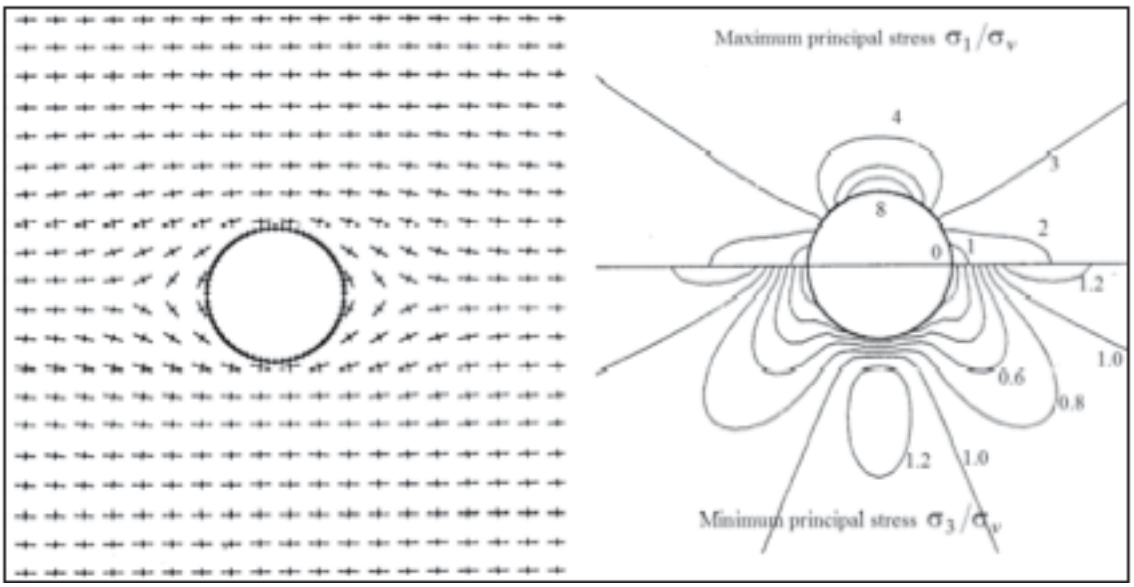

Figure 3.14 *Left: strength and orientation of maximal and minimal principal stress in the adjacency of a cavity. Right: Maximal and minimal stress divided by the in situ vertical stress in the closeness of a tunnel. (www.rocscience.com/education/hoeks_corner)*

The presence of an underground cavity induces stress and strain in the surrounding material. The magnitude and the relation of the induced stress and strain and with it the potential of roof collapse, depend on the dimensions of the underground cavities (see following chapter) and the composition and properties of the surrounding rocks.

The stress-strain diagram in Figure 3.15 shows the behavior of rock under stress and strain conditions. During the elastic deformation part a constant rise of stress and strain can be observed. The extent of the plastic deformation depends on the consistence of the rock material, if rock is brittle it comes immediately to a failure, if the material is more ductile the strain increases whereas the stress remain more or less on a high level till it comes to a failure and a drop in stress. Under consideration of Eq.3.11 and 3.12 the shear modulus (and with it the shear velocity) should rise during the elastic phase of the stress strain curve and than fall during the ductile phase, the time of failure or immediately before failure.

A practical example can be observed in borehole studies using full wave sonic tools in combination with imaging tools. On the well logs it can be seen that in weak zones the

velocities are reduced. Winkler (2005) made studies on stress induced velocity variations to indicate borehole damages. He compared velocities from deeper structures with velocities from near-wellbore areas. He found out that in zones where the drilling process induces a high stress level and the zones approach a critical state immediately before breakout occurs, deep and near-wellbore velocities (decrease) deviate from each other.

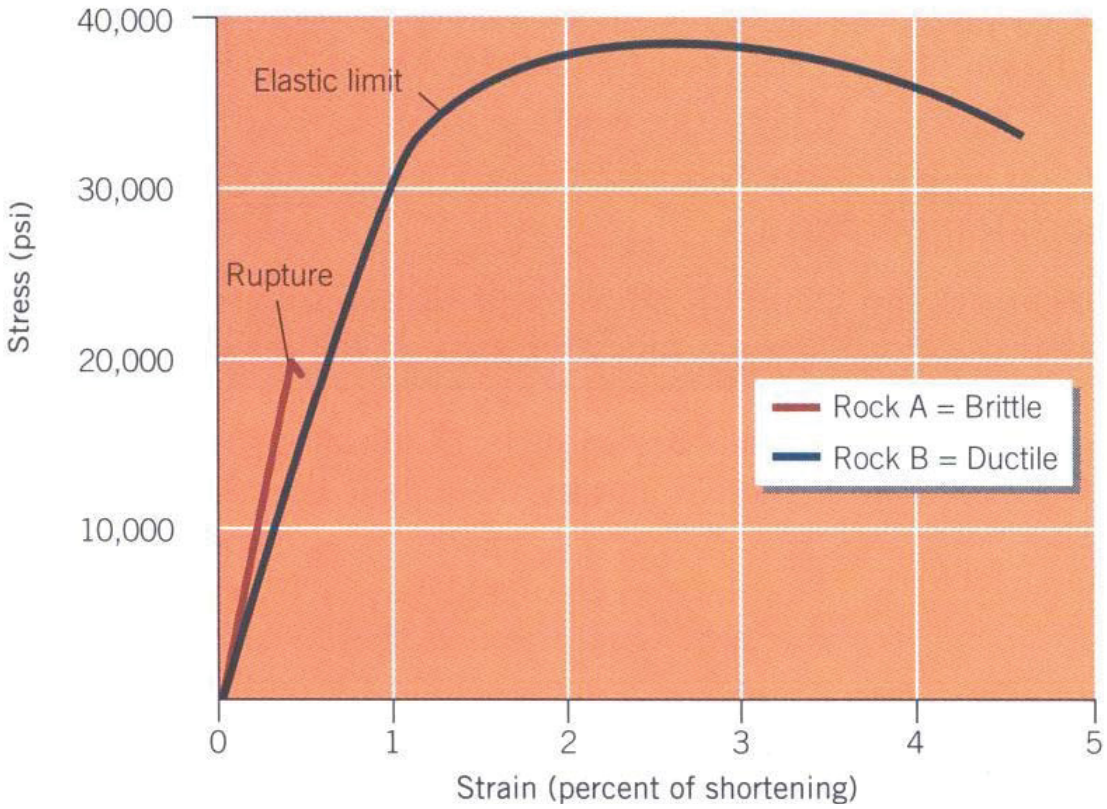

Figure 3.15 *Stress strain diagram for ductile and brittle rocks. (After Heard et al.,1972).*

In conclusion, in an ideal case scenario a certain pattern has to be found in the distribution of shear wave velocity above and around cavities with an increased potential of collapse:

Because of an increased induced stress around underground cavities, a S-wave velocity increase is expected, growing with the dimensions of the void. As the stress strain diagram in Figure 3.15 illustrates, if the process of collapse and subsidence is already induced, a drop of S-wave velocity should be observed.

4 Geology of the test area and salt dissolution mining

The test area for this study is located in Hutchinson (Central Kansas), a city with a long history of salt mining.

The Hutchinson salt member is of Permian age and has an extension from central Kansas to northwestern Oklahoma and the northeastern part of Texas (Figure 4.1). In Kansas the salt layer reaches an average net thickness of 75 m. The increasing thickness of the salt member is a consequence of increasing salt thickness and more additional interbedded anhydrites (Dellwig, 1963; Holdoway, 1978; Kulstad,1959; Merriam, 1963; Watney et al., 1988).

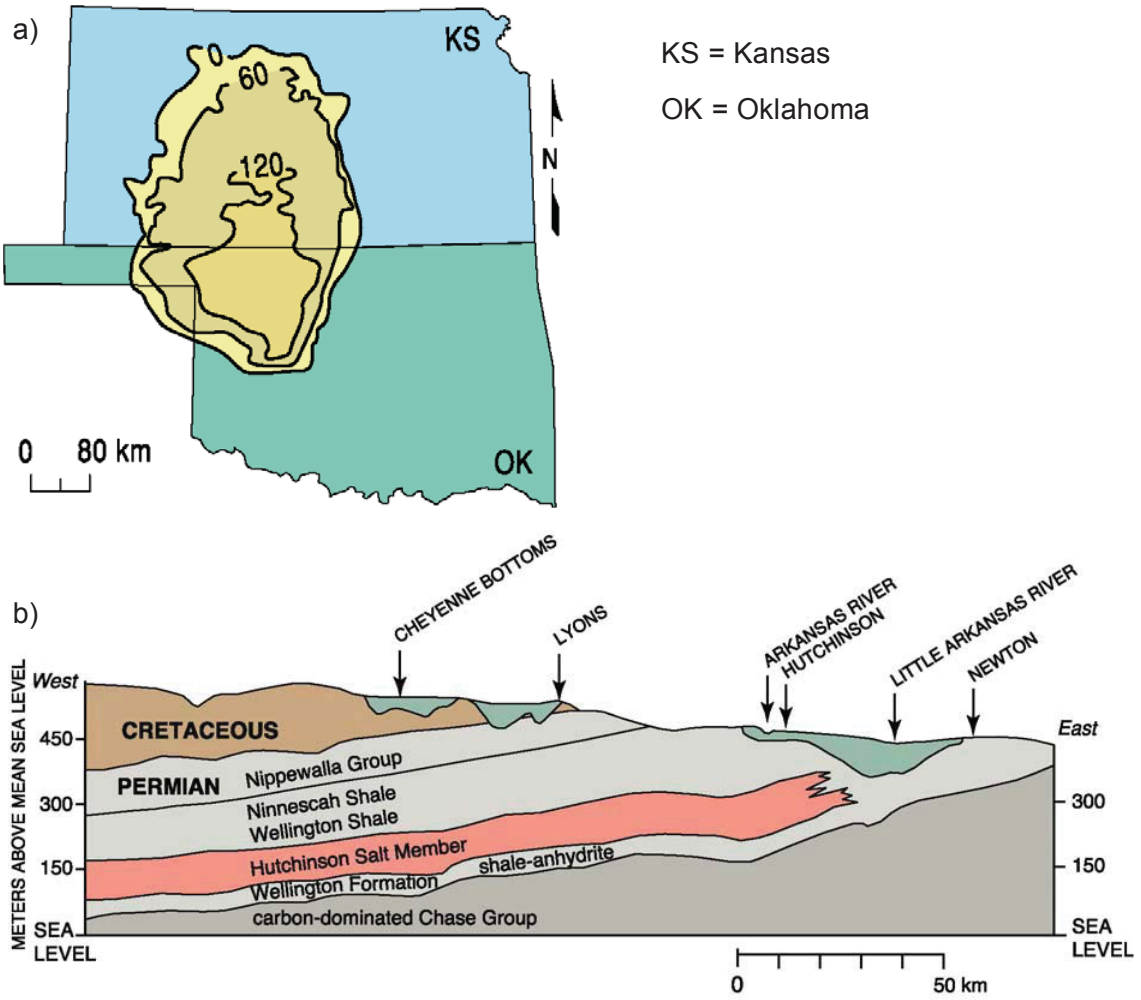

Figure 4.1 *a) Thickness contour map of the Hutchinson Salt Member (modified (Miller, 2007) from Walters, 1978). b) Geologic cross section crated out of well data (modified (Miller, 2007) from Spinazola et al., 1985).*

In Hutchinson the salt layer is under- and overlain by Permian shales, red or reddish-brown shales, known as "red beds". The Permian formation sequence is composed as follows (Merriam, 1963): The lower Wellington Shale (top at about 240m), the Hutchinson Salt member (top at about 120m), the upper Wellington Shale (top at about 70m) and the Ninnescah Shale (top at about 23m); the top of Ninnescah Shale forms the bedrock. Directly over the bedrock unconsolidated Pliocene and Pleistocene sediments are deposited.

The Permian shales form an impermeable seal between the water-soluble Hutchinson salt member and the freshwaters in the younger unconsolidated sediments. In the upper Wellington formation directly above the salt/shale contact lays an approximately 6m thick, extremely weak dark shale. The shale is pervaded with joints and bedding planes filled with red halite (Walters, 1978). Once unsaturated brine intrudes the contact between Hutchinson Salt and Wellington Shale and reaches the weak dark shale, the red-halite immediately is leached and the 6m thick shale remains as an extremely unstable layer.

The mining of salt in Hutchinson, Kansas, has lead to several occurrences of sinkhole during the past 100 years. There are three typical techniques used in the area to recover salt: multi-well technique, room-and-pillar technique and Single well technique; whereof the latter is responsible for the maninduced sinkhole formation. A single well has been used to inject fresh water near the bottom of the salt layer and pump the brine out at the top of the salt layer over the same borehole. During the early years of production the boreholes were cased only below top of bedrock, in that way up to 75m of shale (above top of salt) had fluid contact and was exposed to the brine (Miller, 2007).

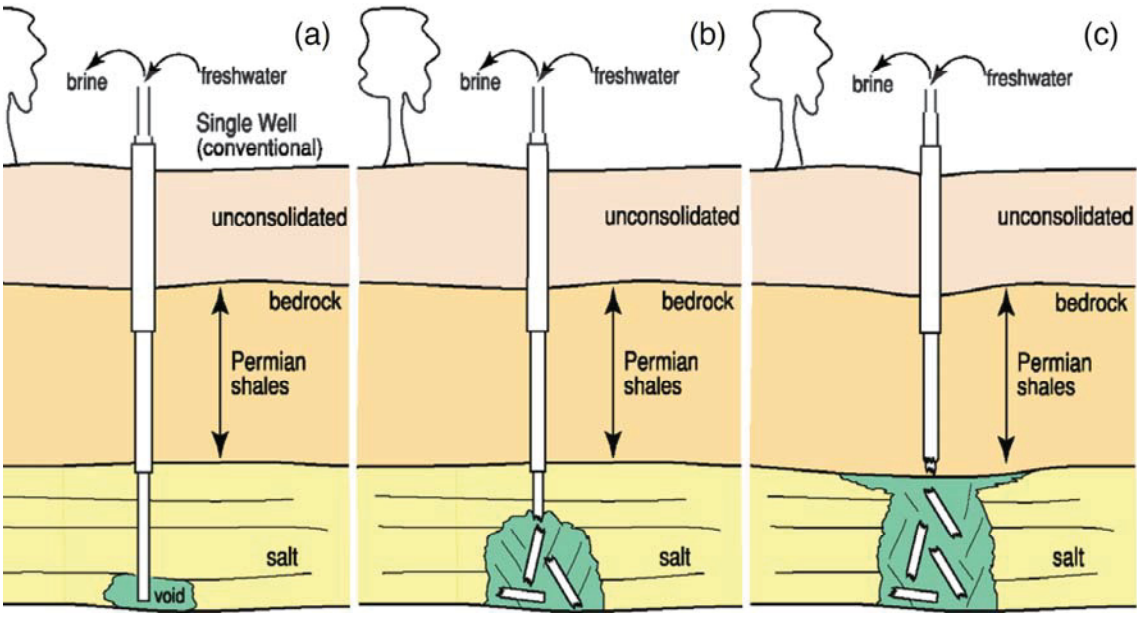

Figure 4.2 *Single well dissolution mining a) dissolution void reaches shale / anhydrite layer, b) rupture of the freshwater tube, c) horizontal migration of void and forming of a morning -glory structure. (From*

Miller, 2007)

When the dissolved salt volumes became too large the shale and anhydrite stringers within the Hutchinson salt layers were exposed to excessive strength and failed, which is a major problem in this area. This failure often had as consequence a damage of the freshwater tubes so that they lost in the underground and dissolution moved upwards (Figure 4.2). If the dissolution front reached bottom of the Permian shales, the migration continued horizontally under the caprock. The horizontal migration can connect two voids with each other by forming a gallery, which can result in a sag on the surface (Figure 4.3). When caprock fails the process of layer failure migrates up to the surface and results in a sinkhole.

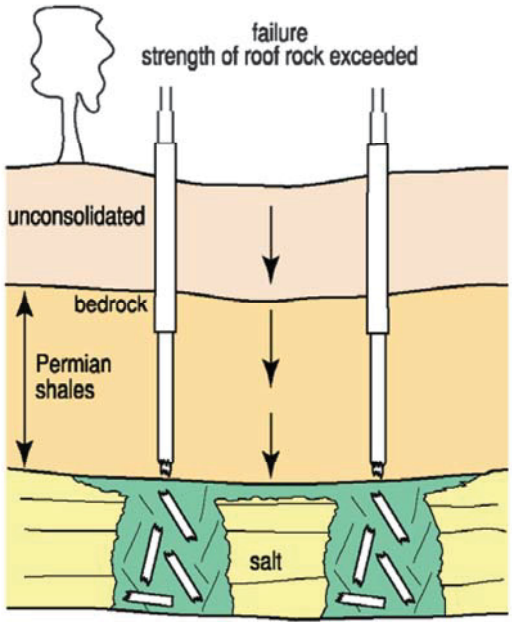

Figure 4.3 *Two adjacent production wells get connected by horizontal migration and form a gallery. On the surface it can come to the forming of a sag. (From MIller, 2007)*

5 Former investigations on the test site

The former salt dissolution-mining field in Hutchinson, Kansas, is an interesting testing area. The mining field borders directly on the city and is intersected by a busy railroad line. Several sinkholes appeared during past decades, e.g. in 1991 a sinkhole formed near a city street and in 2005 directly under the railroad tracks (Figure 5.1).

Figure 5.1 *Sudden formation of a sinkhole within the city of Hutchinson near an important railroad, in 2005 (from Lambrecht et al, 2006).*

Because of the permanent danger the city government is highly interested to identify areas with risk of collapse. Several investigations have therefore been done. Some of the former producing wells have been drilled and surveyed with a series of geophysical logs, amongst others an acoustic televiewer to localize and estimate the dimensions of underground voids. The drilling process causes additional stress to an already sensitive site and therefore non-invasive methods are to be preferred. In response to the two catastrophes in 1991 and 2005 seismic reflection lines have been recorded adjacent to the sinkholes to estimate the possibility of a future expansion (Miller et al.,1993).

In 2008 a series of measurements have carried out with the purpose to evaluate surface methods to locate stressed areas. Therefore several lines of shear wave reflection seismic and additional to it some lines of active MASW were deployed and recorded in adjacency to known underground voids (Miller et al. 2009). The map in

Figure **5.2** shows the location of the lines.

The reflection data showed over some known voids an unambiguous variation in the reflection characteristics. An estimation of the degree of stress, induced from an underground cavity, was not successful. Further developments of methods and techniques are necessary.

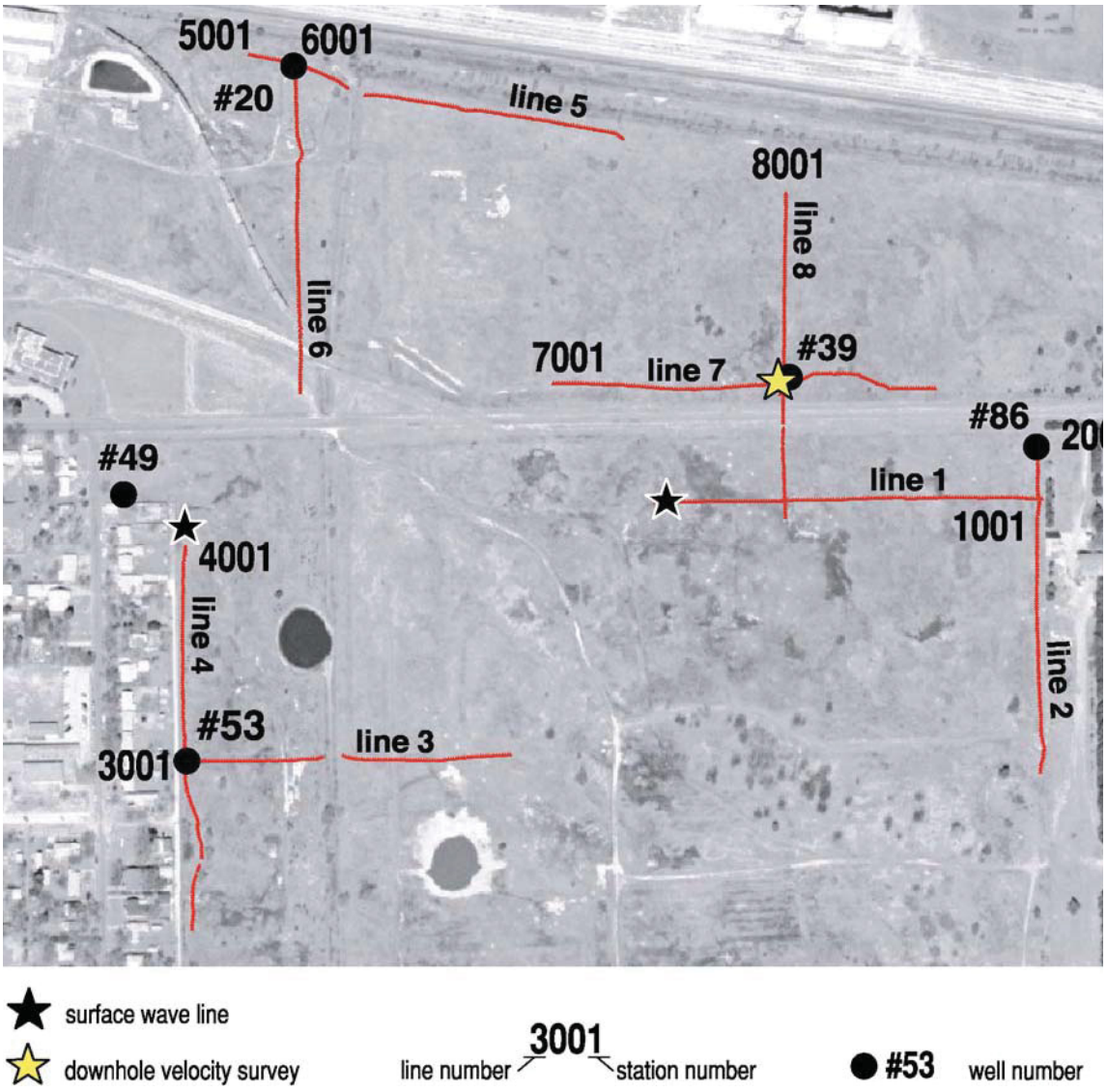

Figure 5.2 *Map from the former salt dissolution field with the shear wave reflection seismic lines (red lines) and the active MASW lines (lines marked with a black star) from 2008 (from Miller et al.,2009).*

The surface wave analysis showed velocity anomalies in the area above a known void and correlates with reflection disturbances found with the shear wave reflection seismic (Figure 5.3). The limits for the active surface wave analysis on the site were the production of low frequency signals. Even with an accelerated weight drop the lowest frequencies that could be generated were approximately 7 Hz and that implied a resolution of at best 20m. The bedrock thickness in the test field is about 23m.

One of the lines of research pursued in this thesis is based on the results of active surface wave analysis measurements from 2008. With trains as passive source frequencies low enough should be reached to resolve stress strain conditions at bedrock and even deeper layers.

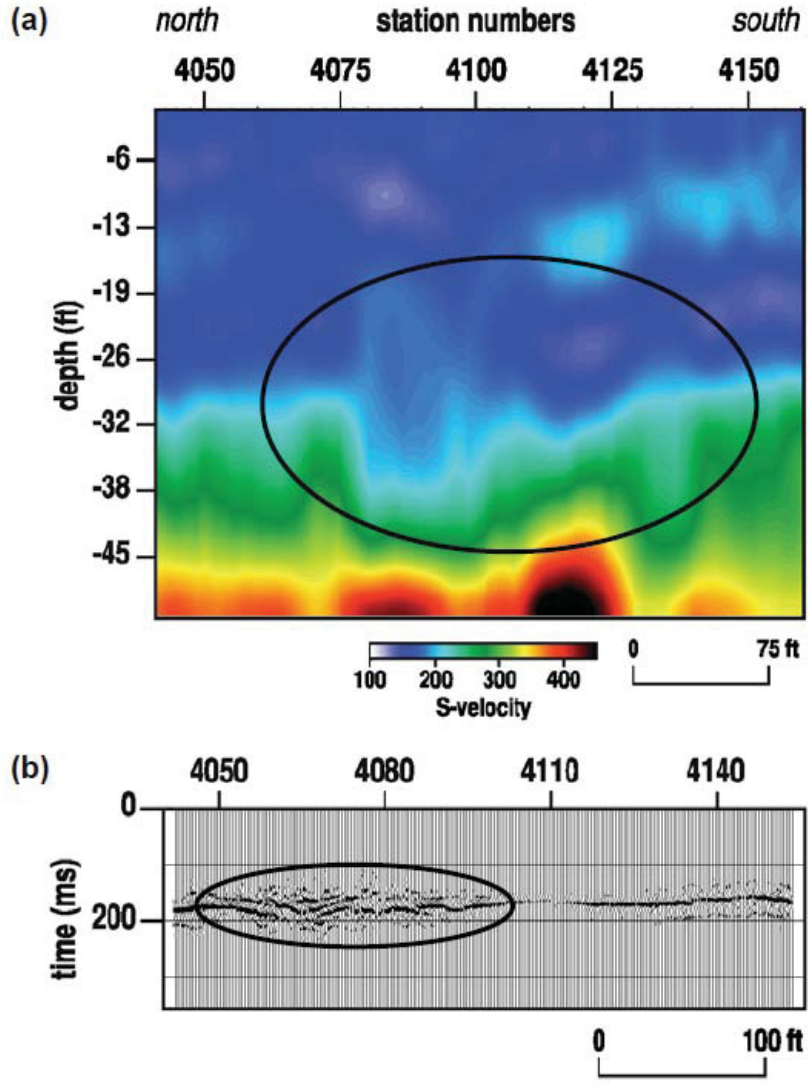

Figure 5.3 *Line 4 shows a) velocity anomalies in the surface wave analysis and b) reflection disturbances in the shear wave reflection seismic.(From Miller et al., 2009)*

6 Advances in the Passive MASW Method

In extension of the measurements in 2008 (see previous chapter), passive MASW records were executed during the summer periods of 2010 and 2011. With the help of this data the local stress fields over underground voids should be detected and furthermore their potential of collapse identified. Beyond the analysis of the local stress fields, the passive MASW method should be improved and tested on its feasibility by using trains as a source.

In this chapter array design is discussed and optimal parameters for a passive MASW study are established.

6.1 Array configurations and their data acquisition parameters

The former salt dissolution-mining field with more than 100 wells and a set of voids of various sizes and migrating stages is an optimal field to test the stress sensitivity of the passive MASW method.

Figure 6.1 *Former salt dissolution mining field in Hutchinson, Kansas. Overview of the 5 arrays (yellow, western: array 2000; yellow, eastern: array 3000; red line: array 4000; blue box: array 5000a; blue crossing lines: 5000b) deployed and recorded for this project. Three round sinkholes filled with water are recognizable in the illustration (red arrows). (From Google maps, 2011)*

Figure 6.1 gives an overview over the arrays deployed and recorded for this study. For all passive data a record length of 32 seconds was chosen, it enabled to record long datasets when trains were around, without loosing precious data because of the time needed to trigger the data record again and again. Afterwards high quality sections could be separated and used for further processing. A sampling rate of two milliseconds was used.

6.1.1 Array 2000

In summer 2010 a 2D-spread was deployed around the former production well with the number 40 (Figure 6.1, western yellow array). Well 40 was at the time of the measurements already known as a well with a migrating void underneath. The question which array 2000 should answer was, if the stress and strain conditions are obviously larger than over an uninfluenced site and if there is urgency for filling up the void with sand to prevent the development of a sinkhole.

The investigation array 2000 consists of 336 receivers. The 4.5 Hz vertical geophones were orientated at parallel and orthogonal alignments to nearby railroad tracks in seven West-East lines and five North-South lines (Figure 6.2).

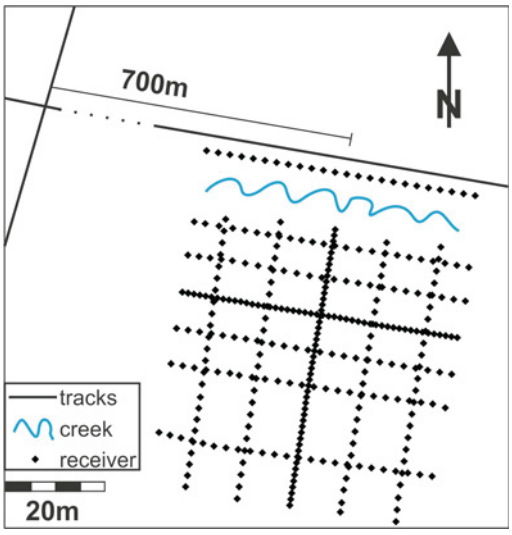

Figure 6.2 *Schematic illustration of Array 2000.The solid lines north and west of the array represent railroad tracks.*

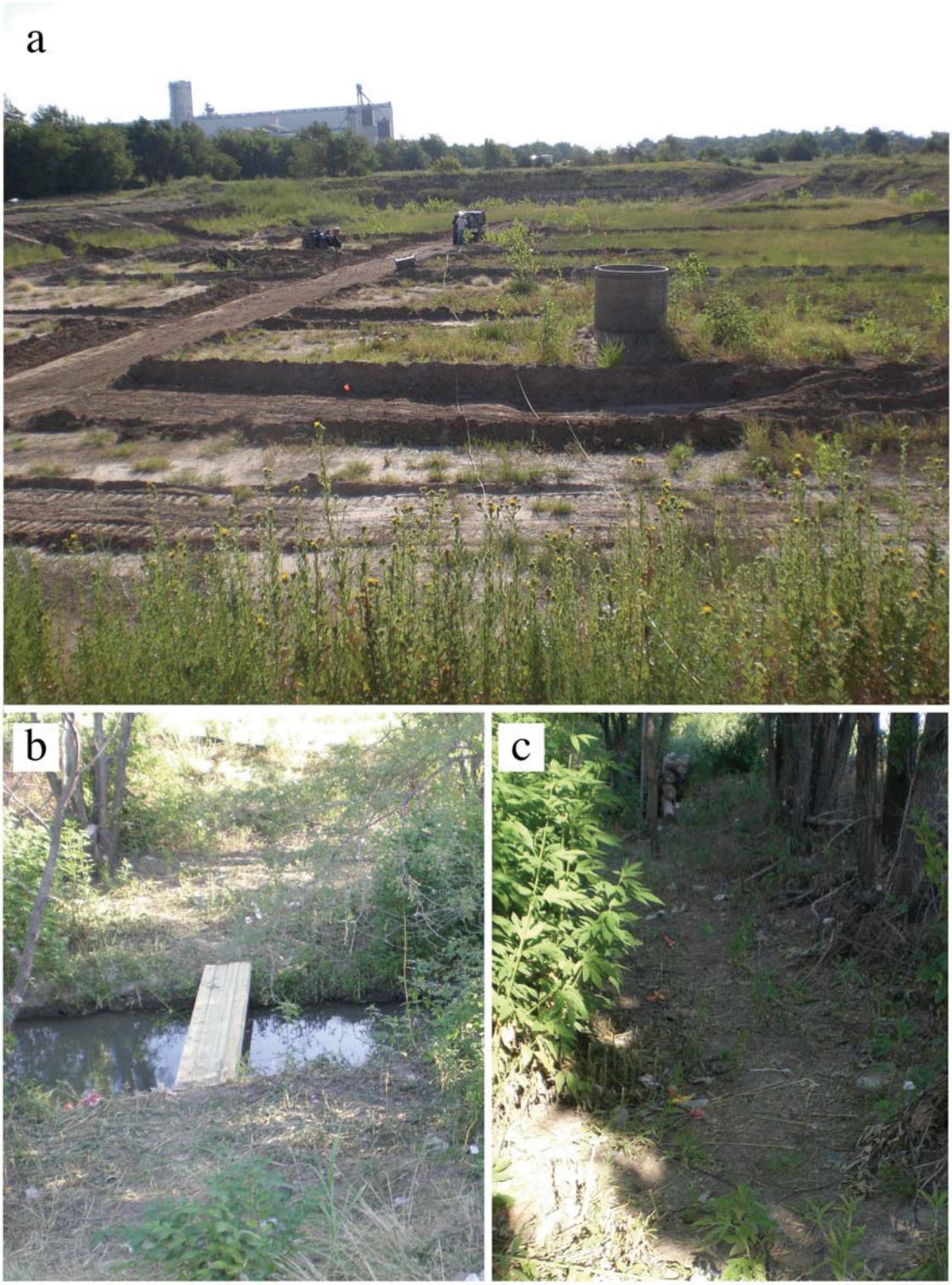

Figure 6.3 (*a) Testing area 3000; the positions for the geophone lines were cleaned to guarantee optimal geophone coupling; b) Small creek with passage to the northern line; c) Geophones along the northern line.*

The positions for the geophone lines were cleaned from high grass, bushes and bumps to guarantee optimal geophone coupling (Figure 6.3a). The alignment on the railroad should improve the recording and analysis of the signals coming from the passing trains that are used as sources. Ten of the twelve lines that made of the 2-D spread included 24 receivers with a receiver spacing of 2.5 m. Two of the lines, they are orthogonal to each other and positioned in the centre of the array, included 48 receivers with a separation of 1.2 m. The northern West-East line is separated by a small creek from the other geophones and lays in a depression of about 1 to 2m (Figure 6.3b and c). This line was attractive for beavers and they produced some noise by nibbling on the cables.

The orientation of the spread lines is important for the further processing. The orientation is calculated counter clockwise from East. The West-East lines have an orientation of 170°(coming from West)/350° (coming from East). The North-South lines are orientated towards 80°(coming from North)/ 260°(coming from South).

6.1.2 Array 3000

Figure 6.4 *Array 3000 lies adjacent to Array 2000, Lines have been cleaned up to guarantee easier and faster geophone planting and optimal geophone coupling.*

Array 3000 (Figure 6.1 eastern yellow array) is deployed about 400m eastern of Array 2000 with the parameters (geophone amount, spacing etc.) exactly as described in the previous paragraph. Figure 6.4 shows site 3000. The surface of site 3000 is in comparison to the before discussed site 2000 a bit smoother nevertheless also on array 3000 the northern West -East line lies across the small creek (Figure 6.3b).

Array 3000 is located around well 94, which is known to have no underground cavities. Measurements over this uninfluenced area should be used for calibration and should give directions over the range of shear wave velocities that can be expected over an uninfluenced site. In case velocities from Array 2000 show obvious deviations, the variations can be ascribed to the induced stress/strain conditions of the cavity. Array 3000 was deployed and recorded one day after Array 2000 with the identical equipment, so deviations due to weather, soil conditions or equipment can be excluded.

6.1.3 Array 4000

Array 4000 was deployed and recorded in summer 2011. The 360 geophones of Array 4000 are deployed as a line parallel to the West–East running railroad along several wells (Figure 6.1 red line, Figure 6.5). As receiver spacing 2.5 meters were chosen.

Figure 6.5 *Array 4000 is deployed along the West- East orientated railroad tracks, the red circles show the numbered wells immediately along the spread.*

In some parts of the line geophones are missing, because of surface obstacles, like a ditch west of well 25 and a sinkhole around well 19 that is recognizable also in Figure 6.5. Nevertheless the receiver spacing is always maintained. A typical passive MASW seismic record, with a recording time of 32 seconds, is displayed in Figure 6.6. The signals are coming from a train traveling towards West positioned at the moment of recording at the west end of the line. The black bars indicate missing geophone stations because of ditch, creek or sinkhole, or geophone connection problems because of difficult terrain.

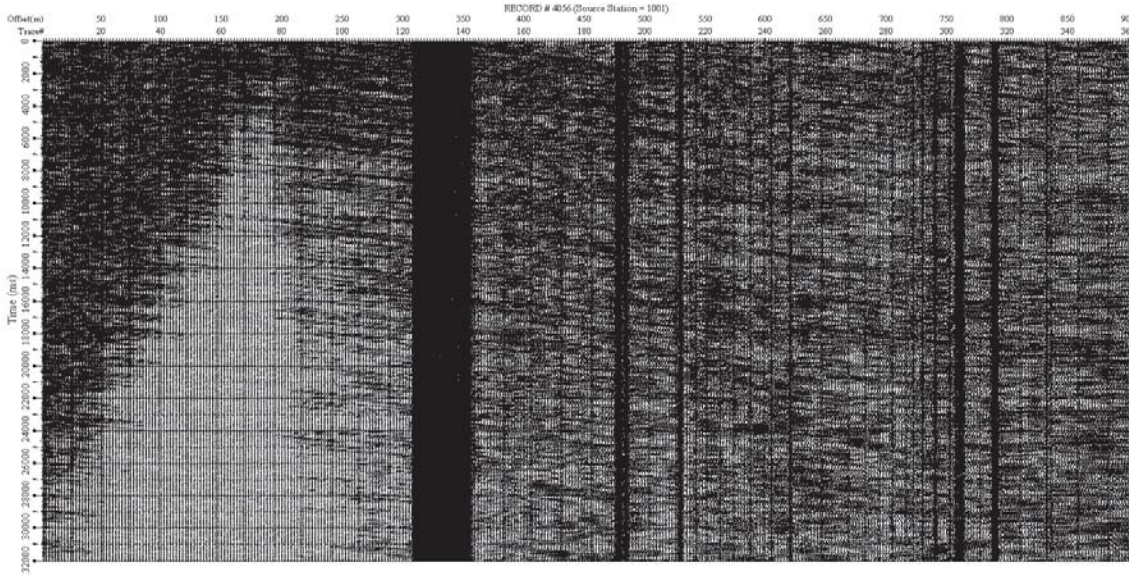

Figure 6.6 *Seismic section of Array 4000. The receivers are plotted from west to east on the horizontal-axis; the time is plotted on the vertical-axis. Vertical black bars originate from the gaps in the array because of passing sinkholes or creeks, or from bad geophone coupling because of difficult underground.*

Originally it was intended to deploy a small 2D spread at the center of the line to identify the direction where the source signal is coming from (see section 7.2). Because of some geophone malfunction this step had to abandoned and therefore as counteraction roads and railroad tracks were monitored in all directions, to know detailed train/source positions when data were recorded.

The records were collected during the night, to avoid noise from direction other than from the West-East rail tracks. The line is orientated towards 170°/350° counterclockwise from east.

6.1.4 Array 5000a

Array 5000a was recorded during summer of 2011. An amount of 275 receivers was deployed in a 2-D spread. This array is marked by a blue square in Figure 6.1. The array was deployed on an area of former human settlements. The houses had to be dismantled because of the adjacency to the dangerous zones where sinkhole developments are highly possible. The underground was therefore (foundations, pipes and other installations) not ideal for MASW analysis. The 4.5 Hz vertical geophones were planted at 12 West-East lines with each 24 receivers (Figure 6.7). The receiver spacing in the West-East lines is 5 meters. In North-South directions the lines are 5 meters apart. Every other line is shifted 2.5 meters to the East. The shift of the lines should

provide more straight lines with constant geophone spacing in various azimuths. The array is located over well 53, which is known to have a void underneath. According to drilling confirmed information by Burns and McDonnell, the void migrates horizontally. Because of the special receiver array lines (extensions between 60m and 120m) with the following angles where possible (counter clockwise from east): 0°, 90, 180, 270, 116.5°, 63.5°, 296.5, 243.5° etc.

For this array optimal source energy was unfortunately coming only from the in the North running railroad. Depth profiles could be calculated hence only for a short linear section in the center of the array. Array 5000a is therefore treated in this dissertation only in chapter 6 where several records are used to find optimal parameter for passive MASW.

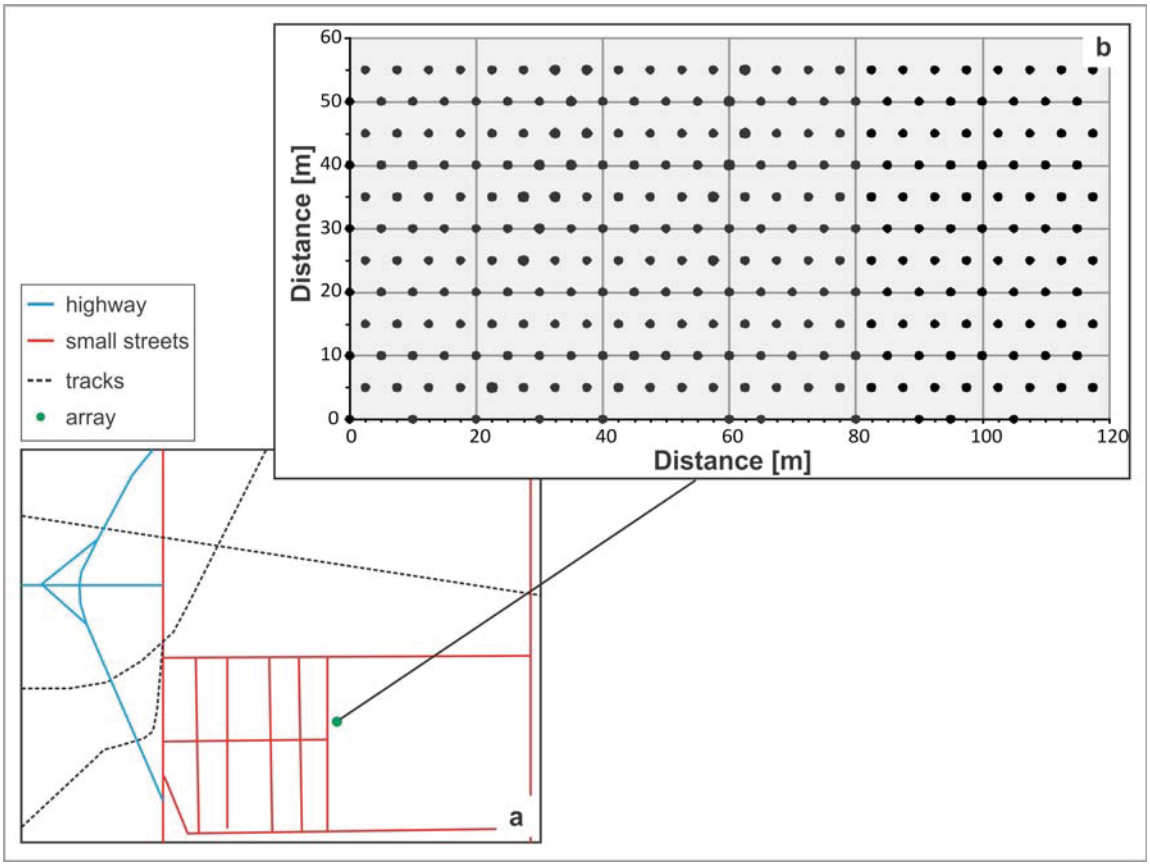

Figure 6.7 *a) Sketch of the surroundings of Array 5000a. b) Black dots show the configuration of the receivers in Array 5000a.*

6.1.5 Array 5000b

Array 5000b (Figure 6.1, northern blue array) was connected to Array 5000a and recording was hence triggered at the same time. The spread has three lines that cross each other. Each line has

24 geophones (receiver spacing is 2.5 m, one line is orientated from North to South, angles between North-South line and the other lines are both 12˚). Array 5000b is located over well 49. From former logging measurements (Burns & McDonnell) well 49 is known to have a small void underneath. Position, surroundings, layout (highly restricted) and underground made it difficult to get valuable results. During the recording of Array 5000a and 5000b a lot of cultural noise coming from all direction complicated the analysis. As a consequence of this Array 5000b will only be briefly discussed in chapter 6.

6.2 Investigation Parameters of Passive MASW

The passive MASW method makes use of surface waves generated by road or rail traffic and other sources of noise. When using a passive source, the location and over all the direction a source signal is coming from is unclear. For investigation of the source signal Azimuth-Frequency diagrams (e.g. Figure 6.6, upper left) are used. The Azimuth-Frequency diagram visualizes the directional distribution of signals in various frequency bands.

To create such an Azimuth-Frequency diagram, a raw seismic record is at first filtered consecutively for each narrow frequency band. Scanning the filtered record then for different directions and stacking the amplitudes of every single trace for each direction creates the Azimuth-Frequency diagram. It should be noted that in SurfSeis®, the program used to generate the diagrams, azimuthal angles are specified counter clockwise from east.

For the calculation of shear wave velocities, in the passive MASW application exactly as in the active MASW method, dispersion curve images have to be generated. For creating a dispersion curve image in the passive MASW method, additional to the frequency and phase velocity, a raw seismic record has to be scanned also for the Azimuth.

In this chapter examples from different spreads are shown; various records are chosen, with energy arriving from singular or multiple directions. They are investigated for optimal sub-arrays, best signal noise ratio in the dispersion curve images and best resolution in low frequencies.

6.2.1 Passive MASW and Array Dependence

In the following sections dispersion curve images from different arrays (original or sub-arrays) are analyzed. The dispersion curve images are generated from records that are scanned for signals coming from all directions. The energy is than stacked over the whole Azimuth spectrum (0 - 360°) for each single frequency and phase velocity combination. The frequency is investigated in the range from 1- 25Hz in increments of 0.5 Hz and the phase velocity is analyzed in 10m/s steps from 1 to 1000m/s.

To analyze the influence of the geometry on the Surface Wave Analysis results, Time-Shift parameters are investigated and shown additionally to the Dispersion curve images and the Azimuth-Frequency diagrams in this chapter. Single Frequencies will be chosen and investigated in various Azimuth-Phase velocity diagrams with Amplitude and Time-Shift difference distribution. The comparison between the distributions should allow a statement over the dependence of the energy distribution on the array-geometry.

A detailed explanation of the Time-Shift difference parameter can be found in the explanation-box below *(see Explanation 6.1)*

Explanation 6.1:

Time-Shift difference parameter

In the Passive MASW method the origin of the seismic signal is not known, therefore the Time-Shift parameter plays a decisive role. To analyze where incoming energy is coming from, seismic signals of each channels (filtered consecutively for the needed frequency span) are shifted in time according to their 2D area position and under the assumption of energy arriving from a certain angle and at a certain phase velocity.

The amplitudes of the channels are then stacked for each frequency and each combination of azimuth and phase velocity value. The result is an Azimuth - Phase velocity image like in Figure 6.6 (upper left).

In certain combinations of phase velocity and azimuth parameters, the time shift of an array can be similar to the Time-Shift of other parameters. For example:

Array 2000 (Figure 6.6, lower right) is composed of straight lines. Five of the lines are deployed from NNE to SSW, in azimuth degrees used in this paper it is from 80° to 260°. Seven of the lines go from WNW to ESE, or from 170° to 350°. Assuming that maximum incoming energy for a 5Hz signal is coming from 85° with a velocity of 350 m/s. Scanning now through all the azimuths and phase velocities to find the parameters for a maximum amplitude, one comes to an angle of 80°, where the receiver spacing for a NNE to SSW line are from this angle position larger than for the 85° angle. By increasing the Phase velocity, one gets a similar Time-Shift for the channels as if processing it with the real parameter. This implies that it is possible to receive high amplitude at "wrong" parameters. So for linear arrays stacking variously over the Azimuths is absolutely forbidden. If there are more complex arrays like the one suggested in literature (cross, square, circle (irregularly sampled)) this effect gets less prominent, but could still induce errors (aliasing).

To control the effect of geometry based errors, in the following chapters, illustrations (e.g. Figure 6.7c and d) are shown with the “Time-Shift difference” between Time-Shift coefficient $TS_{(PV,AZI)}$ (sum over all geophones) of all possible Azimuth and Phase velocity combinations and Time-Shift coefficient $TS_{(440m/s;350°)}$ (sum over all geophones) from real Phase velocity and real angle of maximum incoming energy :

$$TS_{diff(PV,AZ)} = \sum_{i=1}^{no.Geo.} \left(TS_{i(PV,AZ)} - TS_{i(440m/s,350°)} \right) \quad (6.1)$$

AZ ... Azimuth, values from 0 to 360°

PV ... Phase velocity, values from 1 to 1000 m/s

no. Geo.... Number of Geophones in array

A small Time-Shift difference coefficient implies similarity to the maximum incoming energy scenario and induces therefore geometry-based errors.

6.2.1.1 Passive MASW of the original arrays

The following examples show dispersion curves, energy distributions and Time-Shift difference distributions created out of the original arrays using source signals from all directions.

Example 1 (Array 2000)

The first example is processed from Record 2217 from Array 2000. From the 32 seconds long Record 2217 the time section between 3 and 5 seconds has been used. Array 2000 consists of lines going from 350° to 170° and lines going from 80° to 260°, both parallel to the W-E or the N-S rail tracks. The main energy comes from a train travelling east on the W-E tracks; the back of the train is about 2.5 kilometres east of the spread (Figure 6.6). The Azimuth-Frequency diagram shows the main energy for frequencies from 4 to 6Hz at an angle of 352° (upper diagram in Figure 6.6, left red circle). The higher frequencies accumulate mainly around 280° (upper diagram in Figure 6.6, right red circle). For the dispersion curve image in Figure 6.6 all receiver traces of the record are used to create a single dispersion curve. The energy is stacked over all azimuths. The dispersion curve for the whole spread can be interpreted to a frequency of 6Hz, indicative of an approximate investigation depth of about 26 meters (Xia et al. 1999). In the Azimuth-Frequency diagram and in the dispersion curve image of Figure 6.6 the frequencies 5.5 Hz and 10 Hz are marked with black dashed vertical lines. On the basis of this frequencies

the influences of the geometry of Array 2000 on the surface wave analysis results are investigated.

By plotting the amplitude values for the frequency of 5.5Hz in a phase velocity (x-axis) - azimuth (y-axis) diagram (Figure 6.7b) the amplitude maxima (green) for each azimuth can be tracked. The red colored area shows the overall amplitude maxima for 5.5 Hz. It has an angle of 350° and a phase velocity of 440 m/s. In the last row the amplitudes stacked over all azimuths is shown; the red ellipse shows the highest value of the stacked amplitudes, which lies at 550 m/s. The last row is also the energy distribution that is shown in the dispersion curve for the frequency of 5.5 Hz in Figure 6.6.

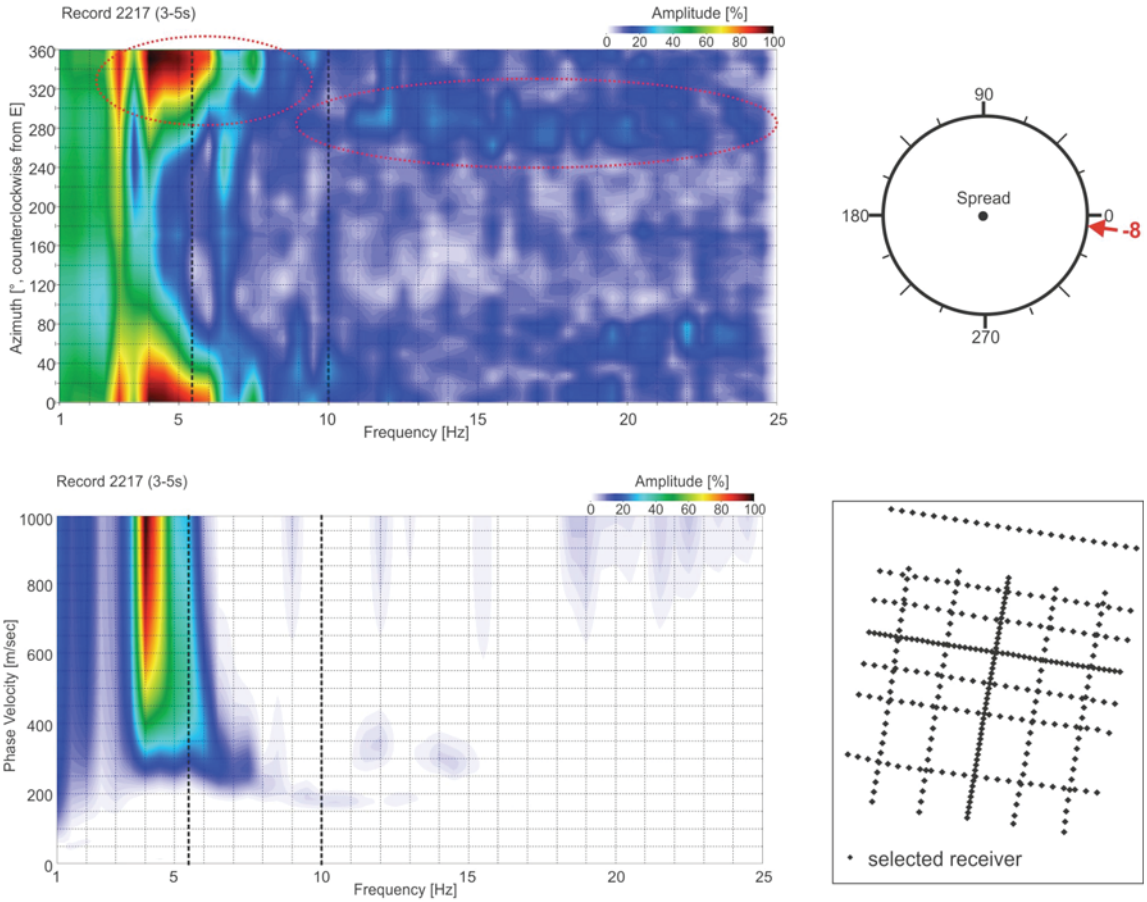

Figure 6.6 *Record 2217 (3-5s) upper left: Azimuth vs. Frequency diagram, red circles marks maximum incoming energy, black dashed lines assigns tested frequencies; upper right: Azimuth circle; lower left: Phase velocity vs. Frequency diagram; lower right: array with selected receivers.*

Figure 6.7a shows the same information as Figure 6.7b, but with the colored amplitude scale it gives also an impression of the distribution of the energy. One can see that the energy is high for the amplitudes stacked over an angle of 350° with phase velocities between 400 and 500 m/s.

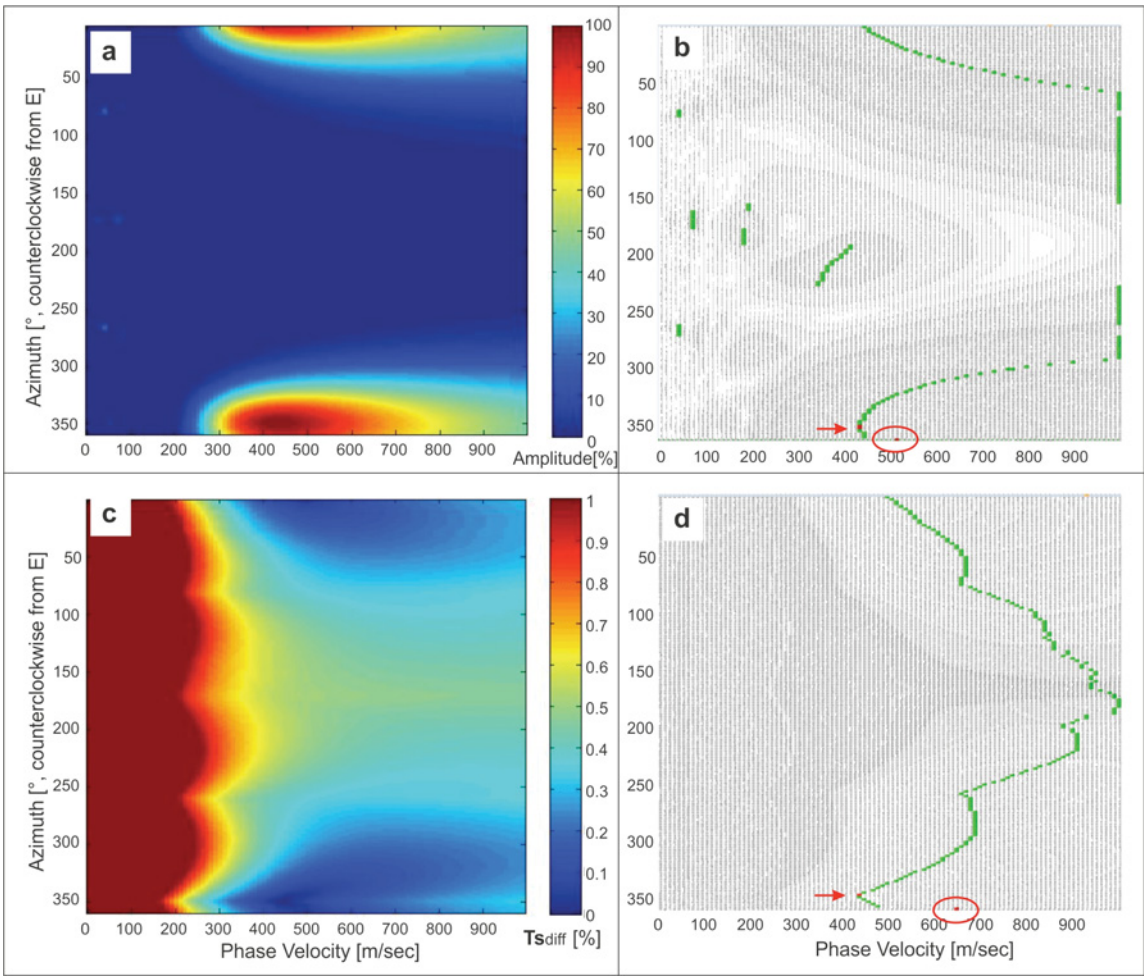

Figure 6.7 *Record 2217(3-5s), 5.5Hz* ***Energy distribution:*** *a) Phase velocity vs. Azimuth diagram, with Amplitude scale b) Phase velocity vs. Azimuth diagram, green curve: highest Energy for each Azimuth row, red arrow: overall maximum, last line: sum of all amplitudes stacked over the azimuths, red circle: Azimuth-stacked maximum energy.* ***Time-Shift difference distribution:*** *c) Phase velocity vs. Azimuth diagram, with TS_{diff} scale d) Phase velocity vs. Azimuth diagram, green: lowest variation of TS_{diff} for each Azimuth row, red arrow: overall minimum, last row: Azimuth-stacked TS_{diff}, red circle: Azimuth-stacked minimum TS_{diff}.*

To control the array induced errors the Time-Shift Difference parameter is displayed in a Phase velocity - Azimuth diagram. If there is a significant influence of the array geometry on the data the distribution of the TS_{diff} minimum zones should correspond with the patterns shown by the stacked amplitudes. In Figure 6.7d the lowest Time-Shift difference of each azimuth is shown in

green. Under consideration of Figure 6.7c, where the absolute distribution of the Time-Shift difference parameter is shown, -low around the angle of energy incidence (330° to 10°) at phase velocities between 400 and 550 m/s and relative high at the opposite orientation angles (160° to 180°, which implies no significant influence on the results) -, the colored areas in 6.7d, symbolize the pattern which is induced of an array, and which can manipulate the result. The last row shows the sum of all Time-Shift coefficients stacked over the azimuths, the lowest variation is at a Phase velocity of 640 m/s.

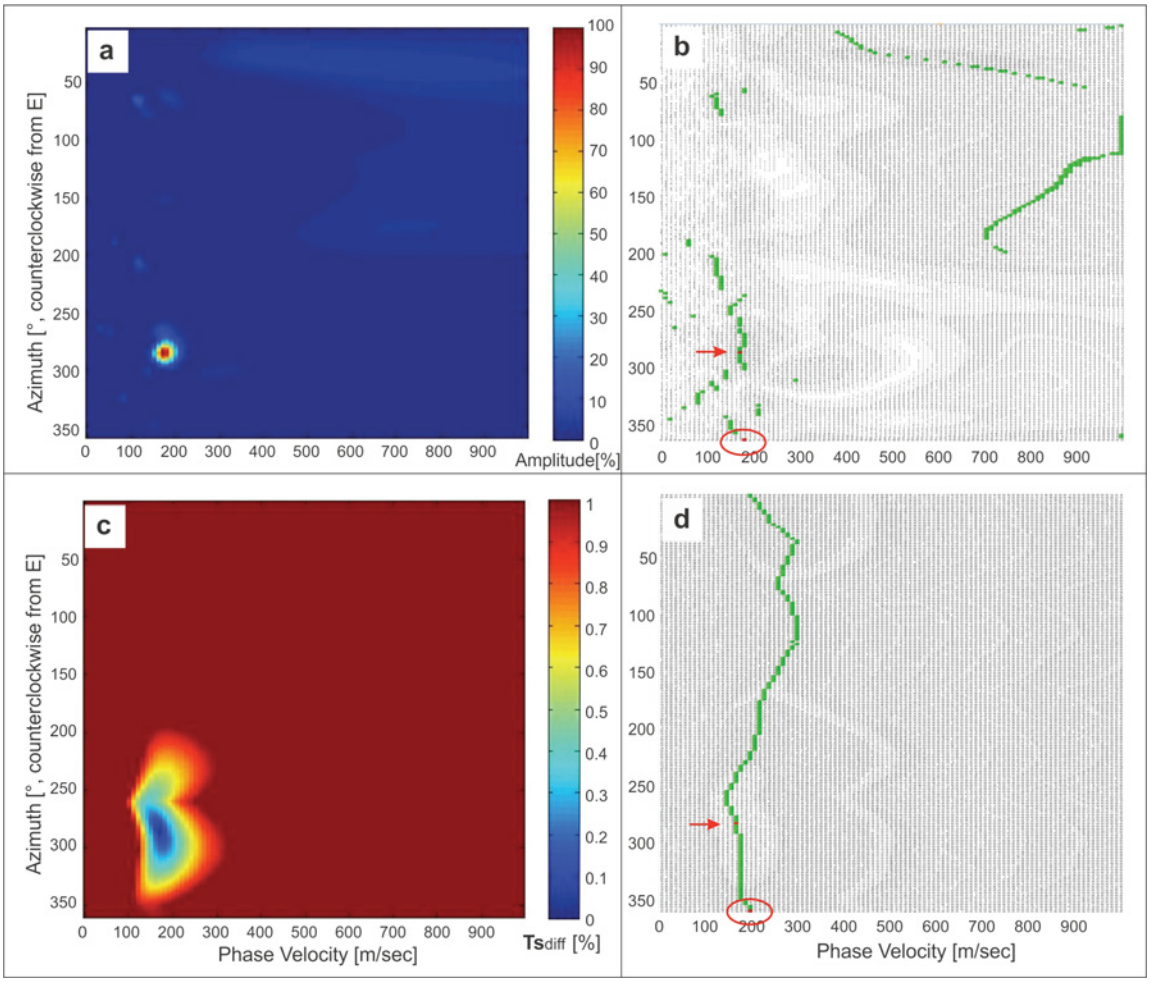

Figure 6.8 *Record 2217 (3-5s), 10 Hz* ***Energy distribution:*** *a) Phase velocity vs. Azimuth diagram, with Amplitude scale b) Phase velocity vs. Azimuth diagram, green curve: highest Energy for each Azimuth row, red arrow: overall maximum, last line: sum of all amplitudes stacked over the azimuths, red circle: Azimuth-stacked maximum energy.* ***Time-Shift difference distribution:*** *c) Phase velocity vs. Azimuth diagram, with TS_{diff} scale d) Phase velocity vs. Azimuth diagram, green: lowest variation of TS_{diff} for each Azimuth row, red arrow: overall minimum, last row: Azimuth-stacked TS_{diff}, red circle: Azimuth-stacked minimum TS_{diff}.*

The deviation from the result stacked over the azimuths (highest value at 550m/s) and the non-stacked high (440m/s) in Figure 6.7b could have different reasons. One reason could be interference between signals coming from sources out of different directions. In this case the presence of sources from more directions which emit 5.5 Hz signals are not obvious (Figure 6.6a), or from the fact that the spread is too short *(see chapter 6.3.5)*. Another reason could be the influence of the geometry of geophones. This assumption is supported due to the relation between the highest amplitude curve in Figure 6.7b and the lowest Time-Shift difference curve in Figure 6.7d. Both curves are open to the higher phase velocities and drag the stacked (over azimuths) maximum/minimum results away from the non-stacked results in direction to the higher velocities. A mix of all the mentioned problems could also be possible.

Additional to the 5Hz signal in Record 2217(3-5s) also the 10Hz signal is investigated, because its main signal comes from a different direction, not consistent with a direction of the single array lines.

In the Phase velocity versus Azimuth diagram of Figure 6.8b the amplitude-maxima for a frequency of 10 Hz of array 2000 are shown. The highest amplitude-maximum for the 10Hz signal is at an angle of 286° and at a phase velocity of 170 m/s. The sum of the amplitudes stacked over the azimuths has its high at a phase velocity of 180 m/s. As the Azimuth intervals are selected in increments of 10 m/s, these results agree very well. Figure 6.8a shows that the energy is not distributed over phase-velocity or azimuths. The high appears very sharp and localized. Stacking over the azimuths does not influence the Phase velocity significantly.

The Time-Shift difference distributions in the Phase velocity versus Azimuth diagrams for the 10Hz signal in Figure 6.8c and d confirm the geometry independence already expected from the amplitude distribution. In comparison to the Time-Shift difference distribution for the 5Hz signal, the Time-Shift difference of the 10Hz signal increases fast away from the basic value (170m/s, 286°). This implies that this particular event is well resolved and the geometry allows hardly any similar Time-Shifts out of the combination of the scanning parameter. A minimal deviation directed towards the 260° mark, which is the orientation of the N-S lines, is observable. Comparing again Figure 6.8a and d this dependence seems to play no rule in the result. Hence there is no effective geometry dependence. Additionally to it the higher frequency and with it the smaller wavelengths can contribute that the signals are less affected by similar Time-Shifts.

Example 2

From Array 2000 another example shall be shown here. For the second example the time window from 30.6 to 32 seconds has been extracted out of Record 2200. The main energy comes here from a train travelling west of the spread moving from South to North. In comparison to the first example the energy is less focused, coming from a broader azimuthal range.

The Azimuth versus Frequency diagram (Figure 6.9a) shows an accumulation in the low-frequency part of the spectrum at about 150° (Figure 6.9b). The higher frequency energy is distributed (red eclipses) across other Azimuth quadrants. The energy distribution of the dispersion image (6.9c) allows an interpretation to a frequency of about 6.5 Hz, which equates to an investigation depth of around 25 meters (Xia et al. 1999).

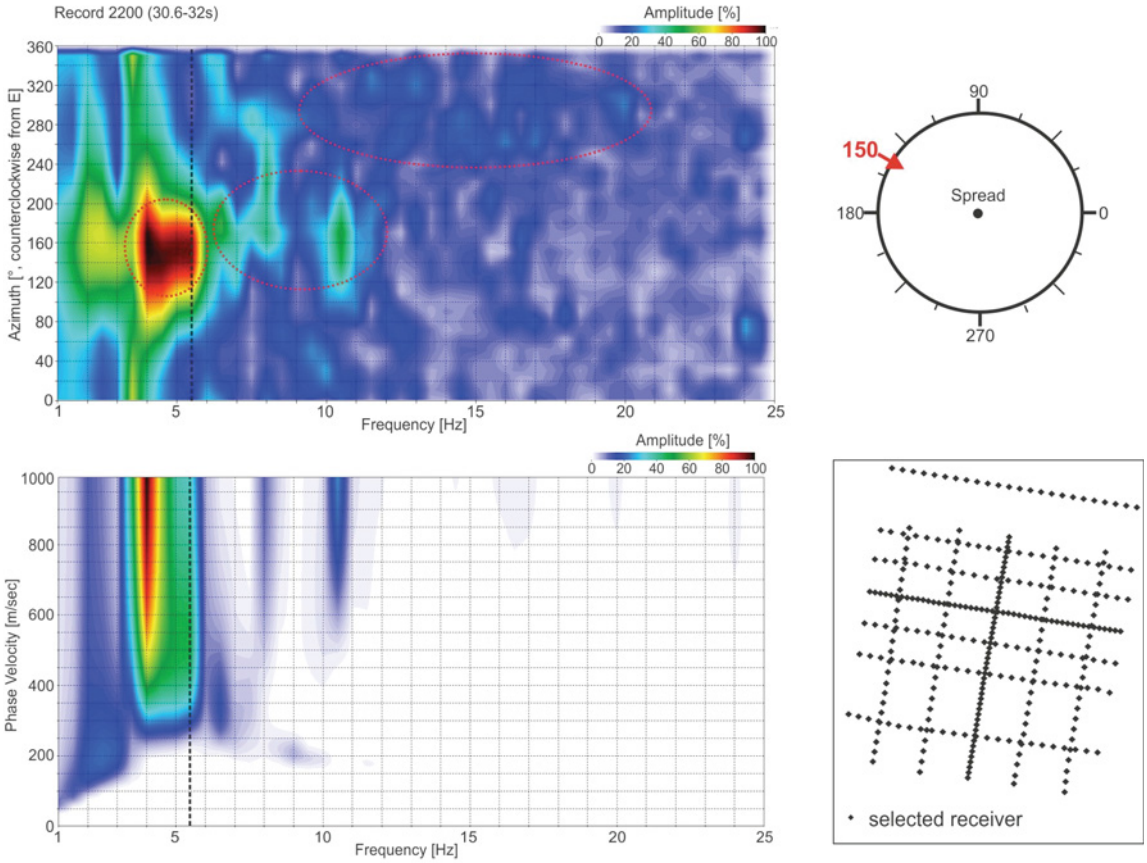

Figure 6.9 *Record 2200 (30.6-32s) upper left: Azimuth vs. Frequency diagram, red circles marks maximum incoming energy, black dashed lines assigns tested frequencies; upper right: Azimuth circle; lower left: Phase velocity vs. Frequency diagram; lower right: array with selected receivers.*

The Phase velocity - Azimuth diagrams of Figure 6.10 show the amplitude and Time-Shift difference distributions for a frequency of 5.5 Hz. One can see that high amplitudes concentrate around an angle of 150° between 400 and 500 m/s. The highest amplitude maxima can be found at an angle of exact 150° and a phase velocity of 450 m/s (Figure 6.10a and b). The maximum of the amplitudes stacked over the azimuths is found at a phase velocity of 580 m/s (Figure 6.10b). Whether this shift to the higher phase velocities is a consequence of the array geometry shall be investigated on the Time-Shift difference visualizations.

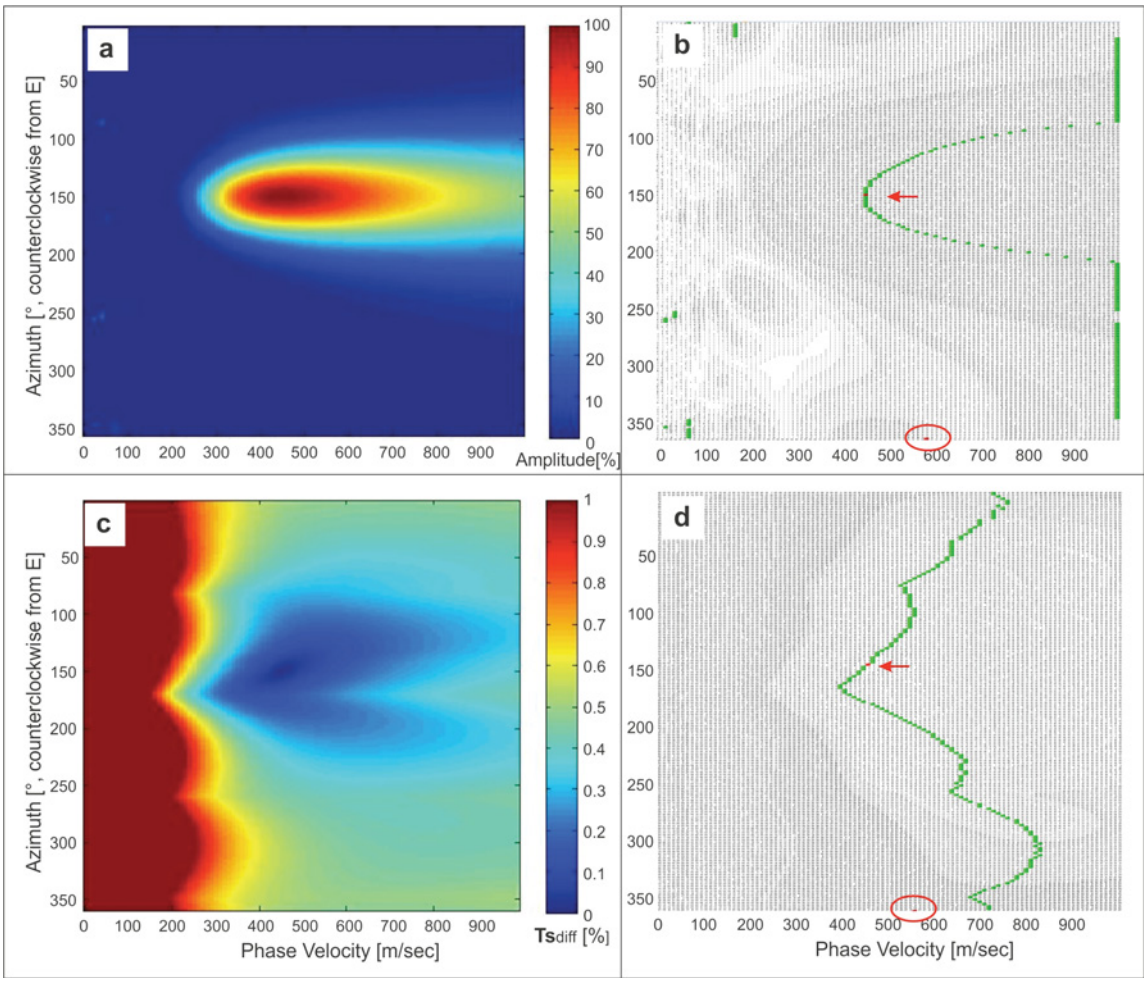

Figure 6.10 *Record 2200 (30.6-32 s), 5.5 Hz* ***Energy distribution:*** *a) Phase velocity vs. Azimuth diagram, with Amplitude scale b) Phase velocity vs. Azimuth diagram, green curve: highest Energy for each Azimuth row, red arrow: overall maximum, last line: sum of all amplitudes stacked over the azimuths, red circle: Azimuth-stacked maximum energy.* ***Time-Shift difference distribution:*** *c) Phase velocity vs. Azimuth diagram, with* TS_{diff} *scale d) Phase velocity vs. Azimuth diagram, green: lowest variation of* TS_{diff} *f for each Azimuth row, red arrow: overall minimum, last row: Azimuth-stacked* TS_{diff}*, red circle: Azimuth-stacked minimum* TS_{diff}*.*

Using the velocity (450 m/s) and the direction (150°) parameters from the maximum amplitude (determined from Figure 6.10a/b) for the Time-Shift difference calculation, the patterns in Figure 6.10c and d develop. In Figure 6.10c is recognizable that the Time-Shift difference influence concentrates around the angle of maximum incoming energy (130° to 160°) and gets negligible in the farther distant azimuths. The Time-Shift difference influence on the results is stretched in favour to the higher phase velocities. In Figure 6.10d the green curve shows the

Time-Shift difference minima. All major Phase velocity minima of the green curve correspond to an angle of the array geometry (80°, 170°, 260°, 350°).

The last row of Figure 6.10d shows the sum of Time-Shift differences by stacking over the azimuths; the lowest variation is at a Phase velocity of 550 m/s. Regarding Figure 6.9c one notices that the energy concentration above 5.5 Hz is nearly constant, no clear maximum is recognizable. This appears often at lower frequency levels and is mostly the case when the dimensions of the receiver layout reach their limits of resolution *(see chapter 3.3)* or the source energy gets to weak. By investigating this event in more detail with single phase velocity and azimuth steps in Figure 6.10b, the maxima of the stacked energy is found at 580m/s, but this maximum is rather smooth.

As the non-stacked phase velocity maxima for 5.5 Hz of Record 2200 (30.6 - 32 s) at an azimuth of 150° lies around 450 m/s and the summed energy maximum lies at 580 m/s, it becomes clear that the geometry influence which shows a shift to a phase velocity of 550 m/s is for sure involved, but not the only influencing parameter.

Example 3

The third example is from array 5000 (Figure 6.11d). The main energy comes from a train travelling north of the spread. The Azimuth-Frequency diagram (Figure 6.11a) from the selected time window shows an accumulation in the low and high-frequency part of the spectrum at about 84° (NE- quadrant, Figure 6.11b). An accurate picking of the dispersion curve in Figure 6.11c is only possible down to a frequency of 7Hz.

For this record again the Frequency of 5.5Hz is investigated. In both, the Azimuth-Frequency and the Phase velocity-Frequency images 5.5Hz is marked with a black dashed line. In addition to the strong signal from 84˚ a weak signal is recognizable at about 270°.

Observing Figure 6.12a the energy distribution with the concentrations mention before at 270° and the more prominent energy at about 84° is visible in more detail. In comparison, the 270° signal travels at a higher phase velocity than the 84° signal.

In Figure 6.12b the green curve for Amplitude maxima shows in both energy concentrations a similar shape. The 84° signal has its high at a phase velocity of 340m/s, the 270° signal is shifted to a higher Phase velocities to about 570m/s. The higher phase velocities could indicate a higher mode signal and by investigating in more detail the dispersion curve image in Figure 6.11c, a hint of an eventual higher mode branch is visible. Another reason for the different phase velocities of the signals coming from different directions could be the diverse origin of the source signal (car instead of train). The waves are also passing different terrain (streets, underground foundations, installations, voids...); this could also lead to the velocity difference. As the investigated area is known for underground cavities and as the terrain was a formerly

inhabited area, underground variations would not only be possible but would also be expected. Only the magnitude of the velocity difference may possibly be not easy to explain.

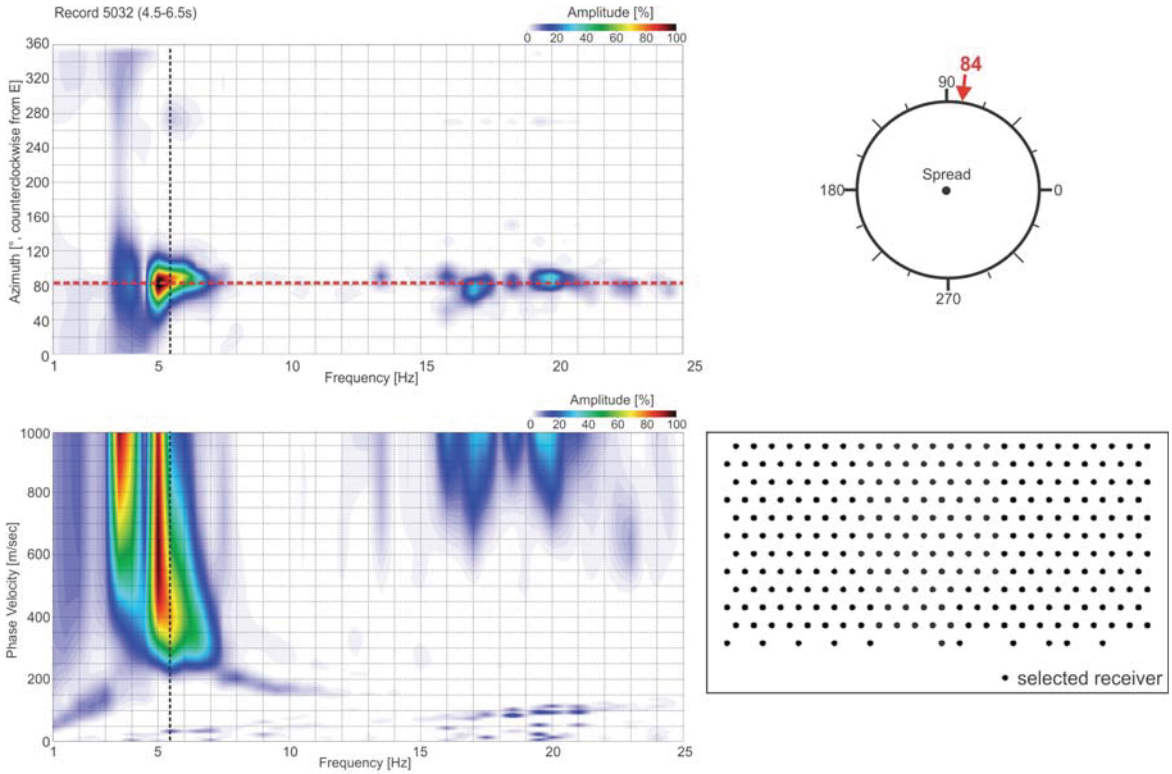

Figure 6.11 *Record 5032 (4.5 - 6.5 s) upper left: Azimuth vs. Frequency diagram, red dashed line marks maximum incoming energy, black dashed lines assigns tested frequencies; upper right: Azimuth circle; lower left: Phase velocity vs. Frequency diagram; lower right: array with selected receivers.*

The maximum amplitude value at 84° on the green curve does not entirely match the green curves phase velocity minimum of Figure 6.12b; the minimum is shifted slightly to the higher Azimuths at about 90°. This matches with the geometry of array 5000. Considering Figure 6.12d the shift towards the lower phase velocities to 90° is recognizable. As the array is elongated in West-East direction, a reduction in Phase velocity when being at the side of shortest extension (90°, 270°) is reasonable. A wavetrain from an angle of 90° (270°) needs with an identical velocity the shortest time to pass all geophones. The lowest Time-Shift difference at 90° to the real parameters has to be at a small reduction of the phase velocity to compensate for the for shortened array length.

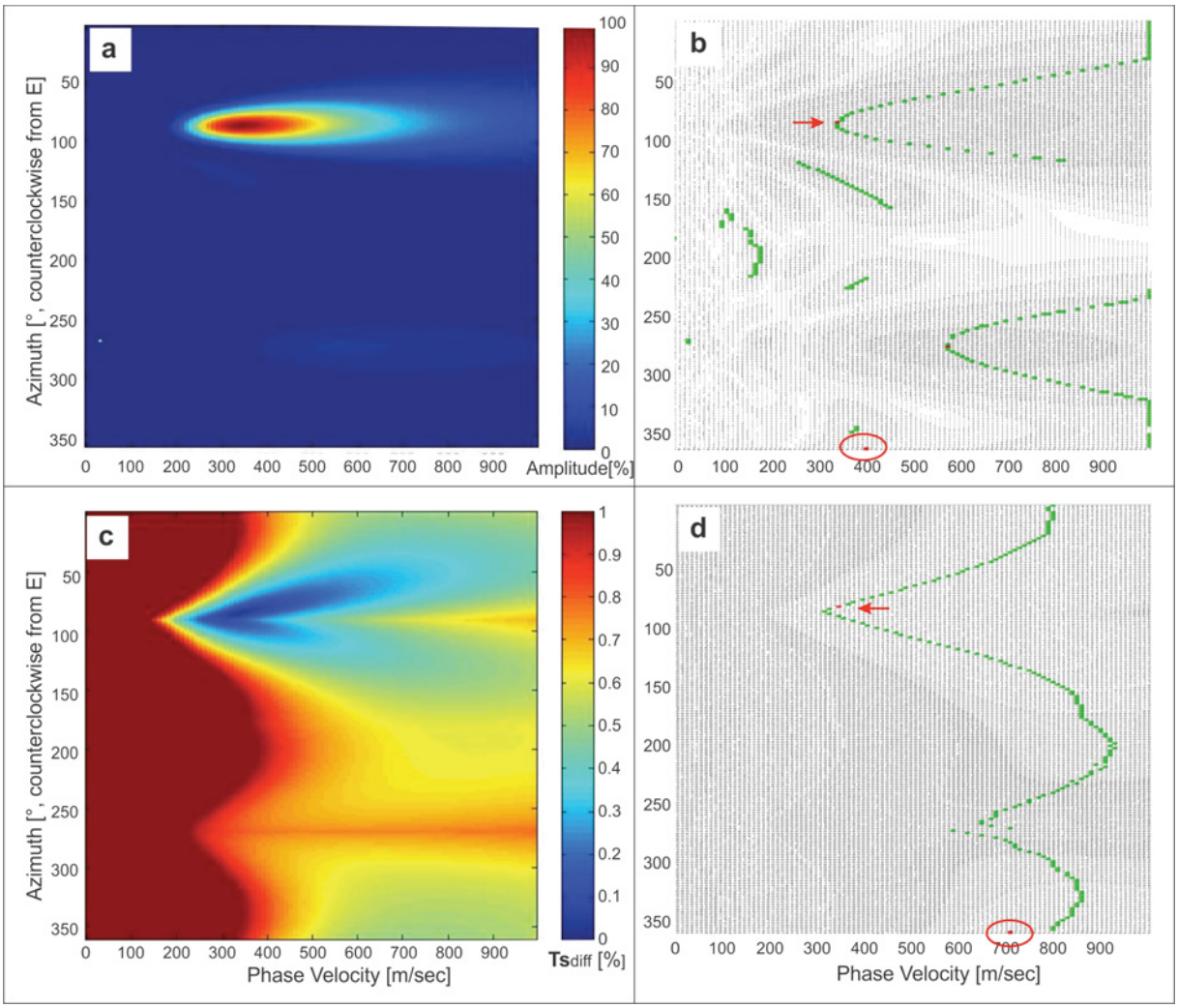

Figure 6.12 *5032 (4.5 - 6.5 s), 5.5Hz* ***Energy distribution:*** *a) Phase velocity vs. Azimuth diagram, with Amplitude scale b) Phase velocity vs. Azimuth diagram, green curve: highest Energy for each Azimuth row, red arrow: overall maximum, last line: sum of all amplitudes stacked over the azimuths, red circle: Azimuth-stacked maximum energy.* ***Time-Shift difference distribution:*** *c) Phase velocity vs. Azimuth diagram, with TS_{diff} scale d) Phase velocity vs. Azimuth diagram, green: lowest variation of TS_{diff} f for each Azimuth row, red arrow: overall minimum, last row: Azimuth-stacked TS_{diff}, red circle: Azimuth-stacked minimum TS_{diff}.*

Figure 6.12c and d show the Time-Shift Difference variation according to the geometry of array 5000 (main minima at 90° and 270°, smaller local ones at 180° and 360°). The minimum around 270° and 580m/s seems on the first sight to be too similar to the low energy concentration in Figure a and b to be ignored. Investigating Figure 6.12c in more detail on can recognize that the area around 270° has high Time-Shift difference values, which implies no geometry influence in this section. The additional energy concentration seems to be no artefact created during processing or geometry, but real influences from another source. From the

geometry induced shift towards higher phase velocity is when observing the over the azimuths summed energies (Figure 6.12b) only minimal influences recognizable.

6.2.1.2 *Passive MASW of various sub-arrays*

To find the optimal spread dimensions and geometry to record ambient noise for passive MASW the following examples show dispersion curves of different sub-arrays (square, cross, circle, filled circle, various, orientated rectangles) calculated from record 2217(3-5s), Figure 6.13, from Array 2000 with main energy coming out of East-South-East direction. For each array the chosen receiver data are shown as dispersion curve image, Frequency against Phase velocity, with the energy stacked over all Azimuths. For the 5 Hz signal of each array the energy and the Time-Shift difference are plotted in each a Phase velocity against Frequency diagram in two different ways of visualization.

The comparison between the different arrays should show their ability to process out of them truthful results, with as less as possible artefacts and at the same time best resolution.

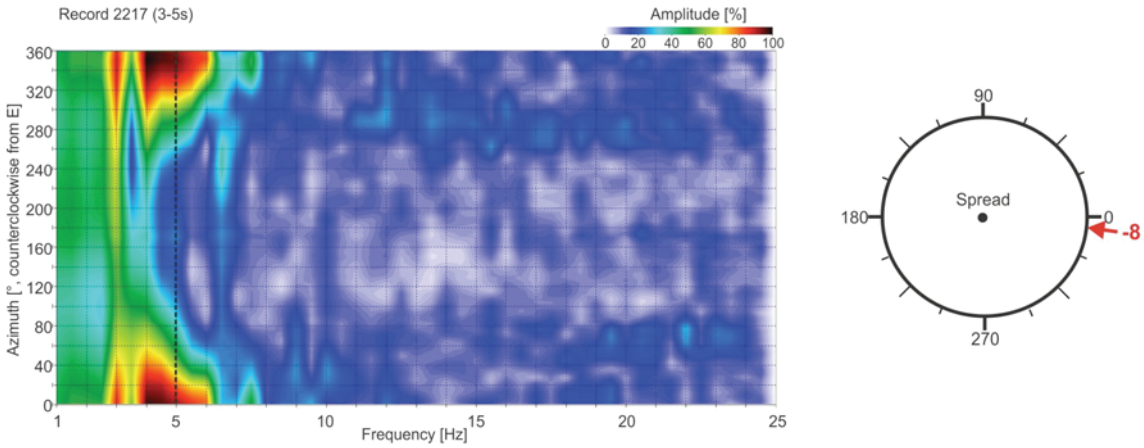

Figure 6.13 *Record 2217 (3-5s) left: Azimuth vs. Frequency diagram, main incoming energy from 352°, right: Azimuth circle.*

Square Array

For the sub-array "Square" 97 geophones are chosen from the original layout in a quadratic shape. The angles of the lines forming the square are identical to the original array parallel to the rail tracks, 80°/260° and 170°/350°. When comparing the dispersion curve of the square in Figure 6.14 with the dispersion curve of the whole array in Figure 6.6 only minor differences can be detected; very similar results have been obtained utilizing less than a third of the initial number of geophones. The dispersion curve can be resolved to a frequency of 6 to 6.5 Hz.

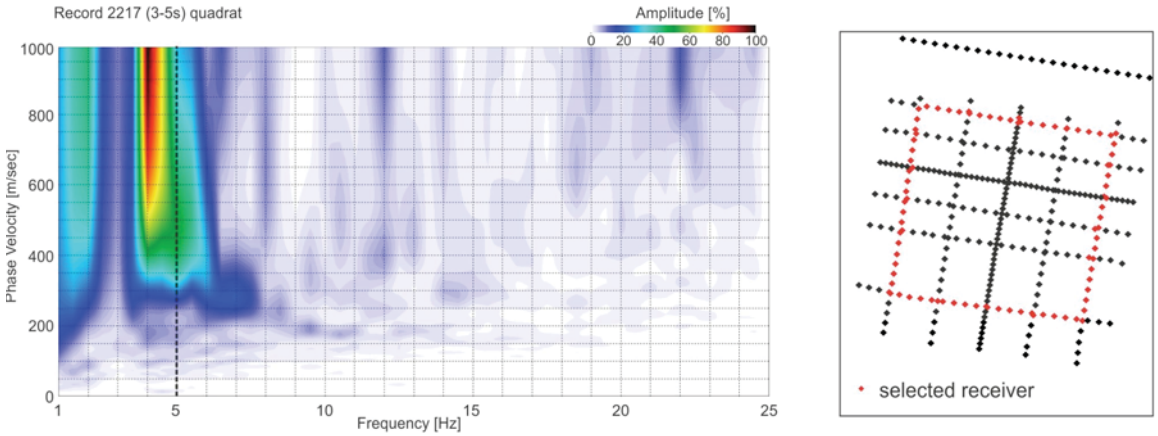

Figure 6.14 *Record 2217 (3-5 s) left: Phase velocity vs. Frequency diagram, black dashed line marks investigated Frequency, right: Array with selected receivers.*

The diagrams in Figure 6.15 show the relations of a frequency of 5 Hz recorded with the squared array. In Figure 6.15a and b, the Azimuth - Phase velocity diagrams, the amplitude maximum is found at an Azimuth of 352° and a Phase velocity of 440m/s. Amplitudes stacked over the Azimuth as shown in the dispersion curve image, have their maximum at 470m/s. In Figure 6.15a at low Phase velocities energy anomalies around the angles of the geometry of the square are recognizable, as they are low in velocity they seem not to interfere with the higher energy concentrations. At about 170° is an energy concentration with only a bit lower phase velocities as the one from maximum incoming energy. The relation of the energy accumulation around 170° to the geometry is questionable.

The Time-Shift difference variation images in Figure 6.15c and d show some geometry dependency +/- 50° around the angle of maximum incoming energy in direction to the higher phase velocities. In positive and negative direction from the angle of maximum incoming energy the geometry influence decreases with minimum influence at the opposite side of maximum incoming energy at 172°.

The influence of the geometry, which drags the maximum amplitudes towards higher velocity, stands in the case of investigated data, against the anomaly at an azimuth of about 170° that shows towards lower velocities. As result of both deviating influences, the stacked maximum amplitude is shifted in comparison to the non-stacked maximum incoming energy, 30m/s towards the higher phase velocities.

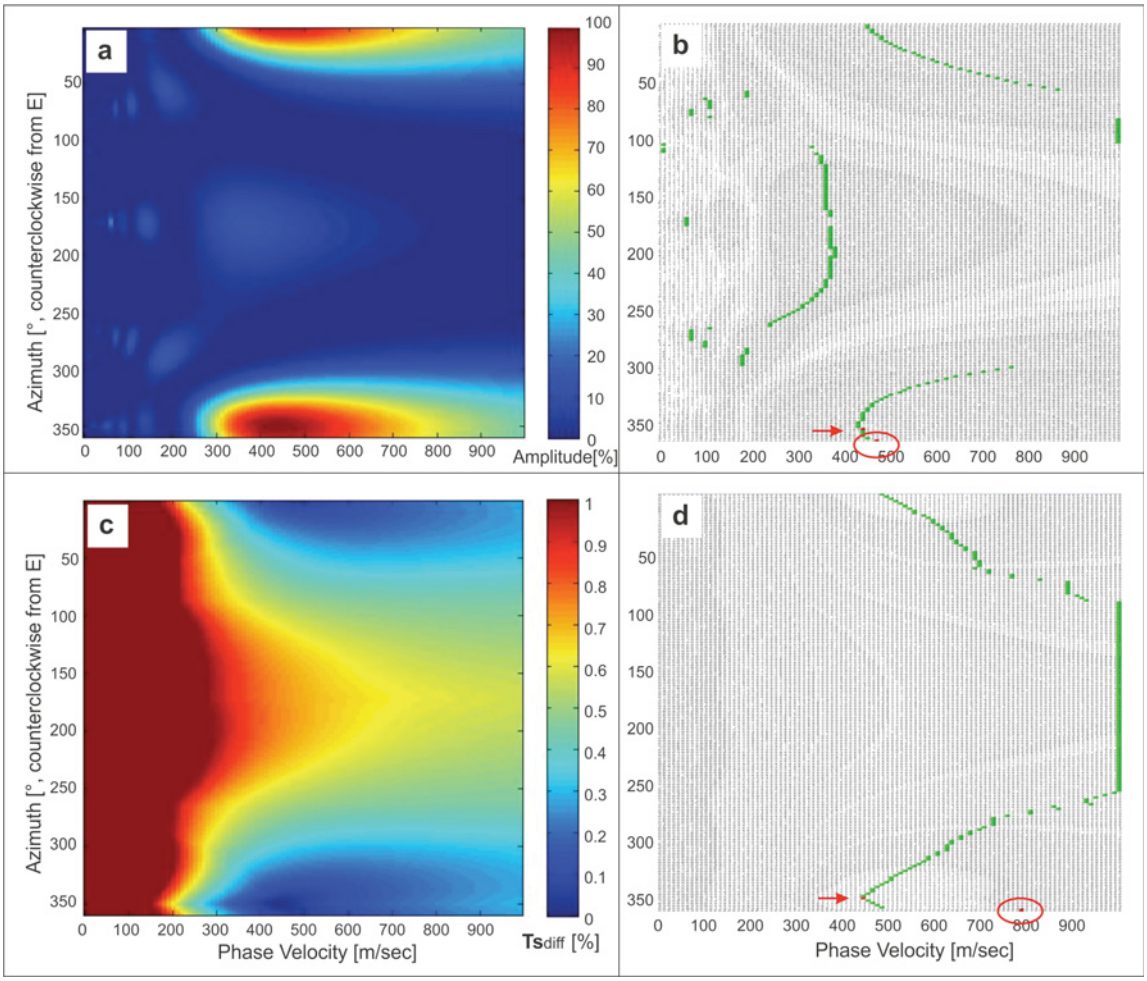

Figure 6.15 *Record 2217 (3-5 s), 5Hz* ***Energy distribution:*** *a) Phase velocity vs. Azimuth diagram, with Amplitude scale b) Phase velocity vs. Azimuth diagram, green curve: highest Energy for each Azimuth row, red arrow: overall maximum, last line: sum of all amplitudes stacked over the azimuths, red circle: Azimuth-stacked maximum energy.* ***Time-Shift difference distribution:*** *c) Phase velocity vs. Azimuth diagram, with TS_{diff} scale d) Phase velocity vs. Azimuth diagram, green: lowest variation of TS_{diff} f for each Azimuth row, red arrow: overall minimum, last row: Azimuth-stacked TS_{diff}, red circle: Azimuth-stacked minimum TS_{diff}.*

Cross Array

For the second spread 105 geophones are selected to form the sub-array “Cross”. The lines are parallel to the rail tracks, with the angles 80°/260° and 170°/350°. The dispersion curve image seems to have a bit more distributed energy in comparison to the original array and is resolvable down to a frequency of 6.5 to 7 Hz (Figure 6.16).

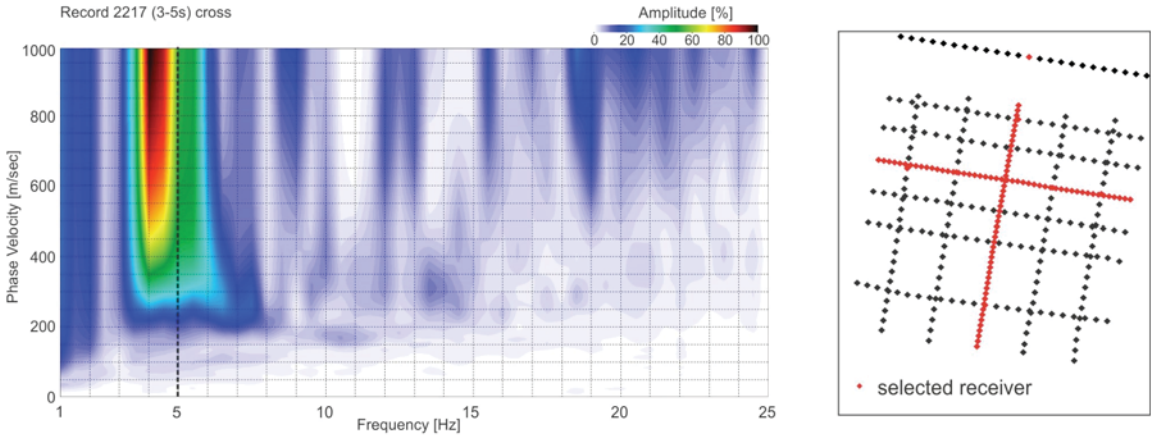

Figure 6.16 *Record 2217 (3-5 s) left: Phase velocity vs. Frequency diagram, black dashed line marks investigated Frequency, right: array with selected receivers.*

The energy distribution in the Phase velocity versus Azimuth diagrams in Figure 6.17 a and b is as expected similar to the curve of highest energy for each azimuth-step to the original and the square array: open to the higher phase velocities with the peak at the 350°, the geometry angle to the azimuth of maximum incoming energy. The energy maximum can be found at an angle of 354° and a Phase velocity of 410 m/s. Different from the former two distributions the higher energy concentration is stretched to the higher phase velocities, so that the stacked energy over the azimuth reaches the maximum of the displayed phase velocities. Clearly recognizable are also the geometry induced energy artefacts which are spreading from the induced azimuths (80°,170° and 350°) and near-zero phase velocity, with a bend towards higher phase velocities.

The Time-Shift difference illustrations in Figures 6.17 c and d show a more complicated relation as in the former examined array. The green curves marking minimal Time-Shift difference curves show several Phase velocity troughs and peaks. Thereby the Phase velocity decreases only immediately in the near to the angle of maximum energy, all other array dependent angles show their maximum Time shift similarity at higher phase velocities, but with maximum Phase velocity deviation of 300m/s from the true one.

The behaviour of the Time shift difference curve is easy to understand: The maximum incoming energy hits the geophones of the N-S line more or less all at the same time, where as the surface wave has to travel between the W-E orientated geophones the longest possible distance. By slightly changing the direction of assumed incoming energy to the NW or SW the N-S receiver offset change is still insignificant, whereas the receiver offset between the W-E geophones decreases and the phase velocity has to be reduced to receive a similar Time shift to the original one. After increasing the angle further from the true original one, the N-S receiver's influence increases and the phase velocity has to be augmented to compensate the effect of larger receiver offsets. With further deviation from the original azimuth the Time shift difference parameter increases and the geometry looses the influence on the data.

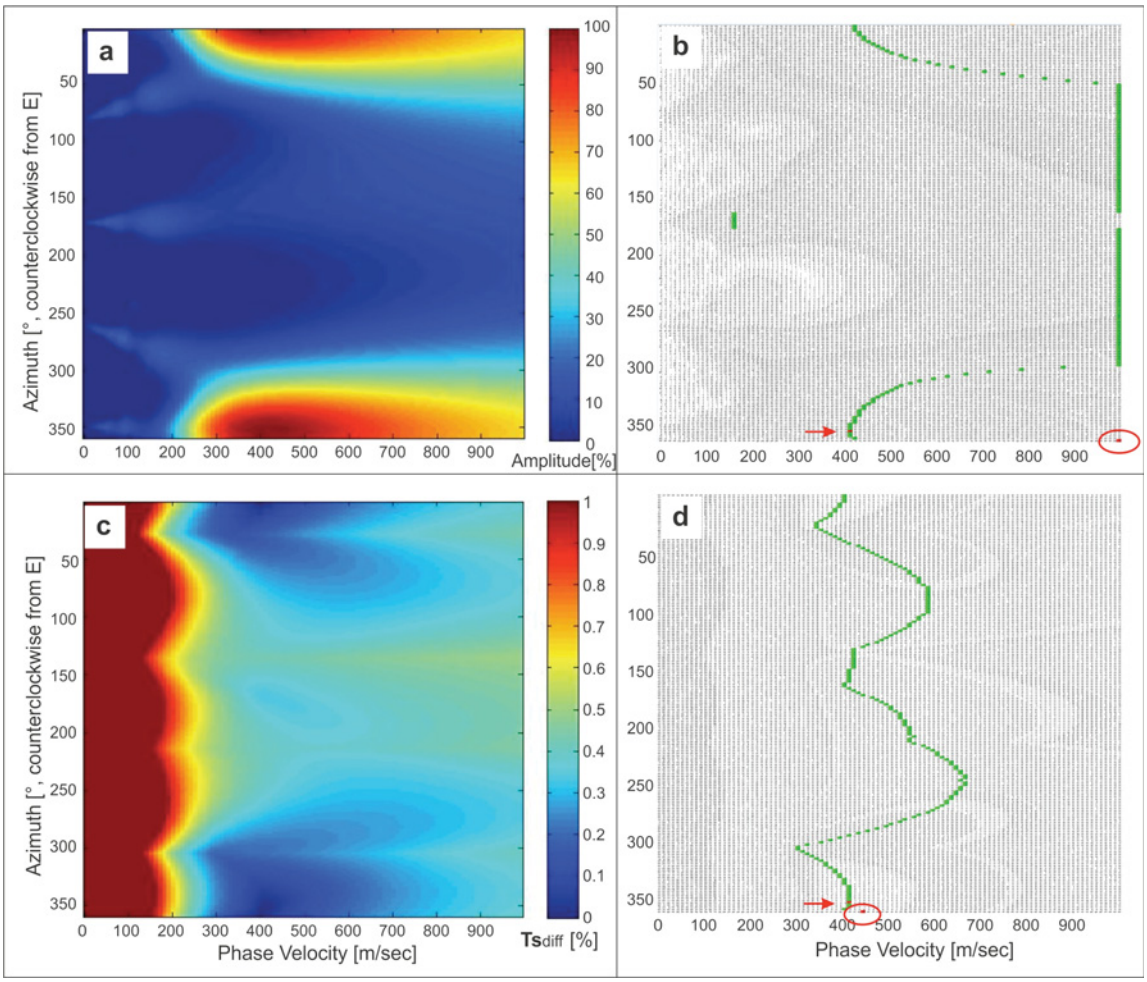

Figure 6.17 *Record 2217 (3-5 s), 5Hz,* ***Energy distribution:*** *a) Phase velocity vs. Azimuth diagram, with Amplitude scale b) Phase velocity vs. Azimuth diagram, green curve: highest Energy for each Azimuth row, red arrow: overall maximum, last line: sum of all amplitudes stacked over the azimuths, red circle: Azimuth-stacked maximum energy.* ***Time-Shift difference distribution:*** *c) Phase velocity vs. Azimuth diagram, with TS_{diff} scale d) Phase velocity vs. Azimuth diagram, green: lowest variation of TS_{diff} f for each Azimuth row, red arrow: overall minimum, last row: Azimuth-stacked TS_{diff}, red circle: Azimuth-stacked minimum TS_{diff}.*

The balanced dimensions of the array lead to an overall stacked Time shift difference parameter with its minimum close to the data of origin. Nevertheless the result in Figure 6.17 b shows that the stack over the azimuth does not show a maximum within the range of analyzed and reasonable phase velocities .

Comparing Figure 6.17c with the identical diagrams of the former arrays shows that even if the stacked value is similar to the original value, the distribution of the geometry influence (blue

colors) is more significant than in the former arrays. This and perhaps the fact that the spread could be in its overall dimensions, with only two lines and one line nearly directly orthogonal to the incoming energy, not ideal or large enough for the resolution of the 5 Hz signal.

Circle Array

The sub-array "Circle" (Figure 6.18b) has been created out of 21 geophones chosen from the original array. The sub-array has not totally the dimensions of a real circle but is stretched a bit in north-south direction.

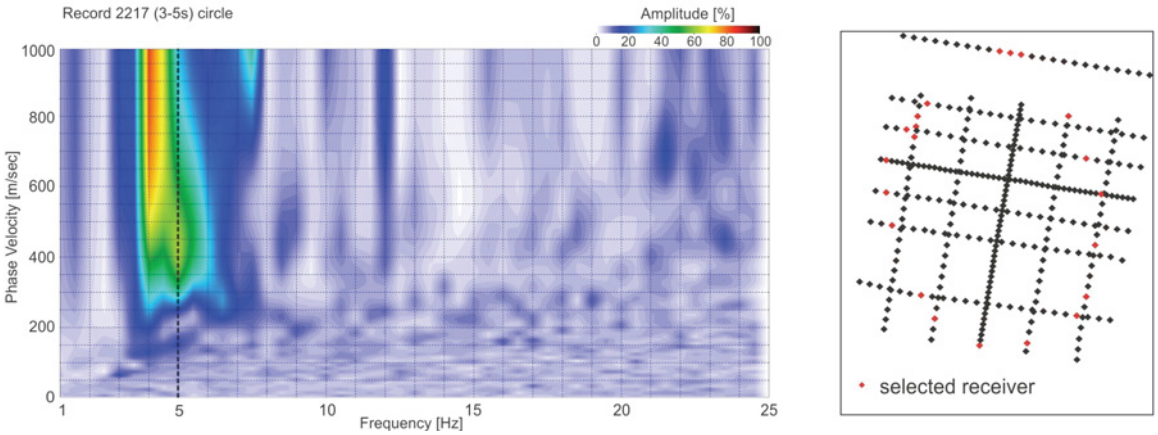

Figure 6.18 *Record 2217 (3-5 s) left: Phase velocity versus Frequency diagram, black dashed line marks investigated Frequency right: array with selected receivers.*

The Frequency-Phase velocity diagram in Figure 6.18 (left) seems to deviate a bit from the one of the former sub-arrays and the original array: Whereas in the higher Frequencies only a low signal-to-noise ratio can be observed, and a dispersion curve can be assumed only to maximal frequency of 9Hz, the resolution towards the lower frequencies seems to allow results down to a still clearly defined Frequency of 5 Hz.

In Figure 6.19 a and b, the Azimuth Phase velocity distributions of the 5 Hz signal show an Energy maximum at an Azimuth of 354° and a Phase velocity of 410m/s. The energy seems strongly concentrated around the maximum and than to decrease fast towards al sides, except towards the higher Phase velocities the energy seems to decrease a bit slower, but much faster than in comparison to the former investigated sub-arrays. By stacking the energy over the Azimuth (red circle, Figure 6.19b) the maximum energy concentration can be found at 420m/s; this result is also displayed in the dispersion curve image (6.18, right) over the 5 Hz signal.

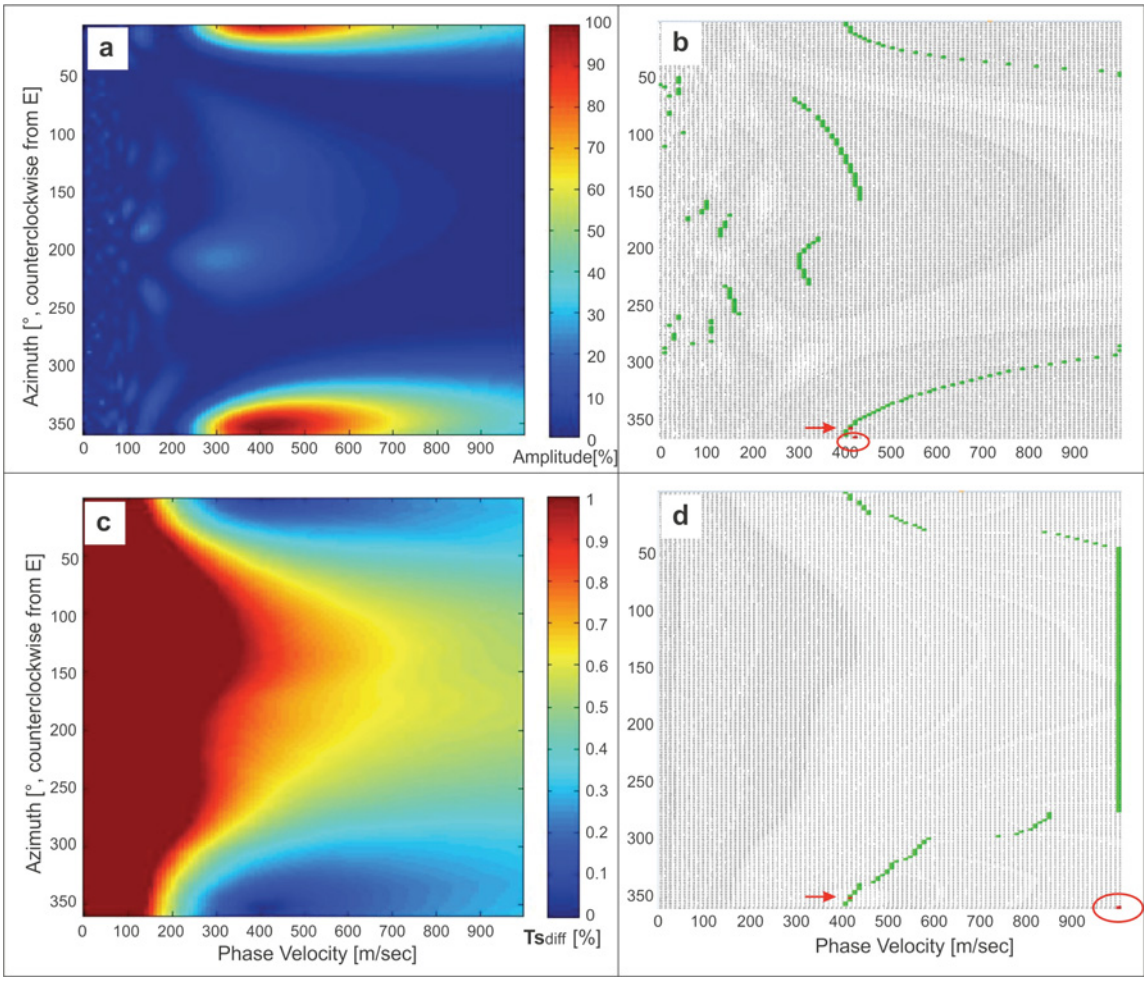

Figure 6.19 *Record 2217 (3-5s), 5 Hz* ***Energy distribution:*** *a) Phase velocity vs. Azimuth diagram, with Amplitude scale b) Phase velocity vs. Azimuth diagram, green curve: highest Energy for each Azimuth row, red arrow: overall maximum, last line: sum of all amplitudes stacked over the azimuths, red circle: Azimuth-stacked maximum energy.* ***Time-Shift difference distribution:*** *c) Phase velocity vs. Azimuth diagram, with* TS_{diff} *scale d) Phase velocity vs. Azimuth diagram, green: lowest variation of* TS_{diff} *f for each Azimuth row, red arrow: overall minimum, last row: Azimuth-stacked TSdiff, red circle: Azimuth-stacked minimum TSdiff.*

At an Azimuth of about 200° and a Phase velocity of about 300 m/s an energy accumulation can be recognized, that, without closer investigations, cannot be brought into relation with the geometry depending parameters.

The Time-Shift difference distribution in the Figure 6.19c shows a geometry dependency of the results only in the vicinity of the maximum incoming energy, in form of an ellipse elongated towards the higher Phase velocities. In direction of the Azimuth axis the Time-Shift difference increases fast with the distance from the maximum income of energy, which implies that the influence of the geometry decreases. At an Azimuth of 200° where there has been found an energy accumulation in Figure 6.19a, the Time-Shift difference distribution shows a small, but

unexpected reduction in the variation factor, which would enhance a geometry induced artefact in position of the already existing energy concentration.

Figure 6.19d shows the Time-Shift difference minimum (green) of each Azimuth row. The green curve has its Phase velocity minimum at an Azimuth of about 360° and their maximum outside the investigated range of Phase velocities. Most of the Azimuths (50° - 290°) seem to have their Time -Shift difference minimum at Phase velocities equal or higher than 1000 m/s. That can be explained as follows:

The in north-south direction elongated circular (elliptic) sub-array has it's shortest distance between all receivers by observing them from a direction of about 180°/360° (west/east). As 360° is near the angle of maximum incoming energy, a decrease in the Phase velocity, because off the smaller distance between the receiver, would imply a similar Time=Shift parameter to the one of the maximum incoming energy. To all other sides the phase velocity has to be increased to get smallest Time-Shift difference Values. As the form of a circle in comparison to lines or other shapes, changes with the observing angle relatively fast, the order in which the geophones are reached by the waves, the influence of increasing (or reducing) the Phase velocity on the Time-Shift difference parameter is restricted only to the near closeness of the real angle of incoming energy. A regular circular array has hence nearly no area where geometry is influencing the results, if the array is deviating from the regular circle an influence on the results has to be expected.

So, even if the stacked minimum Time-Shift difference parameter lies at the upper end of investigated Phase velocities, the influence of the geometry is too small to drag the results towards higher Phase velocities. This is clearly recognizable from the stacked energies in the dispersion curve image in Figure 6.18 and the energy distribution of Figure 6.19b, where the maximum incoming energy coincides with the overall stacked energy.

Filled circle Array

For the sub-array “Filled circle”, the geophones enclosed from the contour of the above-described array “circle” were added to the existing array (Figure 6.20, right). Even if the contours of the “filled circle” and the “circle” array are identical, the results differ obviously from each other. Whereas the former array resolves in the dispersion curve image a frequency of 5 Hz and fails in the higher frequencies, the “filled circle” array, behaves like the original array: clear in the higher frequencies, also a higher mode is visible, but has insufficient resolution in the lower frequencies (Figure 6.20, left). The resolution of the dispersion curve allows a distinction only down to 6.5 Hz.

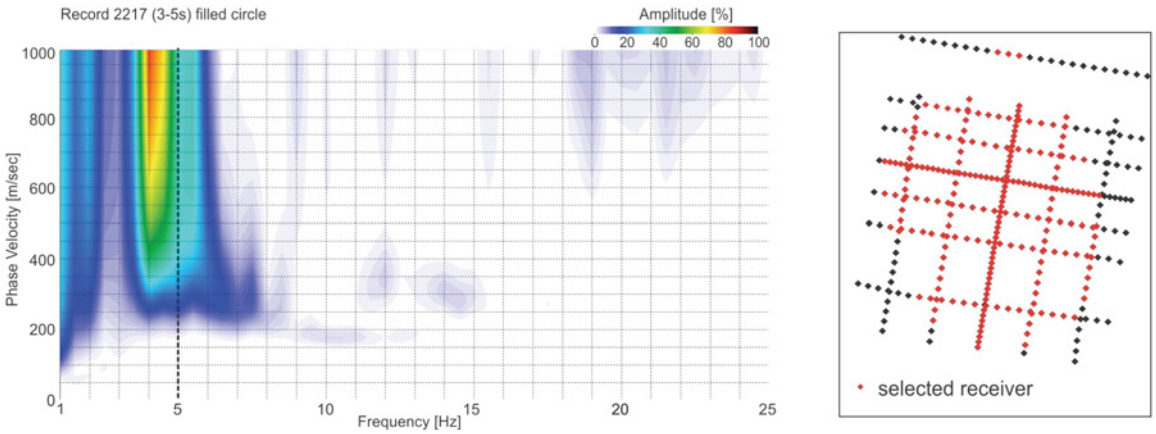

Figure 6.20 Record 2217 (3-5 s) left: Phase velocity vs. Frequency diagram, black dashed line marks investigated Frequency, right: array with selected receivers.

The energy distribution for the 5 Hz signal in the Azimuth - Phase velocity diagrams, Figure 6.21a and b, show an energy maximum at an Azimuth of 354° and a Phase velocity of 390m/s. Amplitudes stacked over the Azimuth as shown in the dispersion curve image have their maximum at the upper limit (Figure 6.21b, red circle) of the investigated phase velocity range (0 -1000m/s).

The green Time-Shift difference minimum curve in Figure 6.21d is formed once again by the 4 directions (80°, 170°, 260°, 350°) given from the geophone geometry. The minimum value of the Azimuth-stacked Time-Shift difference results at a Phase velocity of 600m/s. This value is misleading: Considering Figure 6.21c one recognizes low Time-Shift differences around an Azimuth of 354°, the angle of maximum incoming energy, whereas at the opposite direction ~170°, high Time-Shift difference values appear. The Time-Shift difference at 170° indicates a local minimum at about 520m/s. These local low values that are already too high to have a significant influence on the data, drag the Azimuth-stacked Time-Shift difference minimum towards lower Phase velocities.

The comparison between the dispersion curves of circle and filled circle show again: To resolve low frequencies an array is needed, which doesn't introduce angles of orientation different from the incoming energy. It only produces noise. For higher frequencies smaller receiver distances are advantageous.

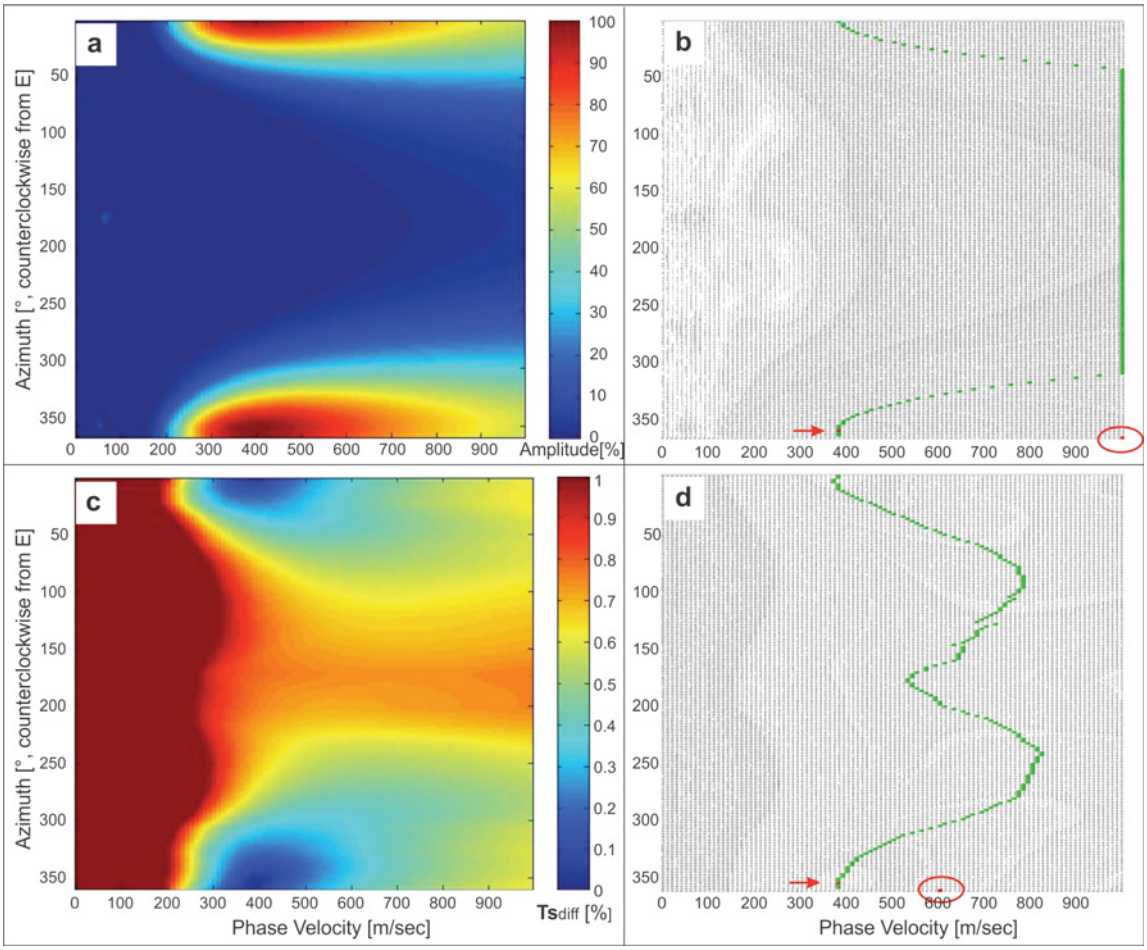

Figure 6.21 *Record 2217 (3-5s), 5 Hz* ***Energy distribution:*** *a) Phase velocity vs. Azimuth diagram, with Amplitude scale b) Phase velocity vs. Azimuth diagram, green curve: highest Energy for each Azimuth row, red arrow: overall maximum, last line: sum of all amplitudes stacked over the azimuths, red circle: Azimuth-stacked maximum energy.* ***Time-Shift difference distribution:*** *c) Phase velocity vs. Azimuth diagram, with TS_{diff} scale d) Phase velocity vs. Azimuth diagram, green: lowest variation of TS_{diff} f for each Azimuth row, red arrow: overall minimum, last row: Azimuth-stacked TS_{diff}, red circle: Azimuth-stacked minimum TS_{diff}.*

Random Array

For the generation of the sub-array "Random", 41 geophones were picked randomly out of the original array (Figure 6.22, right). With the help of this sub-array the influences of the preferential orientation of geophone lines in the original array, should be reduced. The dispersion curve image in Figure.6.22 (left) shows a resolution to 6.5Hz/ 6Hz.

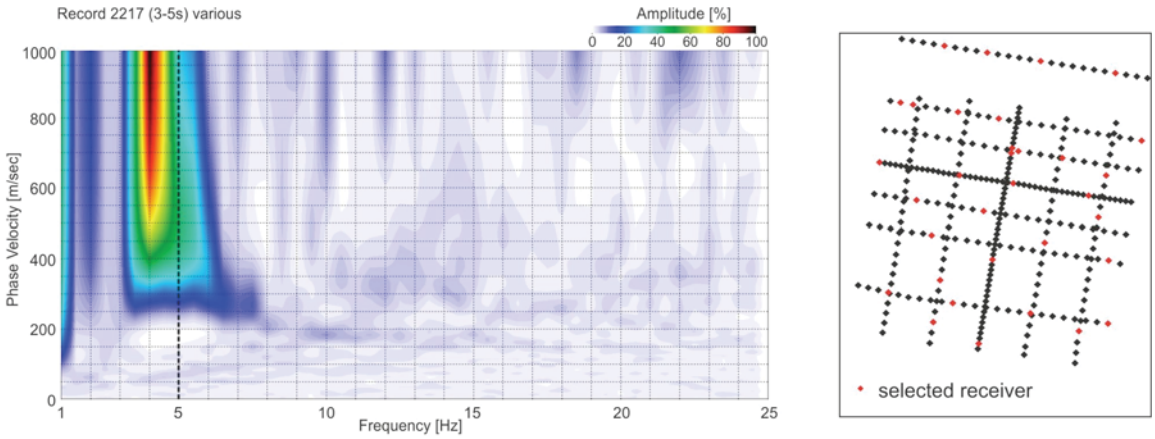

Figure 6.22 *Record 2217 (3-5 s) left: Phase velocity vs. Frequency diagram, black dashed line marks investigated Frequency, right: array with selected receivers.*

In the Azimuth - Phase velocity diagrams (Figure 6.23a and b) for the Frequency of 5Hz one can see an energy maximum at an azimuth of 350° and a phase velocity of 410m/s. Another energy accumulation appears with a low amplitude around an angle of 140° and a Phase velocity of 450 m/s. It seems to have no obvious link to the array geometry. The stacked energy shows its maximum at a Phase velocity of 500 m/s (Figure 6.23b). The dispersion curve image of Figure 6.22 (left) reflects this result.

The Time-Shift difference distribution in Figure 6.23c shows that the Time-Shift varies from the one of maximal incoming energy with increasing angle to it. By increasing the Phase velocity the Time-Shift difference gain gets reduced. The green curve of Figure 6.23d, has its Phase velocity minimum around 350° and is slowly increasing to other directions. This behaviour can be explained by the in north-south direction elongated dimensions of the random array. Towards north or south, respectively, the receiver offsets get larger and the arrival times and with it the Time-Shifts become longer. By manipulating the Phase velocity towards higher values, the Time-Shift difference to the maximum incoming energy is kept low.

The Azimuth-stacked Time-Shift differences have their minimum at about 580m/s (Figure 6.23d), which lets suggest that the shift between Azimuth-stacked energy high (500m/s) and non stacked energy high (410m/s) is to a part geometry-induced.

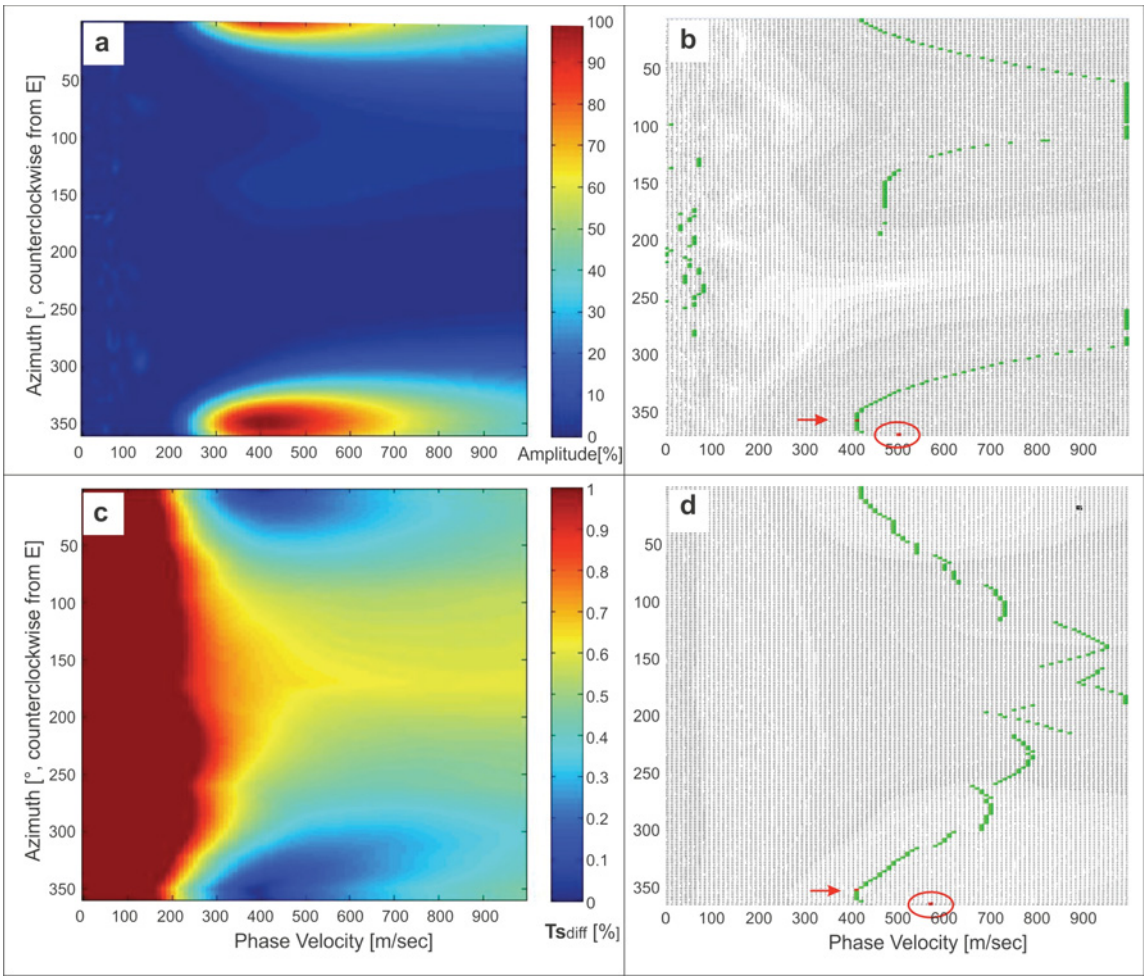

Figure 6.23 *Record 2217 (3-5s), 5 Hz* ***Energy distribution:*** *a) Phase velocity vs. Azimuth diagram, with Amplitude scale b) Phase velocity vs. Azimuth diagram, green curve: highest Energy for each Azimuth row, red arrow: overall maximum, last line: sum of all amplitudes stacked over the azimuths, red circle: Azimuth-stacked maximum energy.* ***Time-Shift difference distribution:*** *c) Phase velocity vs. Azimuth diagram, with TS_{diff} scale d) Phase velocity vs. Azimuth diagram, green: lowest variation of TS_{diff} f for each Azimuth row, red arrow: overall minimum, last row: Azimuth-stacked TS_{diff}, red circle: Azimuth-stacked minimum TS_{diff}.*

Orientated rectangle Array

The sub-array "Orientated rectangle" exists of a narrow rectangular array with 32 receivers, a width of 5 m and a length of 56.5 m, orientated parallel to the direction of the incoming surface waves (strongest energy in the frequency range between 4 and 6 Hz, azimuth 352° (Figure 6.24, right)). The dispersion curve image calculated out of the orientated rectangle seems to be resolvable to about 4.5Hz.

In contrast to the previous sub-arrays, the orientated rectangle shows in all distributions (Figure 6.25) curves or energy distributions open to the lower phase velocities, with the curve maximum at the orientation angle of the rectangle. The reason for it is that the long side of the sub-array lies for the first time in west-east direction and with deviating from the orientation direction, calculated distances between receivers become smaller and by reducing the Phase velocity a similar Time-Shift to the one of maximum energy income gets simulated.

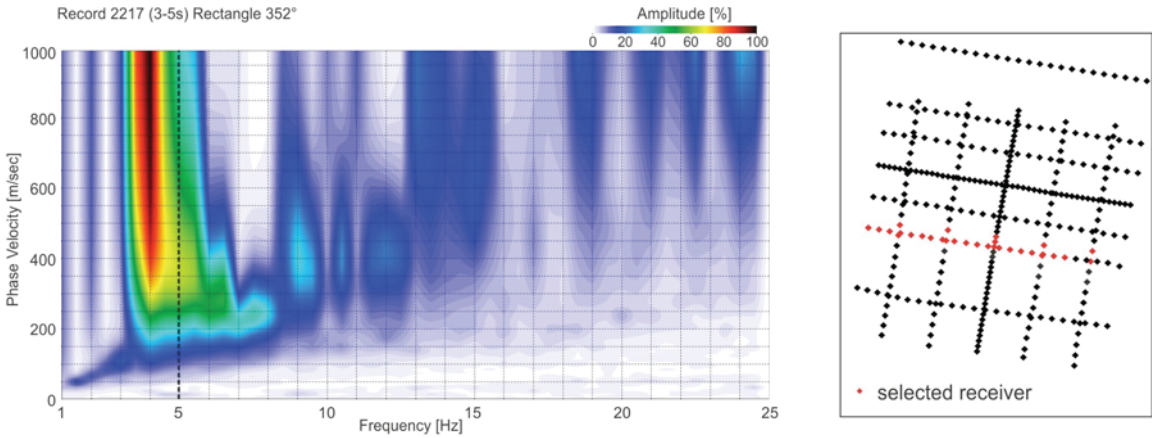

Figure 6.24 *Record 2217 (3-5 s) left: Phase velocity vs. Frequency diagram, black dashed line marks investigated Frequency, right: array with selected receivers.*

The energy maximum in Figure 6.25a and b is found at an Azimuth of 356° and a Phase velocity of 430 m/s (Figure 6.25b, red arrow). Amplitudes stacked over the azimuth as shown in the dispersion curve image (Figure 6.24, left), have their maximum at 370m/s (Figure 6.25b, red circle).

The Time-Shift difference calculations in Figure 6.25c and d show strong Time-Shift similarities at deviations up to 90° to both directions when combined with Phase velocity decreases. In addition, Time-Shift similarities appear also at the maximum incoming energy angle along higher Phase velocities. The latter is a result of the nearly one dimensional receiver distribution. The shift of the Azimuth stacked energy towards lower Phase velocities is a result of the chosen geometry.

Due to the vulnerability of the array in terms of geometry-induced errors, the array should not be used without knowing the maximum incoming energy and the geometry induced error distribution. As the orientated rectangular array bears also different advantages an adapted way of working with this receiver configuration will be handled later in this thesis.

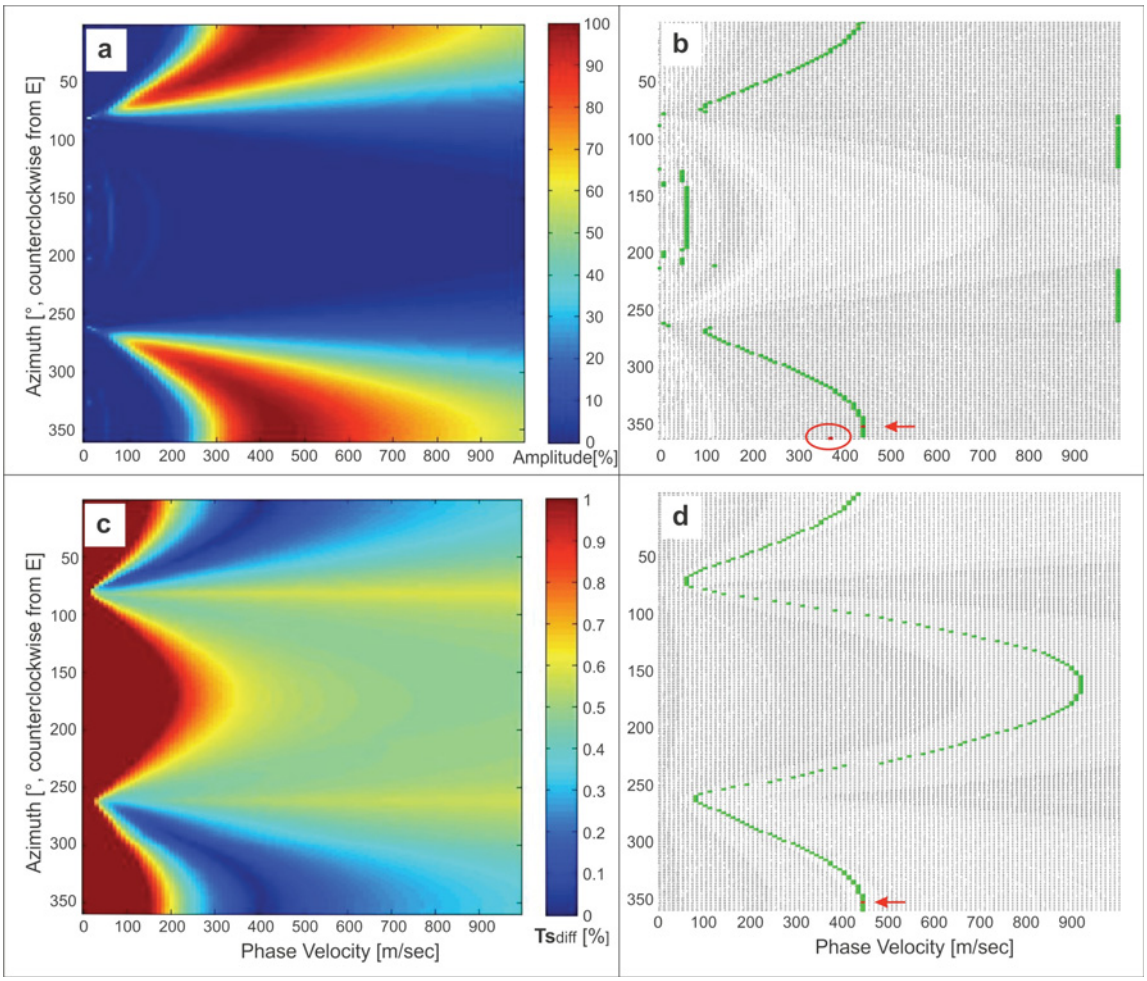

Figure 6.25 Record 2217 (3-5s), 5 Hz ***Energy distribution:*** *a) Phase velocity vs. Azimuth diagram, with Amplitude scale b) Phase velocity vs. Azimuth diagram, green curve: highest Energy for each Azimuth row, red arrow: overall maximum, last line: sum of all amplitudes stacked over the azimuths, red circle: Azimuth-stacked maximum energy.* ***Time-Shift difference distribution:*** *c) Phase velocity vs. Azimuth diagram, with TS_{diff} scale d) Phase velocity vs. Azimuth diagram, green: lowest variation of TS_{diff} f for each Azimuth row, red arrow: overall minimum, last row: Azimuth-stacked TS_{diff}, red circle: Azimuth-stacked minimum TS_{diff}.*

6.2.1.3 Summary

The examples discussed here demonstrate that in most cases the receiver configuration strongly affects the energy distribution calculated in the array analysis. The variations of the overall energy distribution and the differences in the stacked energy between various receiver arrays can be explained only to some so far unquantifiable degree with aliasing effects induced by the array geometry. With different receiver layouts one might analyze wave fields, which did not necessarily "see" exactly the same medium on their way from the source to the receivers; Phase velocity differences may also be affected by the diversity of near-surface structures in the survey area.

From the investigations presented in this chapter one can conclude that stacking amplitudes over azimuths for the creation of dispersion curve images may yield incorrect results when potential "footprints" of the array geometry are ignored.

6.2.2 Energy segregation

As shown in the previous section (*6.3.1 Passive MASW and Array Dependence)*, the method of stacking energy for a certain frequency and phase velocity span for a number of geophones over all the azimuths, leads to dispersion curves with insufficient resolution especially in the lower frequencies. The main disturbances seem to have the origin in the interference of the source energy, coming from different directions, and sub-optimal arrays. The combination of the two attributes, incoming energy direction and array configuration can lead to erroneous results.

In the following examples, the arrays discussed above are investigated again. The azimuth of the maximum incoming energy (for distinctive frequencies) is determined, and amplitudes are stacked over the investigated azimuth with increments of 2 degrees. With this method any source energy, that is artificially generated or amplified to a broader azimuth spectrum because of the Time-Shift difference similarity, should be excluded.

Example 1

From Record 2217, which belongs to array 2000, the time section between 3 and 5 seconds is extracted and analyzed. The dispersion curves of the different arrays, which have already been investigated in the former section, are shown here again. This time their dispersion curves are refined by using a smaller increment of azimuth.

In the top of Figure 6.26 the Azimuth versus Frequency diagram shows that the main incoming energy for the lower frequencies comes from about 352° and for the higher frequencies the source of the signals is located around 288°.

The dispersion curve images of Figure 6.26 indicate that by narrowing the stacking range around the incoming energy, the dispersion curves are becoming better defined in the lower frequencies. In comparison to the former section where the Phase velocities have been stacked over all azimuths, the Phase velocities in the dispersion curves stacked over the Azimuth with ± 2°from the maximum incoming energy (352°), can be distinguished down to a frequency of 4Hz. This improvement from 6.5 Hz to 4 Hz increases the investigation depth from about 26 meters to about 57 meters (Xia et al. 1999).

The different dispersion curve images shown in Figure 6.26 are only defined in the frequency range between 4 and about 7.5 Hz. This can be explained by considering the Azimuth – Frequency diagram of Record 2217 (3-5s) (top diagram): The geophones seem to receive signals out of the chosen direction of 352°, only for the frequencies of 3 Hz and 4 Hz to about 7.5Hz. Any energy arriving from different directions for the remaining frequencies is ignored, when narrowing the Azimuth window.

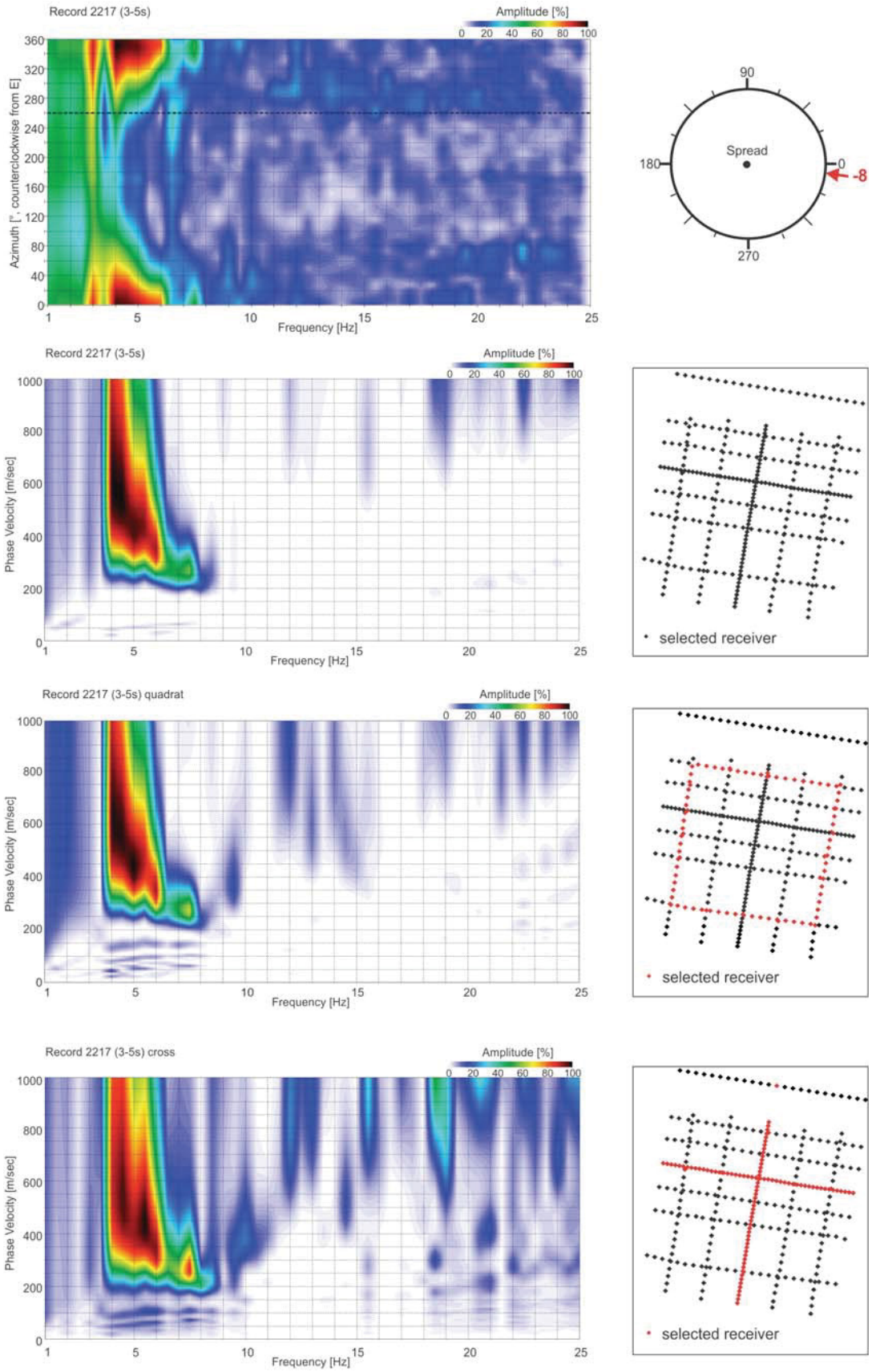
Record 2217 (3-5s)
Amplitude [%]
0 20 40 60 80 100
Azimuth [°, counterclockwise from E]
Frequency [Hz]
90
180
0
270
Spread
-8
Record 2217 (3-5s)
Phase Velocity [m/sec]
selected receiver
Record 2217 (3-5s) quadrat
selected receiver
Record 2217 (3-5s) cross
selected receiver

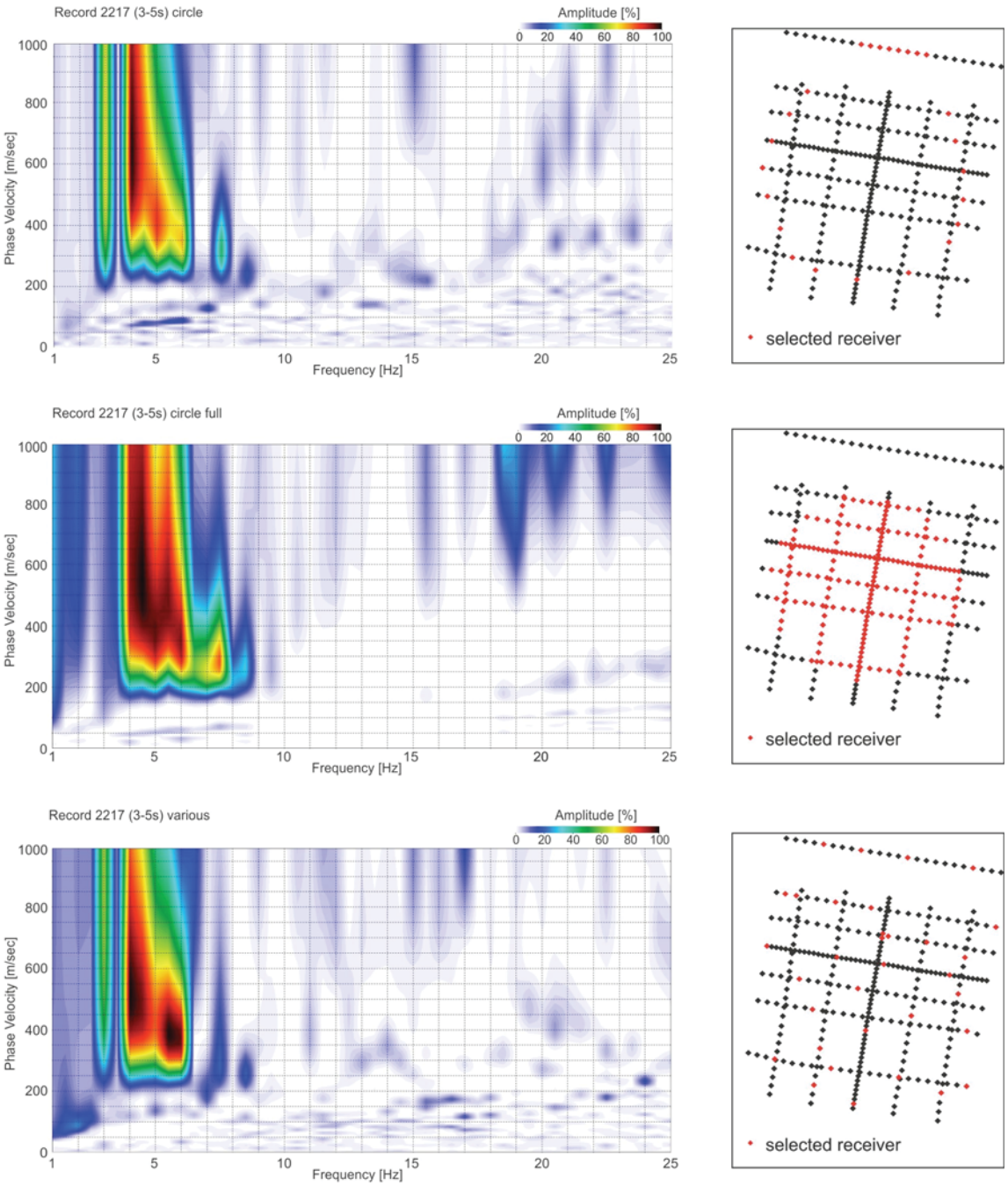

Figure 6.26 *Record 2217 (3-5s), from top to bottom: Azimuth vs Frequency diagrams with energy segregation; dispersion curve image of the original array; dispersion curve image of a square array; dispersion curve image of a cross array; dispersion curve image of a circle array; dispersion curve image of a filled circle array; dispersion curve image of a "random" various array.*

The quality of a dispersion curve image can be assessed by the energy distribution along phase velocity over a given frequency. If the energy is distributed over a wider range of phase

velocities, defining a point for a curve is less exact and the error bar for the resulting velocities increases.

The dispersion curve images in Figure 6.26 for record 2217 (3-5s) after azimuthal energy filtering show quite concentrated energy patterns down to a frequency of about 4.5 to 5 Hz. Towards still lower frequencies energy gets stretched over a wide range of phase velocities, indicating that these wavelengths are beyond the limits of resolution, e.g. because of limited array dimensions.

Every array shown in Figure 6.26 shows small differences in its energy pattern. The "various" seems to show in the lowest resolvable 4 Hz signal the best tuned energy concentration. Whereas in the continuity of the result, the original, the squared and the cross receiver pattern seem to be ahead.

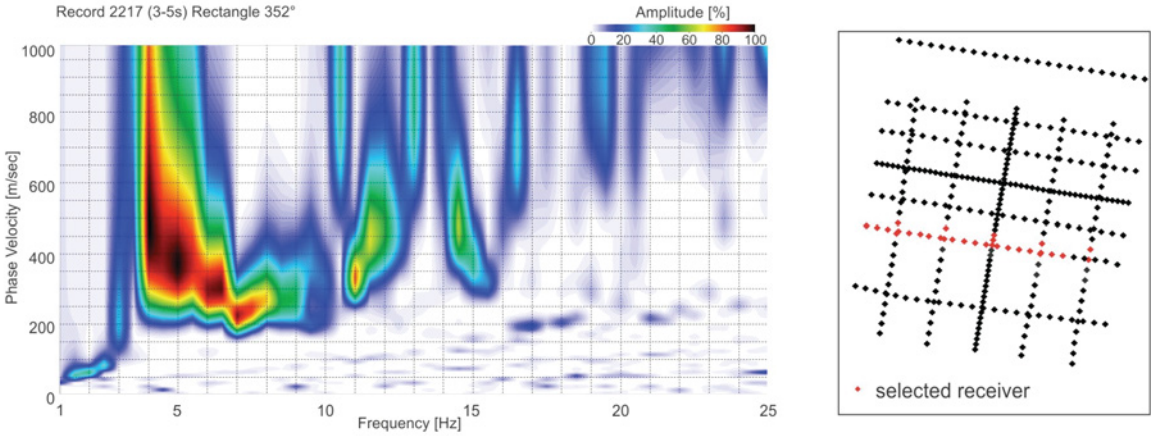

Figure 6.27. *Record 2217 (3-5s) dispersion curve of a orientated rectangular array with orientation angle 352°.*

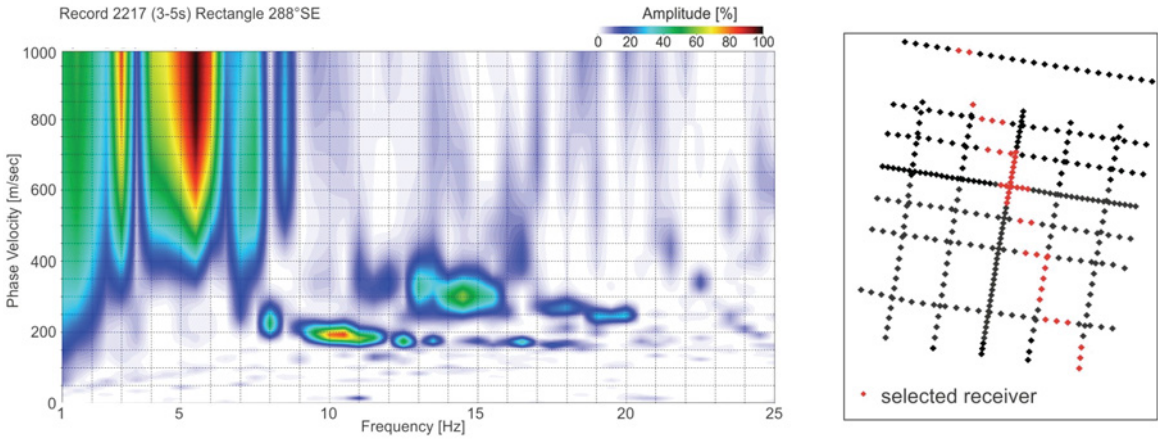

Figure 6.28. Record 2217 (3-5s), dispersion curve of a orientated rectangular array with orientation angle 288°.

Of course detecting the arrays with different source conditions (different angle of maximum energy influx) could change the quality ranking of arrays.

The dispersion curve image of Figure 6.27 shows the result of a narrow rectangular array which is orientated towards the energy of maximum influx for the lower frequencies. In this case the rectangle is orientated towards 352°.

Even with the small number of receivers (28 processed geophones) the result compares well with the results shown in Figure 6.26. The dispersion curve image of the orientated rectangle seems to unify continuity and energy concentration which improves the identification process of the dispersion curve analysis.

The rectangular array offers also the advantage to construct several sub-arrays out of one array and one record, and so different midpoints, from which the information can be used to make a detailed 3D underground analysis (this point is elaborated in Chapter 7).

As mentioned above at higher frequencies the source energy arrives from a different azimuth. By using the method of array tuning (orientated rectangle) and energy segregation, also the higher frequency signals can be brought to the best. Figure 6.28 shows the result of energy segregation (286°-290°) and array orientation versus maximum incoming energy of the higher frequencies (288°). The dispersion curve image shows a clear curve energy pattern for the frequencies between 8 and 19 Hz and additionally a higher mode curve at higher phase velocities. Combining information from several optimally orientated rectangles can give shear wave velocities for a 3D underground structure.

Explanation 6.2:

Selection process of an optimal Record

For the orientated rectangluar method, records gets selected after the amount of frequencies of interest coming from one source direction. The reason for this selection process is the fact, that by using an orientated array and a segregated energy span,- depending on the array orientation-, the results are only valid for the frequency span that gets exactly energy out of that certain direction.

Outside the initially defined frequency range artefacts may be genarted, which create, when not excluded, erroneous/ incorrect results. The orientated rectanglular dispersion curve image of the lower Frequencies (Figure 6.27) shows an example for such artefacts, which can lead to wrong results:

The energy concentration over 11 Hz is to high and gives no real and no usable value. In the Azimuth –Frequency diagram is shown that in the area around 352° no main energy concentration for 11 Hz exists.

An important preprocessing step is therefore, scanning the records for time sections which have their energy coming mainly from one direction for an as large as possible frequency range.

Records get only processeced when the criteria listed below (criteria 1 to 3) are fulfilled:

$$1.\ criteria,\ for\ Frequency: \quad \frac{\sum_{i=1°}^{360°}\left(100-\frac{Energy_{(AZI_i,F)}*100}{Energy_{(AZI\,1°-360°,F)\max}}\right)}{AZI_{step}} > 70$$

$$2.\ criteria,\ for\ Azimuth: \quad \frac{Energy_{(AZI_i,F)}*100}{Energy_{(AZI\,1°-360°,F)\max}} > 99\%$$

3. *criteria, for the selection of a Record:*

For at least three different frequencies of one Record the1st criteria has to be valid and for each of these frequencies the 2nd criteria has to be vaild for an identical Azimuth.

Example 2

The second example is from Record 2200 (30.6 - 32s) which has been recorded with Array 2000. In the Azimuth-Frequency diagram at the top of Figure 6.29 it is evident that the main energy is coming from about North-West (150°). This strong energy concentration is only valid for the lower frequencies, mainly from 4 Hz to 5.5 Hz.

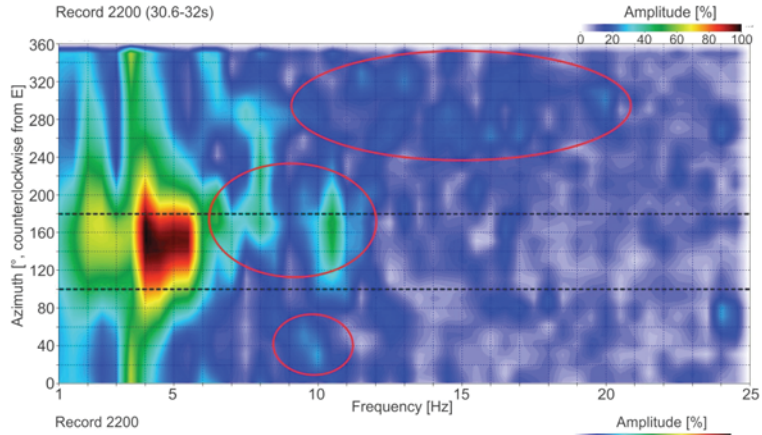
Record 2200 (30.6-32s)
Amplitude [%]
0 20 40 60 80 100
Azimuth [°, counterclockwise from E]
Frequency [Hz]

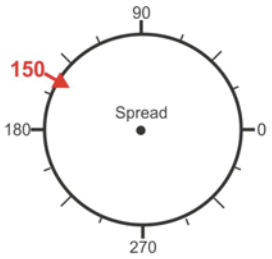
90
150
180
0
270
Spread

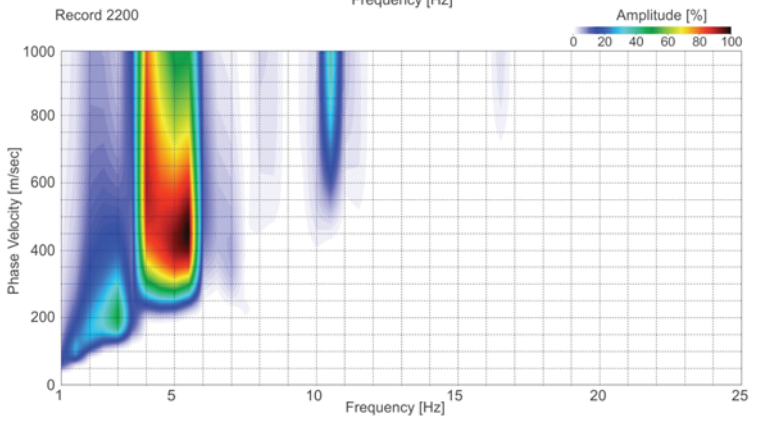
Record 2200
Amplitude [%]
0 20 40 60 80 100
Phase Velocity [m/sec]
Frequency [Hz]

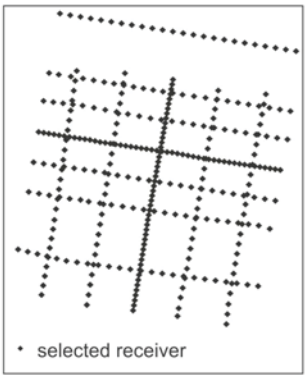
selected receiver

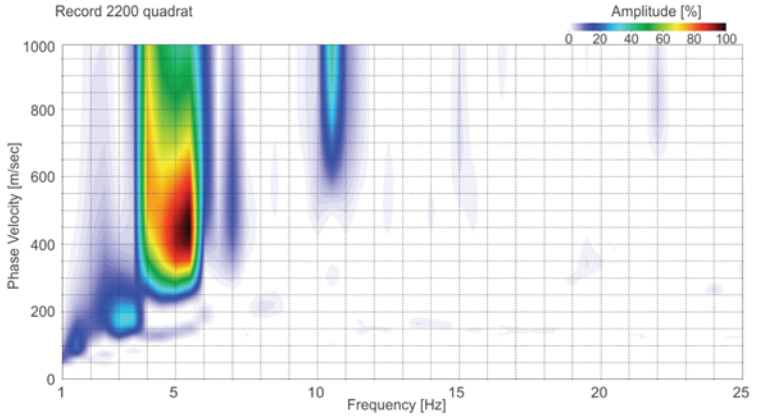
Record 2200 quadrat
Amplitude [%]
0 20 40 60 80 100
Phase Velocity [m/sec]
Frequency [Hz]

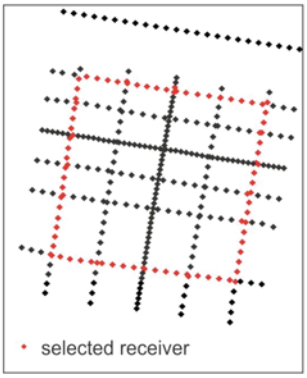
selected receiver

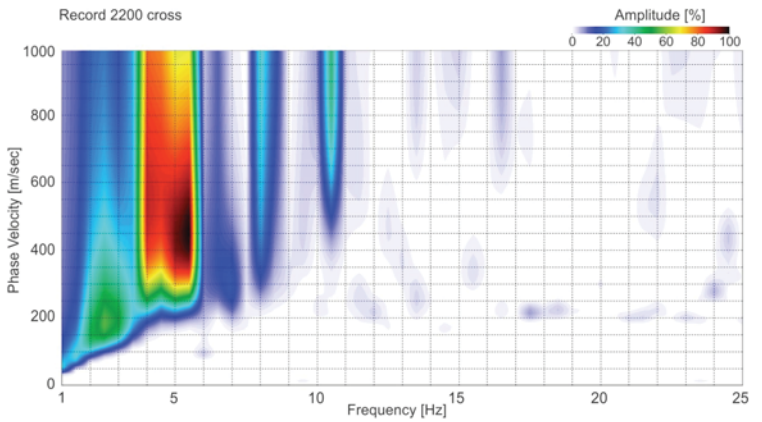
Record 2200 cross
Amplitude [%]
0 20 40 60 80 100
Phase Velocity [m/sec]
Frequency [Hz]


selected receiver

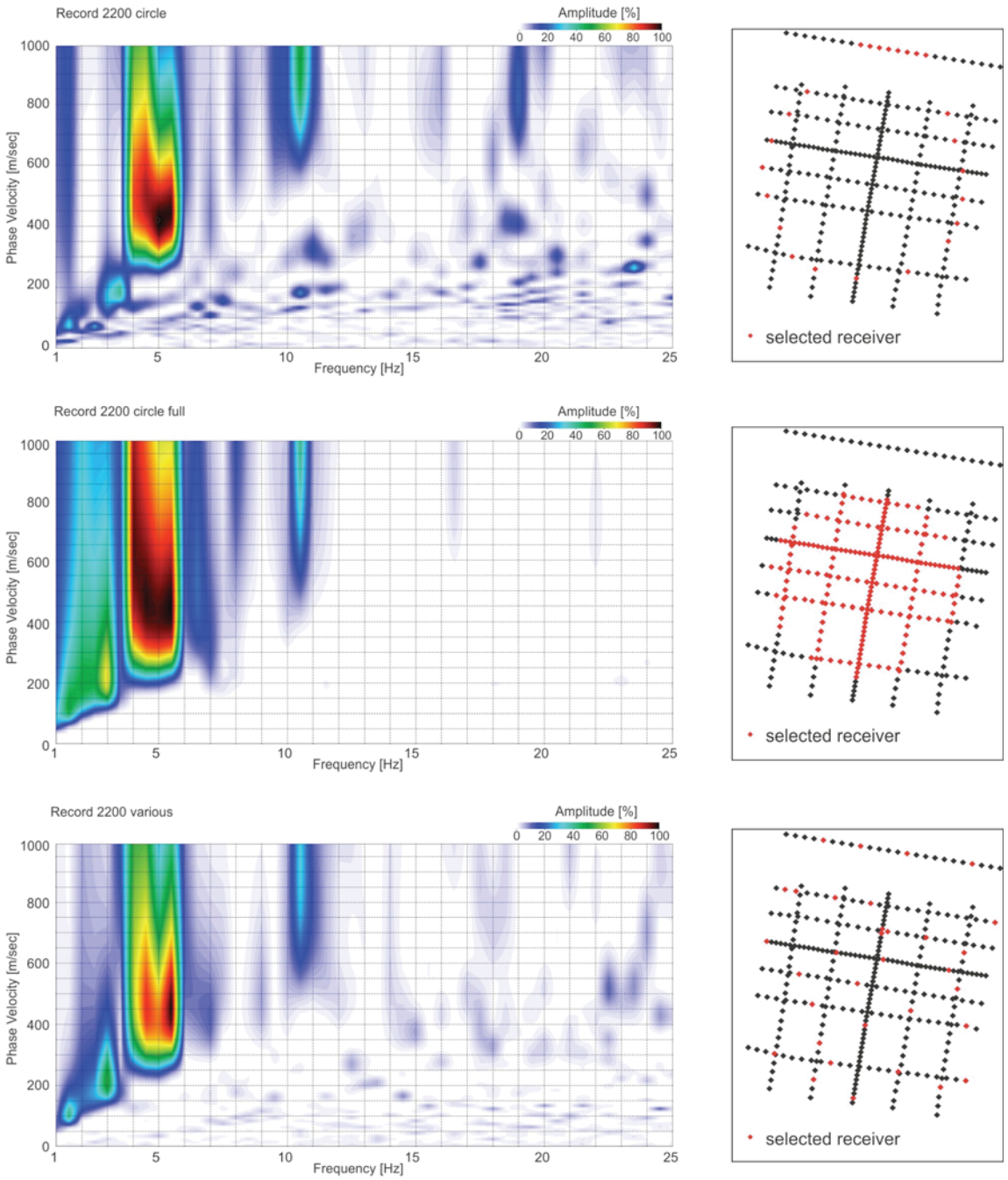

Figure 6.29 *Record 2200 (30.6 - 32s), from top to bottom: Azimuth versus Frequency diagram; dispersion curve of the original array; dispersion curve of a square array; dispersion curve of a cross array; dispersion curve of a circle array; dispersion curve of a filled circle array; dispersion curve of a various array.*

Following the process described above with Example 1, also for this record segment the maximum energy has been segregated and used for further processing. For all the phase velocities and frequencies the energy of the chosen azimuth span (± 2° of 150°) has been

stacked for all the arrays analysed in the former chapter. In comparison to the results from the chapter before, where the phase velocities have been stacked over all azimuths, the resolution in the dispersion curves where energy is stacked over the azimuth from 148° to 152° has been improved from 6.5 to 4.5 Hz. This improvement increases the investigation depth in this case from about 25 meters to about 52 meters (Xia et al., 1999).

Important for this particular record is to keep the Azimuth vs. Frequency image in mind, which shows a main incoming energy at 150° exclusively for the frequencies between 4 Hz and 5.5 Hz, eventually also 7 Hz and 10.5 Hz. So, with the used properties only the mentioned frequency ranges should be picked. Investigating Figure 6.29 shows that the processing procedure has mainly eliminated information from the higher Frequencies shown in the dispersion curve image of the former chapter, but instead has refined the energy concentration in the Frequencies around 4Hz and 5.5Hz, so that together with the initial curve a much better dispersion curve development is recognizable.

On the other hand with the criteria listed in the Explanation box 6.2 record 2200 (30.6 - 32) is on the limit of acceptable properties. In this record where energy is strongly distributed the conventional arrays seem not to fulfill their duties as well as in record 2217(3 - 5s) (Figure 6.26). Energies seem to be more distributed and also partially too high. The orientated rectangle on the other hand seems to cope with the challenge and provides obvious results (Figure 6.30) for the frequencies determined from the Azimuth-Frequency diagram. The orientated rectangle array shows also some energy concentrations around 6.5 Hz and 7.5 Hz which are amplified by the orientation of the array and the energy segregation, but should not be picked.This topic will be discussed in the following section.

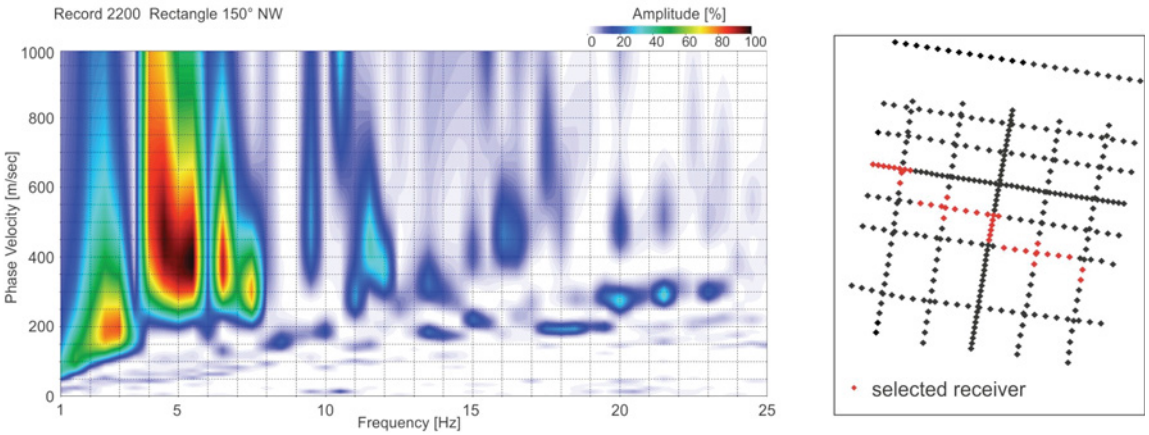

Figure 6.30. *2200 (30.6 - 32s), dispersion curve of a orientated rectangular array with orientation angle 150°.*

Example 3

In the third example, where record 5032 (time section: 4.5-6.5 s), from array 5000 is investigated, the processes already tested in the examples discussed above, are conducted. In the Azimuth –Frequency diagram the record shows in comparison to the former examples an excellent energy distribution. Main energy income for the frequencies that are registrated lie around an angle of 84° (Figure 6.31, top). Plus minus two degrees from the azimuth of maximum incoming energy results accordingly to a stacking span between 82° and 86°.

Even if the Azimuth-Frequency diagram shows a strong energy concentration at 4 Hz (Figure 6.31,top), the dispersion curve images of the tested arrays do not resolve the 4 Hz signal (Figure 6.31, dispersion curve images). The spread, which has a north south extension of 55m, seems not large enough to resolve frequencies lower than 5 to 5.5 Hz with the existing underground and record conditions. The effect of array length will be discussed in one of the following sections (see chapter 6.3.5). As surface waves got mainly emitted from the North because of the surrounding condtions (see chapter 6.1), no good examples can be displayed which would show the resolution improvement when waves travel over the whole width of the array.

The original array, the “filled circle” sub-array and the “orientated rectangular” sub-array deliver the best results (Figure 6.31). But taking into account the amount of geophones used for each array, - original array 275 geophones, “filled circle” sub-array 128 geophones and “orientated rectangle” sub-array 30 geophones-, the result of the latter seems even more impressive. From the array configuration of the orientated rectangular array, the advantage of the small array is recognizable. One can construct several sub-arrays from the original array to receive an image of the subsurface

With the increase of resolution in the dispersion curves from a frequency of 7 Hz to 5.5 Hz, the investigation depth gets expanded for about 20 meters, from 12.5m to 32m (Xia et al., 1999).

Figure 6.31. (following pages) *Record 5032 (4.5 - 6.5 s), from top to bottom: Azimuth versus Frequency diagram; dispersion curve of the original array; dispersion curve of a square array; dispersion curve of a cross array; dispersion curve of a circle array; dispersion curve of a filled circle array; dispersion curve of a various array; dispersion curve of a orientated rectangular array with orientation angle 84°.*

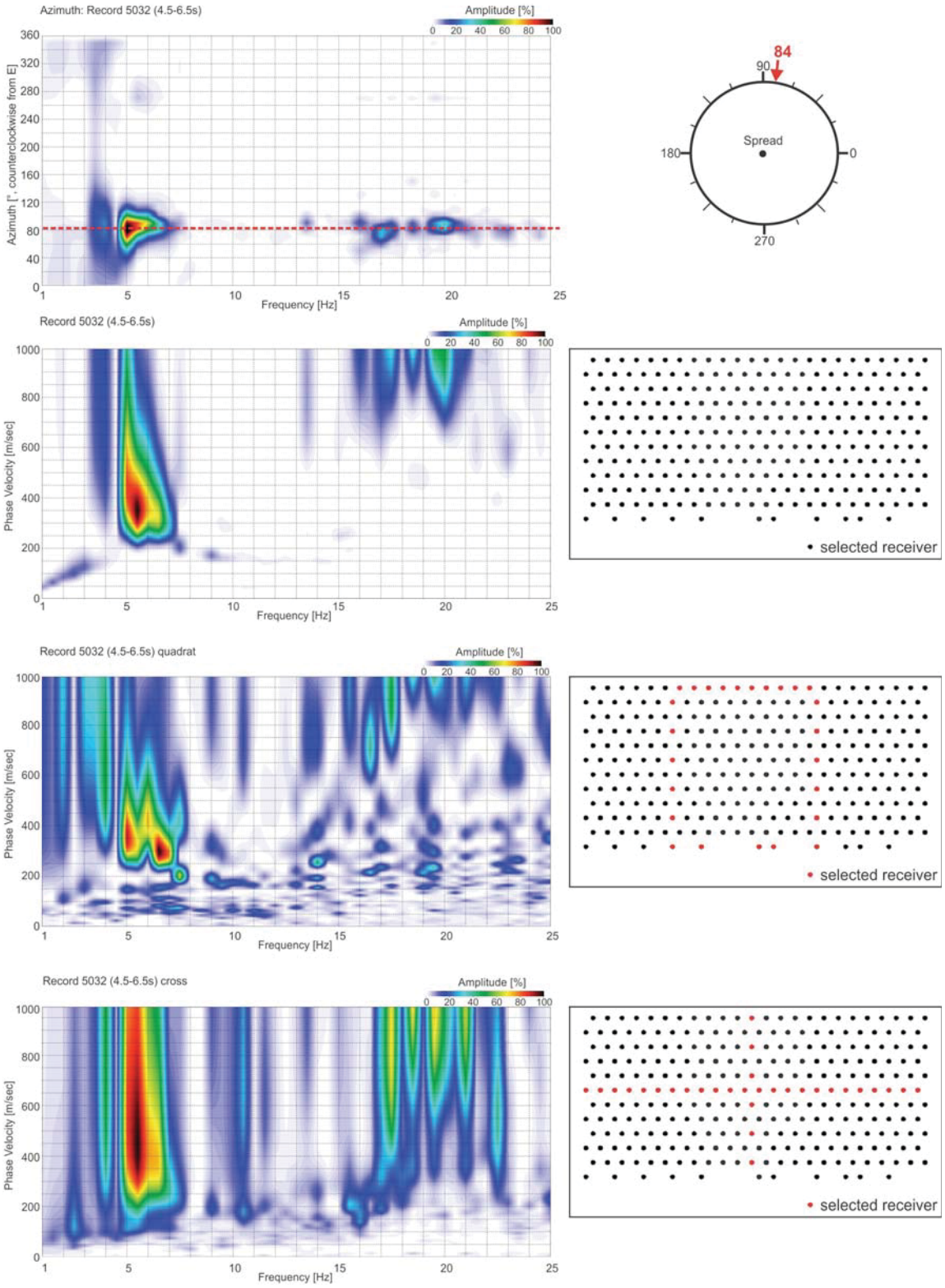
Azimuth: Record 5032 (4.5-6.5s)
Amplitude [%]
0 20 40 60 80 100
Azimuth [°, counterclockwise from E]
Frequency [Hz]
84
90
180
0
270
Spread
Record 5032 (4.5-6.5s)
Phase Velocity [m/sec]
selected receiver
Record 5032 (4.5-6.5s) quadrat
Record 5032 (4.5-6.5s) cross

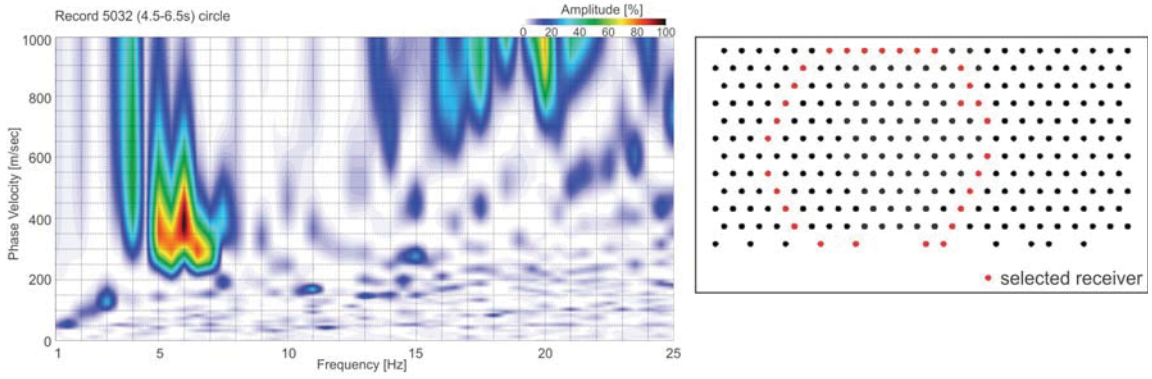
Record 5032 (4.5-6.5s) circle
Amplitude [%]
0 20 40 60 80 100
Phase Velocity [m/sec]
0 200 400 600 800 1000
1 5 10 15 20 25
Frequency [Hz]
selected receiver

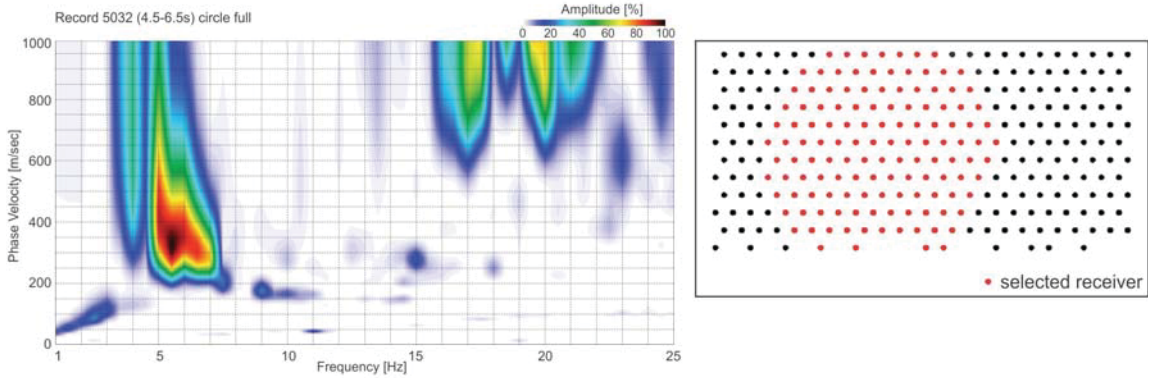
Record 5032 (4.5-6.5s) circle full
Amplitude [%]
0 20 40 60 80 100
Phase Velocity [m/sec]
0 200 400 600 800 1000
1 5 10 15 20 25
Frequency [Hz]
selected receiver

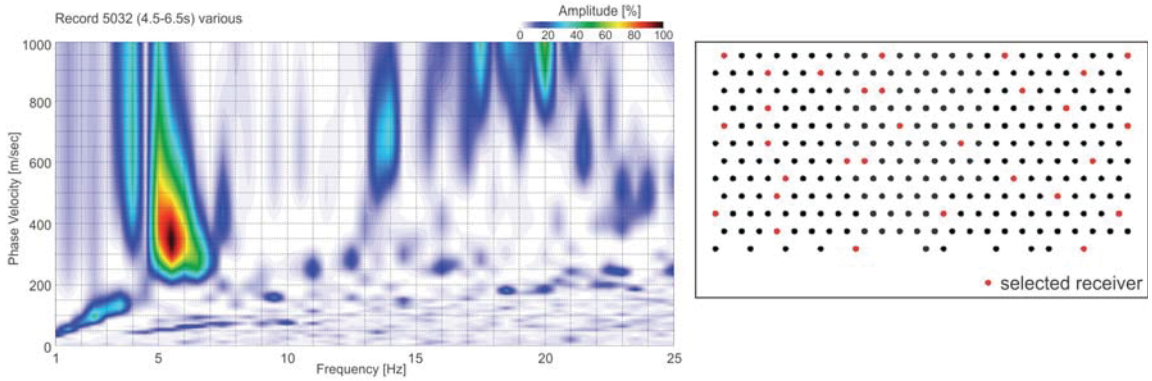
Record 5032 (4.5-6.5s) various
Amplitude [%]
0 20 40 60 80 100
Phase Velocity [m/sec]
0 200 400 600 800 1000
1 5 10 15 20 25
Frequency [Hz]
selected receiver

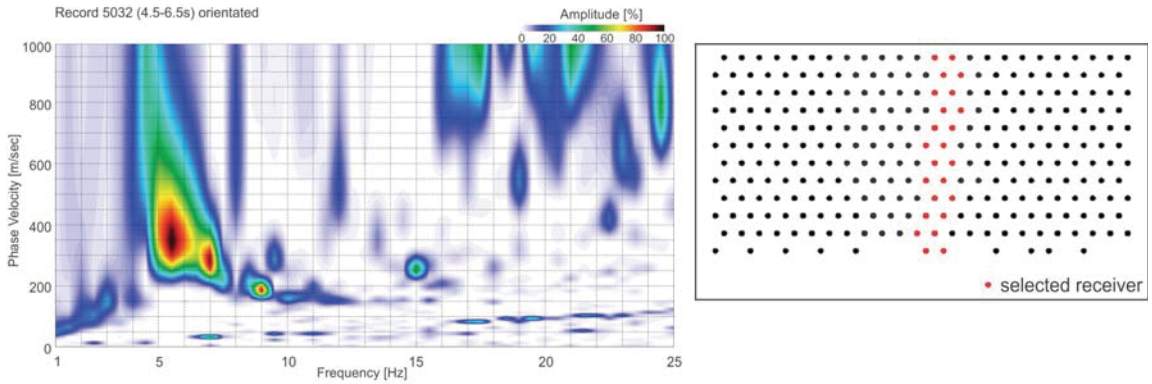
Record 5032 (4.5-6.5s) orientated
Amplitude [%]
0 20 40 60 80 100
Phase Velocity [m/sec]
0 200 400 600 800 1000
1 5 10 15 20 25
Frequency [Hz]
selected receiver

Example 4

As final example is shown record 5032 (time section: 13-15s), which is the same record as the one from example 3, but represents a later time section.

Similar to example 3 the main energy income is for all registered frequencies about the same and lies two degrees from the former record fragment at around an azimuth of 82° (Figure, 6.32, top). The energy influx below 5 Hz appears to be higher in comparison to example 3. Stacking is carried out over the azimuths from 80 to 84°.

The quality of the data seems similar as in the former example. Also as in the earlier choosen time window of record 5032, the original array, the "filled circle" sub-array and the "orientated rectangular" sub-array show the best resolution. The original and the filled circle array have a resolution until 5 Hz.

The orientated rectangular sub-array is placed in comparision to the former example in the right part of the original array and shows a rather continuous dispersion curve image with a higher mode energy concentration. The orientated array shows also over the 4 Hz signal an energy concentration, which is stretched, but closed in direction to the higher phase velocities and allows so at least an estimation of phase velocity for the 4 Hz signal.

The increase in resolution in comparison to example 3 could be a question of the gain of length of the sub-array, because of the slight orientation difference of about two degrees. It could also be the consequence of a higher source energy or caused by the differences in the underground, because of the location chosen differently as the one from the sub-array of the former example (Figure 6.31, bottom, left vs. Figure 6.32, bottom, left).

Record 5032 (13-15s) shows a stretched energy distribution in the lower frequencies, 4.5 Hz and 5.5Hz (Figure 6.32, top), this could lead to a distortion of the results. The influences of multiple sources in a record is discussed in the following chapter.

Figure 6.32.(following pages) *Record 5032 (13 - 15 s), from top to bottom: Azimuth versus Frequency diagram; dispersion curve of the original array; dispersion curve of a square array; dispersion curve of a cross array; dispersion curve of a circle array; dispersion curve of a filled circle array; dispersion curve of a various array; dispersion curve of a orientated rectangular array with orientation angle 82°.*

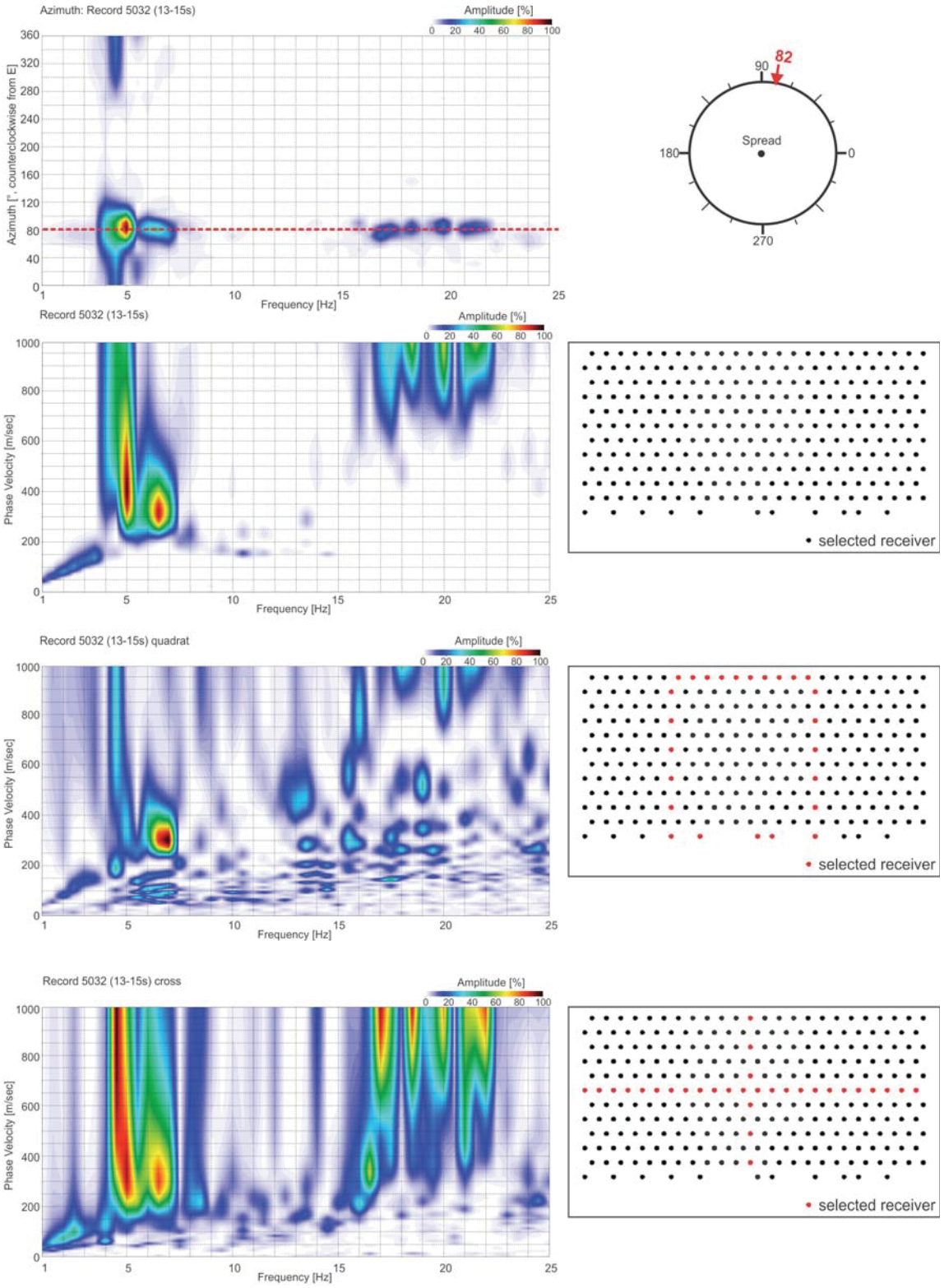
Azimuth: Record 5032 (13-15s)
Amplitude [%]
0 20 40 60 80 100
Azimuth [°, counterclockwise from E]
Frequency [Hz]
82
90
180
0
270
Spread
Record 5032 (13-15s)
Phase Velocity [m/sec]
selected receiver
Record 5032 (13-15s) quadrat
selected receiver
Record 5032 (13-15s) cross
selected receiver

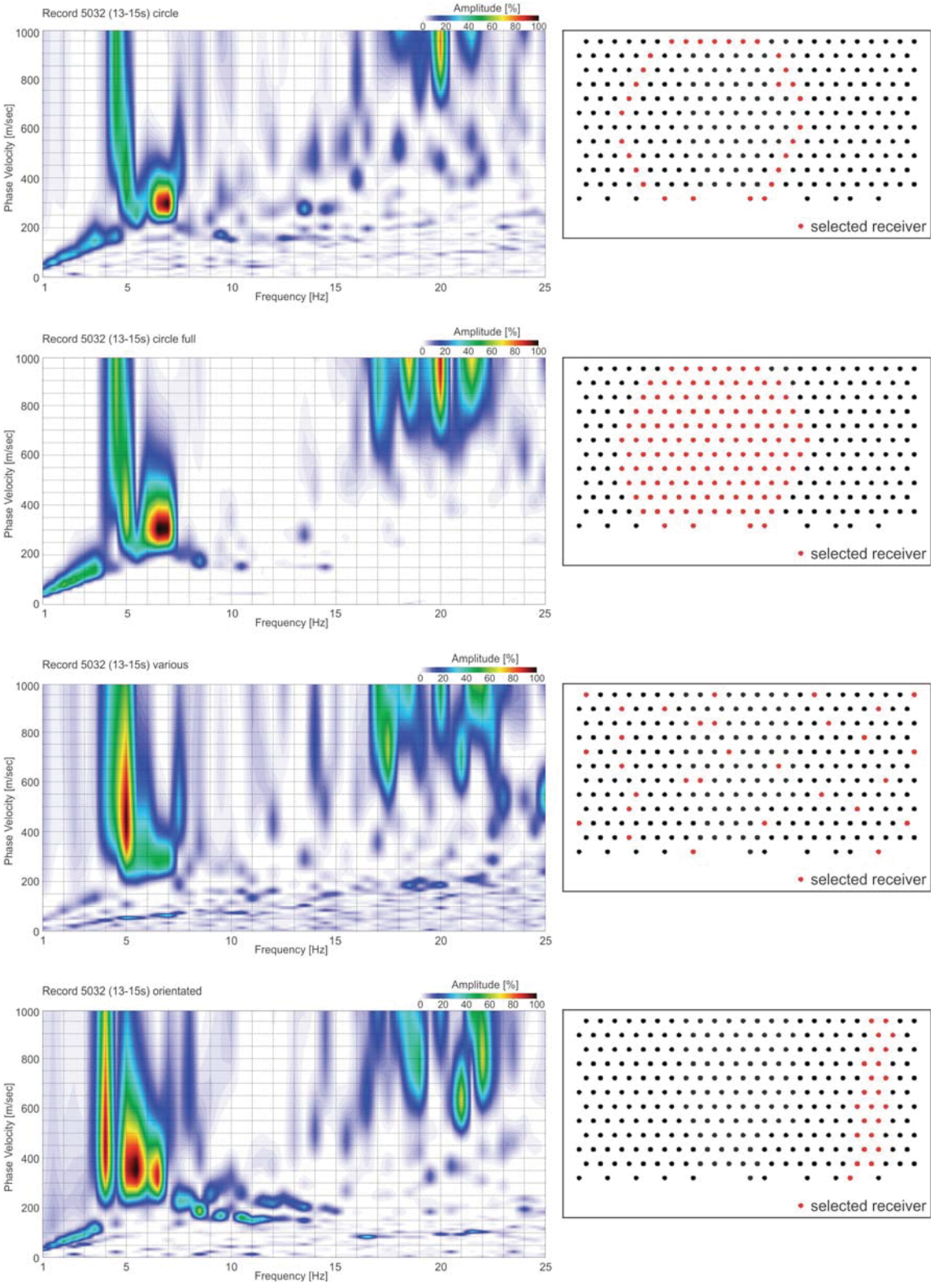
Record 5032 (13-15s) circle
Amplitude [%]
0 20 40 60 80 100
Phase Velocity [m/sec]
Frequency [Hz]
selected receiver
Record 5032 (13-15s) circle full
Amplitude [%]
0 20 40 60 80 100
Phase Velocity [m/sec]
Frequency [Hz]
selected receiver
Record 5032 (13-15s) various
Amplitude [%]
0 20 40 60 80 100
Phase Velocity [m/sec]
Frequency [Hz]
selected receiver
Record 5032 (13-15s) orientated
Amplitude [%]
0 20 40 60 80 100
Phase Velocity [m/sec]
Frequency [Hz]
selected receiver

6.2.2.1 Summary

The processing steps investigated and defined in this chapter bear several benefits:

As preliminary work with major significance an adequate time window of a record has to be defined with maximum energy coming from mainly one direction and as much as possible frequencies which fulfill the criteria listed in *Explanations 6.2*.

The step of energy segregation significantly improves resolution and accuracy of the dispersion curve images of all arrays. The choice of a small rectangular array and the procedure of array orientation makes it possible to react flexibly on the surrounding conditions and variations in the location of the energy source. The combination of choice of array configuration, array orientation towards the maximum incoming energy and energy segregation creates a dispersion curve image which is at least comparable but mostly (as shown in all examples above) exceeds the results of other arrays. In relation of the low amount of geophones against the depth and frequencies, that can be resolved, the application of the procedure implies a clear improvement.

In addition to the, for the conditions, excellent resolution, the small rectangular sub-array allows several other surrounding sub-arrays. This implies a various amount of midpoints for which shear wave velocities in several depth steps are defined. So, instead of one singular shear wave velocity profile, in the best case an underground model can be designed. Additionally because of the small number of geophones processing time for one depth profile gets diminished.

The following sections are addressed to improve parameters and investigate and detect uncertainties regarding the method of array orientation and energy segregation.

6.2.3 Importance of accurate angle calculation and the recognition of multiple sources

As shown in the former sections energy segregation and array constitution can improve the resolution of the dispersion curve images and with it the investigation depth significantly. To apply the "orientated rectangular" method on a record, the record has to be investigated for its appropriateness. Otherwise results may contain artifacts which lead to wrong dispersion curves and, consequently, to wrong shear wave velocities.

The importance of accurate calculations of the maximum incoming energy is shown in the Figures 6.33 and 6.34 of this chapter. The images are created from Record 2217 (time window: 3-5s), which is also shown in example 1 of the former section. The chosen record has a main incoming energy from about 352° (WSW). Therefore a rectangle was orientated towards 352° and the energy was segregated between 350° and 354°. For the dispersion curve image the data were stacked over that direction span. For comparison the same record was processed for a rectangle with orientation towards 333° and stacked over an orientation span between 331° and 335°.

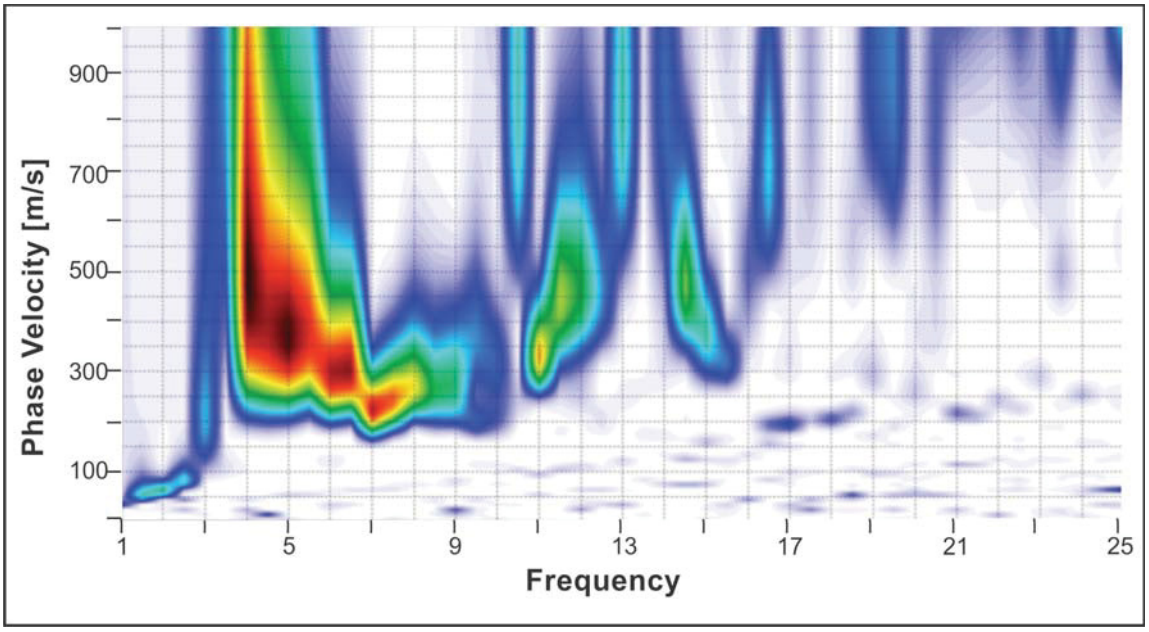

Figure 6.33 *Dispersion curve image of Record 2217 (3-5s) processed from an orientated (352°) rectangular array and stacked over the Azimuth section from 350° to 354°.*

Comparing the two resulting images shows that a change of 20° in orientation and energy selection during processing can influence the gradient of the dispersion curve significantly and lead to connotatively deviating results. The phase velocity at about 4.5 Hz in Figure 6.33 lies at

a value of about 400 m/s, whereas in Figure 6.34 the velocity seems to receive about 550 m/s. The difference between the areas of high amplitudes in the two plots is clearly visible. Picking curves in the image, created out of wrong properties, would cause a total distortion of the resulting depth related shear wave velocities.

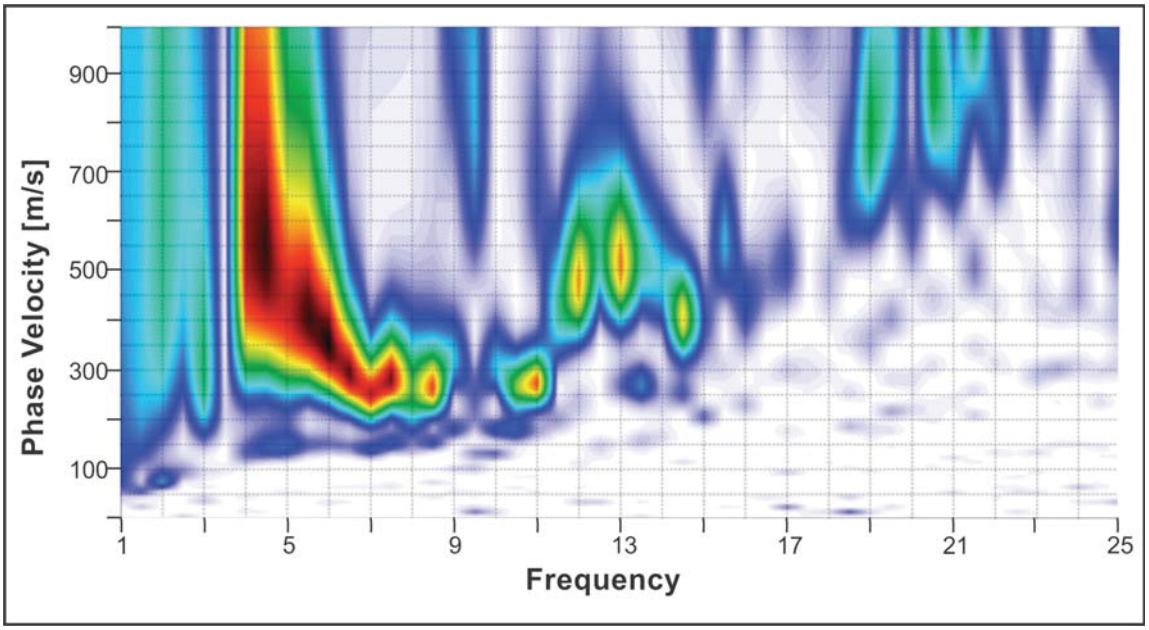

Figure 6.34 *Dispersion curve image of Record 2217 (3-5s) processed from an orientated (331°) rectangular array and stacked over the azimuth section from 331° to 335°. Orientation direction and energy segregation have been selected freely for comparison purpose.*

For the study below (Figures 6.35 to 6.40), data with energy mainly from one direction are compared with data that has also the maximum incoming energy from a similar direction, but additional noise energy coming from other angles. In the following examples showed be investigated how this additional energy affects the results of the orientated rectangle passive MASW method.

Figures 6.36 to 6.39 show dispersion curve images (part a in each Figure) processed with an orientated rectangular array and an energy segregation defined by the maximum incoming energy. The images are calculated out of four different two seconds time windows from array 5000. Besides each dispersion curve image also the distribution of energy for the processed time window is illustrated as an Azimuth Frequency diagram (part b) in each figure). The black dashed lines in the Azimuth Frequency diagrams mark the angle of maximum incoming energy, based on which the sub spreads are orientated and energy was stacked (+-2 °). The red dashed lines indicate the frequencies and their energy distribution, which are investigated in each case.

Two time sections are investigated for the same frequencies, respectively, to have an adequate basis for comparison.

Figure 6.35b gives an overview of the array configuration, position, number of geophones and their distances to each other.

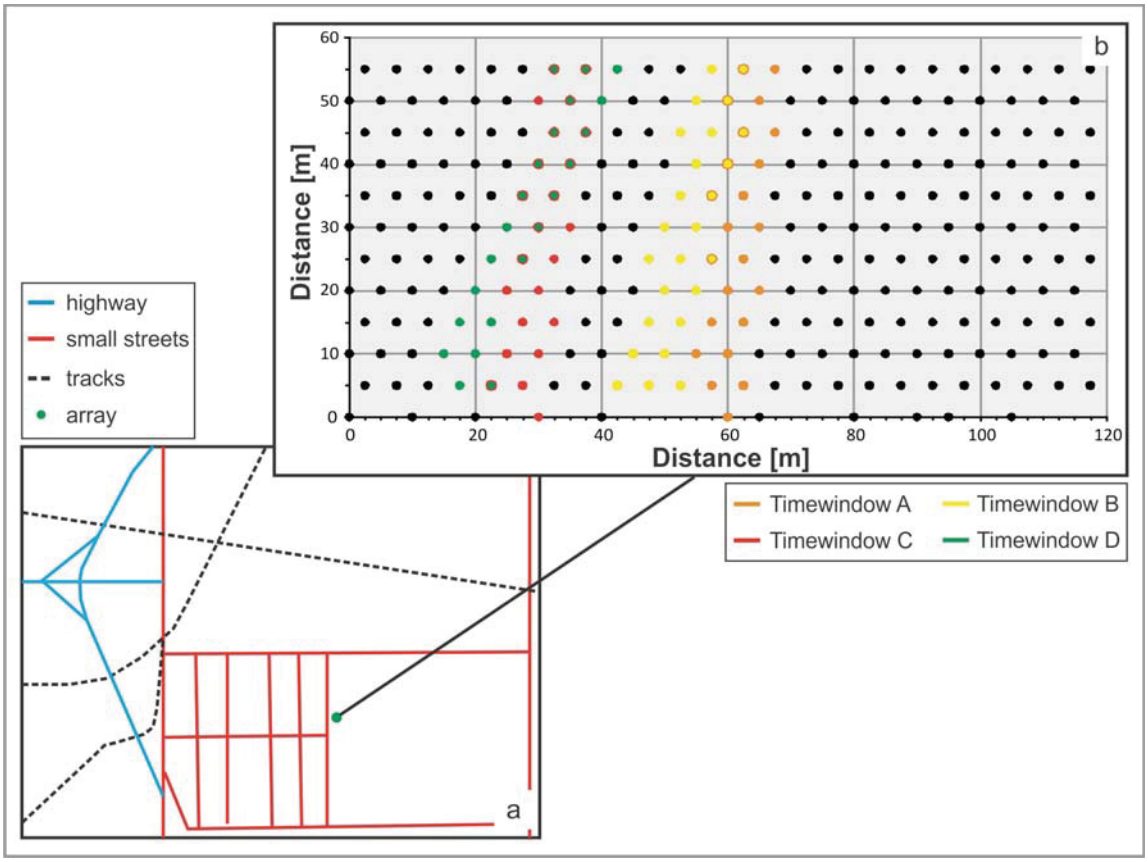

Figure 6.35 *a) Surroundings of the spread, b) receiver layout with sub-array of Figure 6.36 to Figure 6.39.*

As first example the dispersion curve images of two different two seconds time window sections (Figure 6.35b Time window A (Figure 6.36) and Time window B (Figure 6.37)) should be compared. For this purpose the frequencies 6 and 6.5 are investigated in more detail.

To obtain the optimum parameter for array orientation and energy segregation the Azimuth versus Frequency diagrams are analysed in more detail. The example in Figure 6.36b shows a maximum incoming energy for the frequencies of interest at an angle of about 82 ° counter clockwise from east. By contrast in Figure 6.37b the energy distribution is more scattered, even if the maximum incoming energy is concentrated around 68°. Especially for the marked frequencies of 6.5 Hz, the energy is more diffuse than in Figure 6.36.

The dispersion curve images are processed out of the arrays shown in Figure 6.35b, which have an orientation of 82°and 68°, respectively. The energy section that is used for stacking lies in the range of ±2° around the orientation direction.

The dispersion curve image of Figure 6.36a shows high amplitude concentration over the Frequencies of interest (6 and 6.5 Hz), which appear easy and distinctively to pick. The Phase velocity for 6 Hz reaches about 325 m/s and for 6.5 Hz the velocity shows the highest energy at 310 m/s.

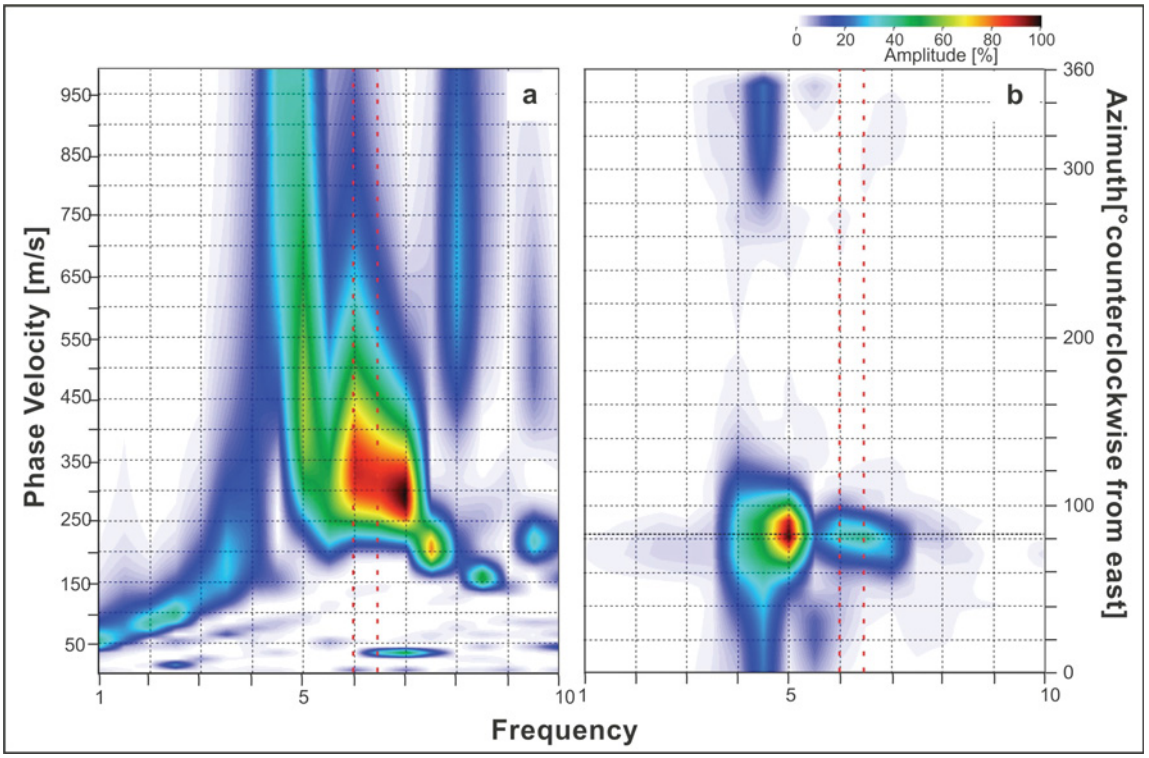

Figure 6.36 *a) Phase velocity vs. Frequency image, b) Azimuth vs Frequency diagram, black dashed line assigns angle of sub spread orientation (82°), red dashed lines mark the investigated Frequency and energy distributions.*

In comparison to Figure 6.36a, the maximum amplitudes of the indicated Frequencies (especially 6.5 Hz) of Figure 6.37a are more stretched and show higher phase velocities. The 6 Hz Frequency reaches a Phase velocity of 340 m/s and the 6.5 Hz Frequency has a stretched amplitude distribution with a centre at about 425 m/s. The increased velocity at 6.5 Hz, which fits for sure in no usable dispersion curve, is a result of the scattered energy distribution for which the method of orientated rectangle is not valid. The deviation of the Phase velocity of the 6 Hz signal from the example of Figure 6,35 can be a result of the different array location and array midpoint, which implies a surface wave propagation over diverse underground. It can perhaps additionally also be a result of the interpolation with the results from the scattered surrounding energy and to minor part also be the energy-scatter in the own frequency.

Because of the energy distribution characteristics of Figure 6.37b the frequency for 6.5 Hz would not fit the criteria listed in the explanation box (6.2) of the former section.

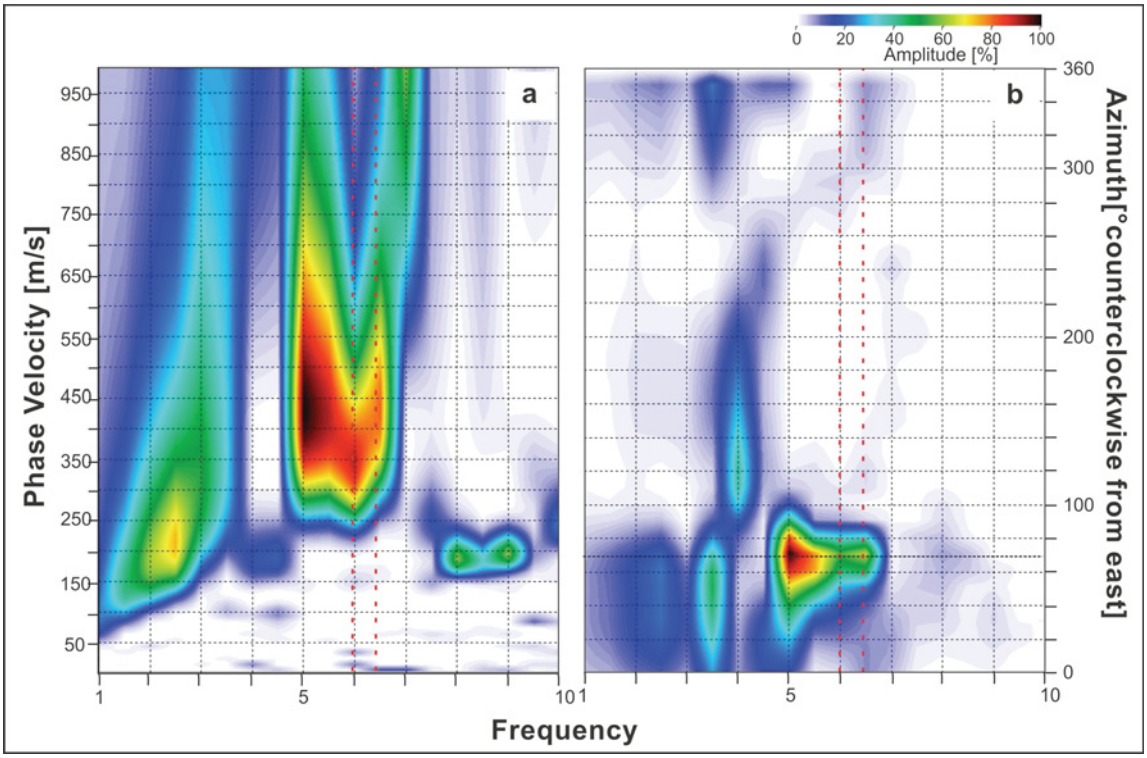

Figure 6.37 *a) Phase- velocity vs. Frequency image, b) Azimuth vs. Frequency diagram, black dashed line assigns angle of sub spread orientation (68°), red dashed lines mark the investigated frequencies and energy distributions.*

As second example the dispersion curve images of two different two seconds time window sections (Figure 6.35b time window C (Figure 6.38) and time window D (Figure 6.39)) should be compared. For this purpose the frequencies of 5.5 Hz and 7.5 Hz are investigated in more detail.

The Azimuth Frequency diagram in Figure 6.38b shows an energy concentration for the Frequencies between 5 Hz and 10 Hz at an angle of about 84° counter clockwise from east (NNE).

For Figure 6.39b the energy distribution is more scattered, even if there is still a overall maximum incoming energy which is in this case coming from 76°. Especially for the Frequencies marked with the red dashed lines, - 5.5 Hz and 7.5 Hz -, a major part of energy or rather the maximum part, is also coming from an Azimuth between 10° to 100° and additionally a small percentage is located in the diagram around an Azimuth of 300° to 350°.

To process the Phase velocity Frequency diagram of Figure 6.38a, a rectangular array orientated towards 84° has been chosen and processed over the isolated energy section between 82° to 86°. The resulting dispersion curve image shows a quite continuous curve down to a frequency of 5.5 Hz. To resolve the lower frequencies, the length of the array seems to be not enough. Quite well concentrated amplitude maxima are evident at the Frequencies of 5.5 Hz and 7.5 Hz. The

surface wave with a frequency of 5.5 Hz seems to travel with a phase velocity of about 360 m/s, the one with 7.5 Hz travels with 220 m/s.

For the dispersion curve image in Figure 6.39a an orientated (76°) rectangular array was processed for the energies between 74° and 78°. The dispersion curve image shows over the Frequencies of 5.5 Hz and 7.5 Hz elongated and towards higher Phase velocity shifted amplitude concentrations. The too high Phase velocity values become evident when comparing the results to the one of Figure 6.38a or when comparing the results with the values that are indicated from the own dispersion curve image over the frequencies of 6.5 Hz, 8 Hz and higher frequencies. The stretched phase velocity centres for 5.5 Hz and 7.5 Hz reach for both frequencies a velocity of about 450 m/s, which seems far too high and can not be implemented in a dispersion curve which is congruent with the side characteristics, adjacent frequencies of the same record and surrounding dispersion curves.

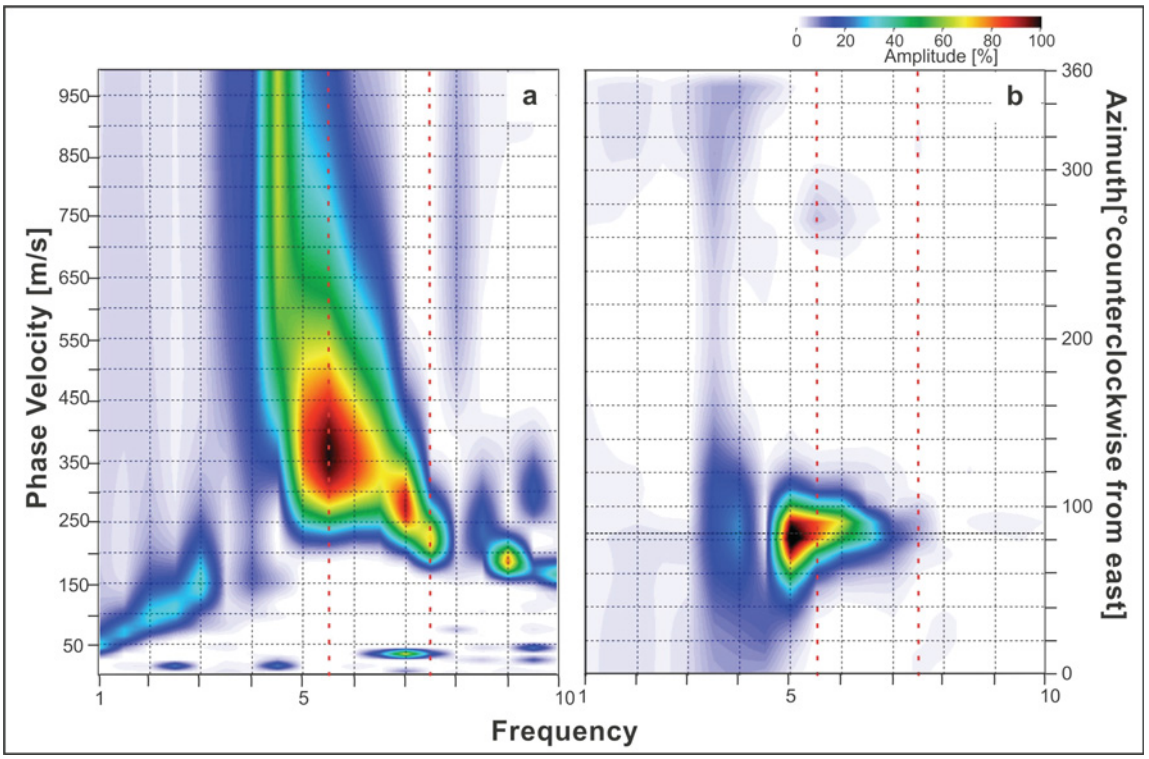

Figure 6.38 *a) Phase- velocity vs. Frequency image, b) Azimuth vs. Frequency diagram, black dashed line assigns angle of sub spread orientation (84°), red dashed lines mark the investigated frequencies and energy distributions.*

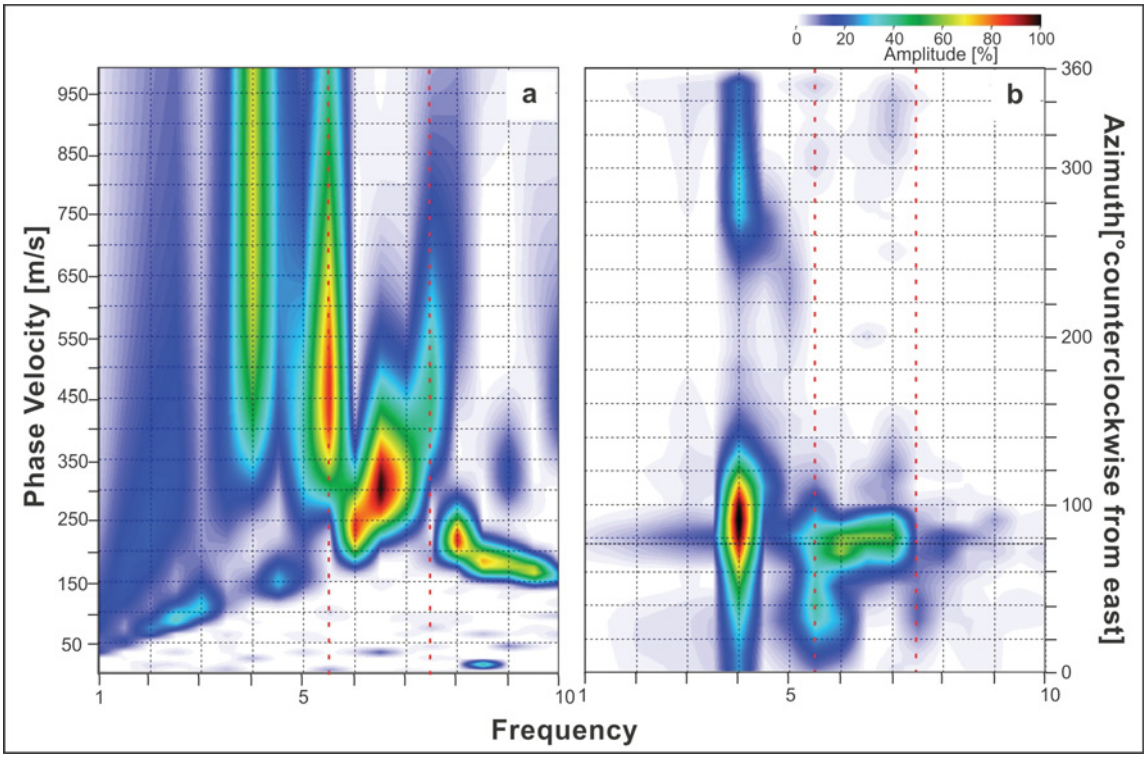

Figure 6.39 *a) Phase- velocity vs. Frequency image, b) Azimuth vs. Frequency diagram, black dashed line assigns angle of sub spread orientation (76°), red dashed lines mark the investigated frequencies and energy distributions.*

In Figure 6.40 time window D (Figure 6.35b, Figure 6.39), has been investigated in more detail. A non-stacked distribution of the phase velocity against the azimuth for 5.5 Hz shows that the signal travelling from about 76°, shows a different phase velocity than the one coming from about 36°. The one from 36°, seems to be more concentrated and has a higher energy than the one from the higher phase velocity. This could imply that there exist two separate modes for the frequency of 5.5 Hz.

Orientating now a rectangular array after the maximum incoming energy for 5.5 Hz and 7.5 Hz, the resulting dispersion curve image in Figure 6.40c seems to have a much more reasonable result for the Frequencies of investigation than in Figure 6.39a. With 350m/s (5.5 Hz) and 250 m/s (7.5 Hz) the Phase velocity concentrations seem to fit by far better with the results from Figure 6.39a for the frequencies of 6.5 Hz and for the frequencies from 8 Hz up.

If the results of the valid frequencies of the two dispersion curves, respectively, are matched and preconditioning that they have the same array midpoint, the resolution of a dispersion curve can be increased by far.

Accuracy in the investigation of the energy distribution, subsequently an adequate reaction on the data which is available and attentiveness during the picking process increases resolution in

both Frequency and Phase velocity and minimizes the deviation from the calculated to the real shear wave velocities.

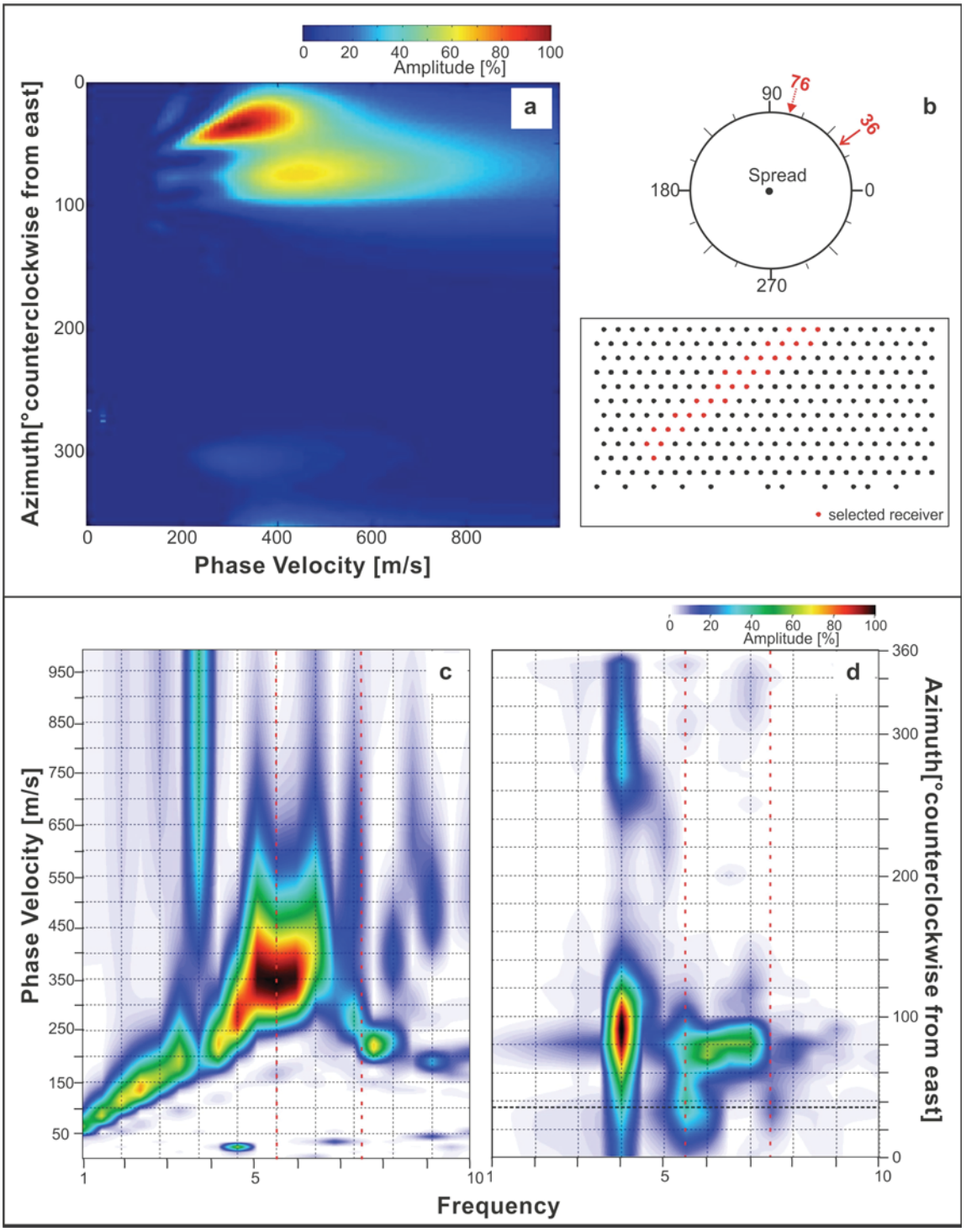

Figure 6.40 *a)Phase velocity vs. Azimuth for 5.5 Hz, b)Selected receiver and orientation of the array, c) Frequency vs. Phase velocity image, d)Azimuth vs. Frequency diagram, black dashed line assigns angle*

of sub spread orientation (36°), red dashed lines mark the investigated Frequencies and energy distributions.

6.2.4 Time window search and time window length

The original records registered in the field for this study have each a length of 32 seconds. The more than sufficient length of the record has the advantage to register the long-lasting signals of trains in a few records and to allow cutting the original record, in for the processing optimal windows, later in the office. In this section it is shown on the basis of an example the importance to find an adequate time window size and an adequate time window location in the original Record.

Figure 6.41 shows a 32 seconds record typical for the data registered for this study. The vertical axis indicates the time in milliseconds; on the horizontal axis the traces are stringed together. The black concentrations, in the form of vertical lines, show the noise, which is emitted from a train departing from the spread 2000 towards an eastern direction. The signals seem to be in a line orthogonal to the time axis because the time window of 32s is too large to see the signal arriving consecutively to each receiver. The colored rectangles show the different time windows used for the analysis below. The yellow window encloses a section where the train signal has a higher amplitude in comparison to the time section enclosed by the orange rectangle.

The results of the 32s window are presented in Figure 6.42a; results of the window from 13 to 15s are shown in Figure 6.42b, and results of the window from 3 to 5s are illustrated in Figure 6.42c.

In succession of this chapter the time windows illustrated in Figure 6.41 are presented and explained in more detail after being processed with the orientated rectangle method.

On the right side of Figure 6.42 for each window an Azimuth versus Frequency diagram is processed which shows the energy distribution for the frequencies between 1 and10 Hz. In this case the departing train from the spread towards East forms the main source of the signals.

On the left side of Figure 6.42 is illustrated for each window a Frequency versus Phase velocity diagram.

Concentrating first on the Azimuth versus Frequency diagrams, one can see that the energy in Figure 6.42b seems more stretched than in Figure 6.42f. As for this study trains are used as a source, it has to be taken into consideration that a train is a moving source, so that the signal direction and distance change fast over the time. Using now a too long time section increases the distribution factor of energy over the azimuths and creates too much noise. The effect on the time window length will be presented on the basis of Figure 6.43 below in this chapter.

The comparison between Figure 6.42d (13s-15s) and 6.42f (3-5s), with each two seconds as time window length, shows that also the ideal relation of distance to the source and with it the strength of signal plays a significant role. A receiver array has to be far distant enough from the

source so that the surface wave can develop into a so called plain wave, for which the ideal conditions are effective. The necessary distance depends from the wave length (see chapter 2.). The furthest distance from the source for which a high quality signal can be received depends on the source strength.

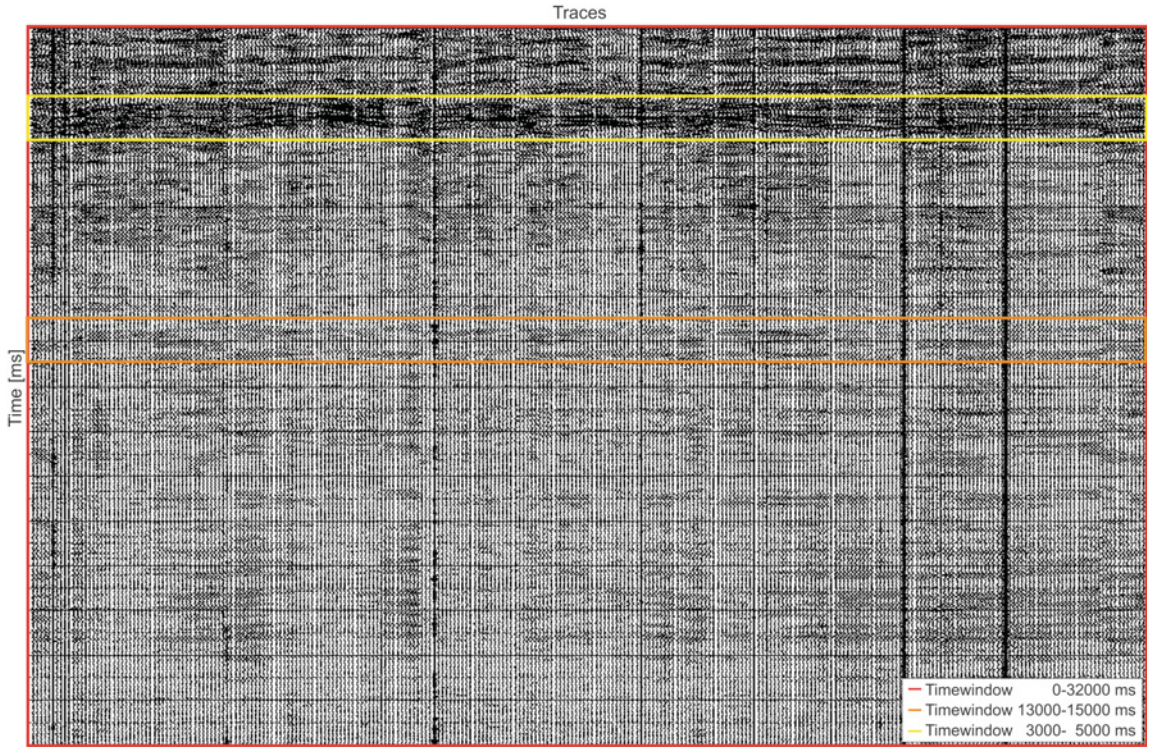

Figure 6.41 *Seismic section of record 2217, plotted with different time windows, which are processed in Figure 6.42*

Figure 6.42 (following page) *Record 2217: a) Phase- velocity versus Frequency diagram and b) Azimuth versus Frequency diagram, both for the whole 32 seconds record, c) Phase- velocity versus Frequency diagram and d) Azimuth versus Frequency diagram, both for time window 13 to 15 seconds, e) Phase-velocity versus Frequency diagram and f) Azimuth versus Frequency diagram, both for time window 3 to 5 seconds.*

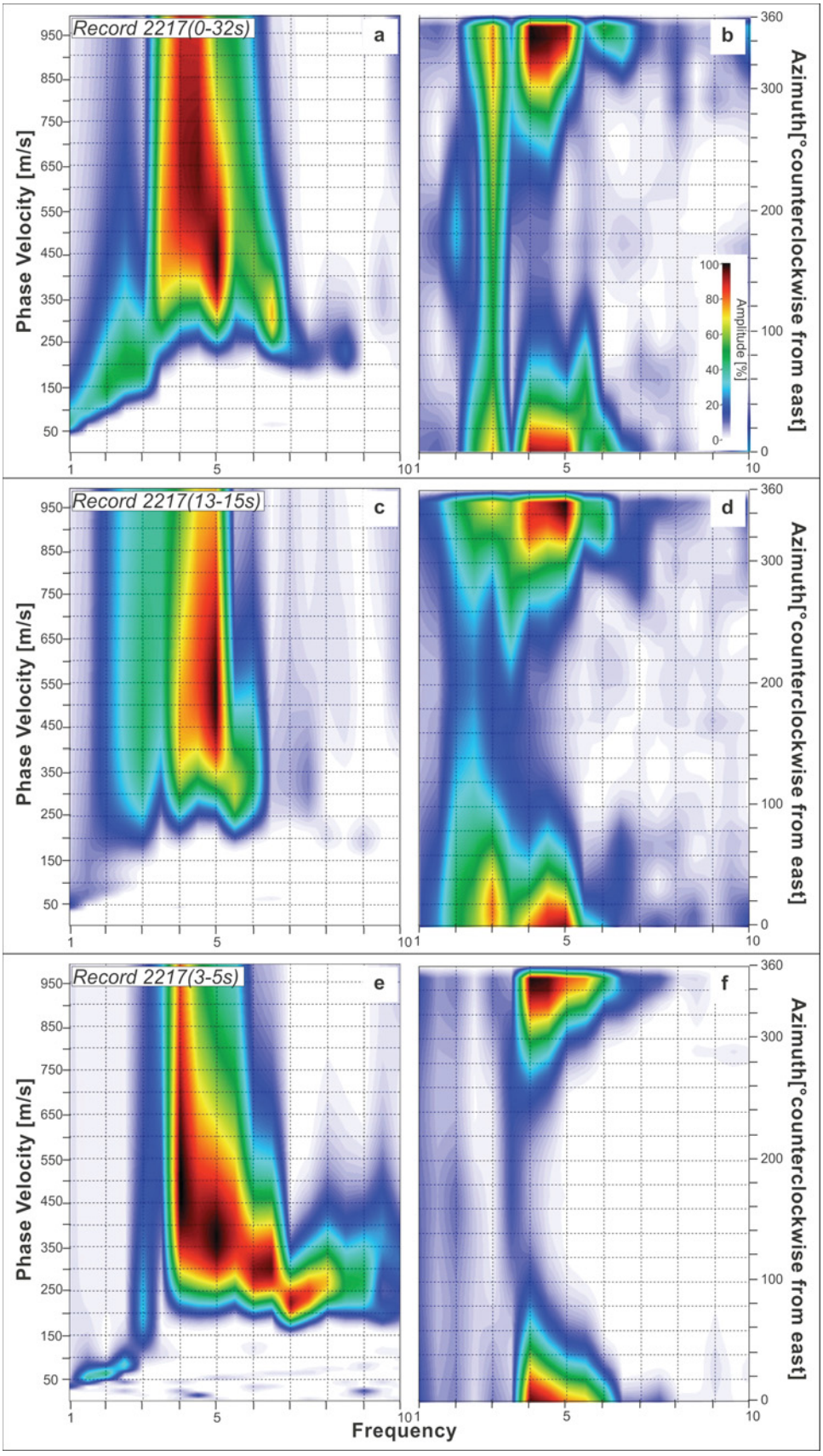
Record 2217(0-32s)
a
b
Record 2217(13-15s)
c
d
Record 2217(3-5s)
e
f
Phase Velocity [m/s]
Azimuth[°counterclockwise from east]
Amplitude [%]
Frequency

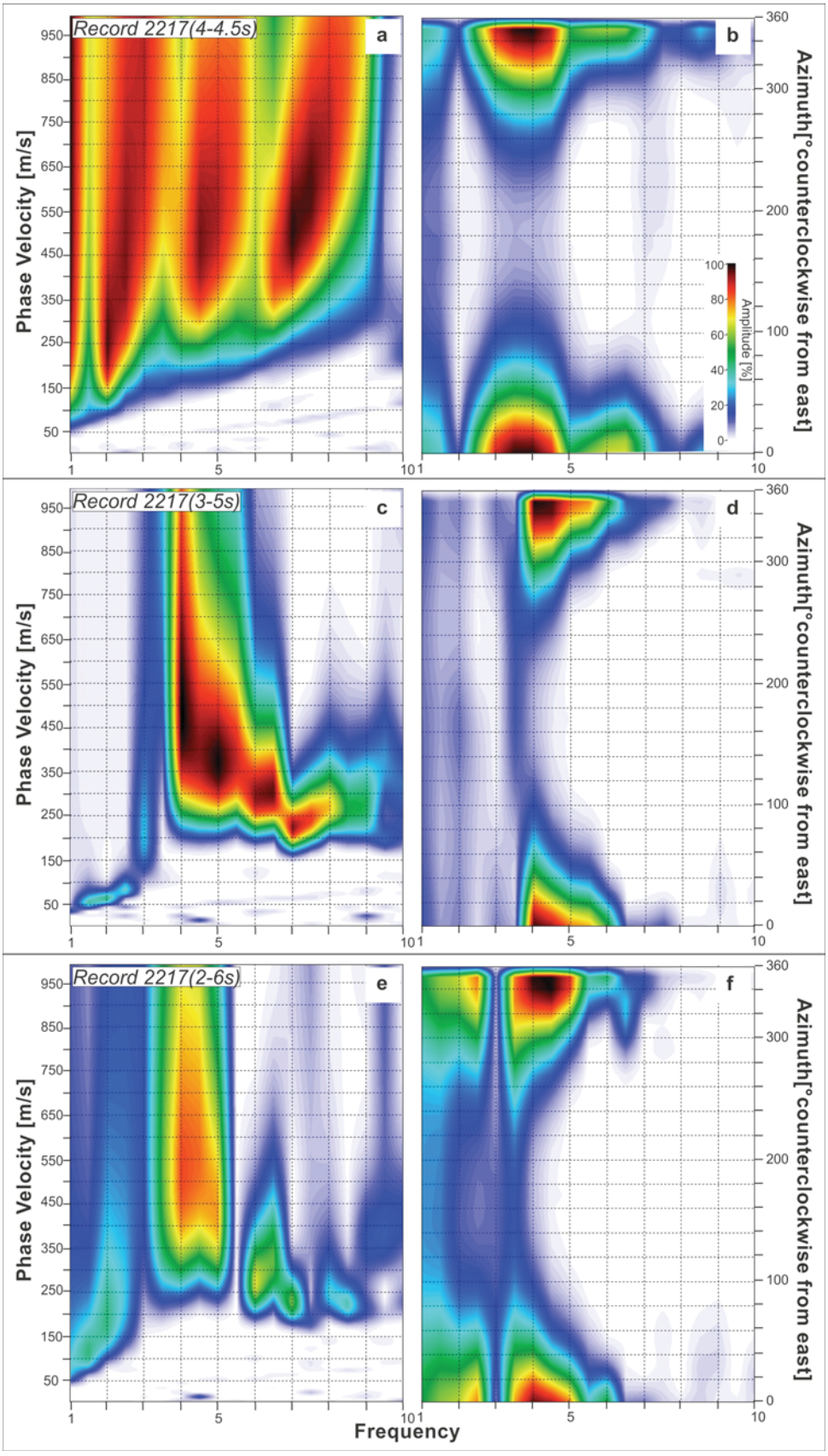
Record 2217(4-4.5s)
a
b
Record 2217(3-5s)
c
d
Record 2217(2-6s)
e
f
Phase Velocity [m/s]
Azimuth[°counterclockwise from east]
Amplitude [%]
Frequency

Figure 6.43 (previous page) *Record 2217: a) Phase- velocity versus Frequency diagram and b) Azimuth versus Frequency diagram, both for a 0.5 seconds time window, c) Phase- velocity versus Frequency diagram and d) Azimuth versus Frequency diagram, both for a 2 seconds time window, e) Phase- velocity versus Frequency diagram and f) Azimuth versus Frequency diagram both for a 4 seconds time window.*

Going from Figure 6.42b downwards and concentrating on the resolvable frequencies from 4 Hz up, Figure 6.42f shows the less stretched signals over the azimuths. Selecting a record on the basis of the Azimuth frequency diagrams, Record 2217 (3-5s) seems to have the best quality.

Considering also the dispersion curve images it's clearly visible, that Record 2217(3-5s) has by far the best resolution. Considering again Figure 6.41, indicates that probably also the energy reduction in the window between 13 and 15s is too large.

After finding an adequate record with a good broadband energy coming from mainly one direction and after filtering out of this record a time section with the best attributes for distance of source, energy strength, etc., the ideal time section length has to be determined. The time section needs to be long enough to capture a representative segment of information, but short enough to constrain energy to a stable azimuth angle, -at least for the frequencies of interest. Figure 6.43 shows dispersion curve images and Azimuth versus phase velocity diagrams processed of data with different time window length, 0.5 seconds, 2 second and 4 seconds.

Investigating the Azimuth Frequency diagrams first (Figure 6.43b, d, f), it catches one's eye that the 500 milliseconds time window's maximum energy seems concentrated quite dense around 350°. By checking then the Phase velocity frequency image it shows that there is no valuable information in the lower 9 Hz. So, even if a short time section avoids artifacts from a moving source, the information content for lower frequencies is not sufficient.

In Figure 6.42f the energies are stretched again over the azimuth, so that it can cause distortions during the processing of the dispersion curve diagrams. Under consideration of the dispersion curve diagrams it becomes clear that the result of the two seconds time window in Figure 6.43c is the best choice for this selected record.

For most of the records of the two-dimensional arrays used in this study (with only a few exceptions) a length of two seconds came out to be ideal. If not handling with a moving source the longer time windows can for sure improve in many cases the signal resolution.

6.2.5 Width and Length of array

Width and length of an array is, of course, depending on the surrounding and technical restrictions. Exemplary, for the arrays of this study significant restrictions factors were the following:

- Array 2000: Creek in the North, fences, and elevation differences
- Array 3000: Had to have for comparison reasons the identical parameters as array 2000
- Array 4000: One-dimensional array, available amount of receivers
- Array 5000: surrounding fences, streets and underground because ground was formerly used as area of settlement.

The sub-arrays are of course restricted by the array parameters and also by the ideal signal income direction, which is not always predictable in advance.

Width

The width of the rectangular sub-array depends on how the original array has been chosen. Figure 6.44 shows an example from Array 2000 (Record 2217 (3-5s)). The geophone lines of the original array have two main directions, one at about 80° /260° and one at about 350° /170°. All examples are calculated after the orientated rectangle method (including energy segregation).

The direction of maximum incoming energy for Record 2217 is at about 352°. In Figure 6.44 two arrays are compared. Figure 6.44a and b show the results of a six meter wide spread, Figure 6.44c and d, of a three meter wide spread. In the six meter wide sub spread the 80° direction gets more pronounced and additionally the 350° direction gets underlined with a second geophone line in that direction. Also if the latter is of minor importance because of the closeness to the maximum incoming energy, the 352° direction cannot be distinguished anymore in the sub-array. The consequence is an increase in the Phase Velocity and a falsification of the results which gets evident when comparing the dispersion curve image with three meter wide spread.

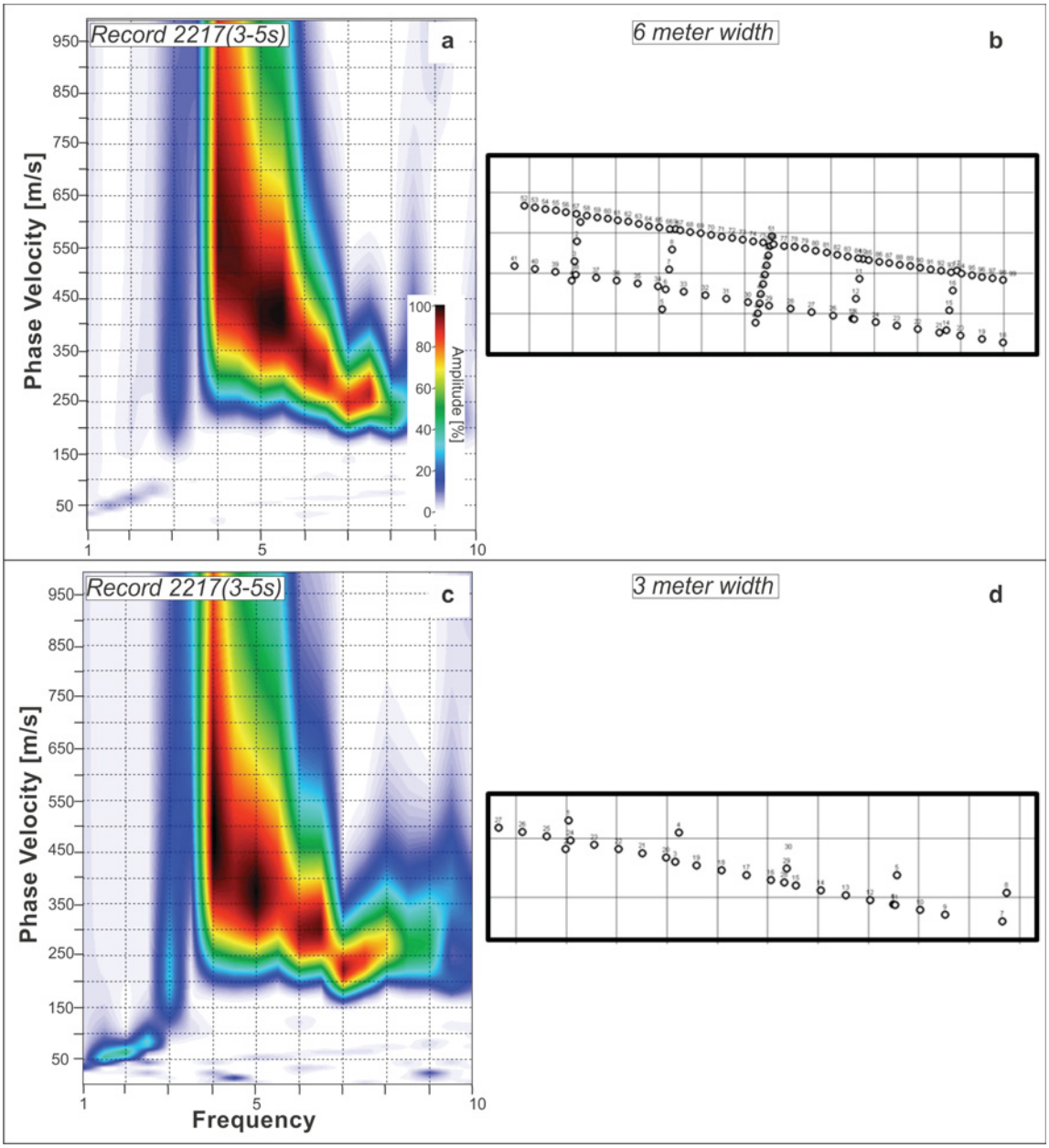

Figure 6.44 *a) Phase- velocity versus Frequency diagrams with spread b), b) 6 meter wide spread with 99 geophones, c) Phase- velocity versus Frequency diagrams with spread c), c) 3 meter wide spread with 30 geophones.*

Length

The length of an array determines directly the area of the underground that gets packed into one dispersion curve. After the inversion all the information that the wave collected on its way over the geophones is integrated in the calculated vertical depth shear wave velocity profile over the midpoint of the selected geophones. If the underground is laterally continuous a long array has the advantage that long wavelength signal can be investigated and therefore the investigation

depth can be increased with the wavelength. If the underground is laterally inhomogeneous the length of the array has to be kept as short as possible (depending on the desired investigation depth) to avoid over-interpolation.

The importance of the choice of the length parameter is shown in succession with the help of array 4000. Array 4000 consists of a singular line parallel to the railroad, and it is therefore ideal to show the effect on the results when changing the array length. Only data is used where the train is in line with the array and has already passed the geophones and where there is no surrounding noise (Record have been collected over night).

Figure 6.45 shows the seismic Record 4055 (0-16s), with the time on the y-axis and the traces stringed on the x-axis. The traces are consecutively numbered from West to East. From the energy pattern one can see that a train is moving near the western part of the array (at traces between 0 and 180) and produced for the MASW method unusable noise. The pattern recorded by the eastern receivers show that the train was moving towards West; also the noisy part is shifted with the time (y-axis) to the West.

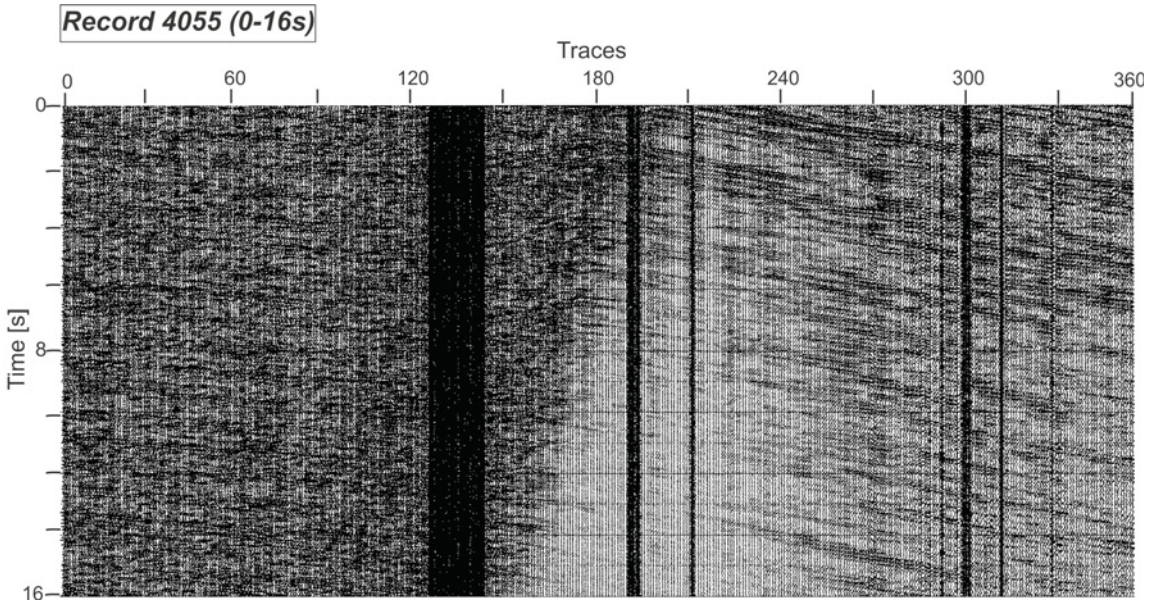

Figure 6.45 *seismic section for record 4055, 0 to 16 seconds, sampling rate 2 milliseconds, 360 geophones, train in the West, black corridors are places without geophones because of obstacles on surface.*

In the images illustrated on the following pages, are compared the results of the four seconds long time section (0-4s) of Record 4055 processed with a different amount of traces from the stations between180 and 360.

In Figure 6.46a to i Record 4055 (0-4s) is processed with a decreasing amount of geophones. Whereas Figure 6.46a has a spread length of 450 meters, Figure 6.46i has a spread length of only 50 meters. Figure 6.46a to g show a resolution till a frequency of 3.5 Hz. With decreasing

spread length the energy gets more distributed over the phase velocities and is not so clearly concentrated in a “bulls eye” as in Figure 6.46a. The energy distribution starts to spread from the lowest frequency up by decreasing the spread length.

The phase velocities especially of the lowest resolvable frequency of 3.5 Hz differ in Figure 6.46a and b noticeably from the smaller arrays. This could have several reasons:

- It could be a consequence of the underground variation; the investigated site is because of several former producing wells lateral strongly inconsistent.
- The differences in the smaller arrays could be a question of unfinished surface wave development, because of the long wavelength of the 3.5 Hz signal. The arrays are too small to resolve the signal completely.
- Another possible answer could be the angle sensibility of the method. As the train rail tracks show a minimal curvature, the closeness of the two larger arrays could have a negative consequence in term of angle accuracy. The signals are possibly not travelling directly in line with the linear spread and could cause maybe an increase in velocity.
- The difference in velocity could also be a reason of the fact that at the nearest geophones to the trains the waves cannot yet be handled as plane waves because of the long wavelength and the nearness to the source.

Figure 6.46 (following pages) *Phase- velocity versus Frequency diagrams of record 4055, time section 0 to 4 seconds, receiver spacing 2.5 meters: a) 450 meters, b) 400 meters, c) 350 meters, d) 300 meters, e) 250 meters, f) 200 meters, g) 150 meters, h) 100 meters, i) 50 meters spread length.*

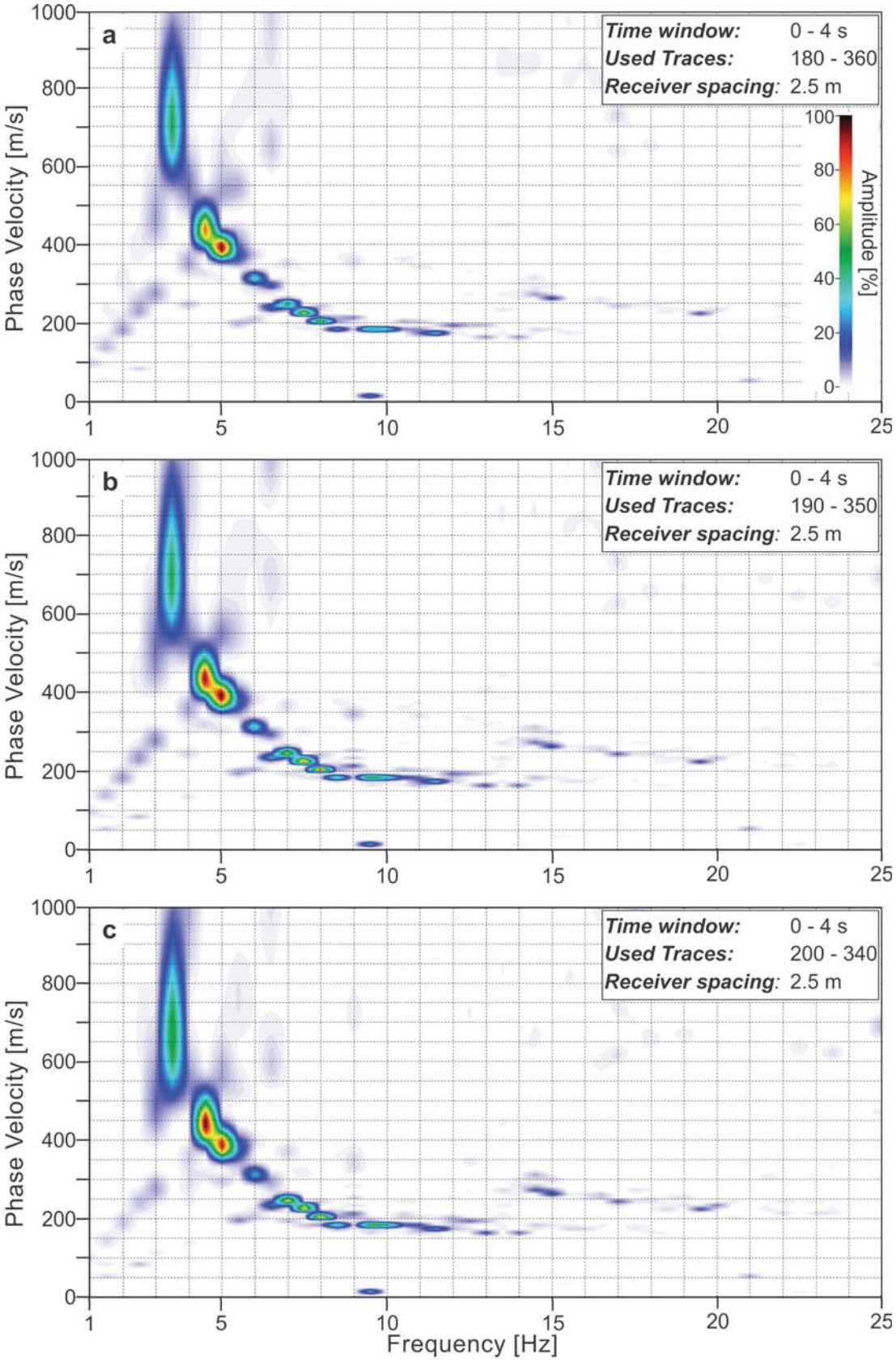
a
Time window: 0 - 4 s
Used Traces: 180 - 360
Receiver spacing: 2.5 m
b
Time window: 0 - 4 s
Used Traces: 190 - 350
Receiver spacing: 2.5 m
c
Time window: 0 - 4 s
Used Traces: 200 - 340
Receiver spacing: 2.5 m
Phase Velocity [m/s]
Frequency [Hz]
Amplitude [%]
0
200
400
600
800
1000
1
5
10
15
20
25
0
20
40
60
80
100

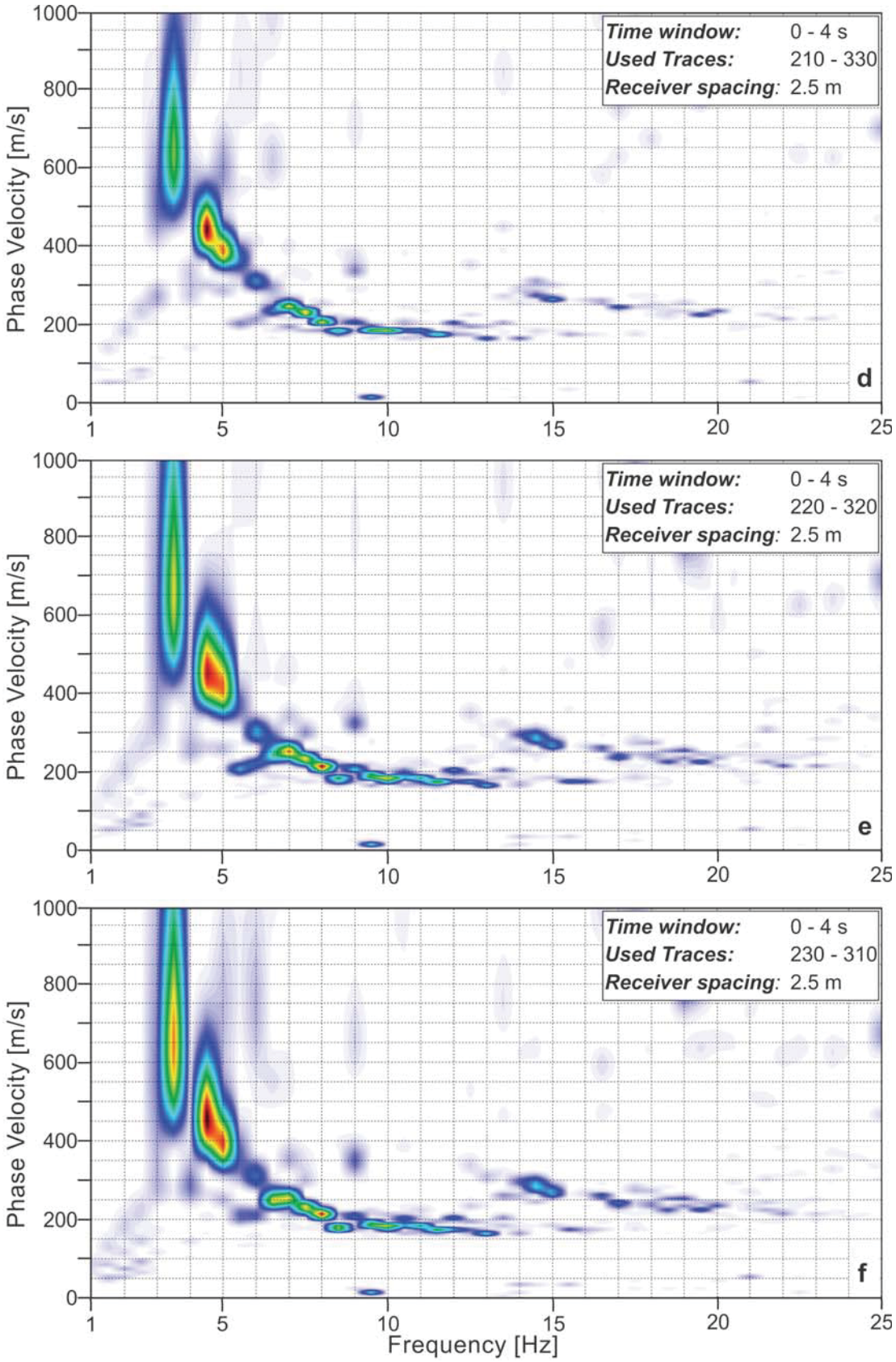
Time window: 0 - 4 s
Used Traces: 210 - 330
Receiver spacing: 2.5 m
d
Time window: 0 - 4 s
Used Traces: 220 - 320
Receiver spacing: 2.5 m
e
Time window: 0 - 4 s
Used Traces: 230 - 310
Receiver spacing: 2.5 m
f
Phase Velocity [m/s]
Frequency [Hz]
0
200
400
600
800
1000
1
5
10
15
20
25

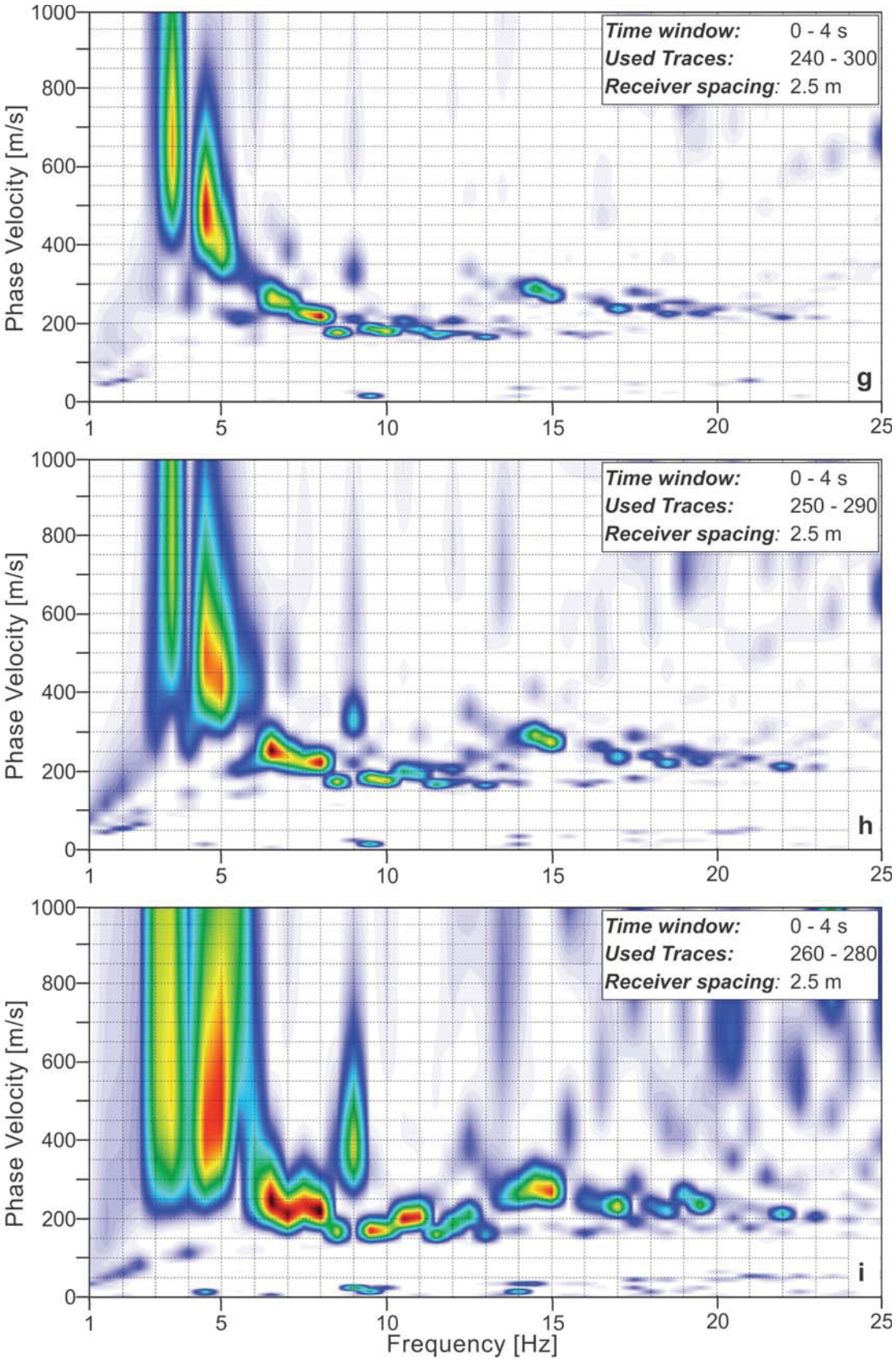
Time window: 0 - 4 s
Used Traces: 240 - 300
Receiver spacing: 2.5 m
g
Time window: 0 - 4 s
Used Traces: 250 - 290
Receiver spacing: 2.5 m
h
Time window: 0 - 4 s
Used Traces: 260 - 280
Receiver spacing: 2.5 m
i
Phase Velocity [m/s]
Frequency [Hz]
0
200
400
600
800
1000
1
5
10
15
20
25

Different from Figure 6.46a to g, in Figure 6.46h the lowest resolvable frequency for the spread length of 100 meters averages to 4.5 Hz. The energy distribution for the spread with a length of 50 meters (Figure 6.46i) is at a Frequency of 5Hz already significantly stretched and not resolvable in an accurate way. Clear results for the 50meter spread are starting at 6 or better 6.5 Hz. The Amplitude spectrum in Figure 6.47 shows the reason for the energy gap between 5Hz and 6Hz.It is caused from a lack of source energy around that area.

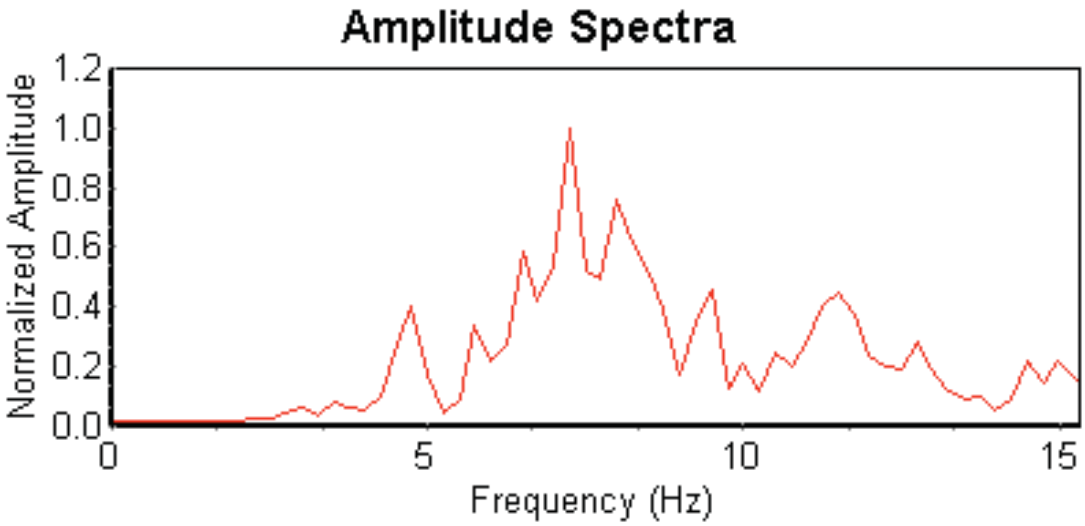

Figure 6.47 *Amplitude spectrum for Figure 6.46i.*

A resolution until 3.5 Hz implies for the investigated site with phase velocities between 650m/s and 700 m/s an investigation depth between 93m and 100m (Xia 1999). A reduction of the resolution to 4.5Hz decreases the investigation depth to about 53 meters (Xia 1999).

For the first 4 seconds of record 4055 Figure 6.46g with a spread length of 150 meters and 60 geophones would be a good choice as a compromise between resolution and limited lateral influence.

Figure 6.48a to c show dispersion curves for the same record as used in the former example, but with a time section prolonged to 16 seconds, Record 4055(0 - 16s). For this Record and spread it makes sense to try larger windows because the mowing source is not introducing new angles, because it is moving in line with the spread. These examples should give an answer on the questions if waves with longer wavelength have to be recorded over longer time periods and if with longer records the resolution gets improved. It should also give a solution to the former problem of the phase velocity variation at 3.5 Hz and if the variation is depending on the lateral underground variation, the source nearness and with an angle problem.

The results of Figure 6.48 lead to the following assumptions:

Figure 6.48a shows the phase velocity frequency diagram for a spread of 450 meters. Different from Figure 6.46a is only that it has been used a longer time section. The resolution goes like in the former example (Figure 6.46a) down to a Frequency of 3.5 Hz. From the dispersion curve image at 3.5Hz a phase velocity of about 660 m/s can be computes. As this velocity is similar to the results received from Figure 6.46c to 6.46g, this speaks in favor to the presumption that the traces of 180 to 200 at time section 0 to 4 seconds were selected to near to the source, either in terms of wave developing and handling as plane wave or in terms of wrong angle to the source.

Figure 6.48b with a spread length of 250 meters shows still a very good resolution even if the amplitude concentrations are slightly less concentrated than in Figure 6.48a

Figure 6.48c with a spread length of 100meters shows like in the 0 to 4 seconds time window a resolution until 4.5 Hz.

When comparing the result of the different time window length, can be seen as expected, that the resolution of the lower frequencies gets not improved, but the energy and with it the consistency of a dispersion curve can be improved to a considerably degree. In both examples a higher mode dispersion curve is recognizable from about 14 Hz up.

Length and width of an array have to be chosen uniquely, depending on source position to the spread, underground variations, quality of the record and depending on available processing time, need and resources.

Figure 6.48 (on the following page) *Phase- velocity versus Frequency diagrams of record 4055, time section 0 to 16 seconds, receiver spacing 2.5 meters: a) 450 meters, b) 250 meters, c) 100 meters spread length.*

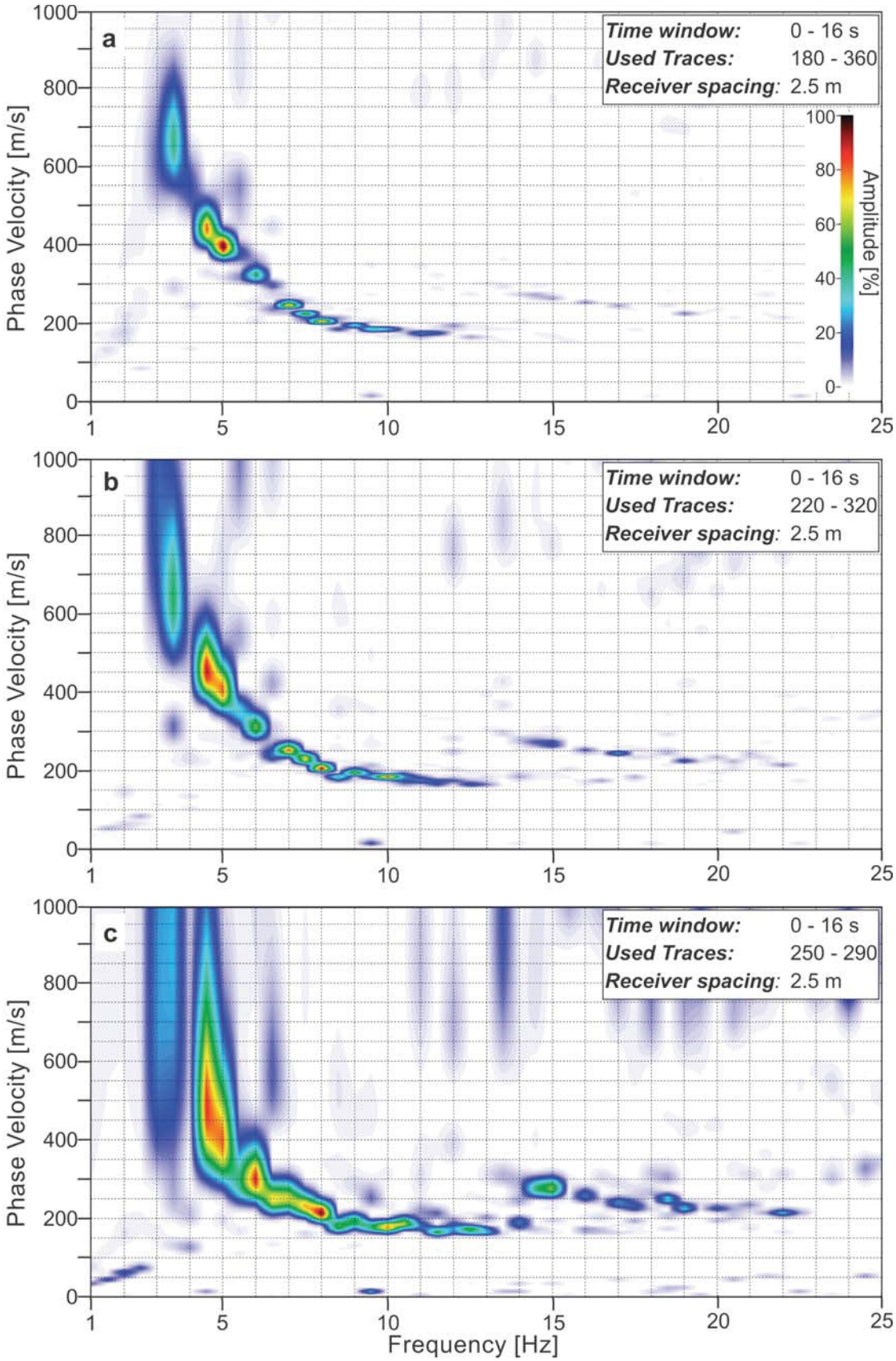
a
Time window: 0 - 16 s
Used Traces: 180 - 360
Receiver spacing: 2.5 m
b
Time window: 0 - 16 s
Used Traces: 220 - 320
Receiver spacing: 2.5 m
c
Time window: 0 - 16 s
Used Traces: 250 - 290
Receiver spacing: 2.5 m
Phase Velocity [m/s]
Frequency [Hz]
Amplitude [%]

6.3 Processing scheme

The following processing scheme has been evolved from Park et al. (1998, 2004) and from the results gained in the previous chapters.

The first and key step in processing data is sorting out the records that have good broadband energy principally from one direction and then finding an adequate time window within those higher quality 32 seconds records. The time section needs to be long enough to capture a representative segment of information, but short enough to constrain energy to a stable azimuth angle, -at least for the frequencies of interest.

Once the records and time windows are selected the data is processed using the dispersion imaging scheme described by Park et al. (1998 and 2004). For this method the processing scheme for a 2D layout had to evolve by extending the 1D approach described by Park et al. (1998). In the 2D- case, the azimuths of the two scanning parameters (frequency and phase velocity) of the incoming surface wave were added: a particular frequency of surface wave energy is plotted in a phase velocity-azimuth diagram.

Park et al.(2004) stacks than the energy over all the azimuths. The stacked information for every scanned frequency results in the dispersion image. A detailed description can be found in Park et al. (2004).

As extension and modification to the former procedure, for this work, the data were scanned in time windows for the angle of maximum incoming energy at each frequency of interest. Frequency span can be varied as affordable. Time window quality factor increases with the number of frequency intervals with the same angle of maximum incoming energy.

Sub-arrays, in dimension of a rectangle are orientated in direction of the maximum incoming energy for the frequencies of interest. As directions and signal can change slightly by choosing a smaller amount of geophones, the rectangles are scanned again for each frequency in their phase velocity azimuth behaviour for maximum energy. If maximum energy angle is inside certain boundaries close to the orientation angle a restriction factor is increased by one. If the original array is large and results therefore in a large number of sub-arrays, the restriction factor can be set close to the number of initially detected frequencies with the same maximum incoming energy angle.

For the chosen sub-arrays, the energy is then stacked over the orientation azimuth with boundaries of 2 degrees.

Following these processing scheme the results with passive MASW can dramatically be improved.

7. Results and Interpretation of the investigated areas

The improved passive MASW technique is used on various arrays over a former field of salt dissolution mining in Hutchinson, Kansas (see chapter 4). Some of the old cemented production wells were redrilled in order to obtain up-to-date information about the subsurface situation from wireline logs.

With the passive MASW method the investigation depth of the former active MASW tests (20m) should be improved, the target is to reach depths well below bedrock (~23m). The measurements with passive MASW should give information about salt dissolution migration processes in this area in general and, more specifically, about the presence or absence of underground voids and their current state. It should also be tested if the method is suitable for a constant monitoring of underground voids with high collapsing potential.

7.1 Arrays 2000 and 3000

To classify the potential of collapsing voids, at two sites arrays of identical dimensions have been measured. One array is positioned over well 40, which is known to bear the potential of collapse and is suspected to form galleries with other nearby wells. The other array is positioned at well 94, which is believed to not be invaded by migrating saltwater. Both wells lie only 5m away from an important and busy railroad line. The measurements should give information about approximate size of the underground void, its extensions, which depth layer are already invaded by the migration process and if the well has to be drilled up and filled with sand or if the hazard potential is not yet that urgent.

7.1.1 Dispersion curves of array 2000

Array 2000 is positioned over the Well 40. Well 40 is believed to form a gallery with a void under Well 27, which lies south east of array 2000 (Figure 7.1 e). A connection between the underground void of well 40 and well 25, which lies in the Northwest, is also conceivable.

As the extension of the underground void or gallery below array 2000 is laterally inhomogeneous, only information extracted out of waves, passing the void from one direction, should be resumed in the same interpolation result. In case of array 2000 a direction restriction is not necessary because the best and therefore exclusively used data for the array is extracted from records with signals coming from trains working or traveling in the East of the array. East of the spread there is a freight depot where vehicles and coaches are loaded onto or unloaded from trains. Good quality surface wave signals are generated by trains moving at distances between 100 and 1500 meters from the array of sensors. As the best signals are coming mainly

from lateral direction, the midpoints of the orientated sub-arrays lie along the North South line in the center of the West East extension of the array.

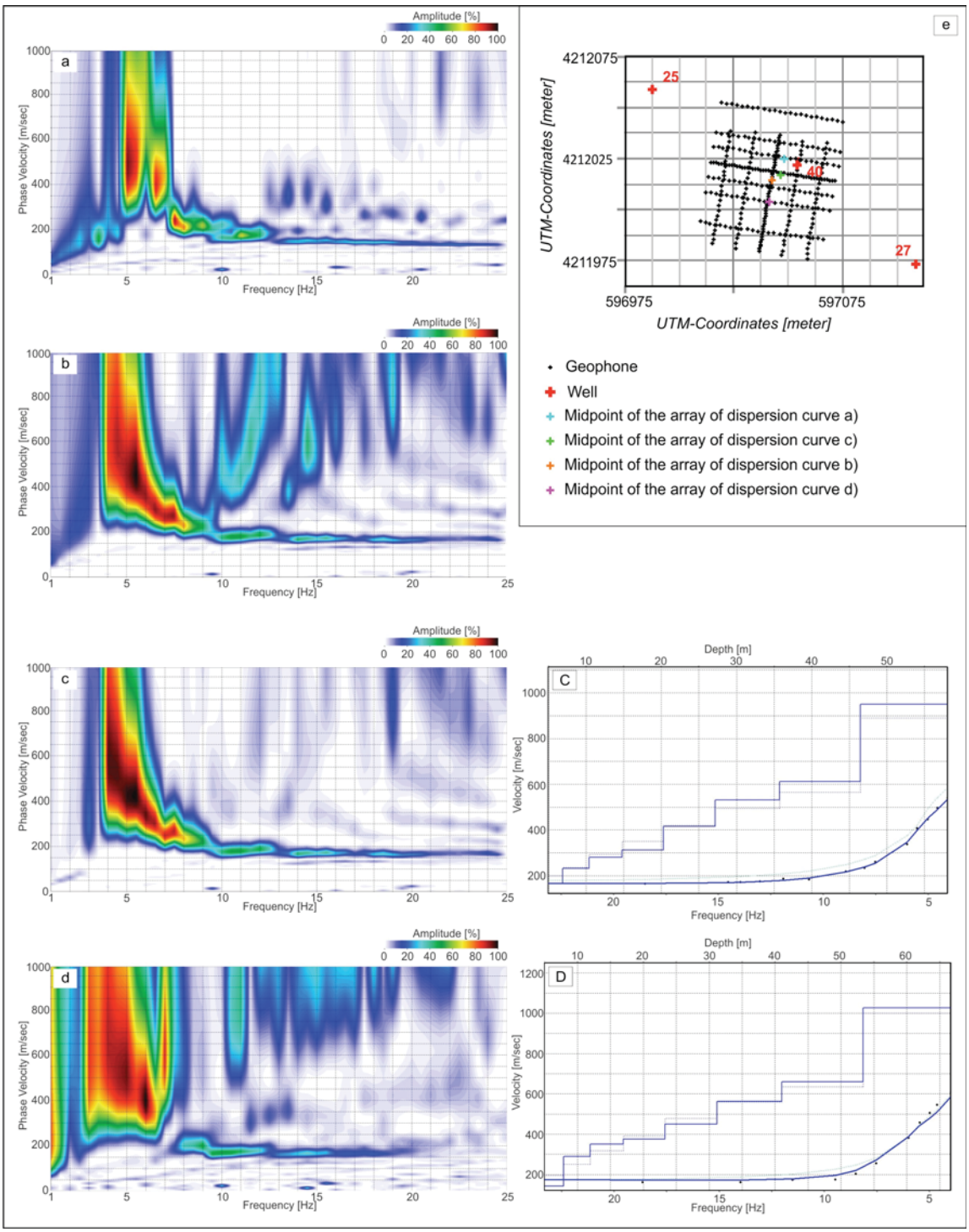

Figure 7.1 *a), b), c) and d): Random overtone images obtained from sub-arrays of array 2000; C) and D): Inversion result for dispersion curve c and d: the dots represent points of the originally picked dispersion curve, which have been interpolated first with a blue curve, the curve is than adapted after*

each run to fit a suitable depth - S-wave model, the block curve (blue) represents the final inversion results, the fine black block curve represents the result of the corresponding previous calculation run; e) Array 2000 with nearby wells and midpoints of sub-arrays from a, b, c and d.

		Depth					
X-Coordinate	Y-Coordinate	7 - 10 m	11 - 20 m	21 - 30 m	31 - 40 m	41 - 50 m	Halfspace
2217 (2.5 - 4.5s) - Orientation: 352°							
597040.54	4211985.65	237.67	382.55	440.49	541.56	615.87	941.28
597040.06	4211985.93	213.74	382.94	420.10	509.57	583.54	893.19
597038.81	4211985.93	233.01	341.10	383.16	490.78	580.29	895.95
597036.79	4211986.65	210.17	354.51	415.13	479.22	541.24	842.64
597035.07	4211986.65	223.48	349.33	418.78	517.64	580.42	880.74
597033.82	4211986.65	228.51	315.96	377.57	466.48	540.46	850.13
597031.48	4211986.65	217.57	311.20	390.25	465.68	519.31	790.28
597034.27	4212003.17	195.13	333.31	311.42	460.18	560.06	856.19
597033.03	4212003.17	224.88	324.00	381.18	474.29	564.44	906.50
597041.06	4212004.95	164.83	319.20	407.10	537.46	640.56	996.40
597038.60	4212004.95	259.00	347.79	386.14	502.75	614.24	969.04
597037.36	4212005.61	252.83	301.39	357.46	477.27	575.60	911.70
597034.27	4212005.61	249.91	341.78	344.25	470.47	602.94	965.20
597033.03	4212005.61	247.62	331.19	352.57	457.31	575.01	935.28
597032.13	4212005.61	178.02	345.42	310.78	420.55	584.50	1007.26
597046.96	4212014.08	265.00	303.84	364.54	471.26		779.45
597045.52	4212014.37	185.51	376.84	375.49	380.71	496.90	920.06
597042.80	4212014.88	231.00	311.30	416.31	531.70	611.48	949.97
597042.21	4212014.88	263.00	308.55	425.04	519.62	587.30	935.98
597041.01	4212015.09	211.00	344.05	389.51	569.69	624.17	907.20
597039.82	4212015.30	195.08	314.71	343.04	441.10	511.90	749.48
597038.02	4212015.51	214.87	311.91	343.16	425.01	509.56	692.23
597036.83	4212015.93	241.31	279.38	343.89	451.84	460.42	683.49
597035.04	4212016.14	182.73	329.06	331.84	386.58	488.57	754.94
597047.01	4212017.37	170.15	369.65	353.47	416.21	533.88	907.43
2228 (26.3 - 30s) - Orientation: 354°							
597045.20	4212002.00	229.69	322.25	454.34	644.15	739.55	694.39
597037.76	4212008.58	161.24	370.63	377.77	533.21	659.47	756.66
597045.52	4212013.43	163.28	341.82	387.06	530.32	650.29	764.90
597047.01	4212017.37	164.04	336.48	409.94	525.04	615.97	768.92
597048.79	4212025.29	141.89	350.94	374.31	449.56	561.78	1027.37
2267 (16-5 -18.5s) - Orientation: 356°							
597042.32	4211989.09	249.95	313.79	405.56	467.94		738.24
597041.60	4212004.38	217.92	400.00	454.79	454.79		800.32
597044.78	4212010.15	206.37	331.43	462.23	505.91		789.03
597041.01	4212016.61	230.07	333.51	433.84	492.57		693.32
597045.36	4212025.46	159.00	411.78	478.30	534.51		853.95
597041.53	4212034.03	163.57	335.08	383.99			625.46

Table 7.1 *Inversion results from dispersion curves of array 2000. Columns 1 and 2: Midpoints of sub-arrays. Columns 3 to 8: shear wave velocities for certain depth steps. Cursive text: Record number; in brackets: chosen time section; maximum incoming energy =orientation angle of the sub-arrays. Highlighted in yellow: Dispersion curves shown in Figure 7.1 a-d.*

The dispersion curves extracted from records of sub-arrays of array 2000 show high amplitude signals mainly in the lower frequencies. To obtain continuous dispersion curves, dispersion curve images (=overtone record) from passive datasets can be combined with active datasets (Park, Miller, Ryden, Xia, & Ivanov, 2005). The overtone records in Figure 7.1 are result from the combination of the passive surface wave detection method (1- 8 Hz) and the active method (8-25 Hz).

The overtone images of array 2000 are resolvable down to a frequency of minimal 4 Hz. The Phase velocities at these lowest reachable Frequencies reach values to about 600 m/s. Figure 7.1 shows 4 overtone images with dispersion curves resolvable down to 4 Hz. The images are extracted from rectangular sub-arrays orientated toward east (352° to 356° counterclockwise from east). The midpoints of the 4 sub-arrays are illustrated in Figure 7.1.

The inversion results of the dispersion curves c and d in Figure 7.1 are shown in Frequency-Velocity-Depth diagrams (Figure 7.1, C and D). For the displayed curves shear wave velocity reaches values between about 500 and 600 m/s at depths between 40 and 50 m. The Root Mean Square Error (RMSE) in the lowest frequencies lies for the inversion result C at 4 m/s. The accuracy for the inversion result D is with 18 m/s much larger. The inversion results of each dispersion curve are applied to the center of respective sub-array.

In Table 7.1 inversion results for array 2000 are listed. This data is processed in the section ‘Comparison of array 2000 and 3000’ as 2D depth layers.

7.1.2 Dispersion curves of array 3000

Array 3000 is positioned around well 94. The data extracted from this measurement are handled as reference model of the undisturbed subsurface, which implies having a production well, but not being invaded by salt dissolution voids.

The best data for this array is extracted from records with signals coming from trains at different distances and from different directions. As array 3000 is handled as reference model for which the average values count there is no need to observe the data from each direction separately.

The dispersion curve a) in Figure 7.2 has its energy from a train traveling towards West; the distance of the train is during the processed recording time between about 30 to 100 meters from the West end of the spread. Dispersion curve b) is processed out of a record where the train is working in the freight depot East of the spread. The lower two dispersion curves in Figure 7.2 have their energy from a train traveling towards North on the tracks, which are leading from Southwest to Northeast, with the position in the Southwest during the time of recording.

In the records for array 3000 the energy is distributed quite continuously over the frequencies. A combination with the active multichannel analysis of surface waves was therefore not necessary (see dispersion curves in Figure 7.2a to d).

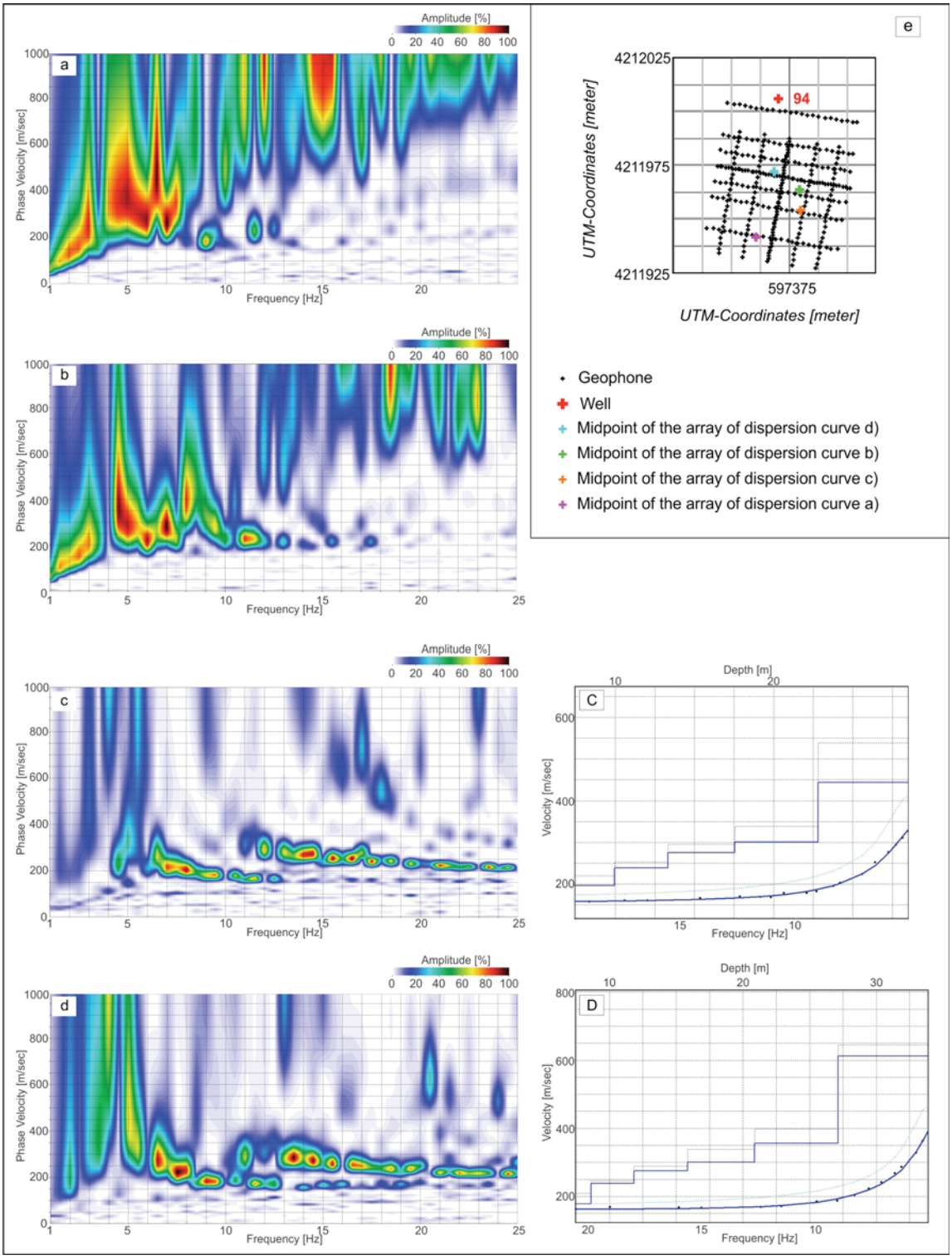

Figure 7.2 *a), b), c) and d): Random overtone images obtained from sub-arrays of array 3000; C) and D): Inversion result for dispersion curve c and d: the dots represent points of the originally picked dispersion curve, which have been interpolated first with a blue curve, the curve is than adapted after each run to fit a suitable depth - S-wave model, the block curve (blue) represents the final inversion*

results, the fine black block curve represents the result of the corresponding previous calculation run; e) Array32000 with nearby wells and midpoints of sub-arrays from a, b, c and d.

X-Coordinate	Y-Coordinate	Depth 7 - 10 m	11 - 20 m	21 - 30 m	31 - 40 m	Halfspace
3200 (2.5 - 4.5 s) - Orientation: 236°						
597359.55	4211960.65					574.00
597360.16	4211961.85	173.00	321.00	351.35	420.04	733.86
597364.83	4211967.47	186.00	313.23	350.00		697.44
597365.01	4211968.68	179.93	306.83	365.00		700.72
597365.43	4211971.20	183.57	298.03	361.71		691.48
597359.28	4211957.78	179.53				682.60
597361.25	4211959.18	184.04				673.63
597366.07	4211967.26	178.44	278.00	319.59		640.37
597368.32	4211970.92	177.07	275.30	356.19		612.04
597372.90	4211975.31	145.40	273.88	360.60		613.71
597373.13	4211976.38	186.43	296.53	333.10		545.00
597373.24	4211970.12	184.36	263.68	324.91		644.00
597374.44	4211970.12	184.80	263.02	325.06		631.00
597374.83	4211972.28	166.55	263.70	322.50		635.06
597375.06	4211973.59	180.89	272.28	330.00		564.35
597378.30	4211961.93	159.71	318.36	384.58		727.20
597382.93	4211968.64	171.34	267.00	381.48		626.37
597381.18	4211959.15	159.83	280.81	339.29		660.54
597385.19	4211967.09	184.93	281.10	334.99		553.03
597380.33	4211953.35	141.10	264.89	307.29		628.72
597380.77	4211955.99	199.01	306.78	338.33		480.99
597381.61	4211955.99	195.84	284.31	307.63		448.33
597381.85	4211957.08	176.36	275.38	300.00		443.80
3260 (11.5 - 13.5s) - Orientation: 164°						
597366.13	4211940.33	166.00	282.52	318.30		441.51
597360.07	4211941.30	201.00	301.00	324.12		465.00
597369.75	4211975.95	184.62	271.59	332.13	404.98	634.38
3260 (16 - 18-5s) - Orientation: 166°						
597361.18	4211942.26	144.66	298.14	348.79	479.65	528.00
597374.47	4211954.39	242.17	290.97	377.34		707.00
3241 (18 - 20s) - Orientation: 26°						
597379.77	4211962.81	172.38	227.24	323.72		512.87
597382.44	4211964.10	182.93	224.39	320.24		525.13

Table 7.2 *Inversion results from dispersion curves of array 3000. Columns 1 and 2: Midpoints of sub-arrays. Columns 3 to 8: shear wave velocities for certain depth steps. Cursive text: Record number; in brackets: chosen time section; maximum incoming energy =orientation angle of the sub-arrays. Highlighted in yellow: Dispersion curves shown in Figure 7.1 a-d*

The resolution of the overtone images is limited at 4.5 Hz. The Phase velocities of the waves travelling with the lowest Frequencies hardly exceed 400 m/s.

The inversion results derived from the dispersion curves c and d of Figure 7.2 are represented in Frequency-Velocity-Depth diagrams (Figure 7.2, C and D). Figure 7.2 C gives impression of a dispersion curve reflecting shear wave velocities of the lower velocity limits of array 3000. Figure 7.2 D shows shear wave velocities near the higher velocity limit of the not invaded area. The Root Mean Square Error lies for both examples below 4 m/s.

In Table 7.2 inversion results for array 3000 are listed. These data are processed in the section 'Comparison of array 2000 and 3000' as 2D depth layers.

7.1.3 Comparison between Array 2000 and 3000

Below Array 2000 a void is present, developed out of the producing well 40; it is strongly suspected that also a gallery has developed. Array 3000 is deployed in the East of the area around well 94, which is known to be free from dissolution voids. Array 3000 is used as reference model for a not invaded underground in an area of former salt dissolution mining.

The presence of two such different test sites provides an excellent investigation area to test the Passive MASW for their resolution of stress and strain differences in the underground.

The next figures in this section show in the upper part the position of the two arrays with the outlines of the 2D layers in green. The position of the nearby wells should give impression how eventual galleries could influence the 2D velocity layers. The 2D velocity layers, on the left hand side in each case the Array 2000 and on the right Array 3000, have a color bar for shear wave velocity with a fixed minimum (140 m/s) and maximum (1030 m/s) effective for all depth layers. The white crosses in the 2D layers show the midpoints of the sub-arrays, from which the dispersion curves have been extracted.

In the depth range between 7 to 10 meters (Figure 7.3) both analyzed areas exhibit low shear wave velocities not exceeding 300 m/s and are rather similar. As this depth layer is mainly influenced by differences at and just below the surface, any stress/strain differences caused by deeper voids would not be transferred to this layer. This depth layer is therefore for the mean of the project not from large interest.

At depths between 11 to 20 meters (Figure 7.4) at the border to the bedrock the 2D shear wave velocities show differences in their distributions. Whereas the velocities from the reference array range between 200m/s and 300m/s, the velocity in the invaded area shows values above 300m/s, in some parts reaching 400m/s. Stress and strain conditions caused from the different underground situations seem to already marginally affect the layers above bedrock.

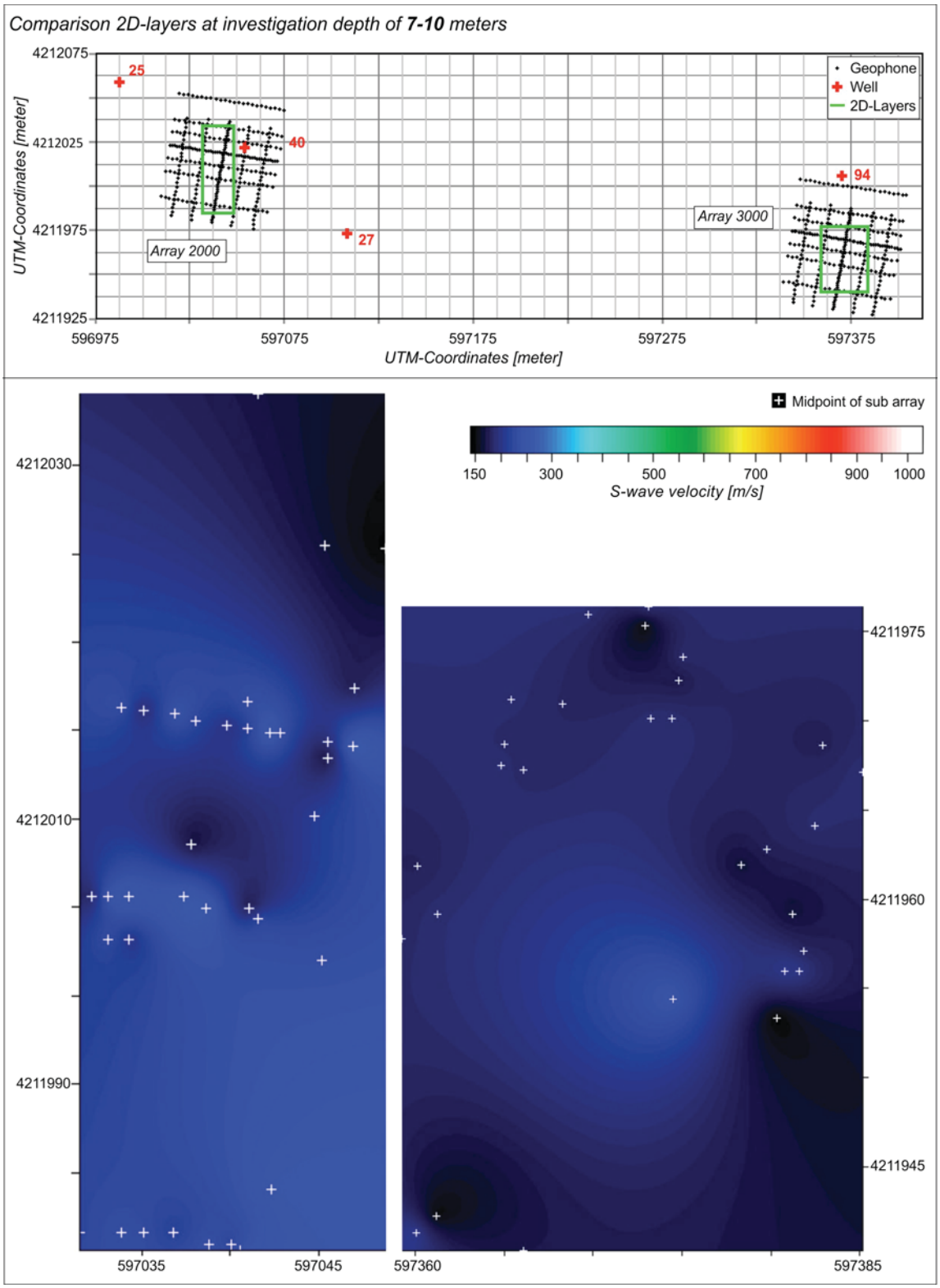

Figure 7.3 *Comparison of 2D layer structures at depth 7-10 meters. Top: Area map. Bottom left: 2D layer below Array 2000, white crosses show midpoints of sub-arrays. Bottom right: 2D layer below Array 3000.*

In the depth range between 21 meters to 30 meters (Figure 7.5) the 2D layers of the two arrays distinguish again in their average velocity level. Whereas the invaded area shows velocities between about 350 m/s and 450 m/s, the reference model indicates velocities between about 300m/s and 380 m/s. Below Array 2000 velocity highs are reached around well 40 and are dragged in direction to well 27, which would confirm a gallery between the two wells. In this depth layer the values toward well 25 seem also higher than for example the one calculated for the more southwesterly area of the array. As there are only a few values available for the Northern part towards well 25, the information is not sufficient to confirm the presence of a gallery between well 40 and the Northwestern well 25.

At depths between 31 meters to 40 meters (Figure 7.6) the number of points obtained from Array 3000 is reduced to four. This is a consequence of the lower frequency resolution of the records of Array 3000 in comparison to those of Array 2000. In association with it, also the fact that undergrounds under higher tension, can reach higher phase velocities and therefore higher investigation depths (Xia, 1999), leads to a reduced number of record that can resolve a depth until 40 meters. The small number of four data points makes the result less meaningful, but the differences to array 2000 are nevertheless reproducible. The 2D interpolation layer for the depths between 31 and 40 meters, in which bedrock is already reached, continues to show the deviating velocity trend between array 2000 and array 3000. The underground around well 40 seems, as expected, to be still under higher stress/strain conditions than the reference cube around well 94. The velocity elevation at the corridor between wells 40 and 27 is still evident.

Figure 7.4 (page, 130) *Comparison of 2D layer at an investigation depth of 11-20meters. Top: Position of array 2000 and array 3000, position of the nearby wells and position of the 2D layers in the arrays. Bottom left: 2D layer of array 2000, white crosses show midpoints of sub-arrays. Bottom right: 2D layer of array 3000, white crosses show midpoints of sub-arrays.*

Figure 7.5 (page, 131) *Comparison of 2D layer at an investigation depth of 21-30 meters. Top: Position of array 2000 and array 3000, position of the nearby wells and position of the 2D layers in the arrays. Bottom left: 2D layer of array 2000, white crosses show midpoints of sub-arrays. Bottom right: 2D layer of array 3000, white crosses show midpoints of sub-arrays.*

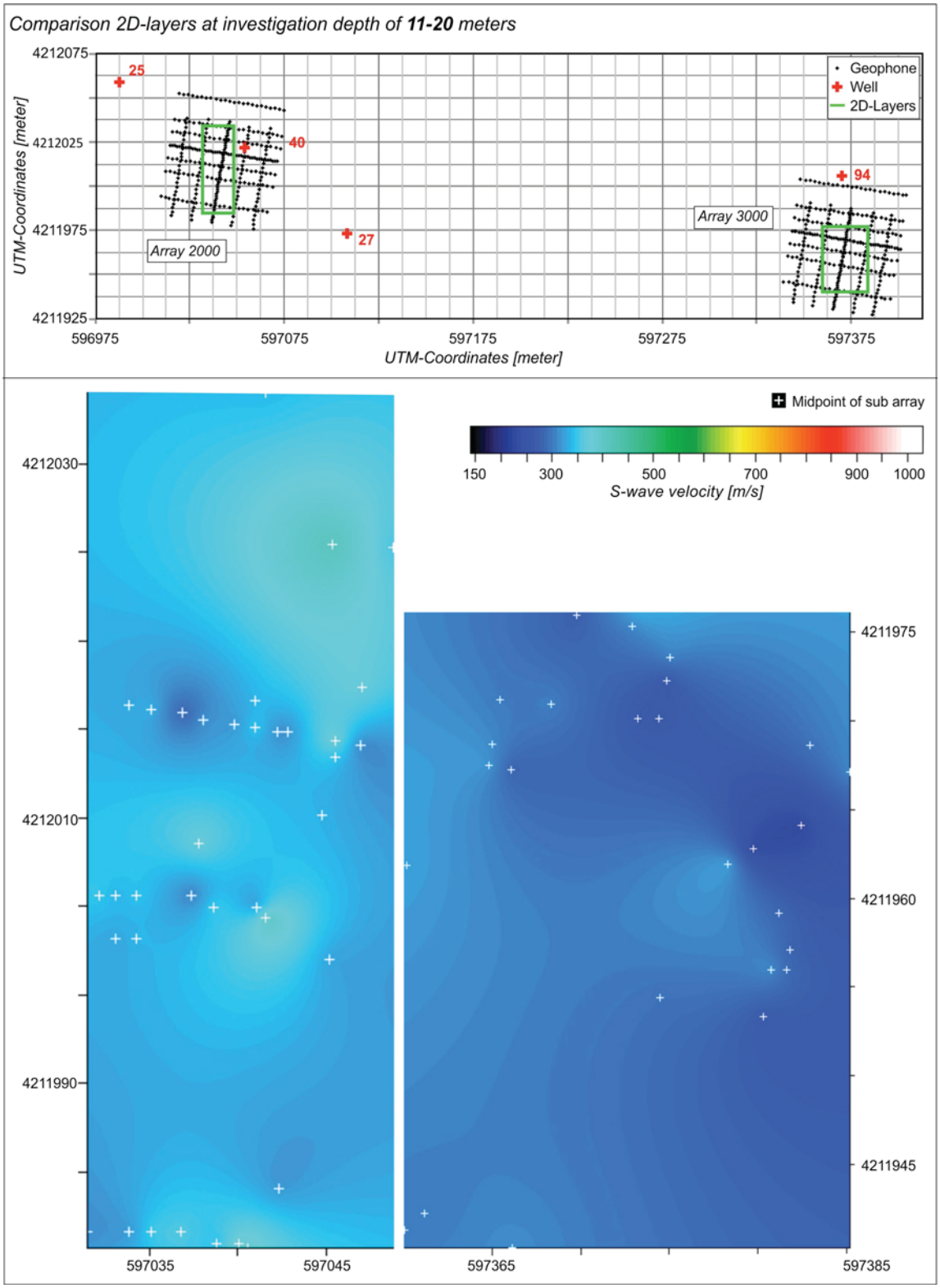
Comparison 2D-layers at investigation depth of 11-20 meters
Geophone
Well
2D-Layers
25
40
27
94
Array 2000
Array 3000
UTM-Coordinates [meter]
4212075
4212025
4211975
4211925
596975
597075
597175
597275
597375
UTM-Coordinates [meter]
Midpoint of sub array
150
300
500
700
900
1000
S-wave velocity [m/s]
4212030
4212010
4211990
4211975
4211960
4211945
597035
597045
597365
597385

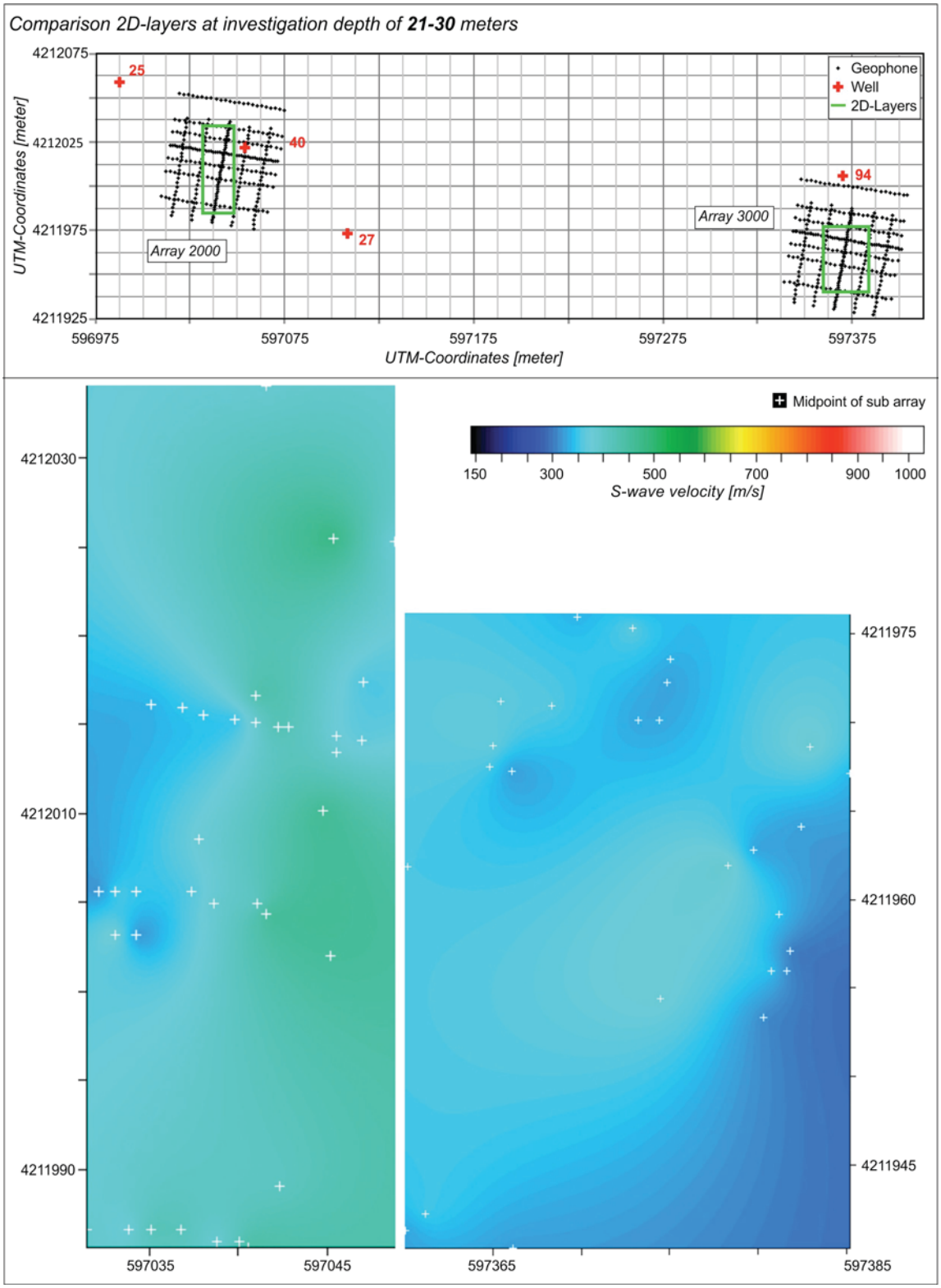
Comparison 2D-layers at investigation depth of 21-30 meters
Geophone
Well
2D-Layers
25
40
27
94
Array 2000
Array 3000
UTM-Coordinates [meter]
4212075
4212025
4211975
4211925
596975
597075
597175
597275
597375
Midpoint of sub array
150
300
500
700
900
1000
S-wave velocity [m/s]
4212030
4212010
4211990
4211975
4211960
4211945
597035
597045
597365
597385

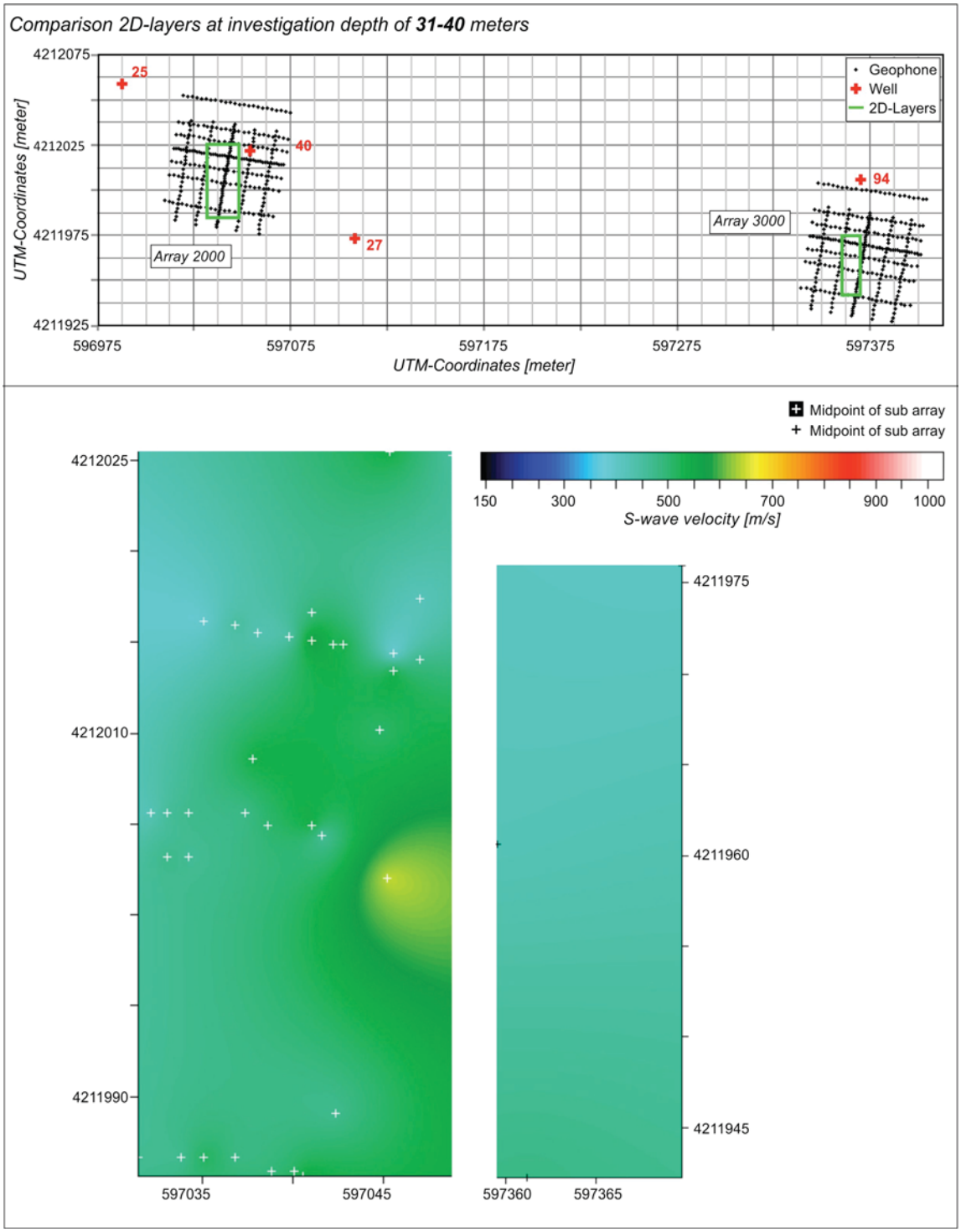

Figure 7.6 *Comparison of 2D layer at an investigation depth of 31-40meters. Top: Position of array 2000 and array 3000, position of the nearby wells and position of the 2D layers in the arrays. Bottom left: 2D layer of array 2000, white crosses show midpoints of sub-arrays. Bottom right: 2D layer of array 3000, white crosses show midpoints of sub-arrays.*

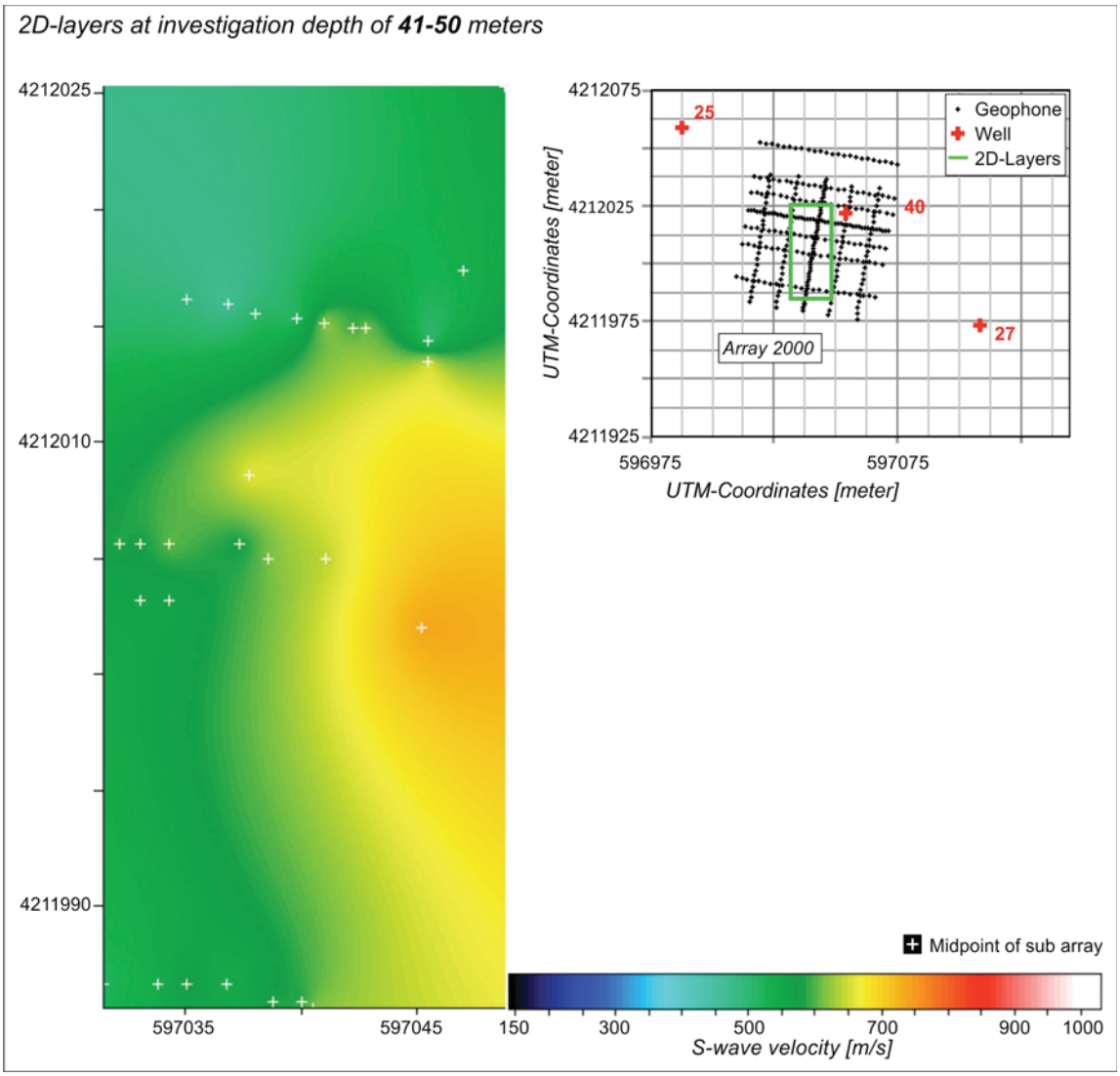

Figure 7.7 *2D layer at an investigation depth of 41-50meters. Right: Position of array 2000, position of the nearby wells and position of the 2D layers in the array. Left: 2D layer of array 2000, white crosses show midpoints of sub-arrays.*

Figure 7.8 (following page) *Comparison of 2D layer at halfspace. Top: Position of array 2000 and array 3000, position of the nearby wells and position of the 2D layers in the arrays. Bottom left: 2D layer of array 2000, black crosses show midpoints of sub-arrays. Bottom right: 2D layer of array 3000, black crosses show midpoints of sub-arrays.*

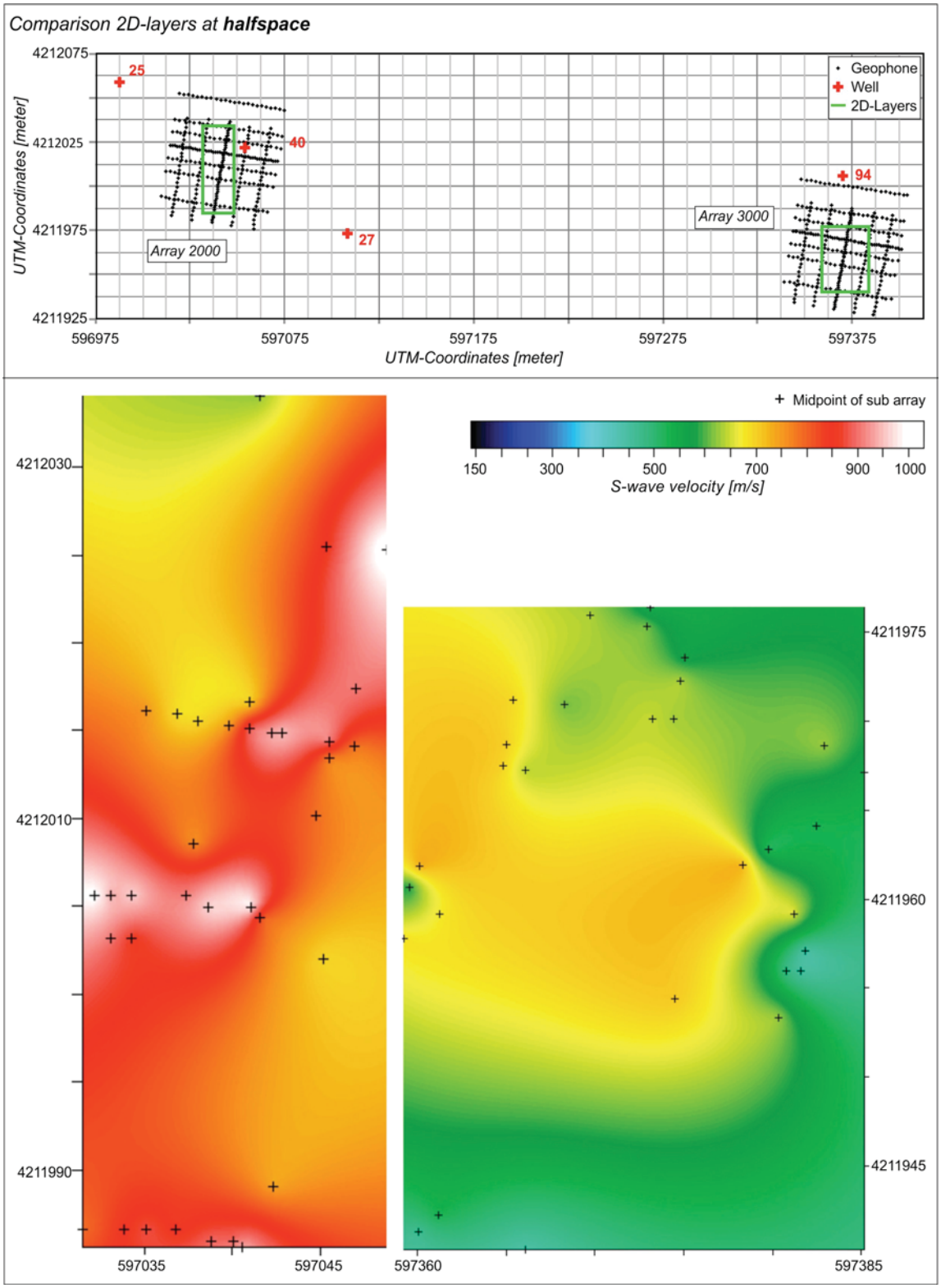
Comparison 2D-layers at halfspace
Geophone
Well
2D-Layers
25
40
27
94
Array 2000
Array 3000
UTM-Coordinates [meter]
4212075
4212025
4211975
4211925
596975
597075
597175
597275
597375
UTM-Coordinates [meter]
Midpoint of sub array
150
300
500
700
900
1000
S-wave velocity [m/s]
4212030
4212010
4211990
4211975
4211960
4211945
597035
597045
597360
597385

In the 2D interpolation layer at depths between 40 and 50 meters (Figure 7.7), results can be obtained from array 2000 only. Again, a shear wave velocity increase South of well 40 towards well 27 is observable, giving strong indications for the presence of a gallery between well 27 and well 40. On the other hand evidence for a connection between well 40 and well 25 can not be given, both because of limited data and because of no definite indications in the neighboring data.

The half space data (Figure 7.8) underline again the velocity differences between array 2000 and array 3000. It lets suspect that there are strong stress/stress abnormalities in the area below well 40. The distribution of the velocity highs inside array 2000 shows patterns that are different from those observed at shallower depth levels. Whereas the data around well 40 again shows maxima, the more Southern data towards well 27 seem less prominent than in the shallower depth layers. As there are not enough data points available at this deepest level, one can cautiously look at explanations. One assumption could be, that in the lower depth between well 40 and well 27 already some breakdowns have happened, which would lead to a shear wave reduction (see chapter 3.).

In summary, there is a significant difference in the shear wave velocities between array 2000 and array 3000 supporting the interpretation for the presence of a gallery between well 40 and well 27. Also a connection between well 40 and well 25 cannot completely be ruled out. A partial breakdown at the lower depths between well 40 and well 27 is conceivable. The area around well 94 seems to be much less exposed to abnormal stress and strain conditions than the area below array 2000. The central and northwestern part towards well 94 seems to have slightly higher shear wave velocity than the southern and eastern areas.

7.2 Array 4000

A railroad line- of great value for the local industries- is striking west-east along the northern border of the former salt dissolution mining field. To provide security for the frequently used traffic connection, the former well locations for dissolution mining and eventually developed underground voids along the rail tracks had to be surveyed. The passive MASW method has several benefits concerning the special challenge that such an investigation implies:

- Quick and uncomplicated measurement procedure requiring limited geophysical equipment and crew.
- Relative short processing time.
- Practicable in the small (about 5m between the ditch and railroad line, Figure 5.9 below) and not constant easy accessible area.
- Not invasive method.

The measurements have been conducted in summer 2011 within one day. During the daytime the geophones, geodes and cables have been deployed in a line along the tracks and during night the data has been collected.

For the railroad line the immediately along the line positioned former wells were of interest. Following questions should be answered with the measurements:

- Are there any voids under the wells; if yes, is there an immediate elevated risk potential for a collapse?
- Have any galleries been formed between the wells?

As a reaction on the results gained out of the measurements collected during summer 2010 (view chapter 7.1), in summer 2011 the void beneath well 40 was filled with sand. Therefore another question had to be answered:

- Are there any changes in the velocity fields around well 40?

The illustration in the bottom of Figure 7.9 shows the railroad line and, south of it, the position of the wells marked with red circles, (with their particular numbering system).

360 geophones were available for the survey. The relatively large number of geophones made it possible to cover all of the wells at once, by choosing a long line as geophone configuration. This receiver layout has the advantage to cope with the small accessible investigation area, additionally it minimized measurements time and reduced the effort on field to its minimum. Furthermore it allowed a comparison between the wells at similar conditions. As the main

propagation path of train-generated surface waves was parallel to the array, this simple geometry was deemed sufficient for the purpose.

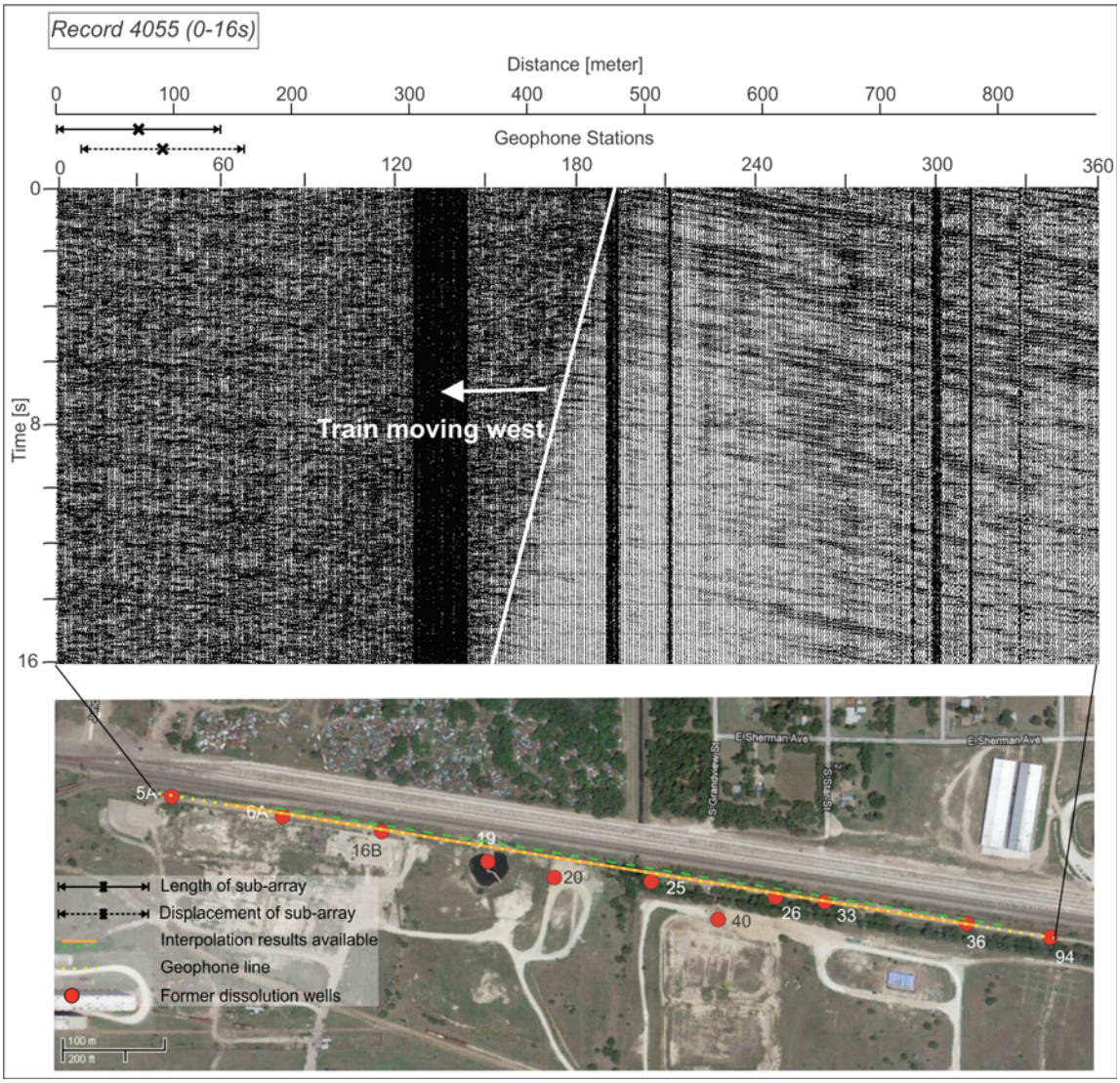

Figure 7.9 *Up: Record 4055 (0-16s) with train moving towards West, bottom: Recording line with 360 receivers and wells in closeness of the line.*

As the chosen array configuration is a one-dimensional one, and not capable to deliver directional determination, the initial plan involved a small 3D array at the midst of the receiver line. That additional receiver layout would have made it possible to localize the origin of passive signal and to process in a further step only time sections which possess only energy that is in line with the geophone line.

A quite large offset of 2.5 m has been chosen as geophone spacing. As the interest lies in the lower investigation depths that offset fulfills its duty by far. But the amount of available geophones was too small to realize the 3D array at the end of the line.

The pointed yellow line in the bottom illustration of Figure 7.9 shows the position and the trajectory of all the deployed geophones. The orange line shows the extension of the underground along the geophones for which results for the shear wave velocity were calculable.

The lack of the 3D array had to be compensated with additional effort: To avoid signals from unknown directions, data were collected at night. Men were positioned near the tracks (West-East and North-South) about 2 km from the seismic recording van, with good view towards west and east or respectively towards north and south. Trains were announced to the van, where the observer started the measurements, even before signals could be detected on the noise monitor. Additional signals were avoided. A small 3D arrangement of geophones could have avoided this additional effort.

The upper picture in Figure 7.9 shows 16 seconds of raw data. In this data a train is moving towards west. At 16 seconds the train has already passed station 150, and here the information from station 150 up to 360 can be converted into dispersion curves. Immediately at the start of the record the train was to close to station 150 and the noise is still too large to see resolvable signals. At the start of the record, usable data reach from geophone 195 till the east end of the line.

Between the two horizontal axes of the raw seismic data in Fig.7.9, distance and geophone number, the length of the black arrow shows the amount of geophones or respectively the surface distance, which was used for the calculation of one dispersion curve. It shows hence also the amount of information (lateral ground coverage) that is used to calculate one depth profile of shear wave velocities. The dashed black arrow shows the position of the used geophones for the adjacent calculation.

Figure 7.10 shows four of the overtone images calculated out of 60 geophones. The resolution of the images is limited at a frequency of about 3.5Hz, which implies in the analyzed area, an investigation depth up to 60m. From the overtone images one can extract clearly the dispersion curves. The inversion results are shown in frequency-velocity-depth diagrams on the right hand side of Figure 7.10 showing the dispersion curve with their phase velocities and the angular curve showing the depth steps with each shear wave velocity respectively In Table 7.3 inversion results for array 4000 are listed. Data marked in yellow present the results gained out of the dispersion curves illustrated in Figure 7.10. The data of Table 7.3 are used to create the 2D shear wave velocity section of Figure 7.12.

Figure 7.10 (followin page) *a, b, c and d: Random overtone images of array 4000; A,B, C and D: Inversion result for dispersion curve a,b,c and d: the dots represent points of the originally picked dispersion curve, which have been interpolated first with a blue curve, the curve is than adapted after*

each run to fit a suitable depth - S-wave model, the block curve (blue) represents the final inversion results, the fine black block curve represents the result of the corresponding previous calculation run;

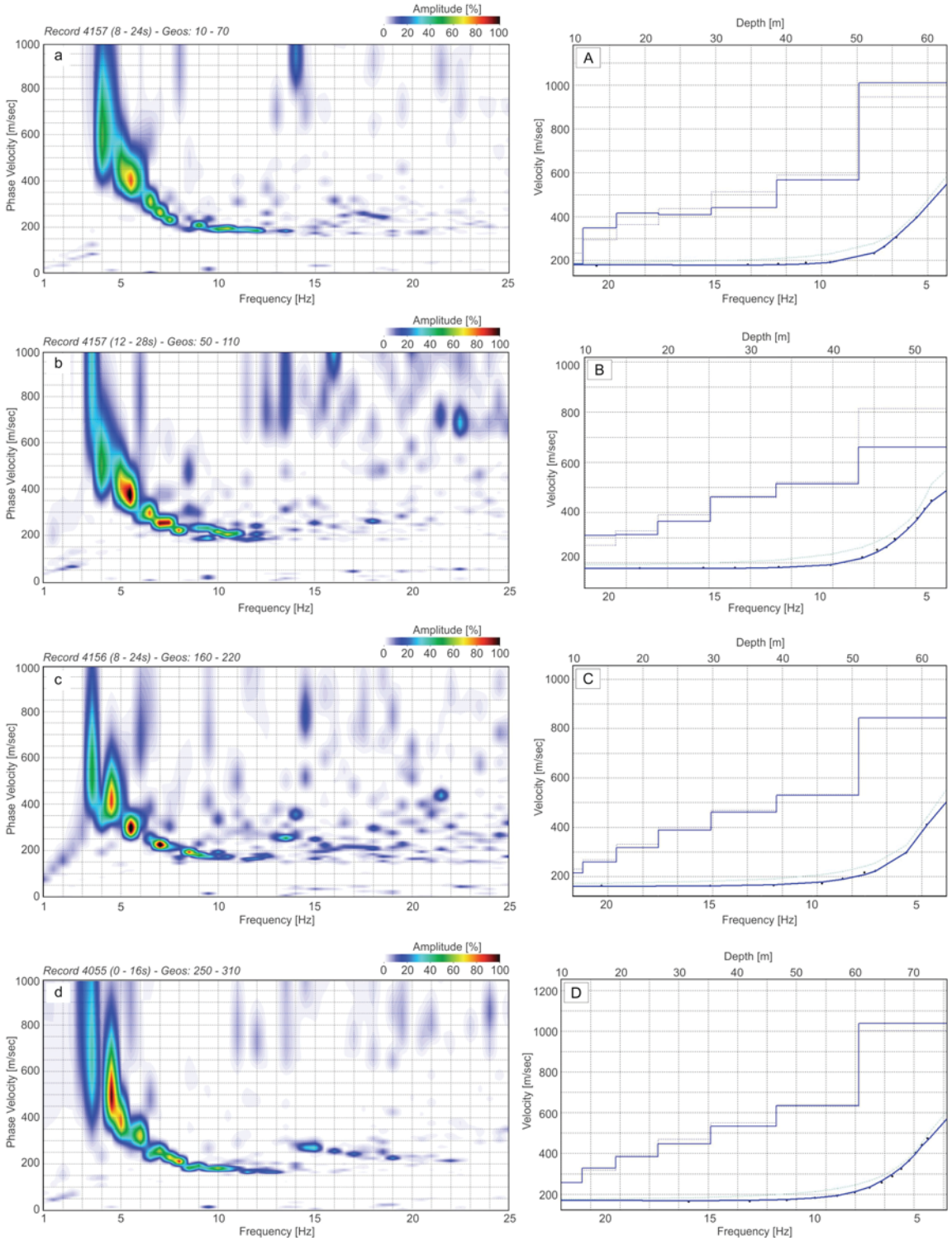

Geophone stations	Profile meters	Record	Depth 11 - 15 m	16 - 20 m	21 - 25 m	26 - 30 m	31 - 40 m	41 - 50 m	51 - 60 m	Halfspace
30	72.5	4157 (12 - 18s)	235.01	321.37	360.93		413.61			709.04
40	97.5	4157 (08 - 24s)	184.23	348.68	416.68	408.50	440.06	567.28		1010.45
50	122.5	4157 (00 - 16s)	224.35	283.81	344.55	414.21	489.81			796.86
60	147.5	4157 (14 - 30s)	208.13	309.78	393.25	404.39	399.86			651.79
70	172.5	4157 (00 - 16s)	214.80	309.19		372.61	442.61			718.78
80	197.5	4157 (12 - 28s)	308.84	311.49		365.10	463.62	514.09		661.19
90	222.5	4056 (14 - 30s)	240.33	341.06	410.73	453.24				666.84
100	247.5	4157 (00 - 16s)	246.68	314.94	365.41	426.27	508.47			838.64
110	272.5	4157 (00 - 16s)	219.49	302.63	371.10	434.50				694.48
120	297.5	4056 (06 - 22s)	317.00	374.77		380.71	436.78			816.46
130	322.5	4056 (14 - 30s)	343.57			366.62	432.09	552.37		995.65
140	347.5	4157 (16 - 32s)	325.00	328.30		341.53	440.05			589.56
150	372.5	4157 (04 - 20s)	185.07	271.90	345.61	402.05	472.05	535.16		797.64
160	397.5	4056 (14 - 30s)	260.29	324.14		331.56	420.10			750.25
170	422.5	4157 (04 - 20s)	259.77	343.26		410.49	463.35			686.07
180	447.5	4056 (00 - 16s)		324.15	380.39	408.11	438.44	474.40		676.41
190	472.5	4156 (02 - 18s)	214.10	258.71	317.92	387.97	460.60	528.51		843.03
200	497.5	4055 (14 - 30s)	228.47	300.60	384.01					799.63
210	522.5	4055 (16 - 32s)	280.62	344.36	360.74		391.33	475.64		829.95
220	547.5	4055 (14 - 30s)	229.85	294.23		373.91	429.56	507.31		869.06
230	572.5	4055 (04 - 20s)	233.25	323.71	370.85		367.43	406.43		713.21
240	597.5	4157 (00 - 16s)	232.92	283.85	391.57		457.62			532.37
250	622.5	4055 (00 - 16s)			315.73		427.90			740.50
260	647.5	4156 (00 - 16s)	244.97	312.72	346.74	394.38	478.69			815.29
270	672.5	4055 (00 - 16s)	293.28	302.26	312.49	359.61	445.79			783.36
280	697.5	4055 (00 - 16s)	257.89	327.67		384.26	447.26	534.24	635.16	1038.33
290	722.5	4156 (00 - 16s)	196.72	338.72	342.30	396.11	534.96		593.73	701.15
300	747.5	4156 (00 - 16s)	211.96	317.02	378.94		415.35	467.91	554.81	927.16
310	772.5	4156 (00 - 16s)	241.17	296.95	353.21		420.05			681.50
320	797.5	4156 (08 - 24s)	218.75	281.04	327.01	395.73	473.60		545.43	867.42
330	822.5	4156 (00 - 16s)	270.51	303.16	311.74		368.59			661.62

Table 7.3 (previous page) *Inversion results from dispersion curves of array 4000. Columns 1 and 2: Midpoints of sub-arrays. Column 3: records with the chosen time section. Columns 4 to 11: shear wave velocities for certain depth steps.*

Figure 7.11 shows a 2D shear wave velocity section created from several 1D results from the linear array 4000. As the estimations for the halfspace are not as reliable as the results for the upper layers, they are not included in the 2D section; the dark blue color substitutes therefore the halfspace data. Halfspace data and results from 40m downwards are shown additionally in Figure 7.12 as lateral 1D layers of each depth step respectively.

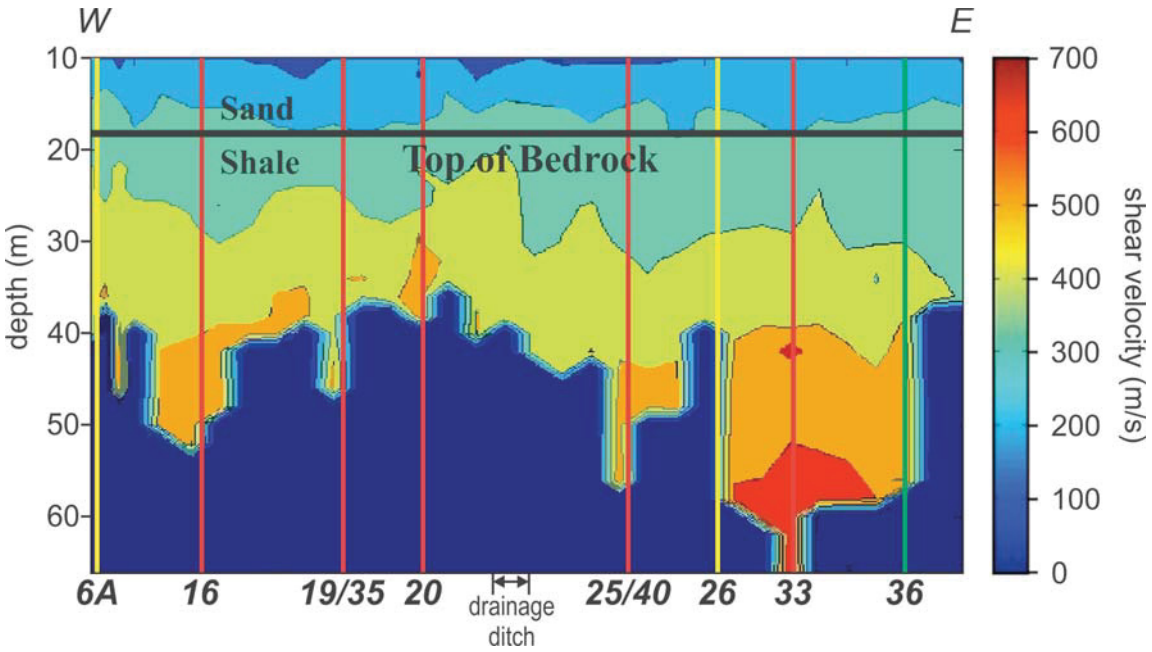

Figure 7.11 *2D shear wave velocity profile of array 4000; red lines mark well with higher velocity buildups, yellow lines stand for extra stress fields, green line marks a well which seems influenced from a nearby stressfield.*

The wells were classified into 3 groups (see Figure 7.11):

- Red: a relative high shear wave velocity zone around the wells (16, 19/35, 20, 25/40, 33) has been detected; each of these wells have also been investigated by invasive methods and they are identified as voids having already migrated into the shale overburden.

- Yellow: no relative high velocity zone has been detected around the investigated wells (6A, 26); invasive investigations confirm that in the shale overburden of these wells no voids are present.
- Green: the well (36) is probably influenced by the stress field of a void of a near by well (33).

The cavern at Well 16 shows a buildup in shear velocity, which seems appropriate concerning that the void near top of salt is relatively small.

The small increase in shear wave velocity around Well 19/35 can be explained by the fact that the void/gallery below the well, has developed to some extent into a sinkhole and leads therefore to a partial stress release.

The cavern at well 20 shows a stress build up already at shallow depth, this seems plausible according to the acoustic borehole imager and other well log data (Ivanov et al., 2013) that show a cavern of a larger size and hints of multiple fractures in the roof rocks. Even if fracturing already releases some of the stress build-up, it is an evidence for irregularly distributed stress and strain behavior above the void. The failure process of the roof rock that follows fracturing usually leads to a reduction of shear wave velocity.

The stress field around the well 25/40 which has a large void underneath and probably also a gallery has been investigated at array 2000 also a year earlier to the investigations of array 4000. During the investigation of array 4000 well 40 has been filled with large amounts of sands. The smaller as expected stress build up could be already a reaction on this action.

Well log data suggest a quite large cavern beneath well 33 and show also relatively few fractures in the roof rock (Ivanov, et al., 2013), in support of a stress build up around well 33.

As well 36 seems to have no significant cavern underneath, the calculated stress field is probably influenced by the elevated stress build up around well 33.

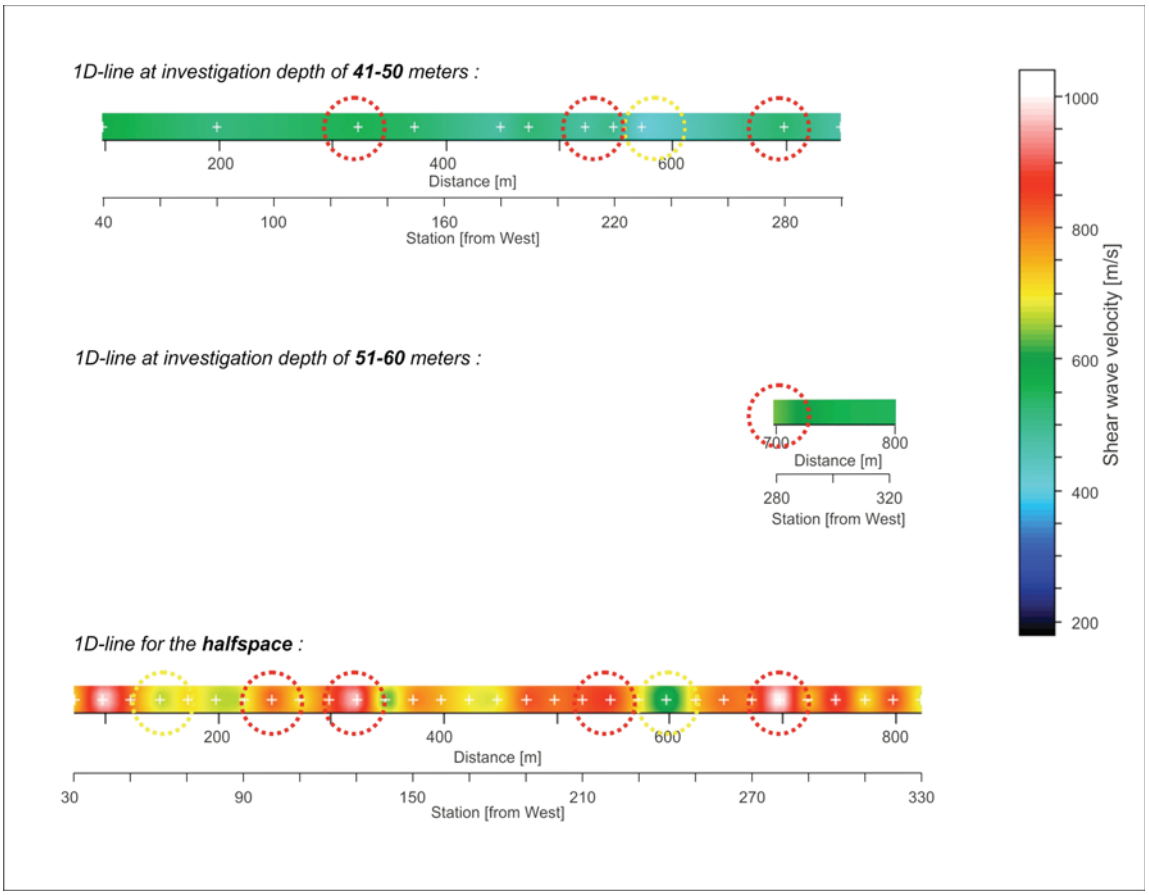

Figure 7.12 *1D lateral layers for the three depth section of 41m to 50m, 51m to 60m and halfspace; red circle show zones of elevated stress field, yellow circles mark zones with no stress elevation.*

8 Conclusions

The present study leads to several results: First, the passive MASW method could be improved and extensively tested with the help of several datasets. The datasets were obtained from various large receiver configurations with freight trains as passive sources and processed with the aid of the program SurfSeis® and further software developed as part of this study. Field techniques as well as data processing and analysis components were studied and developed.

Secondly, the new methodology was employed to investigate the condition of different salt migration voids and their surroundings, which had been studied before by other authors; new and more detailed results could be obtained.

Quality and reliability of results derived from passive MASW depend crucially on the properties of the receiver configuration. Clearly, the array must be safe against aliasing effects and have an optimal "array-dimension / investigation depth" ratio. When passive signals are recorded, they come from an arbitrary distance and direction. As consequence the position of the signal lies normally not in the extension of the 1D linear receiver array as it is in the active MASW method. To obtain an optimal result in resolution, investigation depth and in the amount of depth profiles, it is necessary to know the direction where the passive source is coming from. With a 2D spread it is possible to locate the direction of the recorded energy. From the overall array several sub-arrays are selected. The sub-arrays used here have receivers inside a narrow rectangle that is orientated towards the maximum incoming energy. The signals of each rectangle are stacked over narrow limits around the azimuth of maximum incoming energy.

A key step in processing the passive MASW data is retaining only records that have good broadband energy principally from one direction and then finding an adequate time window within those higher quality records. The time section needs to be long enough to capture a representative segment of information, but short enough to constrain energy to a stable azimuth angle, - at least for the frequencies of interest.

The other task for this study was to detect salt dissolution voids by the registration of irregular stress and strain condition in the bedrock and to evaluate their collapse potential. The trains as passive sources produced signals with frequencies down to 3.5Hz. The large array setting enabled to process these extremely low frequency signals without generating undesirable artefacts and reaching an investigation depth down to 70m. In contrast to the former investigations with active MASW, during this study the bedrock (~20m) could be reached easily. The transmission of the stress and strain behavior over hard rock formations in comparison to hard rock to unconsolidated rock formations is much more undisturbed, this is reflected in the results, which are by far more distinct and reliable.

There could be determined an obvious difference in the shear wave velocities and with it, in the stress field, between areas with voids underneath and analogy terrains with no voids underneath. Also evidences for an existence of galleries between voids could be detected. A differentiation

for a relative risk of collapse between the investigated locations was possible.

The investigation results could be verified, when some of the areas identified as high risk zones were drilled or re-drilled and the underground voids and galleries (assumed to exist because of the data results and verified because of the amounts of sand needed to fill up single wells) were filled up with sand.

References

Aki, K., (1957). Space and time spectra of stationary stochastic waves, with special reference to micro-tremors. Bull. Earthq. Res. Inst., v. 35, p. 415-456.

Al-Eqabi, G. and Hermann, B. R., (1993). Ground roll: A potential tool for constraining shallow shear-wave structure, Geophysics, Vol. 58, No. 5, p.713 – 719.

Asten, M.W., (1978). Geological control on the three-component spectra of Rayleigh-wave microseisms. Bull., Seism. Soc. Am., v. 68, p. 1623-1636.

Brown G. C. and Musset, A. E. (1981). The Inaccessible Earth. George Allen & Unwin Ltd.

Bullen, K.E., (1963). An Introduction to the Theory of Seismology. Cambridge University Press, New York, pp. 381.

Dellwig, L.F., (1963). Environment and mechanics of deposition of the Permian Hutchinson Salt Member of the Wellington shale. Symposium on Salt, Northern Ohio Geological Society, p. 74-85.

Dorman, J., and Ewing, M. (1962). Numerical inversion of seismic surface wave dispersion data and crust-mantle structure in the New York-Pennsylvania area. J. Geophys. Res., v. 67, p. 5227-5241;

Dorman, J., Ewing, M. and Oliver, J. (1960). Study of shear Yelocity distribution by mantle Rayleighwaves, Bull. Seismal. Soc. Am., v. 50, p. 87-115,.

Eberhart-Phillips, D., Han D.-H. and Zoback M.D., (1989). Empirical relationships amongseismic velocity, effective pressure, porosity, and clay content in sandstone. Geophysics, v. 54, p. 82–89.

Ewing, W. M., Jardetzky, W. S. and Press, F., (1957). Elastic Waves In Layered Media. McGraw-Hill Book Company Inc., New York.

Fowler, C. M. R. (1990). The solid earth. Cambridge, UK: Cambridge University Press

Freund, D., (1992). Ultrasonic compressional and shear velocities in dry clastic rocks as a function of porosity, clay content, and confining pressure. Geophysical Journal International, v. 108, p. 125–135.

Heard, H.C., Borg, I.Y., Carter, N.L. and Raleigh, C.B., (1972) Flow and Fracture of Rocks. Geophysical Monograph 16, American Geophysical Union, Washington, D.C..

Herrmann, R. B. and Al-Eqabi, G., (1991). Surface waves: Inversion for shear wave velocity, in Shear Waves in Marine Sediments. Edited by Hovem, J. M., Richardson, M.D. and Stoll, R. D., pp. 545 - 556, Springer, NewYork.

Holdoway, K.A., (1978). Deposition of evaporites and red beds of the Nippewalla Group, Permian, western Kansas. Kansas Geological Survey Bulletin 215.

Ivanov, J., Leitner, B., Shefchik, W. T., Schwenk, T. J. and Peterie, S. L., (2013). Evaluating hazards at salt cavern sites using multichannel analysis of surface waves. The Leading Edge, v. 32, p.289-305.

Joh, S.H., (1996). Advances in the Data Interpretation Technique for Spectral-Analysis-of-Surface-Waves (SASW) Measurements. Ph.D. Dissertation, The University of Texas at Austin, pp. 241.

Jones, S.M., (1995). Velocities and quality factors of sedimentary rocks at low and high effective pressures. Geophysical Journal International, v. 123, p. 774–780.

Keilis−Borok, V.I., Kossobokov, V.G. and Mazhkenov, S.A., (1989). On similarity in spatial seismicity distribution. Computational Seismology, v. 22, p. 28−40, Moscow, Nauka.

Khasar, A., Griffiths, C.M. and McCann, C., (1999). Compressional - and shear wave velocities as a function of confining stress in dry sandstones. Geophysical Prospecting, v. 47, n. 4

Knopoff, L., (1972). Observation and inversion of surface-wave dispersion. Tectonophysics v. 13, p. 497–519.;

Kovach, R.L., (1978). Seismic surface waves and crustal and upper mantle structure. Rev. Geophys. Space Phys., v. 16, p. l-13.

Kulstad, R.O., (1959). Thickness and salt percentage of the Hutchinson salt; in, Symposium on Geophysics in Kansas. Kansas Geological Survey, Bulletin 137, p. 241-247.

Lambrecht, J. L. and Miller, R. D., (2006). Catastrophic sinkhole formation in Kansas: A case study. The Leading Edge, v. 25, n. 3, p. 342-347.

Lay, T., and T. C. Wallace (1995). Modern Global Seismology, Academic Press, San Diego, 521pp.

Louie, J.N., (2001). Faster, better: shear-wave velocity to 100 meters depth from refraction microtremor arrays. Bulletin of the Seismological Society of America, v. 91, n. 2, p. 347-364.

Love, A.E.H., (1911). Some problems of geodynamics. Cambridge University Press.

Matthews, M.C., Hope, V.S. and Clayton, C.R.I. (1996). The use of surface waves in the determination of ground stiffness profiles. Proc. Instn. Civ. Engrs. Geotech. Engng, 119 (April): 84-95.

McMechan, G. and Yedlin, M.J., (1981). Analysis of dispersive waves by wave field transformation. Geophysics, v. 46, n. 6, p. 869-874.

Merriam, D.F., (1963). The Geologic History of Kansas. Kansas Geological Survey Bulletin162, p. 317.

Miller, R.D., (2007). High-Resolution Seismic Investigation of Subsidence from Dissolution, Dissertation, Montanuniversität Leoben, Austria, pp. 417.

Miller, R.D., Sloan, S.D., Walters, S.L., Ivanov, J., Leitner, B., Rech, A., Wedel, B.A., Wedel, A.R., Anderson, J.M., Metheny, O.M., Schwarzer, J.C., (2009). Shear-wave Seismic Study above Vigindustries, Inc. Legacy Salt Jugs in Hutchinson, Kansas. Kansas Geological Survey, Open-file Report n. 2009-3, p. 42.

Miller, R.D., Steeples, D.W., Schulte, L. and Davenport, J. (1993). Shallow seismic reflection study of a salt dissolution well field near Hutchinson, Kansas. Mining Engineering, October, p. 1291-1296.

Mokhtar, T. A., Herrmannt, R. and Russell, D. R., (1988). Seismic velocity and Q model for the shallow structure of the Arabian shield from short-period Rayleigh waves, Geophysics, v. 53, p. 1379-1387.

Nazarian, S. and Stokoe, K.H. II, (1984). Use of Surface Waves in Pavement Evaluation. Transportation Research Record, Vol. 1070, pp. 132-144.

Okada, H., (2003).The microtremor survey method. Geophysical monograph series, n. 12, published by Society of Exploration Geophysicists (SEG), Tulsa, OK.

Park, C. B. and Miller, R.D., (2008). Roadside passive multichannel analysis of surface waves (MASW). Journal of Environmental & Engineering Geophysics, v. 13, n. 1, p. 1-11.

Park, C. B., Miller, R. D., Ryden, N., Xia, J., and Ivanov, J., (2005). Combined use of active and passive surface waves. Journal of Environmental & Engineering Geophysics, v. 10, n. 3, p. 323-334.

Park, C., Miller, R., Laflen, D., Cabrillo, N., Ivanov, J., Bennett, B. and Huggins, R. (2004). Imaging dis-persion curves of passive surface waves. [Exp. Abs.] Soc. Expl. Geophys., p. 1357-1360.

Park, C.B., (2008). Imaging dispersion of passive surface waves with active scheme: Symposium on the Application of Geophysics to Engineering and Environmental Problems. (SAGEEP 2008), Philadelphia, April 6-10, Proceedings on CD Rom.

Park, C.B., Miller, R.D. and Xia, J., (1998). Imaging dispersion curves of surface waves on multi-channel record. 68th Ann. Internat. Mtg. Soc. Expl. Geophys., Expanded Abstracts, p. 1377-1380.

Park, C.B., Miller, R.D., Ryden, N., Xia, J. and Ivanov, J., (2005). Combined use of active and passive surface waves: Journal of Environmental & Engineering Geophysics. v. 10, n. 3, p. 323-334.

Park, C.B., Miller, R.D., Xia, J. and Ivanov, J., (2001). Characterization of geotechnical sites by Multichannel Analysis of Surface Waves (MASW) method. Tenth International Conference on Soil Dynamics and Earthquake Engineering (SDEE), Philadelphia, October 2001.

Park, C.B., Miller, R.D., Xia, J., and Ivanov, J., (2007). Multichannel analysis of surface waves (MASW)--active and passive methods. The Leading Edge, January.

Richart, F.E Jr., Hall, J.R., and Woods, R.D. (1970). Vibrations of Soils and Foundations. Prentice Hall, Inc., New Jersey.

Rix, G. J. and Leipski, E. A., (1991). Accuracy and resolution of surfacewave inversion. In Bhatia, S. K., and Blaney, G. W., Eds., Recent advances in instrumentation, data acquisition and testing in soil dynamics:Am. Soc. Civil Eng., 17–32.

Rix, G. J. and Stokoe, K. H., II (1989), "Stiffness Profiling of Pavement Subgrades,"

Schwab, F. and Knopoff, L., (1972). Fast surface wave and free mode computations. In Bolt, B.A., Edition, Methods in computational physics, Academic Press, p. 87 – 180.

Sheriff, R. E., (2002). Encyclopedic dictionary of applied geophysics. SEG Geophysical Reference Series n. 13, Society of Exploration Geophysicists (SEG), Tulsa, Oklahoma, pp. 429.

Spinazola, J.M., Gillespie, J.B. and Hart, R.J. (1985). Ground-water flow and solute transportin the Equus beds area, south-central Kansas, 1940-1979. U.S. Geological Survey,Water-Resources Investigations Report 85-4336, pp. 68.

Stokoe, K. H., II, Wright, G. W., James, A. B., and Jose, M. R., (1994). Characterization of geotechnical sites by SASW method. In Woods, R. D., Ed., Geophysical characterization of sites: Oxford Publ.

Strutt, JW (Lord Rayleigh), (1887). On the Maintenance of Vibrations by Forces of Double Frequency, and on the Propagation of Waves Through a Medium Endowed with a Periodic Structure. Phil. Mag., S.5, vol.24, n.147, pp.145-159.

Subirana, S.J., Zornoza, J.J.M. and Hernández-Pajares, M., (2011). Phase & Group Velocity, Http://www.navipedia.net

Suto, K., (2007). Multichannel analysis of surface waves (MASW) for investigation of ground competence: an introduction. In: Engineering Advances in Earthworks, Proceedings of the Sydney Chapter 2007 Symposium, Australian Geomechanics Society, p. 71-81.

Suzuki, H and Hayashi, K., (2003). Shallow s-wave velocity sounding using the Microtremors array measurements and the surface wave method. Proceedings of the SAGEEP 2003, San Antonio, Texas, SUR08, Proceedings on CD ROM.

Transportation Research Record, No. 1235, Washington, D.C., pp. 1-9.

Van der Pol, C., (1951). Dynamic testing of road constructions. J. appl. Chem., v. 1, July, p. 281-290.

Walters, R.F., (1977). Land subsidence in central Kansas related to salt dissolution. Kansas Geological Survey, Bulletin 214, p. 82.

Watney, W.L., Berg, J.A. and Paul, S., (1988). Origin and distribution of the Hutchinson salt (lower Leonardian) in Kansas. Midcontinent SEPM Special Publication, n. 1, p. 113-135.

Winkler, K.W., (2005). Borehole damage indicator from stress induced velocity variations. Geophysics, v. 70, n .1

Xia,J. Miller, R.D. and Park, C.B.,(1999). Estimation of near surface shear wave velocity by inversion of Rayleigh waves. Geophysics, v. 64, 3.

Xia,J. Miller, R.D.,Park, C.B., Hunter, J.A., Harris, J.B. and Ivanov, J., (2002). Comparing shear wave velocity profiles from multichannel analysis of surface wave with borehole measurements. Soil dynamics and Earthquake Engineering, v. 22, n. 3, p. 181-190.

Yoon, S. and Rix, G., (2004). Combined active-passive surface wave measurements for near-surface site characterization. Proceedings of the SAGEEP 2004, Colorado Springs, CO, SUR03, Proceedings on CD ROM.

Websites:

www.masw.com

www.rocscience.com/education/hoeks_corner

www.navipedia.net, J. Sanz Subirana, J.M. Juan Zornoza and M. Hernández-Pajares, Phase & Group Velocity,